

**Wetland Mapping and Monitoring Using Polarimetric and Interferometric  
Synthetic Aperture Radar (SAR) Data and Tools**

by

© Fariba Mohammadimanesh

A thesis submitted to the  
School of Graduate Studies  
in partial fulfilment of the requirements for the degree of  
**Doctor of Philosophy**

**Faculty of Engineering and Applied Science**  
Memorial University of Newfoundland

October 2019

St. John's, Newfoundland and Labrador

---

*Dedicated to  
my husband and my  
parents*

---

## **Abstract**

Wetlands are home to a great variety of flora and fauna species and provide several unique environmental functions, such as controlling floods, improving water-quality, supporting wildlife habitat, and shoreline stabilization. Detailed information on spatial distribution of wetland classes is crucial for sustainable management and resource assessment. Furthermore, hydrological monitoring of wetlands is also important for maintaining and preserving the habitat of various plant and animal species. This thesis investigates the existing knowledge and technological challenges associated with wetland mapping and monitoring and evaluates the limitations of the methodologies that have been developed to date. The study also proposes new methods to improve the characterization of these productive ecosystems using advanced remote sensing (RS) tools and data. Specifically, a comprehensive literature review on wetland monitoring using Synthetic Aperture Radar (SAR) and Interferometric SAR (InSAR) techniques is provided. The application of the InSAR technique for wetland mapping provides the following advantages: (i) the high sensitivity of interferometric coherence to land cover changes is taken into account and (ii) the exploitation of interferometric coherence for wetland classification further enhances the discrimination between similar wetland classes. A statistical analysis of the interferometric coherence and SAR backscattering variation of Canadian wetlands, which are ignored in the literature, is carried out using multi-temporal, multi-frequency, and multi-polarization SAR data. The study also examines the capability of compact polarimetry (CP) SAR data, which will be collected by the upcoming RADARSAT Constellation Mission (RCM) and will constitute the main source of SAR observation in Canada, for wetland mapping. The research in this dissertation proposes a methodology for wetland classification using the synergistic use of intensity, polarimetry, and interferometry features using a novel classification framework. Finally, this work

introduces a novel model based on the deep convolutional neural network (CNN) for wetland classification that can be trained in an end-to-end scheme and is specifically designed for the classification of wetland complexes using polarimetric SAR (PolSAR) imagery. The results of the proposed methods are promising and will significantly contribute to the ongoing efforts of conservation strategies for wetlands and monitoring changes. The approaches presented in this thesis serve as frameworks, progressing towards an operational methodology for mapping wetland complexes in Canada, as well as other wetlands worldwide with similar ecological characteristics.

**Keywords:** Wetland, remote sensing, Synthetic Aperture Radar (SAR), Interferometric SAR (InSAR), coherence, compact polarimetry, RADARSAT Constellation Mission (RCM), polarimetric SAR (PolSAR), deep convolutional neural network (CNN).

## **Acknowledgement**

I would like to express my sincere gratitude and appreciation to my supervisor Dr. Bahram Salehi for his guidance, encouragement, and advice throughout the research. His suggestions and insights regarding the fundamentals of this topic have been invaluable. I would also like to thank Dr. Brian Brisco and Dr. Eric Gill for serving as my co-supervisors and for providing helpful comments and discussions throughout the preparation of this thesis.

The author's software and hardware enquiries and demands were well attended to by present and former personnel of C-CORE. I would also like to acknowledge the financial support of the Government of Canada through the Federal Department of Environment and Climate Change, the Research & Development Corporation of Newfoundland and Labrador, and Natural Sciences and Engineering Research Council of Canada (NSERC RGPIN-2015- 05027) for their generous financial support, without which the pursuit of this research would not have been possible. I wish to thank the German Aerospace Agency (DLR), the Canada Center for Mapping and Earth Observation, and Environment and Climate Change Canada for providing SAR imagery. Field data were collected by various organizations, including Ducks Unlimited Canada, Government of Newfoundland and Labrador Department of Environment and Conservation, and Nature Conservancy Canada. The author thanks these organizations for providing such valuable datasets. I would also like to thank my parents and sister for their support and encouragement. Finally, this work could not have been completed without the unfailing patience, understanding, and the never-ending love of my husband.

# Table of Contents

<b>ABSTRACT</b>	<b>III</b>
<b>ACKNOWLEDGEMENT</b>	<b>V</b>
<b>TABLE OF CONTENTS</b>	<b>VI</b>
<b>LIST OF TABLES</b>	<b>X</b>
<b>LIST OF FIGURES</b>	<b>XII</b>
<b>LIST OF ABBREVIATIONS AND SYMBOLS</b>	<b>XVI</b>
<b>CHAPTER 1. INTRODUCTION</b>	<b>1</b>
1.1. Overview	1
1.2. Background	3
1.3. Research motivations	8
1.4. Scope and objectives	9
1.5. Contribution and novelty	10
1.5.1. InSAR wetland	11
1.5.2. Interferometric coherence and SAR backscattering variation of Canadian wetland	11
1.5.3. Incorporating interferometric coherence into the classification scheme	12
1.5.4. Optimization of the number and types of input features for wetland classification	13
1.5.5. Wetland classification using Compact Polarimetric (CP) SAR data	13
1.5.6. Wetland classification using deep learning	14
1.6. Organization of the thesis	14
1.7. Other publications and book chapter	16
1.8. References	18
<b>CHAPTER 2. SAR AND INSAR WETLANDS</b>	<b>23</b>
Preface	23
Abstract	23
2.1. Introduction	24

<b>2.2. Wetland water level monitoring using InSAR</b>	<b>26</b>
2.2.1. Wetland InSAR	26
2.2.2. Wetland Phenology	36
2.2.3. The Primary Limitations of InSAR Wetland Application	37
<b>2.3. Trend in using the InSAR technique for wetland monitoring</b>	<b>41</b>
<b>2.4. Discussion of current constraints and direction of future reseach</b>	<b>44</b>
<b>2.5. Conclusion</b>	<b>49</b>
<b>2.6. References</b>	<b>50</b>
<b>CHAPTER 3. COHERENCE AND SAR BACKSCATTER ANALYSES OF CANADIAN WETLANDS</b>	<b>58</b>
<b>Preface</b>	<b>58</b>
<b>Abstract</b>	<b>58</b>
<b>3.1. Introduction</b>	<b>59</b>
<b>3.2. Methods</b>	<b>63</b>
3.2.1. Study area and field data	63
3.2.2. Satellite images	66
3.2.3. Generation of the coherence images	67
3.2.4. SAR backscatter coefficient images	69
3.2.5. Object-Based Random Forest classification	72
<b>3.3. Results</b>	<b>74</b>
3.3.1. Coherence analysis of different SAR wavelengths	74
3.3.2. Coherence comparison between different SAR wavelengths	79
3.3.3. Coherence comparison in multi-polarized C-band SAR images	81
3.3.4. The relationship between coherence and SAR backscatter variation	83
3.3.5. Classification	87
<b>3.4. Discussion</b>	<b>90</b>
<b>3.5. Conclusion</b>	<b>98</b>
<b>3.6. References</b>	<b>100</b>
<b>CHAPTER 4. FEATURE OPTIMIZATION FOR WETLAND MAPPING</b>	<b>103</b>
<b>Preface</b>	<b>103</b>
<b>Abstract</b>	<b>103</b>
<b>4.1. Introduction</b>	<b>104</b>
<b>4.2. Study Area and Data</b>	<b>108</b>

<b>4.3. Methods</b>	<b>110</b>
4.3.1. Feature Extraction	111
4.3.2. Image classification	113
4.3.3. Variable reduction	116
<b>4.4. Results and Discussion</b>	<b>117</b>
<b>4.5. Conclusion</b>	<b>130</b>
<b>4.6. References</b>	<b>131</b>
<b>CHAPTER 5. COMPACT POLARIMETRIC SAR RESPONSES TO CANADIAN WETLANDS</b>	<b>133</b>
<b>Preface</b>	<b>133</b>
<b>Abstract</b>	<b>133</b>
<b>5.1. Introduction</b>	<b>134</b>
<b>5.2. Study Area and Data</b>	<b>140</b>
5.2.1. Study Area and In-Situ Data	140
5.2.2. Satellite Imagery	144
<b>5.3. Methods</b>	<b>145</b>
5.3.1. Full Polarimetric SAR Data Processing	145
5.3.2. Compact Polarimetry SAR Data Processing	147
5.3.3. Backscattering and Separability Analyses	150
5.3.4. Classification Scheme	151
5.3.5. Evaluation Indices	153
<b>5.4. Results and Discussion</b>	<b>153</b>
5.4.1. Backscattering Analysis	153
5.4.2. Separability Analysis	160
5.4.3. Classification Results	164
<b>5.5. Conclusions</b>	<b>170</b>
<b>5.6. References</b>	<b>171</b>
<b>CHAPTER 6. FULLY CONVOLUTIONAL NETWORK (FCN) FOR WETLAND CLASSIFICATION</b>	<b>177</b>
<b>Preface</b>	<b>177</b>
<b>Abstract</b>	<b>177</b>
<b>6.1. Introduction</b>	<b>178</b>
<b>6.2. Convolutional Neural Network</b>	<b>182</b>
6.2.1. Convolutional layers	183

6.2.2. Non-linear function layer	185
6.2.3. Spatial pooling layer	186
6.2.4. Transposed convolutional layer	186
<b>6.3. Proposed network for classification of PolSAR imagery</b>	<b>187</b>
<b>6.4. Experimental design</b>	<b>192</b>
6.4.1. Study area and dataset	192
6.4.2. RADARSAT-2 data and feature extraction	193
6.4.3. Training and testing	195
6.4.5. Evaluation methods	196
6.4.6. Evaluation metrics	198
<b>6.5. Results and discussion</b>	<b>199</b>
6.5.1. Open the <i>black box</i> : feature visualization	199
6.5.2. On the importance of inception module and skip connections - ablation study	204
6.5.3. Classification results	205
<b>6.6. Conclusion</b>	<b>211</b>
<b>6.7. References</b>	<b>212</b>
<b>CHAPTER 7. SUMMARY, CONCLUSIONS, AND FUTURE OUTLOOK</b>	<b>216</b>
<b>7.1. Summary</b>	<b>216</b>
<b>7.2. Conclusions</b>	<b>217</b>
<b>7.3. Future outlook</b>	<b>220</b>
<b>7.4. References</b>	<b>223</b>

## List of Tables

Table 1.1. Organization of the thesis	15
Table 2.1. Characteristics of well-known SAR satellite missions that have been used for wetland monitoring.	33
Table 3.1. A description of land cover classes in this study.	65
Table 3.2. The characteristics of satellite images used in this study.	67
Table 3.3. P-values of the Wilcoxon rank sum test at the 5% significance level on the difference in means of intensity and coherence observations between different wetland classes.	86
Table 3.4. Overall accuracies and Kappa coefficients for RF classifications using different input features.	87
Table 3.5. Classification confusion matrix of the most accurate RF classification obtained by the inclusion of coherence and intensity layers. An overall accuracy of 74.33% and a Kappa coefficient of 0.66 were obtained.	89
Table 4.1. Specification of satellite imagery.	110
Table 4.2. An overview on extracted features in this study.	113
Table 4.3. Different classification scenarios employed in this study.	116
Table 4.4. Overall accuracies and Kappa coefficients for different classification scenarios.	117
Table 4.5. Confusion matrix for scenario 13 using the RF classifier (OA: 78.90%).	120
Table 4.6. Confusion matrix for scenario 13 using the SVM classifier (OA: 82.43%).	121
Table 4.7. Confusion matrix of the SVM classifier based on 22 important uncorrelated features (OA: 85.40%).	129
Table 5.1. Number of training and testing polygons for each class in the three pilot sites.	143
Table 5.2. Characteristics of RADARSAT-2 imagery used in this study.	144

Table 5.3. An overview of the investigated CP SAR features in this study.	148
Table 5.4. The overall accuracies and Kappa coefficients obtained from FP and CP SAR data for the three case studies.	164
Table 5.5. The confusion matrix of the Avalon classification map obtained from the FP SAR data. An overall accuracy of 90.73% and Kappa coefficient of 0.88 were achieved.	167
Table 5.6. The confusion matrix of the Avalon classification map obtained from the CP SAR data. An overall accuracy of 87.89% and Kappa coefficient of 0.85 were achieved.	168
Table 6.1. Configuration of the proposed network in this study.	189
Table 6.2. Configuration of inception and residual modules in this study.	191
Table 6.3. The training time (in seconds) per epoch for training FCNs in this study.	198
Table 6.4. Experimental results of the importance of the inception module and skip connections. The most accurate results are indicated in bold.	204
Table 6.5. Assessment of the segmentation results obtained from different methods. The most accurate results are indicated in bold.	205

## List of Figures

- Figure 2.1. Frequency of studies used InSAR for wetland monitoring in two-year time intervals since 2000. 41
- Figure 2.2. World map illustrating the location and frequency of wetland InSAR studies (red dots). 43
- Figure 2.3. Summary of studies that have used the InSAR technique for wetland water level monitoring. The applied frequencies, wetland classes, polarizations, and validation approaches are indicated. 44
- Figure 3.1. Level 3A RapidEye image (bands 3, 2, and 1), acquired on June 18, 2015, illustrating the geographic location of the study area with overlays of the Synthetic Aperture Radar (SAR) scenes. The circles mark the location of referenced polygons used for the coherence and backscattering analysis. 63
- Figure 3.2. Total precipitation in the Avalon study area for each month in 2016. 64
- Figure 3.3. ALOS PALSAR-1 coherence analysis results for wetland classes plotted as a function of perpendicular and temporal baselines. Dot sizes and colors are proportional to different coherence values. 76
- Figure 3.4. RADARSAT-2 (Ultrafine mode) coherence analysis results for wetland classes plotted as a function of perpendicular and temporal baselines. Dot sizes and colors are proportional to different coherence values. 77
- Figure 3.5. TerraSAR-X coherence analysis results for wetland classes plotted as a function of perpendicular and temporal baselines. Dot sizes and colors are proportional to different coherence values. 78
- Figure 3.6. Comparison between the interferometric coherence obtained with ALOS-1, RADARSAT-2, and TerraSAR-X data for each of the four wetland classes as a function of temporal baselines. Note the exponential decay rates between different SAR wavelengths. Also,  $f(x) = ae^{bx}$  and coefficients were obtained with 95% confidence bounds. 80
- Figure 3.7. Coherence in different polarization channels obtained by RADARSAT-2 FQ22 product for wetland classes. The two SAR images were acquired in 2016/06/7 and 2016/07/25. 81
- Figure 3.8. The coherence comparison between three polarization channels for wetland classes. Three interferometric coherence images are (a) 24, (b) 48, and (c) 24 days apart. 82

Figure 3.9. Relationships between interferometric coherence and mean SAR backscattering responses for wetland classes in the ALOS-1 observations.	84
Figure 3.10. Relationships between interferometric coherence and mean SAR backscattering responses for wetland classes in the RADARSAT-2 observations.	85
Figure 3.11. Relationships between interferometric coherence and mean SAR backscattering responses for wetland classes in the TerraSAR-X observations.	86
Figure 3.12. The land cover map of the most accurate RF classification obtained by inclusion of coherence and intensity layers (108 input features).	88
Figure 3.13. Measured coherence decay for different SAR frequencies as a function of temporal baseline in different wetland types. Note that a temporal baseline of less than 20 days is required to obtain a coherence of greater than 0.4 for C- and X-band data.	92
Figure 3.14. Normalized variable importance for the most significant RF classification map.	96
Figure 4.1. An overview of the study area with overlays of Synthetic Aperture Radar (SAR) scenes.	108
Figure 4.2. Distribution of reference data: (Left) training and (Right) testing polygons	109
Figure 4.3. Flowchart of the proposed methodology.	111
Figure 4.4. Visualization of SVM tuning parameters of $\gamma$ and $C$ for RBF kernel.	115
Figure 4.5. The classification maps obtained from combining all feature types using (Left) RF and (Right) SVM classifiers (scenario 13 using 81 features).	119
Figure 4.6. Normalized variable importance for scenario 13.	123
Figure 4.7. The correlation matrix of full polarimetric RADARSAT-2 (FQ22) features obtained using Spearman's rank-order correlation ranging between 0 (i.e., no correlation) and 1 (i.e., the highest correlation).	124
Figure 4.8. The correlation matrix of single polarized RADARSAT-2 (U16W2) features obtained using Spearman's rank-order correlation. Different features are represented as follows: F1- F5 ( $\sigma_{HH0}$ sorted by time) and F6- F15 (coherence sorted by time). Note: see Table 4.1 for the time sequence.	125
Figure 4.9. The correlation matrix of single polarized TerraSAR-X features obtained using Spearman's rank-order correlation. Different features are represented as follows: F1- F9 ( $\sigma_{HH0}$ sorted by time) and F10- F45 (coherence sorted by time). Note: see Table 4.1 for the time sequence.	126

Figure 4.10. The final land cover map in this study obtained from the SVM classifier using 22 important uncorrelated features (OA: 85.40%).	128
Figure 5.1. The red polygons illustrate the geographic location of the three study areas.	141
Figure 5.2. Examples of land cover classes in the Avalon study area, including (a) bog, (b) fen, (c) marsh, (d) swamp, (e) shallow water, (f) urban, (g) deep water, and (h) upland.	142
Figure 5.3. Box-and-whisker plots demonstrating the distribution of the SAR backscattering coefficients of FP SAR data for wetland classes obtained from the pixel values of the training data set. Note that the horizontal bars within boxes indicate median values, boxes illustrate the lower and upper quartiles, and whiskers range from minimum to maximum values.	154
Figure 5.4. Box-and-whisker plots for extracted features from the Freeman-Durden decomposition for wetland classes obtained from the pixel values of the training data set.	155
Figure 5.5. Box-and-whisker plots for extracted features from the Cloude-Pottier decomposition for wetland classes obtained from the pixel values of the training data set. Note: H: entropy, A: anisotropy, and $\alpha$ : alpha angle.	156
Figure 5.6. Box-and-whisker plots demonstrating the distribution of the SAR backscattering coefficients of CP SAR data for wetland classes obtained from the pixel values of the training data set. The red horizontal line highlights the nominal NESZ (-24 dB) of the RCM medium resolution mode.	157
Figure 5.7. Box-and-whisker plots for extracted features from the m-delta decomposition for wetland classes obtained from the pixel values of the training data set.	158
Figure 5.8. Box-and-whisker plots for extracted features from the CP SAR data for wetland classes obtained from pixel values of the training data set. Note: $\mu c$ : circular polarization ratio, $m$ : degree of polarization, $\mu$ : conformity coefficient, and $\rho$ : correlation coefficient.	159
Figure 5.9. K-S distances between pairs of wetland classes using the extracted features from FP SAR data. Note that gray, blue, green, and yellow indicate poor, some, good, and excellent separability, respectively.	160
Figure 5.10. K-S distances between pairs of wetland classes using the features extracted from CP SAR data. See Table 5.3 for parameter description.	162
Figure 5.11. (a) A true color composite of RapidEye optical imagery (bands 3, 2, and 1) acquire on June 18, 2015. The classification maps of the Avalon study area obtained from (b) FP (OA: 90.73%, K: 0.88) and (c) simulated CP SAR data (OA: 87.89%, K: 0.85).	165

Figure 5.12. (a) A true color composite of RapidEye optical imagery (bands 3, 2, and 1) acquire on June 18, 2015. The classification maps of the Deer Lake study area obtained from (b) FP (OA: 84.75%, K: 0.81) and (c) simulated CP SAR data (OA: 80.67%, K: 0.77).	166
Figure 5.13. (a) A true color composite of RapidEye optical imagery (bands 3, 2, and 1) acquire on June 18, 2015. The classification maps of the Gros Morne study area obtained from (b) FP (OA: 90.93%, K: 0.88) and (c) simulated CP SAR data (OA: 84.07%, K: 0.80).	166
Figure 6.1. An illustration of (a) convolutional and (b) transposed convolutional layers.	185
Figure 6.2. The proposed network architecture in this study. Note that the encoder and decoder stages of the network are presented in solid-line and dashed-line boxes, respectively.	188
Figure 6.3. Architecture of (a) inception and (b) residual modules in this study.	190
Figure 6.4. The geographic location of the study area. The yellow square displays one tile of the testing set, which was selected for the purpose of illustration.	192
Figure 6.5. Ground reference photos illustrating land cover classes in the study area: (a) bog, (b) fen, (c) marsh, (d) swamp, (e) shallow water, (f) urban, (g) deep water, and (h) upland.	193
Figure 6.6. Visualization of learned features from the first convolutional block once the training has been terminated. The yellow-dashed squares demonstrate 4 of 64 features selected for further evaluation.	200
Figure 6.7. Four learned features from the first convolutional block and their frequency responses.	201
Figure 6.8. Visualized 16 of the 128 output feature maps from the third convolutional block. Note that more abstract feature maps are produced as the network becomes deeper.	203
Figure 6.9. (a) True color composite of RapidEye optical image (bands 3, 2, and 1) and (b) ground truth map. The classification maps obtained from (c) RF, (d) FCN-32s, (e) FCN-16s, (f) FCN-8s, (g) SegNet, and (h) the proposed method.	206
Figure 6.10. Normalized confusion matrices for wetland classification using (a) FCN-8s, (b) SegNet, and (c) the proposed network.	209
Figure 6.11. Feature visualization using the UMAP algorithm [52] for the extracted features from the last convolutional layer of (a) FCN-8s, (b) SegNet, and (c) the proposed network.	211

## List of Abbreviations and Symbols

<b>Acronyms</b>	<b>Description</b>
A	anisotropy
AA	average accuracy
AIT	average inference time per image tile
ALOS	Advanced Land Observation Satellite
ASF	Alaska Satellite Facility
CARTs	Classification And Regression Trees
CCMEO	Canada Centre for Mapping and Earth Observation
CF	calibration coefficient
CGSM	Cienaga Grande de Santa Marta
CNN	convolutional neural network
COSMO-SkyMed	Constellation of Small satellites for the Mediterranean basin Observation
CP	compact polarimetry
CP	Cloude-Pottier
CTLR	circularly transmitting, linearly receiving
CUDA	Compute Unified Device Architecture
CV-CNN	complex-valued CNN
CWCS	Canadian Wetland Classification System
D1	Date1
D2	Date2
DB	Double-bounce scattering
DEM	Digital Elevation Model

DL	Deep Learning
DN	digital number
DP	Dual polarimetry
DT	decision trees
E	Even-bounce scattering
EDEN	Everglades Depth Estimation Network
ENT	entropy
ENVISAT	Environmental Satellite
EO	earth observation
ERN	Edge-loss Reinforced Network
ERS	Earth Remote-sensing Satellite
ESA	European Space Agency
FBD	Fine Beam Double
FBS	Fine Beam Single
FCN	fully convolutional network
FD	Freeman-Durden
FP	Full polarimetry
FQ	Fine resolution Quad-polarization
FSN	Fine Segmentation Network
GB	Gigabyte
GHz	Gigahertz
GIM	Geocoded Incidence Angle Mask
GPS	Global Positioning System
GPU	Graphics Processing Unit

HH	Horizontal transmit and horizontal receive
HSN	Hourglass-Shaped Network
HV	Horizontal transmit and vertical receive
InSAR	Interferometric SAR
JERS-1	Japanese Earth Remote-sensing Satellite-1
Kappa or K	Kappa coefficient
K-S	Kolmogorov-Smirnov
Landsat	Land Remote-Sensing Satellite
Lidar	LIght Detection and Ranging
MD	minimum distance
ML	maximum likelihood
MLC	Maximum Likelihood Classifier
MRS	Multi-Resolution Segmentation
<i>Mtry</i>	number of variables
NDVI	normalised difference vegetation index
NESZ	Noise Equivalent Sigma Zero
NI	no inception
NL	Newfoundland and Labrador
NS	no skip
<i>Ntree</i>	number of decision trees
OA	overall accuracy
OBIA	Object-Based Images Analysis
ODD or O	Odd bounce scattering

OOB	out-of-bag
PA	producer's accuracy
PolSAR	polarimetric SAR
PS	persistent scatterer
RADARSAT	Radar Satellite
RAM	random access memory
RBF	radial basis function
RCM	RADARSAT Constellation Mission
ReLU	Rectified Linear Unit
RF	random forest
RS	Remote sensing
RSAT-2	RADARSAT-2
SAR	Synthetic Aperture Radar
SBAS	Small Baseline Subset
SDFCN	symmetrical dense-shortcut FCN
SFCN-SC	sliding window FCN and sparse coding
SGD	stochastic gradient descent
SGDM	stochastic gradient descent with a momentum
SLC	Single Look Complex
SNAP	Sentinel Application Platform
SNFCN	symmetrical normal shortcut FCN
SP	Single polarimetry
SPOT	Systeme Pour l'Observation de la Terre
SRTM	Shuttle Radar Topography Mission

STBAS	Small Temporal BAseline Subset
SVM	support vector machine
SWOT	Surface Water and Ocean Topography
t-SNE	t-distributed stochastic neighbor embedding
TSX	TerraSAR-X
U16W2	Wide Ultra-Fine
UA	user's accuracy
UMAP	Uniform Manifold Approximation and Projection
USDA	U.S. department of Agriculture
UTM	Universal Transverse Mercator
V	Volume scattering
VCF	Vegetation Continuous Field
VH	Vertical transmit and horizontal receive
VV	Vertical transmit and vertical receive
WGS84	World Geodetic System 1984
Y	Yamaguchi decomposition

<b>Letters in equations</b>	<b>Description</b>
A	Gain value
$b_j^l$	Bias
CF	Calibration coefficient
CV	Calibrated value
DN	Digital number

$f(x)$	Nonlinear activation function
H	Filter size (height)
$k_s$	Calibration and processor scaling factor
P	Patch size (row)
Q	Patch size (column)
S	Stride
$S_i$	Complex pixel values of backscattering coefficient
W	Filter size (width)
$w_{i,j}^l$	Weight
$X_i^{l-1}$	Input image
$Y_j^l$	Filter output
Z	Zero padding
$\beta^0$	Normalized backscattering coefficient in slant range
$\theta_{loc}$	Local incidence angle
$\sigma^0$	Normalized backscattering coefficient
$\gamma$	Coherence

## **Chapter 1. Introduction**

### **1.1. Overview**

A simple, straightforward definition of wetland is “land that is saturated with water long enough to promote wetland or aquatic processes as indicated by poorly drained soils, hydrophytic vegetation and various kind of biological activity adapted to wet environment” [1]. Wetlands provide a variety of environmental functions, including a desirable habitat for both plant and animal species, freshwater, food supply, water purification, flood control, nutrient retention and transformation, carbon sequestration, as well as climate change and erosion mitigation [2]. Despite these benefits, wetlands have been increasingly degraded due to both anthropogenic process, such as extensive agriculture, oil spills, plant and animal introduction, change in land cover and water use, urbanization, industrial and infrastructural developments [3], as well as natural processes, such as sea level rise, global warming, changes in precipitation patterns, costal plain subsidence, and coastal erosion [2]. Furthermore, the loss of wetland hydrological connectivity due to human activities leads to massive destruction of coastal wetlands [4]. Such ecosystem disturbances could ultimately result in serious environmental damage and loss of wetland production, as well as long-term human health issues.

Since 1884, the U.S government included the locations of marshes and swamps (i.e., two common wetland classes) among other features in their topographic maps. The production of the first wetland inventory maps in the North America date back to the early 1910s, when the U.S. department of Agriculture (USDA) produced the first two national wetland inventory maps for the purpose of wetland reclamation for agriculture (e.g., ground surveying) [5]. Survey of peats and muck were also conducted by the USDA on their soil survey maps in the early 1900s.

Importantly, much effort has been expended in reclamation of wetlands to fulfill human needs (e.g., feeding livestock and agricultural activities). The economical and environmental values of wetland ecosystems were recognized after a century of reclamation of wetlands in American society by government wildlife biologists in the 1950s. Since that time, several activities have been initiated for the preservation of these valuable ecosystems. For example, the Ramsar Convention on Wetlands was the first modern global intergovernmental treaties on the sustainable management of these important natural resources. Specifically, to support global preservation of wetlands, this Convention has been in place since 1971, wherein the main purpose is “the conservation and wise use of all wetlands through local and national actions and international cooperation, as a contribution towards achieving sustainable development throughout the world” [6]. Over the years, several countries (163 nations as of January 2013) have joined the convention and demonstrated their commitments to wetland preservation.

Over the last three decades, the advent of remote sensing data and tools has significantly contributed to the ongoing efforts of conservation strategies for wetlands. This is because the remoteness, vastness, and ever-changing nature of wetland ecosystems make traditional approaches to wetland mapping (e.g., ground surveying) laborious and costly. However, advanced remote sensing tools have addressed the intrinsic limitations of the traditional approaches. Remote sensing data have ameliorated our understanding of wetlands on a large-scale by offering more accurate and timely information for better preservation of these natural resources. Despite these benefits, wetland mapping using conventional remote sensing tools remains challenging, given the diversity and highly dynamic nature of wetlands, as well as the variability of the landscape they occupy. As such, more advanced remote sensing techniques are required to address these limitations.

## 1.2. Background

Wetland mapping using the interpretation of aerial photography is the earliest attempt for the characterization of wetland ecosystems. These images have been collected since the 1800s and are still useful in validating classification results or preparing classification training data [2]. The flexibility of the aerial platform for collecting images at certain times is advantageous compared to the satellite platform [7]. These images are also characterized by high spatial resolution [8]. Nevertheless, the interpretation of aerial photography for wetland mapping is laborious [9], costly [10], and requires significant domain expertise [11], [12]. The low spectral resolution further hinders the effectiveness of such data for wetland vegetation mapping.

Multispectral satellite images are the most common earth observation (EO) data for wetland mapping [2] and have been broadly applied in several studies [10], [13]. Multispectral data are advantageous compared to aerial imagery in terms of spectral resolution and could have spatial resolutions as accurate as those of aerial imagery [10], [14]. The infrared region of the electromagnetic spectrum is the most suitable portion for wetland mapping, given the high reflectance of vegetation and the strong absorption of water in this region. This enhances the contrast between water and vegetation, making it advantageous for wetland characterization [15], [16]. Multispectral imagery collected by Landsat missions has been extensively used for wetland classification, potentially due to the free-availability of such data [9], [14], [15], [17]. The other common satellite imagery used for wetland classification is data collected by the SPOT group (e.g., fine-to-moderate resolution sensors) [13], [18]. Nevertheless, several studies reported that spatial resolution of data collected by Landsat and SPOT precluded the identification of small-sized and complex wetland classes, resulting in mixed pixels [9], [19], [20]. Data collected at fine spatial resolution by IKONOS and Worldview have drawn attention for wetland mapping and shown

promising results in several studies [21], [22]. However, the expense of acquiring such data hinders their application for wetland classification on large-scales [23]. Despite these benefits and vast applications of multispectral imagery in several research efforts, such data are collected by passive sensors, which rely on sun illumination and weather condition [24]. These limitations hinder the regular and repetitive collection of such data for several wetland studies, especially for forested wetlands.

Data collected by hyperspectral sensors are characterized by various narrow and continuous spectral bands located at the visible and infrared regions of the electromagnetic spectrum [2]. Hyperspectral data are advantageous in terms of spectral resolution compared to multispectral imagery, yet the former has inferior spatial resolution relative to the latter. This enhanced spectral resolution allows the identification of various materials based on their spectral signatures [25]. As such, several studies reported the capability of hyperspectral imagery for plant moisture stress analysis [26], water quality [27], and discrimination of various salt marsh vegetation types [25]. For example, Rosso et al. (2005) demonstrated the capability of hyperspectral imagery for mapping marsh vegetation using the spectral mixture analysis technique and multiple endmember spectral mixture analysis [28]. Compared to multispectral imagery, hyperspectral data have been less examined for wetland classification, possibly due to lower data availability, high spectral resolution, and poor spatial resolution [2]. Variation of the spectral signature of wetland classes with phenology [29], large data volume [27], and less developed and/or complex image processing algorithms [30] are other limitations of such data for wetland characterization.

As mentioned earlier, optical remote sensing satellites have long been the main source of EO data for vegetation and wetland mapping [31], [32], yet cloud cover hinders the acquisition of such data. Consequently, as they are not impacted by solar radiation or weather conditions, Synthetic

Aperture Radar (SAR) sensors are of special interest, particularly in geographic regions with chronic cloud cover, such as Canada, Alaska, and tropical regions [33]. Furthermore, the capability of SAR to penetrate through vegetation and soil makes it advantageous for wetland and vegetation mapping [34]. The capability of SAR signals to detect and characterize wetland vegetation classes depends on their operating parameters, namely wavelength, polarization, and incidence angle. In particular, these characteristics of the SAR signal in combination with certain key specifications of ground targets, such as the dielectric property, surface roughness, and vegetation structure, determine the amount of the backscattering response by the SAR sensor. For example, the backscattering response from ground targets in wetland complexes, such as leaves, branches, trunks, and soils, is a function of the SAR signal properties, wherein ground targets with a relatively similar physical dimension to the incident wavelength produce the highest backscattering response [35]. Accordingly, it is beneficial to identify differences in the instrument specifications and to determine optimal parameters for the characterization of each wetland class. A comprehensive literature review on SAR operating parameters and their influences on the backscattering responses of the Canadian wetland classes are presented in Chapter 2.

The image classification algorithm is another important factor that influences the accuracy of wetland classification [2]. Classification algorithms are broadly categorized into unsupervised and supervised algorithms, the latter of which is the most popular for land cover classification [36]. Unsupervised classification algorithms are advantageous when annotated ground-truth data are unavailable. In this case, pixels are automatically assigned to statistically similar clusters and stratified by class types according to the interpretation of the image analyst or mathematical correlation [36]. Generally, supervised algorithms are divided into parametric and non-parametric approaches [37]. In the parametric approach, the statistical distribution of input data is taken into

account and training data are required to execute the classifier. The most common parametric supervised classification algorithms are the minimum distance (MD) and maximum likelihood (ML) classifiers [38]. Although these traditional classification algorithms have shown promising results in several studies, especially using multispectral imagery (e.g., [39]–[41]), their capability is limited by the distribution of input data.

Non-parametric classification algorithms, such as decision trees (DT), the support vector machine (SVM), and random forest (RF), are advantageous for wetland and land cover mapping, as they addressed the limitations of the traditional parametric approaches [41], [42]. In particular, they are independent of input data distribution and can handle large multi-temporal data from various sources (i.e., different SAR and optical data). DT is comprised of binary decisions, which determine the class of either an object or pixel. In particular, the classifier uses training data to build a bank of binary decisions using input data. The root node of each decision tree comprises both the training data and the possible classes [42]. At each node, the best splitting is determined to separate the data into classes and this procedure continues until the terminal nodes contain one class. The DT classifier has shown promising results for wetland classification using optical [43], SAR [44], and the combination of both types of data [45]. Random forest (RF), which is a sophisticated version of DT, is an ensemble classifier that utilizes a set of Classification And Regression Trees (CARTs) to make a prediction [46]. RF uses the bootstrap aggregating (bagging) approach to grow trees using a random sample from the given training data and determines the best splitting of the nodes by minimizing the correlation between trees. A label is then assigned to each pixel according to the majority vote of trees. RF was found to be advantageous relative to DT in terms of classification accuracy and is easier to execute compared to SVM [47]. In this research,

both RF and SVM classifiers were used for classification and a detailed description of these algorithms will be presented in Chapters 3, 4, and 5.

Despite the great capability of non-parametric approaches for land cover mapping, the accuracy of pixel-based classification algorithms may be less than adequate, as they are based only on the statistical characteristics of single pixels [48]. Accordingly, object-based approaches that consider both spectral and contextual information have drawn attention for land cover mapping [49]. This is of particular importance for the classification of complex land cover ecosystems, such as wetlands, wherein spectral/backscattering similarity of land cover classes affect the accuracy of pixel-based approaches. Incorporating different features, such as object size and shape, combining multiple sources of data with different spectral and spatial resolutions, and utilizing spatial and hierarchical relations of neighbouring pixels are the main advantages of the object-based approach [50]. As such, the success of wetland mapping using an object-based approach with various EO data has been demonstrated in recent studies [21], [51], [52].

To decrease ambiguity within backscattering/spectrally similar wetland classes and increase the classification accuracy, conventional classification algorithms (e.g., DT and RF) rely on extracting a large number of input features. The process of extracting a large number of features is labor-intensive and requires careful engineering design and significant domain expertise. This is because the effectiveness of each feature in a particular problem is unknown *a priori* [53]. Furthermore, these hand-crafted, low-level features provide insufficient capability for distinguishing complex land cover units and for generalization. The latter means that these low-level features are site- and data-dependent and, although well suited for a particular problem, they are less useful in many other cases.

Inspired by the great potential of the human brain for object recognition, Deep Learning (DL) has gained highlighted interests within the remote sensing community for several tasks, such as speckle reduction [54], object detection [55], and classification [31]. The DL methods are characterized by their deep multilayer structures that allow extraction of robust, invariant, and high-level features of data. Furthermore, the end-to-end training scheme is another advantage of these approaches. This means that they have the capability to learn a series of abstract hierarchical features from raw input data and to provide a final, task-specific output, thus removing the heuristic feature design [53]. This is advantageous relative to shallow-structured machine learning tools (e.g., SVM and RF), which incorporate only the low-level features of data into the semantic labelling scheme.

### **1.3. Research motivations**

Canada contains 24% of the world's wetlands within its borders, corresponding to approximately 1.5 million km<sup>2</sup>. Furthermore, 22 to 28% of Canadian lands are covered by wetlands [56]. Accordingly, wetlands are considered a national environmental health indicator in Canada according to the National Round Table on the Environment and Economy [57]. After joining the Ramsar Convention in 1981, Canada established the National Wetland Policy in 1991 [6]. Subsequently, the importance of wetland conservation has been recognized in Canada and the production of wetland inventories has been initiated in several provinces.

Newfoundland and Labrador (NL) is among the richest Canadian provinces in terms of different types of wetlands; however, these valuable ecosystems have been less investigated in this province. This is attributable to the remoteness, vastness, and ever-changing nature of wetlands in NL. Given the current need for up-to-date information of wetland classes in this province, satellite remote sensing data and tools are the most efficient approach for wetland characterization. Due to chronic

cloud cover in NL, data collected by SAR sensors are the most reliable source of EO data for this purpose. However, several challenges still remain, the most important of which may be the backscattering similarity of wetland classes, which hinders the effectiveness of conventional classification algorithms. Discrimination of these similar wetland classes with a sufficient (class-based) classification accuracy using satellite imagery is of great concern in the literature [33], [34]. Accordingly, the identification of the most appropriate SAR frequency and polarization during specific times in the growing season can contribute to the success of discriminating similar wetland classes. The research presented in this dissertation addressed the overarching goal of using SAR to monitor wetland complexes through two different, but relevant, aspects: wetland mapping and wetland hydrological monitoring. These are dependent as wetland classes significantly vary in their hydrology and vegetation. The goal has been to adapt and improve existing methods and develop new methods for analyzing and processing SAR data. Furthermore, this research investigates the influence of various SAR features extracted from different SAR frequencies on the accuracy of wetland classification.

#### **1.4. Scope and objectives**

The scope of this research is to exploit the capability of interferometry and polarimetric data and techniques to improve wetland mapping and monitoring in Canada using advanced remote sensing tools. This research also presents a comprehensive literature review on wetland monitoring using various interferometric techniques, which has been ignored in the literature. Furthermore, the literature reveals that in addition to the capability of the interferometry technique for water level monitoring [58]–[60], interferometric coherence also has a diagnostic function and represents high sensitivity to land cover changes [61], which is of great value for discriminating similar wetland

classes. The methodologies developed in this research are useful for mapping wetlands in other Canadian provinces, and potentially wetlands elsewhere with similar ecological characteristics.

Five chapters (published papers) compose the research contribution of this thesis, and the main objectives are to:

- i. present a comprehensive literature review of studies that used the interferometric SAR technique and its products for wetland mapping and monitoring (Chapter 1);
- ii. investigate the coherence and SAR backscattering variations of Canadian wetland classes using multi-temporal, multi-frequency, and multi-polarization SAR data (Chapter 2);
- iii. identify the discrimination capability of interferometric coherence and examine the synergy of interferometry with polarimetry and intensity for wetland classification (Chapters 2 and 3);
- iv. determine the influence of highly correlated features on the accuracy of wetland classification (Chapter 3);
- v. optimize both the type and number of input features to improve the accuracy of wetland classification using an innovative classification scheme (Chapter 3);
- vi. evaluate the capability of compact polarimetric (CP) SAR data for the characterization of Canadian wetland classes (Chapter 4);
- vii. propose a new fully convolutional network (FCN) that is specifically designed for wetland classification using SAR imagery (Chapter 5).

## **1.5. Contribution and novelty**

This section highlights the contributions of this research and its significance in improving the existing methods for mapping Canadian wetlands. One of the most important objectives of this

research was to integrate interferometry and polarimetry techniques to determine novel methods and tools, which are useful to mitigate identified challenges and address the main objectives of this research. The following is a summary of the contributions and novelties of this study. The details of each identified contribution are presented in the following, relevant chapters of the thesis.

### **1.5.1. InSAR wetland**

Despite the vast application of polarimetric SAR for wetland mapping and monitoring in a variety of applications, such as wetland change detection [62] and classification [63], and several literature review papers with this topic (polarimetric SAR) (e.g., [33], [64], [65]), the application of InSAR for wetland monitoring is substantially limited to a few case studies in the United States (e.g., [59], [60]) and China [66]. Accordingly, there is a need to identify the main challenges associated with this technique for mapping wetlands elsewhere. With the main focus on InSAR wetlands, this research presents a comprehensive literature review of SAR operating parameters and their influence on behaviour of wetland classes. To the best of the author's knowledge, this is the first literature review of wetland mapping with a focus on the InSAR technique and its products. More details are provided in Chapter 2.

### **1.5.2. Interferometric coherence and SAR backscattering variation of Canadian wetland**

Although Canada contains 24% of the world wetlands, no wetland mapping research has yet been carried out to investigate the variation of interferometric coherence as a function of SAR operating parameters (e.g., SAR frequency and polarization). Therefore, this study fills this gap by analyzing statistical variations in the coherence of Canadian wetland classes. Within a multi-temporal framework, this work provides the first insight into the application of the InSAR technique for monitoring wetland complexes in Canada. More details are provided in Chapter 3. Furthermore, by taking into account that both SAR backscatter and coherence are responsive to the flooding

status of vegetation in wetland complexes, this study examines the relationship between these two important SAR variables and identifies the discrimination capability provided by each component for separating various wetland classes. More details are provided in Chapters 3 and 4.

### **1.5.3. Incorporating interferometric coherence into the classification scheme**

Classification of wetland classes with similar backscattering is challenging and often requires the combined use of several features that take into account various characteristics of mapping ecosystems. Several studies examined the capability of SAR backscattering intensity and polarimetric features, or the integration of both, for wetland classification. However, one of the main innovative aspects of this research is the application of interferometric coherence for classification of wetlands and the joint use of coherence with intensity and polarimetric features. Each feature is responsive to the specific characteristics of ground targets. For example, SAR intensity is primarily an indicator of ground conditions due to its sensitivity to surface roughness and dielectric constant [67]. Polarimetric features characterize the type of the ground target scattering mechanism [34], whereas interferometric coherence indicates the mechanical stability of the ground targets [61]. Thus, the synergistic use of these features could enhance semantic land cover information, which is beneficial for wetland characterization. The contribution of this work in terms of using interferometric coherence for wetland applications are twofold: (1) variations of interferometric coherence as a function of multi-temporal, multi-frequency, and multi-polarization SAR observations are comprehensively investigated, which is of great use for the hydrological monitoring of wetlands; and (2) a new application of interferometric coherence is introduced for wetland classification, as this feature is responsive to different characteristics of land cover compared to other conventional SAR features (i.e., intensity and polarimetry). More details are provided in Chapters 3 and 4.

#### **1.5.4. Optimization of the number and types of input features for wetland classification**

One of the common approaches for improving the discrimination capability of classes with similar backscattering (e.g., wetland classes) is to increase the number of input features. However, several of these input features are highly correlated and contain redundant information, meaning that employing such input features insignificantly improves overall classification accuracy, as reported in the literature (e.g., [68]). Accordingly, the author introduces a novel approach to optimize both the type and number of input features to remove redundant, less useful features and enhance the discrimination capability of remaining features. More details are documented in Chapter 4.

#### **1.5.5. Wetland classification using Compact Polarimetric (CP) SAR data**

The RADARSAT Constellation Mission (RCM), the successor mission of RADARSAT-2, is planned to be launched in 2019 and will be the main source of SAR observations in Canada. The main purposes of the RCM mission are to ensure data continuity for RADARSAT users and increase the operational capability by collecting sub-weekly data (i.e., a four day repeat cycle) for various applications, such as maritime surveillance, disaster management, and ecosystem monitoring (e.g., wetlands and agricultural applications) [69]. The successful application of such important EO data for wetland characterization requires understanding the data collected by such a SAR mission. Identifying the ability of such data is important, since it must be compared with that of RADARSAT-2. A review of the existing literature in this area revealed that while the capability of simulated CP SAR data has been extensively examined for sea ice characterization (e.g., [70], [71]), its potential has been underrepresented for wetland classification. Accordingly, this research comprehensively examines the discrimination capability of extracted features from CP SAR data both qualitatively and quantitatively and compares them with those of RADARSAT-2 features. More details are provided in Chapter 5.

### **1.5.6. Wetland classification using deep learning**

Most recently, deep learning (DL) and, in particular, deep convolutional neural network (CNN) have drawn attention within the remote sensing community for a variety of applications, including object detection [72] and classification [31]. Despite the vast applications of CNNs for several tasks, the following shortcomings still remain for their application, since most studies:

- i. focused on the classification of very high resolution aerial and optical imagery from the limited publicly available datasets compared to SAR imagery, yet the former data are not available in most remote sensing studies;
- ii. classified typical land cover classes (e.g., land, water, and forest) rather than complex land cover classes with similar backscattering.

The novelty of this research is to propose a new fully convolutional network (FCN) that is trained in an end-to-end learning scheme and is specifically designed for the classification of wetland classes using SAR imagery. More discussion on the applications of CNN and FCN for land cover classification and the advantages and novelty of the proposed FCN model are provided in Chapter 6.

## **1.6. Organization of the thesis**

This PhD thesis is manuscript-based, including five peer-reviewed journal papers. Table 1.1. presents the published papers during the course of this research study.

Table 1.1. Organization of the thesis

Chapter title	Paper title
Chapter 1: Introduction	N/A
Chapter 2: SAR and InSAR wetlands	Wetland water level monitoring using interferometric synthetic aperture radar (InSAR): A review. <i>Canadian Journal of Remote Sensing</i> , 44(4), pp.247-262, (2018).
Chapter 3: Coherence and SAR backscatter analyses of Canadian wetlands	Multi-temporal, multi-frequency, and multi-polarization coherence and SAR backscatter analysis of wetlands. <i>ISPRS journal of photogrammetry and remote sensing</i> , 142, pp.78-93, (2018).
Chapter 4: Wetland classification	An efficient feature optimization for wetland mapping by synergistic use of SAR intensity, interferometry, and polarimetry data. <i>International journal of applied earth observation and geoinformation</i> , 73, pp.450-462, (2018).
Chapter 5: Compact Polarimetric SAR responses to Canadian wetlands	Full and Simulated Compact Polarimetry SAR Responses to Canadian Wetlands: Separability Analysis and Classification, <i>Remote Sensing</i> , 11(5), p. 516, (2019).
Chapter 6: Fully Convolutional Network (FCN) for wetland classification	A new fully convolutional neural network for semantic segmentation of polarimetric SAR imagery in complex land cover ecosystem. <i>ISPRS Journal of Photogrammetry and Remote Sensing</i> , 151, pp.223-236, (2019).
Chapter 7: Summary, conclusions, and future outlook	N/A

The outline of remaining chapters is described below:

Chapter 2 presents a comprehensive literature review on SAR operating parameters and their influences on wetland classes. Additionally, all existing studies that used the InSAR technique and its product for wetland characterization were evaluated in the time interval from 2000 to 2016.

Advantages and disadvantages of using SAR and InSAR for wetland mapping are discussed in detail and potential solutions are provided.

Next, a statistical variation of the interferometric coherence of typical Canadian wetland classes using SAR data collected by three well-known SAR missions, namely ALOS PALSAR-1 L-band, RADARSAT-2 C-band, and TerraSAR-X is presented in Chapter 3. This chapter also highlights the great significance of interferometric coherence for further discrimination of wetland classes.

Chapter 4 contains an investigation of the added value of coherence as an additional input to wetland mapping and its synergy with intensity and polarimetry features. In this chapter, the author discusses the problems associated with correlated features in classifying a complex land cover ecosystem and their influence on the accuracy of the final results. To address these limitations and further increase the classification accuracy, a novel classification scheme is proposed.

The capability of extracted features from full polarimetry and simulated CP SAR data for discriminating wetland classes is investigated in Chapter 5. The features providing the best discrimination are then identified and used in an object-based classification scheme.

A novel FCN architecture for classification of wetland complexes using SAR features is proposed in Chapter 6. The capability of the proposed architecture is compared with several state-of-the-art FCNs, such as FCN-32s, FCN-16s, FCN-8s, and SegNet.

Finally, this dissertation concludes with Chapter 7. Recommendations and directions of future research are also presented in in this chapter.

## **1.7. Other publications and book chapter**

In addition to the above-mentioned journal papers, the candidate published or contributed to the following peer-reviewed journal papers, either as author or co-author, during her PhD program.

- **Mohammadimanesh, F.**, Salehi, B., Mahdianpari, M., English, J., Chamberland, J. and Alasset, P.J., 2019. Monitoring surface changes in discontinuous permafrost terrain using small baseline SAR interferometry, object-based classification, and geological features: a case study from Mayo, Yukon Territory, Canada. *GIScience & Remote Sensing*, 56(4), pp.485-510.
- Mahdianpari, M., Salehi, B., **Mohammadimanesh, F.** and Motagh, M., 2017. Random forest wetland classification using ALOS-2 L-band, RADARSAT-2 C-band, and TerraSAR-X imagery. *ISPRS Journal of Photogrammetry and Remote Sensing*, 130, pp.13-31.
- Mahdianpari, M., Salehi, B., **Mohammadimanesh, F.** and Brisco, B., 2017. An assessment of simulated compact polarimetric SAR data for wetland classification using random forest algorithm. *Canadian Journal of Remote Sensing*, 43(5), pp.468-484.
- Mahdianpari, M., Salehi, B. and **Mohammadimanesh, F.**, 2017. The effect of PolSAR image de-speckling on wetland classification: introducing a new adaptive method. *Canadian Journal of Remote Sensing*, 43(5), pp.485-503.
- Mahdianpari, M., Salehi, B., **Mohammadimanesh, F.**, Brisco, B., Mahdavi, S., Amani, M. and Granger, J.E., 2018. Fisher Linear Discriminant Analysis of coherency matrix for wetland classification using PolSAR imagery. *Remote sensing of environment*, 206, pp.300-317.
- Mahdianpari, M., Salehi, B., Rezaee, M., **Mohammadimanesh, F.** and Zhang, Y., 2018. Very deep convolutional neural networks for complex land cover mapping using multispectral remote sensing imagery. *Remote Sensing*, 10(7), p.1119.

- Mahdianpari, M., Salehi, B., **Mohammadimanesh, F.**, Larsen, G. and Peddle, D.R., 2018. Mapping land-based oil spills using high spatial resolution unmanned aerial vehicle imagery and electromagnetic induction survey data. *Journal of Applied Remote Sensing*, 12(3), p.036015.
- Mahdianpari, M., Salehi, B., **Mohammadimanesh, F.**, Homayouni, S. and Gill, E., 2019. The First Wetland Inventory Map of Newfoundland at a Spatial Resolution of 10 m Using Sentinel-1 and Sentinel-2 Data on the Google Earth Engine Cloud Computing Platform. *Remote Sensing*, 11(1), p.43.
- Mahdianpari, M., Motagh, M., Akbari, V., **Mohammadimanesh, F.** and Salehi, B., 2019. A Gaussian Random Field Model for De-speckling of Multi-polarized Synthetic Aperture Radar Data. *Advances in Space Research*.
- Salehi, B., Mahdianpari, M., Amani, M., **Mohammadimanesh, F.**, Granger, J., Mahdavi, S. and Brisco, B., 2018. A collection of novel algorithms for wetland classification with SAR and optical data. In *Wetlands*. IntechOpen. (Book Chapter)

## 1.8. References

- [1] C. Tarnocai, "Canadian wetland registry," in *Proc. of a workshop on Canadian wetlands: meeting of the Natl. Wetl. Work. Group, Saskatoon, Saskat., 11-13 June 1979/comp., ed. CDA Rubec, FC Pollett= Compte-rendu d'un atelier sur les terres humides du Canada*, 1980.
- [2] R. W. Tiner, M. W. Lang, and V. V Klemas, *Remote sensing of wetlands: applications and advances*. CRC press, 2015.
- [3] A. L. Gallant, "The challenges of remote monitoring of wetlands." Multidisciplinary Digital Publishing Institute, 2015.
- [4] F. Jaramillo *et al.*, "Assessment of hydrologic connectivity in an ungauged wetland with InSAR observations," *Environ. Res. Lett.*, vol. 13, no. 2, p. 24003, 2018.
- [5] S. P. Shaw and C. G. Fredine, *Wetlands of the United States: their extent and their value to waterfowl and other wildlife*. 1956.
- [6] R. C. Gardner and N. C. Davidson, "The Ramsar convention," in *Wetlands*, Springer, 2011, pp. 189–203.

- [7] C. E. Olson, "Elements of photographic interpretation common to several sensors," *Photogramm. Eng.*, vol. 26, no. 4, pp. 651–656, 1960.
- [8] J. R. Jensen, *Remote sensing of the environment: An earth resource perspective 2/e*. Pearson Education India, 2009.
- [9] C. Wright and A. Gallant, "Improved wetland remote sensing in Yellowstone National Park using classification trees to combine TM imagery and ancillary environmental data," *Remote Sens. Environ.*, vol. 107, no. 4, pp. 582–605, 2007.
- [10] K. R. Harvey and G. J. E. Hill, "Vegetation mapping of a tropical freshwater swamp in the Northern Territory, Australia: a comparison of aerial photography, Landsat TM and SPOT satellite imagery," *Int. J. Remote Sens.*, vol. 22, no. 15, pp. 2911–2925, 2001.
- [11] C. Baker, R. Lawrence, C. Montagne, and D. Patten, "Mapping wetlands and riparian areas using Landsat ETM+ imagery and decision-tree-based models," *Wetlands*, vol. 26, no. 2, p. 465, 2006.
- [12] M. F. Augusteijn and C. E. Warrender, "Wetland classification using optical and radar data and neural network classification," *Int. J. Remote Sens.*, vol. 19, no. 8, pp. 1545–1560, 1998.
- [13] A. Davranche, G. Lefebvre, and B. Poulin, "Wetland monitoring using classification trees and SPOT-5 seasonal time series," *Remote Sens. Environ.*, vol. 114, no. 3, pp. 552–562, 2010.
- [14] J. Töyrä, A. Pietroniro, L. W. Martz, and T. D. Prowse, "A multi-sensor approach to wetland flood monitoring," *Hydrol. Process.*, vol. 16, no. 8, pp. 1569–1581, 2002.
- [15] C. Huang, Y. Peng, M. Lang, I.-Y. Yeo, and G. McCarty, "Wetland inundation mapping and change monitoring using Landsat and airborne LiDAR data," *Remote Sens. Environ.*, vol. 141, pp. 231–242, 2014.
- [16] A. Davranche, B. Poulin, and G. Lefebvre, "Mapping flooding regimes in Camargue wetlands using seasonal multispectral data," *Remote Sens. Environ.*, vol. 138, pp. 165–171, 2013.
- [17] J.-R. B. Bwangoy, M. C. Hansen, D. P. Roy, G. De Grandi, and C. O. Justice, "Wetland mapping in the Congo Basin using optical and radar remotely sensed data and derived topographical indices," *Remote Sens. Environ.*, vol. 114, no. 1, pp. 73–86, 2010.
- [18] B. Poulin, A. Davranche, and G. Lefebvre, "Ecological assessment of *Phragmites australis* wetlands using multi-season SPOT-5 scenes," *Remote Sens. Environ.*, vol. 114, no. 7, pp. 1602–1609, 2010.
- [19] E. W. Ramsey III and S. C. Laine, "Comparison of Landsat Thematic Mapper and high resolution photography to identify change in complex coastal wetlands," *J. Coast. Res.*, pp. 281–292, 1997.
- [20] R. J. Zomer, A. Trabucco, and S. L. Ustin, "Building spectral libraries for wetlands land cover classification and hyperspectral remote sensing," *J. Environ. Manage.*, vol. 90, no. 7, pp. 2170–2177, 2009.
- [21] Z.-T. Ouyang, M.-Q. Zhang, X. Xie, Q. Shen, H.-Q. Guo, and B. Zhao, "A comparison of pixel-based and object-oriented approaches to VHR imagery for mapping saltmarsh plants," *Ecol. Inform.*, vol. 6, no. 2, pp. 136–146, 2011.
- [22] B. C. Timm and K. McGarigal, "Fine-scale remotely-sensed cover mapping of coastal dune and salt marsh ecosystems at Cape Cod National Seashore using Random Forests," *Remote Sens. Environ.*, vol. 127, pp. 106–117, 2012.
- [23] H. Nagendra *et al.*, "Remote sensing for conservation monitoring: Assessing protected areas, habitat extent, habitat condition, species diversity, and threats," *Ecol. Indic.*, vol. 33, pp. 45–59, 2013.

- [24] M. P. F. Costa, "Use of SAR satellites for mapping zonation of vegetation communities in the Amazon floodplain," *Int. J. Remote Sens.*, vol. 25, no. 10, pp. 1817–1835, 2004.
- [25] K. S. Schmidt and A. K. Skidmore, "Spectral discrimination of vegetation types in a coastal wetland," *Remote Sens. Environ.*, vol. 85, no. 1, pp. 92–108, 2003.
- [26] J. E. Anderson and J. E. Perry, "Characterization of wetland plant stress using leaf spectral reflectance: implications for wetland remote sensing," *Wetlands*, vol. 16, no. 4, pp. 477–487, 1996.
- [27] V. Klemas, "Remote sensing techniques for studying coastal ecosystems: An overview," *J. Coast. Res.*, vol. 27, no. 1, pp. 2–17, 2010.
- [28] P. H. Rosso, S. L. Ustin, and A. Hastings, "Mapping marshland vegetation of San Francisco Bay, California, using hyperspectral data," *Int. J. Remote Sens.*, vol. 26, no. 23, pp. 5169–5191, 2005.
- [29] T. S. F. Silva, M. P. F. Costa, J. M. Melack, and E. M. L. M. Novo, "Remote sensing of aquatic vegetation: theory and applications," *Environ. Monit. Assess.*, vol. 140, no. 1–3, pp. 131–145, 2008.
- [30] V. Klemas, "Remote sensing of emergent and submerged wetlands: an overview," *Int. J. Remote Sens.*, vol. 34, no. 18, pp. 6286–6320, 2013.
- [31] M. Mahdianpari, B. Salehi, M. Rezaee, F. Mohammadimanesh, and Y. Zhang, "Very Deep Convolutional Neural Networks for Complex Land Cover Mapping Using Multispectral Remote Sensing Imagery," *Remote Sens.*, vol. 10, no. 7, p. 1119, 2018.
- [32] M. Rezaee, M. Mahdianpari, Y. Zhang, and B. Salehi, "Deep Convolutional Neural Network for Complex Wetland Classification Using Optical Remote Sensing Imagery," *IEEE J. Sel. Top. Appl. Earth Obs. Remote Sens.*, no. 99, 2018.
- [33] F. M. Henderson and A. J. Lewis, "Radar detection of wetland ecosystems: a review," *Int. J. Remote Sens.*, vol. 29, no. 20, pp. 5809–5835, 2008.
- [34] B. Brisco, "Mapping and monitoring surface water and wetlands with synthetic aperture radar," *Remote Sens. Wetl. Appl. Adv.*, pp. 119–136, 2015.
- [35] R. K. Raney, "Radar fundamentals: technical perspective," *Princ. Appl. Imaging Radar, Man. Remote Sens.*, vol. 2, pp. 9–130, 1998.
- [36] P. Mather and B. Tso, *Classification methods for remotely sensed data*. CRC press, 2016.
- [37] G. Mountrakis, J. Im, and C. Ogole, "Support vector machines in remote sensing: A review," *ISPRS J. Photogramm. Remote Sens.*, vol. 66, no. 3, pp. 247–259, 2011.
- [38] L. Ma, M. Li, X. Ma, L. Cheng, P. Du, and Y. Liu, "A review of supervised object-based land-cover image classification," *ISPRS J. Photogramm. Remote Sens.*, vol. 130, pp. 277–293, 2017.
- [39] L. Bruzzone and D. F. Prieto, "Unsupervised retraining of a maximum likelihood classifier for the analysis of multitemporal remote sensing images," *IEEE Trans. Geosci. Remote Sens.*, vol. 39, no. 2, pp. 456–460, 2001.
- [40] A. H. Strahler, "The use of prior probabilities in maximum likelihood classification of remotely sensed data," *Remote Sens. Environ.*, vol. 10, no. 2, pp. 135–163, 1980.
- [41] J. R. Otukei and T. Blaschke, "Land cover change assessment using decision trees, support vector machines and maximum likelihood classification algorithms," *Int. J. Appl. Earth Obs. Geoinf.*, vol. 12, pp. S27–S31, 2010.

- [42] M. Xu, P. Watanachaturaporn, P. K. Varshney, and M. K. Arora, "Decision tree regression for soft classification of remote sensing data," *Remote Sens. Environ.*, vol. 97, no. 3, pp. 322–336, 2005.
- [43] M. A. Friedl and C. E. Brodley, "Decision tree classification of land cover from remotely sensed data," *Remote Sens. Environ.*, vol. 61, no. 3, pp. 399–409, 1997.
- [44] M. G. Parmuchi, H. Karszenbaum, and P. Kandus, "Mapping wetlands using multi-temporal RADARSAT-1 data and a decision-based classifier," *Can. J. Remote Sens.*, vol. 28, no. 2, pp. 175–186, 2002.
- [45] J. Li and W. Chen, "A rule-based method for mapping Canada's wetlands using optical, radar and DEM data," *Int. J. Remote Sens.*, vol. 26, no. 22, pp. 5051–5069, 2005.
- [46] L. Breiman, "Random forests," *Mach. Learn.*, vol. 45, no. 1, pp. 5–32, 2001.
- [47] P. Thanh Noi and M. Kappas, "Comparison of random forest, k-nearest neighbor, and support vector machine classifiers for land cover classification using Sentinel-2 imagery," *Sensors*, vol. 18, no. 1, p. 18, 2018.
- [48] T. Blaschke, "Object based image analysis for remote sensing," *ISPRS J. Photogramm. Remote Sens.*, vol. 65, no. 1, pp. 2–16, 2010.
- [49] U. C. Benz, P. Hofmann, G. Willhauck, I. Lingenfelder, and M. Heynen, "Multi-resolution, object-oriented fuzzy analysis of remote sensing data for GIS-ready information," *ISPRS J. Photogramm. Remote Sens.*, vol. 58, no. 3–4, pp. 239–258, 2004.
- [50] L. F. de Almeida Furtado, T. S. F. Silva, and E. M. L. de Moraes Novo, "Dual-season and full-polarimetric C band SAR assessment for vegetation mapping in the Amazon várzea wetlands," *Remote Sens. Environ.*, vol. 174, pp. 212–222, 2016.
- [51] I. Dronova, P. Gong, and L. Wang, "Object-based analysis and change detection of major wetland cover types and their classification uncertainty during the low water period at Poyang Lake, China," *Remote Sens. Environ.*, vol. 115, no. 12, pp. 3220–3236, 2011.
- [52] C. Zhang and Z. Xie, "Combining object-based texture measures with a neural network for vegetation mapping in the Everglades from hyperspectral imagery," *Remote Sens. Environ.*, vol. 124, pp. 310–320, 2012.
- [53] M. Volpi and D. Tuia, "Dense semantic labeling of subdecimeter resolution images with convolutional neural networks," *IEEE Trans. Geosci. Remote Sens.*, vol. 55, no. 2, pp. 881–893, 2017.
- [54] P. Wang, H. Zhang, and V. M. Patel, "SAR image despeckling using a convolutional neural network," *IEEE Signal Process. Lett.*, vol. 24, no. 12, pp. 1763–1767, 2017.
- [55] G. Cheng, P. Zhou, and J. Han, "Learning rotation-invariant convolutional neural networks for object detection in VHR optical remote sensing images," *IEEE Trans. Geosci. Remote Sens.*, vol. 54, no. 12, pp. 7405–7415, 2016.
- [56] B. G. Warner and C. D. A. Rubec, "By the National Wetlands Working Group / Edited The Canadian Wetland Classification System."
- [57] R. A. Fournier, M. Grenier, A. Lavoie, and R. Hélie, "Towards a strategy to implement the Canadian Wetland Inventory using satellite remote sensing," *Can. J. Remote Sens.*, vol. 33, no. sup1, pp. S1–S16, 2007.
- [58] D. E. Alsdorf, J. M. Melack, T. Dunne, L. A. K. Mertes, L. L. Hess, and L. C. Smith, "Interferometric

- radar measurements of water level changes on the Amazon flood plain,” *Nature*, vol. 404, no. 6774, p. 174, 2000.
- [59] S. Wdowinski, S.-W. Kim, F. Amelung, T. H. Dixon, F. Miralles-Wilhelm, and R. Sonenshein, “Space-based detection of wetlands’ surface water level changes from L-band SAR interferometry,” *Remote Sens. Environ.*, vol. 112, no. 3, pp. 681–696, 2008.
- [60] Z. Lu and O. Kwoun, “Radarsat-1 and ERS InSAR analysis over southeastern coastal Louisiana: Implications for mapping water-level changes beneath swamp forests,” *IEEE Trans. Geosci. Remote Sens.*, vol. 46, no. 8, pp. 2167–2184, 2008.
- [61] A. Ferretti, A. Monti-Guarnieri, C. Prati, F. Rocca, and D. Massonet, *InSAR principles-guidelines for SAR interferometry processing and interpretation*, vol. 19. 2007.
- [62] A. Schmitt and B. Brisco, “Wetland Monitoring Using the Curvelet-Based Change Detection Method on Polarimetric SAR Imagery,” vol. 5, pp. 1036–1051, 2013.
- [63] T. L. Evans and M. Costa, “Landcover classification of the Lower Nhecolândia subregion of the Brazilian Pantanal Wetlands using ALOS/PALSAR, RADARSAT-2 and ENVISAT/ASAR imagery,” *Remote Sens. Environ.*, vol. 128, pp. 118–137, 2013.
- [64] V. Tsyganskaya, S. Martinis, P. Marzahn, and R. Ludwig, “SAR-based detection of flooded vegetation—a review of characteristics and approaches,” *Int. J. Remote Sens.*, vol. 39, no. 8, pp. 2255–2293, 2018.
- [65] L. L. Hess, J. M. Melack, and D. S. Simonett, “Radar detection of flooding beneath the forest canopy: a review,” *Int. J. Remote Sens.*, vol. 11, no. 7, pp. 1313–1325, 1990.
- [66] M. Zhang, Z. Li, B. Tian, J. Zhou, and P. Tang, “The backscattering characteristics of wetland vegetation and water-level changes detection using multi-mode SAR: A case study,” *Int. J. Appl. Earth Obs. Geoinf.*, vol. 45, pp. 1–13, 2016.
- [67] J.-S. Lee and E. Pottier, *Polarimetric radar imaging: from basics to applications*. CRC press, 2009.
- [68] K. Millard and M. Richardson, “On the importance of training data sample selection in random forest image classification: A case study in peatland ecosystem mapping,” *Remote Sens.*, vol. 7, no. 7, pp. 8489–8515, 2015.
- [69] A. A. Thompson\*, “Overview of the RADARSAT constellation mission,” *Can. J. Remote Sens.*, vol. 41, no. 5, pp. 401–407, 2015.
- [70] M. Dabboor and T. Geldsetzer, “Towards sea ice classification using simulated RADARSAT Constellation Mission compact polarimetric SAR imagery,” *Remote Sens. Environ.*, vol. 140, pp. 189–195, 2014.
- [71] M. Dabboor, B. Montpetit, and S. Howell, “Assessment of the High Resolution SAR Mode of the RADARSAT Constellation Mission for First Year Ice and Multiyear Ice Characterization,” *Remote Sens.*, vol. 10, no. 4, p. 594, 2018.
- [72] X. Chen, S. Xiang, C.-L. Liu, and C.-H. Pan, “Vehicle detection in satellite images by hybrid deep convolutional neural networks,” *IEEE Geosci. Remote Sens. Lett.*, vol. 11, no. 10, pp. 1797–1801, 2014.

## Chapter 2. SAR and InSAR wetlands <sup>1</sup>

### Preface

A version of this manuscript has been published in the *Canadian Journal of Remote Sensing*. This is a literature review paper and I am a principal author of this manuscript. I carried out all literature review and compared the results of all investigated papers. I discussed and presented the literature review to all co-authors. I prepared the first draft of the manuscript and revised the manuscript several times according editorial input and scientific insights from other co-authors. I also revised the manuscript three times based on the comments from the journal's reviewers. The co-author Masoud Mahdianpari assisted in reviewing and revising the manuscript. All co-authors reviewed and commented on the manuscript.

### Abstract

The production of spatially detailed quantitative maps of water level variations in flooded vegetation, and the detection of flow patterns and discontinuities in both managed and natural wetland ecosystems provide valuable information for monitoring these unique environments. Hydrological monitoring of wetlands is also critical for maintaining and preserving the habitat of various plant and animal species. Over the last two decades, advances in remote sensing technologies have supported wetland monitoring and management in several aspects, including classification, change detection, and water level monitoring. In particular, Interferometric Synthetic Aperture Radar (InSAR) has emerged as a promising tool for hydrological monitoring of wetland water bodies. However, a comprehensive review of the status, trends, techniques,

---

<sup>1</sup> Mohammadimanesh, F., Salehi, B., Mahdianpari, M., Brisco, B. and Motagh, M., 2018. Wetland water level monitoring using interferometric synthetic aperture radar (InSAR): A review. *Canadian Journal of Remote Sensing*, 44(4), pp.247-262.

advances, potentials, and limitations of this technique is lacking. In this study, we evaluate the use of InSAR for hydrological monitoring of wetlands, discuss the main challenges associated with this technique, recommend possible solutions to mitigate the main problems identified in the literature, and present opportunities for future research.

**Keywords:** Wetlands, water level monitoring, Interferometric Synthetic Aperture Radar, flooded vegetation, hydrological monitoring.

## **2.1. Introduction**

Wetlands are permanently or intermittently wet areas that provide a variety of environmental services, including a desirable habitat for both plant and animal species, freshwater, food supply, water purification, flood control, as well as climate change and erosion mitigation [1], [2]. Despite these benefits, wetlands have been increasingly degraded due to both anthropogenic process, such as extensive agriculture, change in land cover and water use, urbanization, industrial and infrastructural developments [3], [4] and natural process, such as sea level rise, global warming, changing in precipitation patterns, and coastal erosion [2], [5] The sustainable management of wetland hydrology requires more specific information about vegetation patterns, annual precipitation, flooding paths, water level changes, and the local phenological cycle [4].

Given the current need for up-to-date information and the wide-spread distribution of wetland ecosystems, satellite remote sensing tools are the most time- and cost-efficient method for wetland studies [4], [6]. Several studies have used satellite data for wetland classification using optical images [7], [8], Synthetic Aperture Radar (SAR) imagery [9]–[12] or the integration of both [13], [14].

Hydrological monitoring of wetlands is crucial since they are water-dependent ecosystems [2]. During the last decade, Interferometric Synthetic Aperture Radar (InSAR) has gained increased attention for water level monitoring of flooded vegetation. Applying the InSAR technique for water level monitoring is an important area of study that has not yet been fully exploited. Although several conditions should be met and numerous challenges are involved, using the InSAR technique holds great promise for wetland water level monitoring. This is because the relatively new application of InSAR provides a high spatial resolution map of water level changes that is not obtainable using terrestrial techniques [15]. Furthermore, this technique provides data from inaccessible points, which cannot be reached during expensive field investigations. Most wetlands are located in remote areas, where hydrology, topography, and vegetation cover make field investigations challenging and costly. Therefore, the use of repeat-pass InSAR helps to minimize or eliminate the number of field campaigns needed to assess wetlands, particularly, by using advanced/new SAR satellite data such as Sentinel-1. Another problem associated with wetland monitoring is the variability of their characteristics (e.g., water level, vegetation cover, etc.) over time [4], therefore necessitating repeated *in-situ* investigations; however, wetlands can be easily tracked using repeat-pass observations from space. Thus, these issues (i.e., accessibility, repeatability, cost, and time) are addressed using remote sensing tools for wetland monitoring.

Despite the significance of InSAR for water level monitoring (e.g., [16]–[19]), it has not been investigated in various wetlands globally. This is unexpected given the importance of wetland monitoring worldwide and the availability of the InSAR technique. A collective and comparative study of all InSAR applied techniques can, therefore, mitigate the challenges and stimulate more extensive applications of InSAR for wetland monitoring.

For this study, both Google Scholar and ISI Web of Science were used for browsing papers. The main used keywords were as follows: wetland, flooded vegetation, Interferometric Synthetic Aperture Radar, InSAR, water level monitoring, coherence, and SAR backscatter. Different arrangements of the above keywords were used. Because of the limited number of studies in this particular application of InSAR, we did not limit our review using specific criteria. However, we considered all studies that have used the InSAR technique or interferometric products, such as coherence (e.g., [20], [21]), for wetland monitoring. The final number of studies that directly used the InSAR technique or its products for wetland monitoring, included in this review, was 31.

The primary objectives of this review article are to: (1) present a detailed overview of the InSAR techniques, which have been used for wetland water level monitoring to date; (2) identify the main challenges associated with the wetland InSAR technique and possible solutions; (3) evaluate the general trends in remote sensing studies using InSAR for water level monitoring; (4) predict future trends in applying the InSAR technique for wetland monitoring and recommend any priority topics for future research.

## **2.2. Wetland water level monitoring using InSAR**

### **2.2.1. Wetland InSAR**

Using the InSAR technique for wetland water level monitoring, although relatively new, presents challenges. For example, substantial altering of reflectance and energy backscatter of wetland environments occurs, even within hours or days [4], and low backscatter of the water surface lead to difficulties when applying InSAR for monitoring water level fluctuation. As the SAR sensor transmits radar pulses at an off-nadir look angle, two different conditions occur for the open water.

In the first case, if the open water surface is smooth and calm, it acts as a mirror and causes the entire signal to be scattered away from SAR sensors, making open water appear dark in SAR images [17]. Alternatively, if the open water surface is rough and turbulent, part of the signal can be backscattered to the SAR sensors; however, since two SAR images are captured at different times, the SAR signals over open water are not coherent [22].

Despite numerous challenges, InSAR is promising for water level monitoring of flooded vegetation under specific conditions. More precisely, the specific condition, wherein double-bounce scattering occurs between the horizontal water surface and the vertical flooded vegetation [23] should be met when employing the InSAR technique for monitoring water level changes [16]. If the vegetation within or adjacent to the standing water is able to backscatter the radar pulse towards satellite sensor, water level changes are observable in the phase data [24], [25]. Also, vegetation should not be too dense for the penetration of microwave energy [2].

A majority of InSAR wetland studies focused on using the conventional SAR interferometry technique, the so-called repeat-pass interferometry, for wetland water level monitoring. However, the main limitation associated with the conventional InSAR technique is that the deformation signal is often overprinted by unwanted terms (e.g., noise, atmospheric and orbital phase). Thus, in the past two decades, several studies have proposed different techniques, known as advanced InSAR techniques, to mitigate these limitations [26]–[28]. The main objective behind the development of advanced InSAR technique is to produce a time series of interferometric pairs to mitigate the undesirable terms of residual phase (e.g., atmospheric phase screen) using a signal model of a single point in the stack of interferograms [26].

Using the advanced InSAR technique for wetland water level monitoring has been underrepresented due to the specific characteristic of the wetland complex [29]. Wetlands are characterized by distributed scatterers because flooded vegetation (i.e., trees, herbaceous vegetation, and water) is the primary component of wetland complexes. The backscattering, in such an environment, is defined as a coherent sum of many independent scatterers, in which no one is stronger than others [30]. Therefore, the persistent scatterer techniques, which have been widely used in urban areas due to existence of several PSs (e.g., buildings and roads), are not feasible for wetland hydrological monitoring. The time series technique of Small BAseline Subset (SBAS) [27], [31] that combines multiple unwrapped interferograms to produce a time series of displacement maps, is more favorable as it matches to some extent to the wetland complex [29], [32], [33]. The master and slave pairs for interferograms in a SBAS network are selected based on the average baseline parameters for the signal of interest (e.g., 25% of the critical baseline) regardless of the temporal baseline [34]. However, ignoring the temporal separation of interferograms leads to coherence loss in highly variable phenomena such as monitoring water level changes in wetlands. This is because vegetation, as the most important component of wetland ecosystem, loses the interferometric coherence in a few weeks (or even days), especially in the case of using shorter wavelengths, such as X- and C-band [20]. Accordingly, a modified version of SBAS technique, called Small Temporal BAseline Subset (STBAS), has been specifically developed for wetland water level monitoring by [32] and its efficiency was examined in the Everglades wetlands using both C- and L-band data [33]. The main difference between SBAS and STBAS is that, in the latter, the shortest temporal baseline pairs are selected regardless of the spatial separation in order to minimize the temporal decorrelation associated with wetland

complexes. However, the spatial baseline should be still smaller than the critical baseline component.

According to the Canadian Wetland Classification System (CWCS), wetlands may be categorized in five main classes: bog, fen, marsh (i.e., herbaceous wetlands), swamp (i.e., woody wetland), and shallow-water [2]. Each wetland classes have different behaviour depending on SAR wavelength, polarization, spatial resolution, incident angle, wetland phenology as well as environmental variables (e.g., humidity and wind). These factors affect the applicability of the InSAR technique for wetland monitoring and are discussed in more detailed in the following subsections.

#### **2.2.1.1. Interferometric coherence of wetland**

Coherence is a quality indicator of InSAR observations and represents the degree of similarity of the same pixel in the time interval between two SAR acquisitions [35]. Three main sources of losing coherence, the so-called decorrelation, in InSAR observations over wetlands are geometric decorrelation caused by different satellite look angles, volumetric decorrelation caused by vegetation volume scattering, and temporal decorrelation of vegetation [22], [36]. Geometric decorrelation is directly proportional to perpendicular component of the baseline. There is a critical baseline value for the interferogram of each sensor, wherein an interferogram with the perpendicular baseline beyond the critical value loses its interferometric coherence [37]. The effect of baseline decorrelation in surface scattering can be mitigated by applying a common band filtering [38]. Volumetric decorrelation primarily occurs within vegetation canopies and forests, and is usually controlled by the canopy structure. Volume scattering is often due to multiple scattering of the radar pulses within forests and vegetation canopies [36].

Temporal decorrelation is the most problematic issue when applying the InSAR technique for monitoring wetland complexes due to the ever-changing nature of wetlands. Particularly, any condition that alters the physical orientation, composition, or scattering characteristic and distribution of scatterers within a returned signal causes temporal decorrelation [36]. There are several factors that contribute to temporal decorrelation in the case of land cover mapping, including the alterations of (1) leaf and subshrub orientations by wind; (2) the dielectric constant by moisture and rain; (3) the dielectric properties and roughness of the canopy structure by flooding, as well as factors, such as seasonal phenology, growth, and mechanical variations (e.g., cultivation and timber harvesting) [36]. Temporal decorrelation is also a function of wetland classes. For example, temporal decorrelation is more severe for herbaceous wetlands (e.g., marshes), while it is less prevalent for woody wetlands [17]. Additionally, different wetland classes have different coherence level depending on their scattering mechanisms and temporal decorrelation. For example, low coherence value ( $< 0.1$ ) is expected for the open water class given the dominant specular scattering mechanism associated with surface water [22]. This contrasts with flooded vegetation (e.g., marsh and swamp) with dominant double-bounce scattering mechanism, which produces high coherence values. In particular, the coherence varies for flooded vegetation depending on the degree of flooding; thus, the coherence can be used for monitoring the flooding status of the wetland classes [39]. Furthermore, in non-flooded vegetation, the dominant scattering mechanism is volume scattering, which means the signal is diffused in nature and, as a result, it is not as bright as double-bounce scattering in a SAR image producing low/intermediate coherence degree.

Additionally, the coherence has a diagnostic function and can be used along with SAR backscatter for classification of different wetland classes [40]. For example, Ramsey et al. (2006) compared

the potential of interferometric products, coherence and phase, and SAR intensity images for land cover classification [36]. They reported that the SAR intensity was less responsive to land covers and had high temporal variations. Conversely, the interferometric coherence had a higher variation in different classes and provided a better discrimination during leaf-off season.

Geometric, volumetric, and temporal decorrelations are integrated and determine the portion of the SAR signal that is available to produce double-bounce backscattering and, accordingly, coherence degree over the wetland complex [22]. Nevertheless, most of studies reported that the temporal decorrelation was more severe for wetland InSAR especially when shorter wavelengths were employed. While the geometric decorrelation could be problematic when longer wavelengths were used [20].

#### **2.2.1.2. SAR wavelength**

Interaction of the SAR signal with the vegetation canopy is determined by the SAR wavelength. To date, most of SAR satellites have operated in three microwave bands, including X-, C-, and L-bands with wavelength of 3.1, 5.6, and 23.6cm, respectively (see Table 2.1). The InSAR technique has been demonstrated to work well for water level monitoring with all three wavelengths, including L-band [17], C-band [22], and X-band [41].

Each wavelength has its own advantages and disadvantages. In particular, the longest wavelength, L-band, can pass through the vegetation canopy and detect water beneath the flooded trees and/or dense vegetation and, therefore, a higher coherence is maintained over longer time periods. Although ionospheric refraction errors, which are caused by the fluctuations of the electron density in the ionosphere, have much influence on the L-band signal compared to that of C- and X-band [42]. C-band, on the other hand, has less penetration depth, which means it mostly interacts with upper parts of the canopy and maybe water beneath the short vegetation and, therefore, is less

coherent than L-band [43]. In contrast, it is less affected by the ionospheric effects and atmospheric artifacts relative to L- and X-band, respectively [18], [44]. The shortest wavelength, X-band (e.g., TerraSAR-X), is usually characterized with high spatial resolution imagery and shorter satellite revisit time depending on the satellite mission. The main disadvantages associated with X-band, however, are small swath coverage, less penetration depth, and fringe saturation in the case of significant water level changes [41]. Furthermore, shorter wavelengths mostly interact with wind-affected parts of vegetation canopies [45] and lose coherence even in a short period of time [46], [47].

Table 2.1. Characteristics of well-known SAR satellite missions that have been used for wetland monitoring.

Satellite mission	Mission life span	Repeat cycle (days)	Wavelength/band (cm)	Mode	Resolution (m) (azimuth × range)	Incidence angle	Orbital inclination	
ERS-1	1991-2000	35, 3, 168	5.66/C-band		20 × 30	20°-26°	98.52 °	
JERS-1	1992-1998	44	23.5/L-band		18 × 18	35°	97.7 °	
ERS-2	1995-2011	35, 3	5.66/C-band		20 × 30	20°-26°	98.52 °	
RADARSAT-1	1995-2013	24	5.66/C-band	Fine	8.4 × (8,9)	37°-47°	98.6 °	
				Standard	27 × (21-27)	20°-49°		
				Wide	28 × (21,25,33)	20°-45°		
				ScanSAR narrow	50 × 50	20°-49°		
				ScanSAR wide	100 × 100	20°-49°		
				Extended High	27 × (16-18)	52°-58°		
				Extended Low	27 × 39	10°-22°		
ENVISAT	2002-2012	35, 30	5.63/C-band	Image	30 × (30-150)	15°-45°	98.55 °	
				Alternating-polarization	30 × (30-150)	15°-45°		
				Wave	10 × 10	15°-45°		
				Wide swath	150 × 150	17°-42°		
				Global-monitoring	1000 × 1000	17°-42°		
ALOS PALSAR	2006-2011	46	23.6/L-band	Fine 1	10 × (7-44)	8°-60°	98.16 °	
				Fine 2	10 × (14-44)			
				Polarimetric	10 × (24-89)			8°-30°
				ScanSAR	100 × 100			18°-43°
RADARSAT-2	2007-Present	24	5.55/C-band	Ultra-fine	3 × 3	20°-54°	98.6 °	
				Multi-look Fine	8 × 8	30°-50°		
				Fine	8 × 8	30°-50°		
				Standard	26 × 25	20°-52°		
				Wide	26 × 40	20°-45°		
				ScanSAR narrow	50 × 50	20°-46°		
				ScanSAR wide	100 × 100	20°-49°		
				Extended High	26 × 18	49°-60°		
				Fine Quad-polarization	8 × 12	18°-49°		
TerraSAR-X	2007-Present	11	3.11/X-band	Spotlight	2 × (1.5-3.5)	20°-55°	97.4 °	
				High resolution spotlight	1 × (1.5-3.5)	20°-55°		
				Stripmap	3 × (3-6)	20°-45°		
				ScanSAR	(18.5-19.2) × (17-19.2)	20°-45°		

SAR wavelength also demonstrates the sensitivity of different signals to changes. For example, the X-band signal is 3.1cm long, which means it has a higher sensitivity to very small changes. Due to their shorter wavelengths, the end-user maps of X- and C-band observations have a higher

accuracy when compared to L-band [15]. Applying shorter wavelengths with a higher sensitivity to changes is desirable when monitoring solid earth movement, where coherence is maintained over longer time periods; however, it may not be the case for wetlands with their dynamic nature.

Additionally, the selection of an appropriate SAR wavelength depends on the wetland classes since the interaction of SAR wavelength varies widely with different vegetation types depending on their size. As such, the shorter wavelengths (e.g., C- and X-band) are preferred for monitoring the herbaceous vegetation due to relatively same size of SAR wavelength and vegetation canopies (e.g., leaf). However, the longer wavelengths are better suited for woody wetlands since incident SAR signal interacts with larger trunk and branch components [21], [48].

### **2.2.1.3. SAR polarization**

Interferometric coherence analysis of wetlands demonstrates that HH channel is the best polarization for wetland water level monitoring. The HH polarization signal is more sensitive to the double-bounce scattering associated with tree trunks in swamp forest and stems in freshwater marshes [49]. More specifically, the larger Fresnel reflection of HH polarized signal relative to VV is less attenuated by the vertical structural of wetland vegetation, such as trunks and stems [18]. The vertically oriented structure of such vegetation enhances the attenuation of VV polarization signals and, as a result, the radar signal cannot reach to the water surface below the vegetation [48]. However, VV polarization is the second best in this specific application of InSAR [41], especially, at the early stages of emerging vegetation when plants have begun to grow in terms of height, but have less developed vegetation canopy. The HV polarization is not a preferred polarization due to the high sensitivity to the volume scattering inside the canopy [22], [50]. However, Hong et al. (2010b) and Hong and Wdowinski (2012) reported that the HV polarized data could also maintain adequate degree of the coherence in shorter period of times [41], [44].

They also concluded that both volume and double-bounce scattering were dominant scattering mechanisms in cross-pol images. This was due to both observing high coherence and similar fringe patterns in cross-polarized images (HV) comparable to that of co-polarizations (i.e., HH and VV) over flooded vegetation. This was unexpected since according to the vegetation scattering theories only volume scattering can be produced by the cross-polarized observations [51], [52]. Nevertheless, the HH/HV ratio is a good indicator of double-bounce scattering mechanism, wherein a higher value of this ratio is representative of strong double-bounce scattering [18].

#### **2.2.1.4. Other factors**

Spatial resolution and SAR incident angle are other factors, which have effects on InSAR wetland observations [20], [21]. For example, Brisco et al. (2015) used different RADARSAT-2 products and reported that the coherence was maintained in different acquisition modes with varying resolutions as long as the temporal baseline was not exceeded up to 24 days [21]. However, they pointed out that high resolution SAR images provided more detailed information about flooding status of vegetation and, thus, were better suited for wetland monitoring. Table 2.1 lists the most frequently-used SAR satellite data and their spatial resolution.

SAR incident angle is another factor affecting the backscattering response of wetland classes. The effect of different SAR incidence angles on interferometric coherence has been investigated by several researchers who reported that small incident angles are preferred for wetland InSAR applications [20], [48]. This is because steep incident angles allow a deeper penetration of the canopy by the SAR signal and less energy degradation along the radiation path, which enhances the chance of double-bounce scattering between water surface and flooded vegetation [15], [20], [53], [54].

### 2.2.2. Wetland Phenology

The incoherent summation of different scattering mechanisms is the combination of three components in the wetland complex: canopy surface backscattering, double-bounce backscattering of flooded vegetation, and canopy volume backscattering caused by multiple path interactions of canopy structures [55], [56].

The radar signals from tree trunks or stems stimulate backscatter and they (i.e., tree trunks or stems) act like a corner reflector. In the wetland complex, the double-bounce occurrence depends on the wetland phenological cycle, which is a function of the complex relation of vegetation height/density and the water level height [57]. For example, during the high water season, swamp forests and freshwater marshes experience different conditions and, therefore, have different signatures in a SAR image. Specifically, a positive correlation between water level height and SAR backscatter was reported using L-band data over forested wetlands, wherein an increase in the water level enhanced the chance of double-bounce scattering as well as high coherence degree. Conversely, an inverse relationship between water level height and SAR backscattering was reported in herbaceous wetland, wherein an increase in the water level enhanced the chance of specular scattering and thereby, low coherence degree [58], [59]. Other studies also confirmed less correlation between water level height and SAR backscatter variation using C-VV [9] and C-HH [58] images in the freshwater marsh.

Vegetative density is another important factor, which determines different backscattering mechanisms of wetland classes. For example, Lu and Kwoun (2008) reported that the radar backscatter of C-band SAR image during the leaf-off season was much greater than the leaf-on season for swamp forests [22]. This is because the high vegetative density and canopy, during the leaf-on season, convert double-bounce scattering to the volume scattering in the freshwater

swamp, which, in turns, decreases SAR backscatter. Later studies, such as [59], [60], also found same results using L-band SAR images in the Congo River Basin. In particular, they reported a negative correlation between Vegetation Continuous Field (VCF) products obtained by MODIS and SAR backscatter over flooded forests. However, Zhang et al. (2016) reported a positive correlation between normalised difference vegetation index (NDVI) and SAR backscatter in herbaceous wetland (i.e., reed marsh and rice paddy) using L-HH SAR images in all growing cycles [48].

One practical technique to determine different scattering mechanisms of wetland classes is to apply a simple decomposition approach, such as Cloude-Pottier [61], Freeman-Durden [51], or Touzi decomposition [62]. By applying a polarimetric decomposition, three dominant scattering mechanisms are obtained – surface, double-bounce, and volume scattering – and it is a good indicator for applicability of InSAR technique for wetland water level changes in a particular area [41], [44]. However, applying a polarimetric decomposition requires PolSAR data.

### **2.2.3. The Primary Limitations of InSAR Wetland Application**

Although the InSAR technique has great potential for wetland monitoring, there are several limitations that hinder the technique performance. The presence of emergent vegetation inside or next to water bodies, which enhances a greater portion of the SAR signal back to the sensor, is the most important condition for InSAR wetland application [16], [50]. Particularly, the co-existence of both vegetation and water in wetland ecosystems eventuates double-bounce scattering and, subsequently, the applicability of the InSAR technique for wetland water level monitoring.

As previously discussed, interferometric coherence is another limiting factor, which hinders the quality of InSAR observations. Environmental variables, such as flooding condition under the vegetation and the phenological cycle, contribute to the coherence loss in the wetland ecosystem

[48]. The loss of coherence due to presence of some land cover types, such as open water and man-made structures (e.g., levees and canals) [20], causes the phase discontinuity in the InSAR observations and, accordingly, produces unwrapping errors.

Atmospheric phase delay also affects the quality of InSAR observations [22]. This may be more challenging in wetlands due to the lack of persistent scatterers, which are useful for mitigating atmospheric phase screen using advanced InSAR techniques [29], [32]. The atmospheric phase screen decreases the accuracy of InSAR water level maps from at least several millimetres, to several centimeters in the worst case scenario such as coastal wetlands. Thus, the observed fringe patterns should be scrutinized in detail to distinguish signals due to water level changes from atmospheric artifacts. In particular, the atmospheric fringe patterns are correlated spatially, while uncorrelated temporally, whereas fringes due to water level changes show evidence of being controlled by structures, such as levees, canals, and roads [22]. These structures are observable in the SAR intensity image and often exhibit sudden changes in the interferometric phase value. Thus, the fringes, which have been reoccurred in the same place for several times in a series of produced interferograms and controlled by structures, are mainly associated with water level changes [25].

It is worth noting that when using the InSAR technique for monitoring coastal wetland ecosystems, tidal cycles must also be considered. This means that satellite repeat cycles and tidal cycles should not be synchronized. More specifically, repeat-pass SAR images, which have been acquired during tide-induced water level changes, are not useful for InSAR wetland applications. This is because the InSAR technique does not provide reliable information at the same tidal amplitude [5].

Another problem, which further complicates matter, is the great dependency of the technique on ground-based hydrological observations. In particular, InSAR phase observations only provide relative water level changes and, accordingly, hydrological *in-situ* measurements are required to

both calibrate and validate InSAR observations [17], [22]. In other InSAR applications, such as landslide or subsidence monitoring, the reference point for converting relative InSAR measurements to absolute changes is selected in non-affected areas by deformation, which is not applicable to InSAR wetland [41]. Light Detection and Ranging (Lidar) observations, either airborne or spaceborn, are useful for validation and calibration purposes [63], [64], although have not been investigated to date, probably due to the time and cost constraints. Rather, the common approaches, for both calibration and validation of InSAR measurements, are using *in-situ* gauge observations (16 cases) [17] and satellite altimetry data (6 cases) [65].

#### **2.2.3.1. In-situ gauge stations**

Although *in-situ* gauge observations have a good temporal resolution, they have poor spatial resolution since gauge stations are usually distributed several or even tens of kilometers from one another [15]. Particularly, the gauge measurements are limited to sparse locations which, in turn, decrease the accuracy of water level monitoring. These observations are also unable to detect water spatial patterns [32]. Moreover, most gauge stations operate in navigable rivers and canals that are easy to access and control [18], in open water and near-shore [58] and, in the best case scenario, in managed wetlands. However, SAR signals have low backscatter in the river, open water, and shore areas, which cause gauge observations to be incomparable with InSAR observations in this case. Furthermore, the gauge observations in these locations are independent of water level changes in adjacent wetlands. In the managed wetlands, gauge observations are influenced by infrastructures, which mean gauge measurements are underestimated near outflows and overestimated near inflows [17].

Another consideration is that multiple gauge stations should be used as vertical references in different locations for wetland water bodies that are separated by levees and canals. This is because

a single vertical reference point may not provide comparable and sufficient data with InSAR measurements in large wetland areas [18]. Using multiple gauges, as vertical references, allow a least square analysis to estimate the difference between InSAR and gauge observations. It is theoretically expected to obtain an improvement in accuracy by increasing the number of gauge observations. However, the accuracy may decrease in some cases if these additional stations are located in low coherence areas, or close to hydraulic structures [32], [66]. Majorities of wetland InSAR studies, particularly those carried out in the Everglades wetlands, used *in-situ* gauge observations for calibration and validation of the InSAR results [17], [32]. This is because the Everglades wetlands complexes are well controlled with several *in-situ* instruments, including a dense network of up to 200 gauge, meteorological, hydro-geologic, and water quality control stations [17]. Data from these sources are gathered, processed, and converted to the Everglades Depth Estimation Network (EDEN) [67].

#### **2.2.3.2. Satellite altimetry**

Kim et al. (2009) introduced the suitability of ENVISAT satellite altimetry observations for validation of InSAR measurements obtained from ALOS and RADARSAT-1 repeat-pass SAR images. An altimeter satellite has a nadir-viewing geometry and operates by transmitting microwave pulses toward the ground target. Satellite altimetry offers an alternative solution by providing (calibration/validation) data at ungauged locations [68]. However, the coarse spatial resolution of satellite altimetry observation, which varies between tens of kilometers depending on missions [69], as a reference tool, in comparison to that of InSAR measurements is a limiting factor. Particularly, the technique acquires point-wised elevation measurements in a very sparse spatial distribution along the satellite flight pass. Satellite passes are also separated by about 50-100 km from each other, causing several freshwater bodies to be excluded from satellite coverage

due to variations in orbit passes [65]. Furthermore, the quality of radar altimetry observation is often affected by the topographic relief, the target size, and heterogeneous ground targets in the observed scene [68].

### 2.3. Trend in using the InSAR technique for wetland monitoring

Alsdorf et al. (2000) introduced the applicability of the InSAR technique for water level monitoring due to the observation of coherent phase signals over flooded vegetation in the Amazon floodplains in Brazil [16]. Subsequently, the capability of the technique has been further examined by a number of researchers [16]–[18], [22], [49], [70]. As seen in Figure 1, there is an increasing attention in using InSAR for wetland monitoring over the last decade given the accuracy, time and cost efficiency of the technique compared to other approaches (e.g., *in-situ* gauges and satellite altimetry).

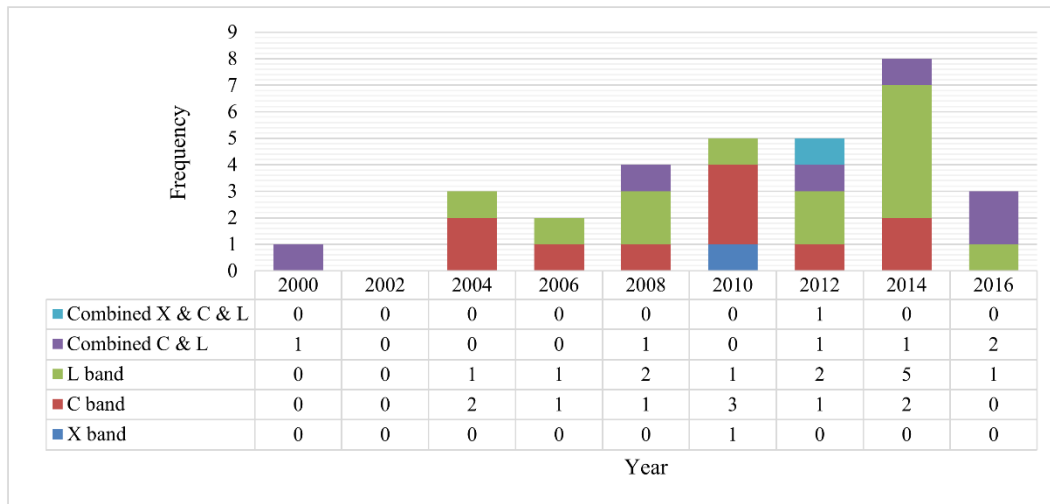


Figure 2.1. Frequency of studies used InSAR for wetland monitoring in two-year time intervals since 2000.

The increasing number of wetland InSAR studies is due, at least in part, to availability of various SAR data, such as ALOS PALSAR-1, ENVISAT ASAR, and ERS1/2 provided by the Alaska Satellite Facility (ASF) (<https://vertex.daac.asf.alaska.edu/>) and the European Space Agency (ESA) (<https://earth.esa.int/web/guest/data-access>). However, although the availability of SAR data has proliferated globally, the InSAR technique for wetland monitoring has not been well developed worldwide. Specifically, the application of InSAR in wetland studies has been limited to particular pilot sites, which is unfortunate, given wetlands cover between 1-2% of the Earth's surface and availability of InSAR technique [2]. The location of wetland InSAR studies and their frequencies are depicted in Figure 2. Most of the studies have been conducted in the Everglades (11 cases) and Louisiana wetlands (5 cases) in the United States, followed by several studies in two different locations in China, the Yellow River Delta (3 cases) and Liaohe River (2 cases). A handful studies have examined the Amazon floodplain (3 cases) in South America and the Congo River (3 cases) in Africa. Finally, other pilot sites, such as the Helmand River in Afghanistan (1 case), the Sian Ka'an in Mexico (1 case), the Danube Delta in Romania (1 case), the Big Bend coastal region of Florida (1 case), the Brockville area in Canada (1 case) have been investigated in single studies. It is worth noting that a number of published studies were conducted in multiple geographic locations [71], [72]. The studies conducted in the Everglades and Louisiana wetlands cause a hot-spot in North America.

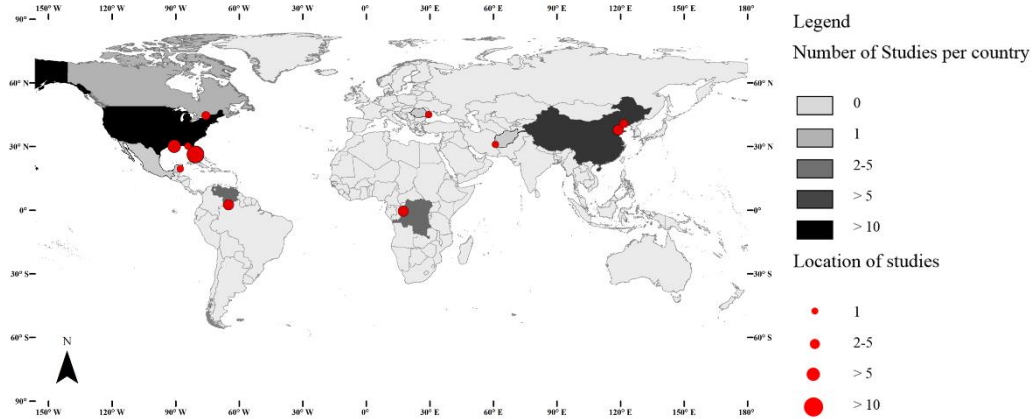


Figure 2.2. World map illustrating the location and frequency of wetland InSAR studies (red dots).

Focusing on applied SAR frequency, most of the studies used L-band due to its higher penetration capability through vegetation canopies, including JERS-1, ALOS PALSAR-1, and SIR-C SAR data (13 cases). The second most exploited frequency was C-band data acquired by ERS1/2, RADARSAT-1/2, and ENVISAT ASAR sensors (10 cases). A number of researchers used a combination of L- and C-band (6 cases) for water level monitoring. X-band SAR images (e.g., TerraSAR-X and COSMO-SkyMed), however, were the least investigated frequency band (2 cases), though it was found to be promising for wetland InSAR applications [41], [73].

Concerning on SAR polarization, most of the studies focused on the HH polarization (19 cases) followed by all polarization (4 cases) and HH-VV (3 cases). Also, HH-HV and VV polarization were less investigated (2 cases). Other studies, however, did not mention the type of applied SAR polarization (see Figure 3).

First author	year	Frequency			Wetland class			Polarization			Validation		
		L	C	X	Herbaceous	Swamp	Upland	HH	HV	VV	Gauge	AL*	InSAR
Alsdorf	2000	■	■					■	■			■	
Wdowinski	2004	■			■	■							■
Lu	2005	■	■							■			
Kim	2005	■			■	■							
Alsdorf	2007	■						■	■				
Lu	2008	■	■		■	■				■	■		
Wdowinski	2008	■			■	■		■	■			■	
Kim	2009	■	■		■	■		■	■			■	■
Lu	2009	■						■	■				■
Hong	2010	■			■	■						■	
Hong	2010b	■			■	■		■	■				
Gondwe	2010	■	■					■	■				
Jung	2010	■						■	■				■
Hong	2012	■			■	■		■	■				
Wdowinski	2013	■	■		■	■		■	■			■	
Poncos	2013	■			■	■		■	■				
Xie	2013	■			■	■						■	
Poncos	2013b	■	■									■	
Poncos	2014	■			■	■							
Hong	2014	■			■	■							
Kim	2014	■	■										
Xie	2015	■			■	■						■	
Yuan	2015	■			■	■						■	■
Lee	2015	■											
Yuan	2016	■			■	■						■	
Zhang	2016	■			■	■		■	■			■	
Cabrerata	2016	■			■	■		■	■			■	

Note: \* illustrates satellite altimetry.

Figure 2.3. Summary of studies that have used the InSAR technique for wetland water level monitoring. The applied frequencies, wetland classes, polarizations, and validation approaches are indicated.

## 2.4. Discussion of current constraints and direction of future reseach

The presented literature on using InSAR for hydrological monitoring of wetland complexes demonstrates that there is a large group of studies focusing on not the same, but have been concentrated in a few geographic locations. Despite large expanses of wetlands worldwide, most of the applied techniques were not developed to account for a large variety of different wetland

environments. The selection of these wetland pilot sites has been biased toward favorable conditions, such as availability of gauges or radar altimetry data, managed wetland ecosystems, and good accessibility.

As the validation of InSAR results is important, future work should generally pursue to find an alternative method rather than *in-situ* observations for this purpose. Accordingly, studies attempting to determine a relationship between the InSAR measurements and SAR backscatter variations hold great promise [58]–[60], [74], although they are currently still in an early experimental stage. Despite the results of these studies to date, it would be beneficial to increase the number of studies quantify the relationship between InSAR observations and SAR intensity variations, particularly for shorter wavelengths (i.e., X- and C-band). This is because both SAR backscatter and InSAR observations are acquired simultaneously, while they are independent of each other. However, determining water level changes using SAR backscatter variations is challenging. A major reason is that SAR backscatter is not only affected by hydrological changes, but other factors such as seasonal variations of vegetation and weather conditions may be influential [58]. Thus, distinguishing SAR backscatter variations due to water level changes from other altering sources is difficult. Importantly, studies that describe the effect of satellite geometrical acquisition are likely to contribute to the success of SAR backscatter images for calibration and validation. Particularly, the SAR backscatter responses of flooded vegetation obtained from descending and ascending satellite acquisitions may provide additional information due to the different appearance of the same target in SAR images [58].

A further general point to be considered in future studies for validation and calibration of InSAR observations is the incorporation of local meteorological data (e.g., temperature, evaporation, and precipitation), since they are available for most wetlands with high temporal resolution [75]. One

obstacle, however, for such an examination is the need for an effective control of wetlands' inflow and outflow from external sources (e.g., dams). Therefore, this approach may particularly be efficient for natural wetlands, wherein hydrological conditions are mainly controlled by the local weather.

It would be also desirable to increase the number of studies that integrate SAR and InSAR observations (i.e., coherence) for both wetland hydrological monitoring and classification. This is because the interferometric coherence shows the mechanical stability of the target, while SAR intensity depends on the electromagnetic structure of the targets. However, the application of integrating SAR and InSAR observations seems to be an under-examined approach investigated in only a few studies [36], [39]. Although SAR backscatter is much noisier than interferometric products [76], it is less influenced by atmospheric effects. By contrast, interferometric products are less affected by noise, but are more influenced by atmospheric effects [36]. Particularly, intensity images may augment the interferometric products to better evaluate the variations in hydrological conditions. Therefore, the combination of these two types of observations (i.e., SAR and InSAR) can mitigate the uncertainty in the end user wetland products. However, these recommendations should be considered in the context of other influential factors (see section Wetland InSAR), since both SAR intensity images and InSAR observations are affected by several factors with intra-relationship. In addition to these general future prospects, the application of multi-temporal interferometric coherence to obtain accurate information about the flooding status of vegetation as well as wetland phenology should be considered, as it has rarely been investigated to date. Thus, future research should concentrate on using these excellent data sources as a promising tool for wetland change detection [77].

Concerning applied methodologies, the literature demonstrates that a large number of studies employed the conventional InSAR technique (i.e., the repeat-pass SAR interferometry technique). A problem associated with such an approach, however, is uncertainty in the end products due to, for example, the atmospheric phase screens [32]. Although advanced InSAR time series methods demonstrate great promise for differentiating atmospheric signatures from interferometric products in other InSAR applications (e.g., landslide and earthquake) [26], [78]; however, their potential for the InSAR wetland applications remain underrepresented [29], [32], [33]. Due to the highly dynamic nature of wetland ecosystems, the short temporal baselines are desirable in order to mitigate the problem associated with temporal decorrelation. For example, while the (advanced) SBAS InSAR technique holds great promise for monitoring distributed scatterers, it requires a modification to be applicable for wetland monitoring. Further research should focus on developing of InSAR time series techniques, compatible with wetland environments. Hence, one promising approach is to develop an algorithm that combines multi-frequency InSAR observations to address the limitation of temporal decorrelation. A drawback of such a method, however, is that uncertainties associated with different frequencies (e.g., X-, C-, and L-band) can vary from one acquisition date to another. Thus, the development of a multi-frequency algorithm requires a careful evaluation of uncertainty levels [33]. The suitability of multi-track ALOS PALSAR repeat-pass observations for wetland monitoring has been previously confirmed by [33]. Therefore, the development of algorithms to integrate multi-polarization, multi-frequency, multi-temporal, and multi-track InSAR repeat-pass observation is one feasible way to achieve the success of wetland InSAR studies by improving both spatial and temporal resolutions. For example, multi-temporal PolSAR data can be utilized to estimate the dominant scattering mechanism of targets in a stack of SAR data to increase the number of coherent distributed scatterers in the SBAS technique [79].

Thus, the synergy between polarimetry and interferometry techniques is more likely to contribute to the application of advanced InSAR techniques for wetland monitoring for future studies.

Future research should also consider alternative sources of data. For example, the Sentinel-1 satellite is the latest SAR mission operating at C-band, which was launched in 2014. Sentinel-1 acquires SAR data for almost every point with a relatively high temporal resolution, while the perpendicular baseline is also well controlled [80]. This makes Sentinel-1 SAR images ideal sources of data for the STBAS technique. The free availability of Sentinel-1 data is also an encouraging factor to investigate the potential of such data for wetland InSAR applications. Despite these benefits, no wetland InSAR study has been conducted using Sentinel-1 images to date. Further data may also be added from RADARSAT Constellation Mission (RCM) in the near future. Particularly, RCM will have three similar C-band satellites, which are expected to be launched simultaneously in 2018, offering daily coverage over Canada [81]. RCM provides improved operational capability and may address the current limitation of InSAR wetland monitoring, namely, destitute temporal resolution. Thus, increasing the number of available SAR scenes per time unit further facilitates developing an algorithm for water level monitoring with both high temporal and spatial resolutions.

Finally, the NASA/CNES planned Surface Water and Ocean Topography (SWOT) mission, which is a bistatic SAR sensor operating at the Ka-band (8.6 mm) Radar Interferometer (KaRIIn) (also known as an interferometric altimeter), may further facilitate water level monitoring in the near future. It has a near nadir swath and is planned to be launched in 2020. The main mission purpose is to enhance the spatial-temporal coverage of continental water surfaces, including oceans, lakes, reservoirs, and wetlands ( $>250 \text{ m}^2$ ) [82]. The short wavelength causes less scattering by the surface water; however, it also has lower penetration depth through vegetation [83]. The SWOT mission

holds great promise for future applications of InSAR techniques for monitoring wetland water level changes.

## **2.5. Conclusion**

The main findings of this review article can be summarized as follows:

- (1) Although the application of the InSAR technique for wetland water level monitoring is relatively new, the number of studies focusing on the capability of InSAR for monitoring flooded vegetation has increased over the last 10 years. However, most of these studies were conducted in the Everglades and Louisiana wetlands in the United States, while the number of studies conducted in Canada, Europe, and elsewhere was sparse.
- (2) Data- or sensor-driven investigations were the greatest concerns. More specifically, most studies applied medium resolution L-band data and reported that L-HH data were the best configuration for monitoring flooded vegetation, especially for woody wetlands, due to both the higher penetration depth of L-band and greater sensitivity of HH polarization to the double-bounce scattering of flooded vegetation. Most of the studies pointed out vegetative density and water level both control double-bounce scattering in woody wetlands. In particular, the vegetative density decreases the double-bounce scattering and enhances the volume scattering, while increasing water level enhances the chance of the double-bounce scattering between tree trunks and water surface. For herbaceous wetlands, alternatively, shorter wavelengths are preferred because the double-bounce scattering in such a class is mainly controlled by water level, while the vegetative canopy and density are less influential. In particular, increasing the water level decreases the chance of double-bounce scattering and converts most of the double-bounce scattering to specular scattering, which is in contrast with woody wetlands. These results have been mainly obtained based

on L- and C-band observations and while studies on X-band SAR data are still sparse, initial results demonstrate their capacity in all polarizations for wetland InSAR applications.

- (3) The literature also demonstrated the high dependency of InSAR wetland monitoring on an independent source of data, either *in-situ* observations or altimetry data, for calibration and validation. However, studies attempting to quantitatively determine a relationship between SAR backscatter and InSAR observation are still sparse and research efforts towards such objectives should be prioritized.
- (4) The repeat-pass SAR interferometry technique holds great promise for InSAR wetland applications. Although studies that have applied advanced InSAR techniques for monitoring flooded vegetation are still sparse, initial results illustrate that they have great potential for hydrological wetland applications.
- (5) To recapitulate, the literature demonstrated that the suitability of SAR wavelength depends on the wetland classes and phenology. However, it was found that HH polarization, small incident angle, high spatial resolution, and small temporal baseline are of great value for wetland InSAR applications.

## 2.6. References

- [1] P. N. Johnson and P. Gerbeaux, *Wetland types in New Zealand*. Department of Conservation, 2004.
- [2] R. W. Tiner, M. W. Lang, and V. V Klemas, *Remote sensing of wetlands: applications and advances*. CRC press, 2015.
- [3] M. Grenier, A.-M. Demers, S. Labrecque, M. Benoit, R. A. Fournier, and B. Drolet, “An object-based method to map wetland using RADARSAT-1 and Landsat ETM images: test case on two sites in Quebec, Canada,” *Can. J. Remote Sens.*, vol. 33, no. sup1, pp. S28–S45, 2007.
- [4] A. L. Gallant, “The challenges of remote monitoring of wetlands.” Multidisciplinary Digital Publishing Institute, 2015.

- [5] T. Oliver-Cabrera and S. Wdowinski, "InSAR-based mapping of tidal inundation extent and amplitude in Louisiana Coastal Wetlands," *Remote Sens.*, vol. 8, no. 5, p. 393, 2016.
- [6] S. L. Ozesmi and M. E. Bauer, "Satellite remote sensing of wetlands," *Wetl. Ecol. Manag.*, vol. 10, no. 5, pp. 381–402, 2002.
- [7] E. Adam, O. Mutanga, and D. Rugege, "Multispectral and hyperspectral remote sensing for identification and mapping of wetland vegetation: a review," *Wetl. Ecol. Manag.*, vol. 18, no. 3, pp. 281–296, 2010.
- [8] C. Huang, Y. Peng, M. Lang, I.-Y. Yeo, and G. McCarty, "Wetland inundation mapping and change monitoring using Landsat and airborne LiDAR data," *Remote Sens. Environ.*, vol. 141, pp. 231–242, 2014.
- [9] E. S. Kasischke, K. B. Smith, L. L. Bourgeau-Chavez, E. A. Romanowicz, S. Brunzell, and C. J. Richardson, "Effects of seasonal hydrologic patterns in south Florida wetlands on radar backscatter measured from ERS-2 SAR imagery," *Remote Sens. Environ.*, vol. 88, no. 4, pp. 423–441, 2003.
- [10] M. W. Lang and E. S. Kasischke, "Using C-band synthetic aperture radar data to monitor forested wetland hydrology in Maryland's coastal plain, USA," *IEEE Trans. Geosci. Remote Sens.*, vol. 46, no. 2, pp. 535–546, 2008.
- [11] M. Mahdianpari, B. Salehi, F. Mohammadimanesh, and M. Motagh, "Random forest wetland classification using ALOS-2 L-band, RADARSAT-2 C-band, and TerraSAR-X imagery," *ISPRS J. Photogramm. Remote Sens.*, vol. 130, 2017.
- [12] F. Mohammadimanesh, B. Salehi, M. Mahdianpari, and S. Homayouni, "Unsupervised wishart classification of wetlands in Newfoundland, Canada using polsar data based on fisher linear discriminant analysis," in *International Archives of the Photogrammetry, Remote Sensing and Spatial Information Sciences - ISPRS Archives*, 2016, vol. 41.
- [13] J. Li and W. Chen, "A rule-based method for mapping Canada's wetlands using optical, radar and DEM data," *Int. J. Remote Sens.*, vol. 26, no. 22, pp. 5051–5069, 2005.
- [14] J.-R. B. Bwangoy, M. C. Hansen, D. P. Roy, G. De Grandi, and C. O. Justice, "Wetland mapping in the Congo Basin using optical and radar remotely sensed data and derived topographical indices," *Remote Sens. Environ.*, vol. 114, no. 1, pp. 73–86, 2010.
- [15] S. Wdowinski and S.-H. Hong, "Wetland InSAR: A review of the technique and applications," in *Remote Sensing of Wetlands*, CRC Press, 2015, pp. 154–171.
- [16] D. E. Alsdorf, J. M. Melack, T. Dunne, L. A. K. Mertes, L. L. Hess, and L. C. Smith, "Interferometric radar measurements of water level changes on the Amazon flood plain," *Nature*, vol. 404, no. 6774, p. 174, 2000.
- [17] S. Wdowinski, S.-W. Kim, F. Amelung, T. H. Dixon, F. Miralles-Wilhelm, and R. Sonenshein,

- “Space-based detection of wetlands’ surface water level changes from L-band SAR interferometry,” *Remote Sens. Environ.*, vol. 112, no. 3, pp. 681–696, 2008.
- [18] J.-W. Kim *et al.*, “Integrated analysis of PALSAR/Radarsat-1 InSAR and ENVISAT altimeter data for mapping of absolute water level changes in Louisiana wetlands,” *Remote Sens. Environ.*, vol. 113, no. 11, pp. 2356–2365, 2009.
- [19] C. Xie, Y. Shao, J. Xu, Z. Wan, and L. Fang, “Analysis of ALOS PALSAR InSAR data for mapping water level changes in Yellow River Delta wetlands,” *Int. J. Remote Sens.*, vol. 34, no. 6, pp. 2047–2056, 2013.
- [20] S.-W. Kim, S. Wdowinski, F. Amelung, T. H. Dixon, and J.-S. Won, “Interferometric coherence analysis of the Everglades wetlands, South Florida,” *IEEE Trans. Geosci. Remote Sens.*, vol. 51, no. 12, pp. 5210–5224, 2013.
- [21] B. Brisco, K. Murnaghan, S. Wdowinski, and S.-H. Hong, “Evaluation of RADARSAT-2 acquisition modes for wetland monitoring applications,” *Can. J. Remote Sens.*, vol. 41, no. 5, pp. 431–439, 2015.
- [22] Z. Lu and O. Kwoun, “Radarsat-1 and ERS InSAR analysis over southeastern coastal Louisiana: Implications for mapping water-level changes beneath swamp forests,” *IEEE Trans. Geosci. Remote Sens.*, vol. 46, no. 8, pp. 2167–2184, 2008.
- [23] J. A. Richards, P. W. Woodgate, and A. K. Skidmore, “An explanation of enhanced radar backscattering from flooded forests,” *Int. J. Remote Sens.*, vol. 8, no. 7, pp. 1093–1100, 1987.
- [24] K. O. Pope, E. Rejmankova, J. F. Paris, and R. Woodruff, “Detecting seasonal flooding cycles in marshes of the Yucatan Peninsula with SIR-C polarimetric radar imagery,” *Remote Sens. Environ.*, vol. 59, no. 2, pp. 157–166, 1997.
- [25] B. R. N. Gondwe, S.-H. Hong, S. Wdowinski, and P. Bauer-Gottwein, “Hydrologic dynamics of the ground-water-dependent Sian Ka’an wetlands, Mexico, derived from InSAR and SAR data,” *Wetlands*, vol. 30, no. 1, pp. 1–13, 2010.
- [26] A. Ferretti, C. Prati, and F. Rocca, “Permanent scatterers in SAR interferometry,” *IEEE Trans. Geosci. Remote Sens.*, vol. 39, no. 1, pp. 8–20, 2001.
- [27] P. Berardino, G. Fornaro, R. Lanari, and E. Sansosti, “A new algorithm for surface deformation monitoring based on small baseline differential SAR interferograms,” *IEEE Trans. Geosci. Remote Sens.*, vol. 40, no. 11, pp. 2375–2383, 2002.
- [28] A. Hooper, H. Zebker, P. Segall, and B. Kampes, “A new method for measuring deformation on volcanoes and other natural terrains using InSAR persistent scatterers,” *Geophys. Res. Lett.*, vol. 31, no. 23, 2004.
- [29] C. Xie *et al.*, “Long term detection of water depth changes of coastal wetlands in the Yellow River

- Delta based on distributed scatterer interferometry,” *Remote Sens. Environ.*, vol. 164, pp. 238–253, 2015.
- [30] A. Ferretti, A. Fumagalli, F. Novali, C. Prati, F. Rocca, and A. Rucci, “A new algorithm for processing interferometric data-stacks: SqueeSAR,” *IEEE Trans. Geosci. Remote Sens.*, vol. 49, no. 9, pp. 3460–3470, 2011.
- [31] R. Lanari, O. Mora, M. Manunta, J. J. Mallorquí, P. Berardino, and E. Sansosti, “A small-baseline approach for investigating deformations on full-resolution differential SAR interferograms,” *IEEE Trans. Geosci. Remote Sens.*, vol. 42, no. 7, pp. 1377–1386, 2004.
- [32] S. H. Hong, S. Wdowinski, S. W. Kim, and J. S. Won, “Multi-temporal monitoring of wetland water levels in the Florida Everglades using interferometric synthetic aperture radar (InSAR),” *Remote Sens. Environ.*, 2010.
- [33] S.-H. Hong and S. Wdowinski, “Multitemporal multitrack monitoring of wetland water levels in the Florida Everglades using ALOS PALSAR data with interferometric processing,” *IEEE Geosci. Remote Sens. Lett.*, vol. 11, no. 8, pp. 1355–1359, 2014.
- [34] B. Osmanoglu, F. Sunar, S. Wdowinski, and E. Cabral-Cano, “Time series analysis of InSAR data: Methods and trends,” *ISPRS J. Photogramm. Remote Sens.*, vol. 115, pp. 90–102, 2016.
- [35] A. M. Guarnieri and C. Prati, “Sar interferometry: a “quick and dirty” coherence estimator for data browsing,” *IEEE Trans. Geosci. Remote Sens.*, vol. 35, no. 3, pp. 660–669, 1997.
- [36] I. I. I. Ramsey Elijah, Z. Lu, A. Rangoonwala, and R. Rykhus, “Multiple baseline radar interferometry applied to coastal land cover classification and change analyses,” *GIScience Remote Sens.*, vol. 43, no. 4, pp. 283–309, 2006.
- [37] H. A. Zebker and J. Villasenor, “Decorrelation in interferometric radar echoes,” *IEEE Trans. Geosci. Remote Sens.*, vol. 30, no. 5, pp. 950–959, 1992.
- [38] F. Gatelli, A. M. Guarnieri, F. Parizzi, P. Pasquali, C. Prati, and F. Rocca, “The wavenumber shift in SAR interferometry,” *IEEE Trans. Geosci. Remote Sens.*, vol. 32, no. 4, pp. 855–865, 1994.
- [39] M. Zhang, Z. Li, B. Tian, J. Zhou, and J. Zeng, “A method for monitoring hydrological conditions beneath herbaceous wetlands using multi-temporal ALOS PALSAR coherence data,” *Remote Sens. Lett.*, vol. 6, no. 8, pp. 618–627, 2015.
- [40] A. Ferretti, A. Monti-Guarnieri, C. Prati, F. Rocca, and D. Massonet, *InSAR principles-guidelines for SAR interferometry processing and interpretation*, vol. 19. 2007.
- [41] S.-H. Hong, S. Wdowinski, and S.-W. Kim, “Evaluation of TerraSAR-X observations for wetland InSAR application,” *IEEE Trans. Geosci. Remote Sens.*, vol. 48, no. 2, pp. 864–873, 2010.
- [42] A. L. Gray, K. E. Mattar, and G. Sofko, “Influence of ionospheric electron density fluctuations on

- satellite radar interferometry,” *Geophys. Res. Lett.*, vol. 27, no. 10, pp. 1451–1454, 2000.
- [43] E. J. M. Rignot, C. L. Williams, J. Way, and L. A. Viereck, “Mapping of forest types in Alaskan boreal forests using SAR imagery,” *IEEE Trans. Geosci. Remote Sens.*, vol. 32, no. 5, pp. 1051–1059, 1994.
- [44] S.-H. Hong and S. Wdowinski, “Evaluation of the quad-polarimetric Radarsat-2 observations for the wetland InSAR application,” *Can. J. Remote Sens.*, vol. 37, no. 5, pp. 484–492, 2012.
- [45] D. G. Leckie and K. J. Ranson, “Forestry applications using imaging radar,” *Princ. Appl. Imaging Radar*, vol. 2, pp. 435–509, 1998.
- [46] H. Hirose, Y. Matsuzaka, and O. Kobayashi, “Measurement of microwave backscatter from a cypress with and without leaves,” *IEEE Trans. Geosci. Remote Sens.*, vol. 27, no. 6, pp. 698–701, 1989.
- [47] E. Mougin, A. Lopes, M. A. Karam, and A. K. Fung, “Effect of tree structure on X-band microwave signature of conifers,” *IEEE Trans. Geosci. Remote Sens.*, vol. 31, no. 3, pp. 655–667, 1993.
- [48] M. Zhang, Z. Li, B. Tian, J. Zhou, and P. Tang, “The backscattering characteristics of wetland vegetation and water-level changes detection using multi-mode SAR: A case study,” *Int. J. Appl. Earth Obs. Geoinf.*, vol. 45, pp. 1–13, 2016.
- [49] Z. Lu and O.-I. Kwoun, “2 Interferometric Synthetic Aperture Radar (InSAR) Study of Coastal Wetlands Over Southeastern Louisiana,” *Remote Sens. Coast. Environ.*, p. 25, 2009.
- [50] Z. Lu, M. Crane, O. Kwoun, C. Wells, C. Swarzenski, and R. Rykhus, “C-band radar observes water level change in swamp forests,” *EOS, Trans. Am. Geophys. Union*, vol. 86, no. 14, pp. 141–144, 2005.
- [51] A. Freeman and S. L. Durden, “A three-component scattering model for polarimetric SAR data,” *IEEE Trans. Geosci. Remote Sens.*, vol. 36, no. 3, pp. 963–973, 1998.
- [52] Y. Yamaguchi, T. Moriyama, M. Ishido, and H. Yamada, “Four-component scattering model for polarimetric SAR image decomposition,” *IEEE Trans. Geosci. Remote Sens.*, vol. 43, no. 8, pp. 1699–1706, 2005.
- [53] F. M. Grings *et al.*, “Monitoring flood condition in marshes using EM models and Envisat ASAR observations,” *IEEE Trans. Geosci. Remote Sens.*, vol. 44, no. 4, pp. 936–942, 2006.
- [54] T. L. Evans and M. Costa, “Landcover classification of the Lower Nhecolândia subregion of the Brazilian Pantanal Wetlands using ALOS/PALSAR, RADARSAT-2 and ENVISAT/ASAR imagery,” *Remote Sens. Environ.*, vol. 128, pp. 118–137, 2013.
- [55] E. S. Kasischke and L. L. Bourgeau-Chavez, “Monitoring South Florida wetlands using ERS-1 SAR imagery,” *Photogramm. Eng. Remote Sensing*, vol. 63, no. 3, pp. 281–291, 1997.

- [56] O. Kwoun and Z. Lu, "Multi-temporal RADARSAT-1 and ERS backscattering signatures of coastal wetlands in southeastern Louisiana," *Photogramm. Eng. Remote Sens.*, vol. 75, no. 5, pp. 607–617, 2009.
- [57] E. W. RAMSEY III, "Radar remote sensing of wetlands," *Remote Sens. Chang. Detect.*, 1999.
- [58] J.-W. Kim, Z. Lu, J. W. Jones, C. K. Shum, H. Lee, and Y. Jia, "Monitoring Everglades freshwater marsh water level using L-band synthetic aperture radar backscatter," *Remote Sens. Environ.*, vol. 150, pp. 66–81, 2014.
- [59] T. Yuan, H. Lee, and H. C. Jung, "Toward estimating wetland water level changes based on hydrological sensitivity analysis of PALSAR backscattering coefficients over different vegetation fields," *Remote Sens.*, vol. 7, no. 3, pp. 3153–3183, 2015.
- [60] H. Lee, T. Yuan, H. C. Jung, and E. Beighley, "Mapping wetland water depths over the central Congo Basin using PALSAR ScanSAR, Envisat altimetry, and MODIS VCF data," *Remote Sens. Environ.*, vol. 159, pp. 70–79, 2015.
- [61] S. R. Cloude and E. Pottier, "An entropy based classification scheme for land applications of polarimetric SAR," *IEEE Trans. Geosci. Remote Sens.*, vol. 35, no. 1, pp. 68–78, 1997.
- [62] R. Touzi, "Target scattering decomposition in terms of roll-invariant target parameters," *IEEE Trans. Geosci. Remote Sens.*, vol. 45, no. 1, pp. 73–84, 2007.
- [63] L. A. James, D. G. Watson, and W. F. Hansen, "Using LiDAR data to map gullies and headwater streams under forest canopy: South Carolina, USA," *Catena*, vol. 71, no. 1, pp. 132–144, 2007.
- [64] K. L. Jones, G. C. Poole, S. J. O'Daniel, L. A. K. Mertes, and J. A. Stanford, "Surface hydrology of low-relief landscapes: Assessing surface water flow impedance using LIDAR-derived digital elevation models," *Remote Sens. Environ.*, vol. 112, no. 11, pp. 4148–4158, 2008.
- [65] F. Frappart, S. Calmant, M. Cauhopé, F. Seyler, and A. Cazenave, "Preliminary results of ENVISAT RA-2-derived water levels validation over the Amazon basin," *Remote Sens. Environ.*, vol. 100, no. 2, pp. 252–264, 2006.
- [66] S. Lin and R. Gregg, *Water budget analysis: Water conservation area 1*. Water Resources Division, Resource Planning Department, South Florida Water ..., 1988.
- [67] P. A. Telis, "The Everglades Depth Estimation Network (EDEN) for support of ecological and biological assessments," Geological Survey (US), 2006.
- [68] C. M. Birkett, L. A. K. Mertes, T. Dunne, M. H. Costa, and M. J. Jasinski, "Surface water dynamics in the Amazon Basin: Application of satellite radar altimetry," *J. Geophys. Res. Atmos.*, vol. 107, no. D20, p. LBA-26, 2002.
- [69] M. Zhang, "Satellite radar altimetry for inland hydrologic studies." The Ohio State University, 2009.

- [70] V. Poncos, S. Molson, A. Welch, and S. Brazeau, "Detection of flooded vegetation and measurements of water level changes using RADARSAT-2," in *2013 IEEE International Geoscience and Remote Sensing Symposium-IGARSS*, 2013, pp. 2208–2211.
- [71] S. W. Kim, S. Wdowinski, F. Amelung, and T. H. Dixon, "C-band interferometric SAR measurements of water level change in the wetlands: Examples from Florida and Louisiana," in *2005 IEEE International Geoscience and Remote Sensing Symposium, IGARSS 2005*, 2005.
- [72] H. C. Jung *et al.*, "Characterization of complex fluvial systems using remote sensing of spatial and temporal water level variations in the Amazon, Congo, and Brahmaputra Rivers," *Earth Surf. Process. Landforms J. Br. Geomorphol. Res. Gr.*, vol. 35, no. 3, pp. 294–304, 2010.
- [73] S. Wdowinski, S.-H. Hong, A. Mulcan, and B. Brisco, "Remote-sensing monitoring of tide propagation through coastal wetlands," *Oceanography*, vol. 26, no. 3, pp. 64–69, 2013.
- [74] M. Yuan, C. Xie, Y. Shao, J. Xu, B. Cui, and L. Liu, "Retrieval of water depth of coastal wetlands in the Yellow River Delta from ALOS PALSAR backscattering coefficients and interferometry," *IEEE Geosci. Remote Sens. Lett.*, vol. 13, no. 10, pp. 1517–1521, 2016.
- [75] V. Poncos, S. Molson, A. Welch, S. Brazeau, and S. O. Kotchi, "SAR for surface water monitoring and public health," in *2014 IEEE Geoscience and Remote Sensing Symposium*, 2014, pp. 1167–1170.
- [76] M. Mahdianpari, B. Salehi, and F. Mohammadimanesh, "The Effect of PolSAR Image De-speckling on Wetland Classification: Introducing a New Adaptive Method," *Can. J. Remote Sens.*, vol. 43, no. 5, 2017.
- [77] B. Brisco, F. Ahern, K. Murnaghan, L. White, F. Canisus, and P. Lancaster, "Seasonal change in wetland coherence as an aid to wetland monitoring," *Remote Sens.*, vol. 9, no. 2, p. 158, 2017.
- [78] C. Colesanti and J. Wasowski, "Investigating landslides with space-borne Synthetic Aperture Radar (SAR) interferometry," *Eng. Geol.*, vol. 88, no. 3–4, pp. 173–199, 2006.
- [79] M. Esmacili, M. Motagh, and A. Hooper, "Application of dual-polarimetry SAR images in multitemporal InSAR processing," *IEEE Geosci. Remote Sens. Lett.*, vol. 14, no. 9, pp. 1489–1493, 2017.
- [80] R. Torres *et al.*, "GMES Sentinel-1 mission," *Remote Sens. Environ.*, vol. 120, pp. 9–24, 2012.
- [81] M. Mahdianpari, B. Salehi, F. Mohammadimanesh, and B. Brisco, "An Assessment of Simulated Compact Polarimetric SAR Data for Wetland Classification Using Random Forest Algorithm," *Can. J. Remote Sens.*, vol. 43, no. 5, 2017.
- [82] E. Rodríguez, "SWOT science requirements document," *JPL Doc. JPL*, vol. 856, 2012.
- [83] R. Fjørtoft *et al.*, "KaRIn on SWOT: Characteristics of near-nadir Ka-band interferometric SAR

imagery,” *IEEE Trans. Geosci. Remote Sens.*, vol. 52, no. 4, pp. 2172–2185, 2014.

## Chapter 3. Coherence and SAR backscatter analyses of Canadian wetlands <sup>2</sup>

### Preface

A version of this manuscript has been published in the *ISPRS Journal of Photogrammetry and Remote Sensing*. I am a primary author of this manuscript along with the co-authors, Bahram Salehi, Masoud Mahdianpari, Brian Brisco, and Mahdi Motagh. I designed and conceptualized the study. I developed the model and performed all experiments and tests. I wrote the paper and revised it based on comments from all co-authors. I also revised the paper according to the reviewers' comments. The co-author, Masoud Mahdianpari helped in performing the experiments and analyzing the results and contributed to revising the manuscript. All co-authors provided editorial input and scientific insights to further improve the paper. They also reviewed and commented on the manuscript.

### Abstract

Despite recent research into the Interferometric Synthetic Aperture Radar (InSAR) technique for wetland mapping worldwide, its capability has not yet been thoroughly investigated for Canadian wetland ecosystems. Accordingly, this study statistically analysed interferometric coherence and SAR backscattering variation in a study area located on the Avalon Peninsula, Newfoundland and Labrador, Canada, consisting of various wetland classes, including bog, fen, marsh, swamp, and shallow-water. Specifically, multi-temporal L-band ALOS PALSAR-1, C-band RADARSAT-2, and X-band TerraSAR-X data were used to investigate the effect of SAR frequency and polarization, as well as temporal baselines on the coherence degree in the various wetland classes.

---

<sup>2</sup> Mohammadimanesh, F., Salehi, B., Mahdianpari, M., Brisco, B. and Motagh, M., 2018. Multi-temporal, multi-frequency, and multi-polarization coherence and SAR backscatter analysis of wetlands. *ISPRS journal of photogrammetry and remote sensing*, 142, pp.78-93.

SAR backscatter and coherence maps were also used as input features into an object-based Random Forest classification scheme to examine the contribution of these features to the overall classification accuracy. Our findings suggested that the temporal baseline was the most influential factor for coherence maintenance in herbaceous wetlands, especially for shorter wavelengths. In general, coherence was the highest in L-band and intermediate/low for both X- and C-band, depending on the wetland classes and temporal baseline. The Wilcoxon rank sum test at the 5% significance level found the significance difference ( $P\text{-value} < 0.05$ ) between the mean values of HH/HV coherence at the peak of growing season. The test also suggested that L-band intensity and X-band coherence observations were advantageous to discriminate complex wetland classes. Notably, an overall classification accuracy of 74.33% was attained for land cover classification by synergistic use of both SAR backscattering and interferometric coherence. Thus, the results of this study confirmed the potential of incorporating SAR and InSAR features for mapping Canadian wetlands and those elsewhere in the world with similar ecological characteristics.

**Keywords:** Wetland, Interferometric Synthetic Aperture Radar (InSAR), Coherence analysis, SAR backscatter, Random Forest.

### **3.1. Introduction**

Wetlands are transitional zones between terrestrial and aquatic regions, which are permanently or temporarily covered with shallow water [1]. They are considered a desirable habitat for a variety of animal and plant species by providing food and shelter. Other wetland ecosystem services include flood storage, shoreline stabilization, and water-quality renovation. However, wetlands are increasingly degraded due to both natural processes, such as global warming, changes in precipitation patterns, and coastal erosion, as well as anthropogenic activities, including industrial runoff, road construction, and plant or animal collection and introduction [1], [2]. Furthermore,

the loss of wetland hydrological connectivity due to human activities leads to massive destruction of coastal wetlands [3].

Wetland monitoring and management have recently gained more attention thanks to advancement in remote sensing technologies in a variety of subjects, including wetland hydrological monitoring [4], change detection [5], and classification [6]. Importantly, the advent of Synthetic Aperture Radar (SAR) sensors has significantly influenced wetland restoration studies and management [3], [7]. This is because microwaves penetrate through soil, cloud, and vegetation and the sensors are not reliant on sun illumination, which means SAR sensors operate in all-weather day/night conditions. Thus, they have facilitated wetland monitoring especially in geographic regions with near-permanent cloud cover.

Hydrological monitoring of wetlands is crucial since they are water-dependent ecosystems. SAR images have been found to be efficient tools for wetland hydrological monitoring using both SAR backscattering signatures [8], [9], and a more detailed and quantitative technique, Interferometric SAR (InSAR) [4]. The flooded and non-flooded statuses of vegetation in wetland environments have distinct differences in radar backscattering response, which plays an important role in sustainable hydrological monitoring of wetlands. In particular, a time series analysis of SAR backscatter signature has provided information about seasonal patterns of flooding in wetland ecosystems and has been examined in number of studies [8], [10], [11].

The potential of the InSAR technique for water level monitoring was first investigated in the Amazon floodplain using SIR-C in C- and L-band frequencies [12]. This study demonstrated that vegetation in or adjacent to the standing water backscatters the radar pulse towards the satellite sensor due to double-bouncing effect. This provided the possibility for monitoring water level changes in the phase data. Subsequently, the capability of the InSAR technique for water level

monitoring has been further examined for a number of other places such as Florida Everglades [4], [13], [14], Louisiana coastal wetland [15]–[17], China wetlands [18], [19], and most recently the Cienaga Grande de Santa Marta (CGSM) wetland located in Colombia [3].

In addition to hydrological monitoring of wetlands using InSAR, the interferometric coherence may be useful for discriminating different wetland vegetation covers. Currently, little is known about the capability of interferometric coherence for classifying different land cover types, which may provide information in addition to SAR intensity (i.e., the portion of the backscattered SAR signal from ground targets). This is because SAR intensity depends on the electromagnetic structure of the targets, while the interferometric coherence shows their mechanical and dielectric stability [20]. Furthermore, the SAR intensity is affected by speckle noise, while the speckle noise is averaged when two images are integrated to generate the interferometric product [21].

Ramsey et al. (2006) used ERS1/2 tandem image pairs to compare the potential of interferometric products (i.e., coherence and phase) and SAR backscatter images for land cover classification in the Big Bend coastal wetland, Florida [21]. They found that intensity was less responsive to land covers and had high temporal variations. However, coherence had more variation in different classes and provided better discrimination, especially, during the leaf-off season. Kim et al. (2013) investigated the interferometric coherence of wetland classes using C- and L-band data in the Everglades wetlands [22]. They reported that longer wavelengths and smaller incident angles are better suited for wetland InSAR application. Zhang et al. (2015) used interferometric coherence obtained by ALOS data for classification of wet and dry marshes in the Liaoh River Delta, China [23]. Brisco et al. (2015) looked at the interferometric coherence in the Everglades wetlands for different RADARSAT-2 products [14]. They observed an adequate degree of coherence in all RADARSAT-2 products, while the coherence was better preserved for images with high spatial

resolution and small incidence angle. Most recently, Brisco et al. (2017) evaluated the temporal variation of coherence in three wetland types, including swamp, marsh, and shallow open water classes using Spotlight RADARSAT-2 images during ice-off and ice-on seasons in Ottawa, Ontario [5]. They reported a sufficient degree of coherence in both swamp and marsh during the periods of the ice-off season and noted the potential of coherence images for wetland change detection.

The majority of these studies have investigated the potential of InSAR products for wetland monitoring from a very specific point of view. Accordingly, studies attempting to address all influential factors for wetland InSAR applications are limited. For example, most of these researches applied only C- and especially, L-band data for coherence analysis, and mainly concentrated on HH polarization. However, the interferometric coherence of wetland classes using X-band SAR imagery, which may contribute to the success of InSAR for wetland applications due to high temporal and spatial resolution, has not yet been investigated. The selection of appropriate SAR wavelengths and polarizations are two influential factors for wetland monitoring using SAR imagery. Thus, the primary goal of this research study was to determine the capability of multi-frequency SAR imagery, including ALOS PALSAR-1 L-band, RADARSAT-2 C-band, and TerraSAR-X images in terms of coherence maintenance for different wetland classes. Specifically, the main objectives were: (1) to determine the most appropriate SAR frequency and polarization for hydrological monitoring of Newfoundland herbaceous wetlands; (2) to identify the most influential factors for coherence preservation of different vegetation types using a multi-temporal coherence analysis framework; (3) to assess the relationship between the variation of SAR backscatter and coherence in complex wetland ecosystems; and (4) to explore the contribution of the interferometric coherence to wetland classification results using an object-based Random

Forest approach. Thus, this study advances towards an operational methodology for mapping Canadian wetlands, as well as those with similar ecological features and vegetation types, that builds upon the relationship between the flooding status of vegetation (i.e., wetland phenological cycle), SAR backscattering responses, and variation of interferometric coherence.

## 3.2. Methods

### 3.2.1. Study area and field data

This study was carried out within a 700 km<sup>2</sup> site located in the northeast portion of Newfoundland and Labrador, the Avalon Peninsula, in the Maritime Barren ecoregion (Figure 3.1).

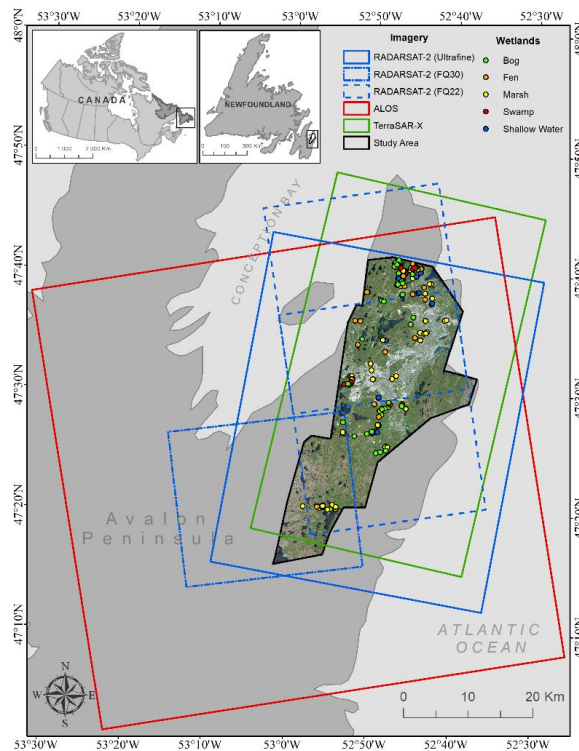


Figure 3.1. Level 3A RapidEye image (bands 3, 2, and 1), acquired on June 18, 2015, illustrating the geographic location of the study area with overlays of the Synthetic Aperture Radar (SAR) scenes. The circles mark the location of referenced polygons used for the coherence and backscattering analysis.

This ecoregion is specified by an oceanic climate, having foggy, cool summers and relatively mild winters [24]. Mean annual precipitation varies between 1200 to 1600mm and mean annual temperatures are approximately 5.5°C [25]. Figure 3.2 depicts the total precipitation (mm) for each month in 2016.

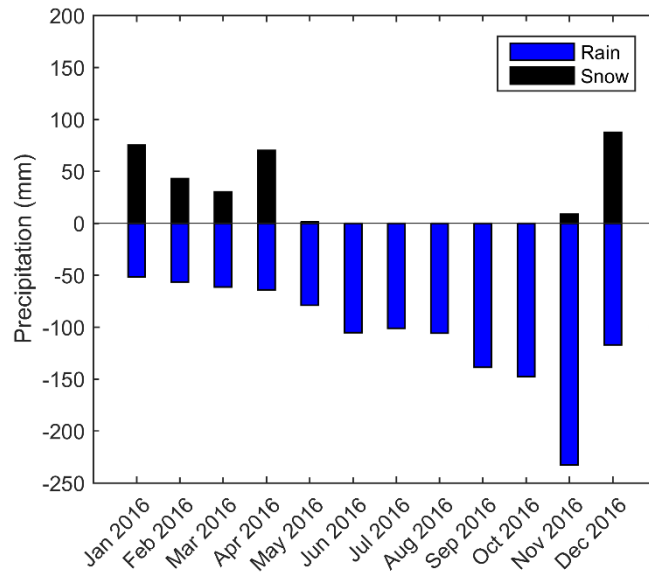


Figure 3.2. Total precipitation in the Avalon study area for each month in 2016.

The study area contains a dense urban area to the north, where the capital city of St. John’s and various closely associated towns and cities are located. Moving south, the urban cover becomes sparse, where balsam fir forests, heathland barrens, and expansive peatland (bog and fen) dominate [26]. The patterns of forest stands separated by large barrens, common in and around the study area, are the result of frequent forest fires, partially a result of colonization [26], [27]. The topography largely reflects past glacial activity in which retreating glaciers helped to form the numerous lakes and ponds across the rolling ground moraine land cover scattered by isolated rocks and boulders [27].

This area has eight land cover classes, five of which are wetlands (see Table 3.1). In particular, all five class of wetlands categorized by the Canadian Wetland Classification System, including bog, fen, marsh, swamp, and shallow-water are found within the study area [28]; however, bog and fen are the most dominant wetland classes relative to the occurrence of swamp, marsh, and shallow-water. For this study, *in-situ* data were collected in the summers and falls of 2015 and 2016 over multiple field-visits during the leaf-on season, and Global Positioning System (GPS) locations were recorded. A total of 168 wetland sites were visited and categorized as bog (54), marsh (46), fen (29), swamp (24), and shallow-water (15).

Table 3.1. A description of land cover classes in this study.

Class	Class Description
Bog	Peatland dominated by <i>spahgnum</i> species
Fen	Peatland dominated by <i>graminoid</i> species
Swamp	Mineral wetland dominated by woody vegetation
Marsh	Mineral wetland dominated by <i>graminoids</i> and emergent plants
Shallow-water	Mineral wetland with standing water at most 2m deep
Urban	Human-made structures
Deep-water	Deep water areas
Upland	Forested dry upland

Wetland boundary delineation was conducted using ArcMap 10.3.1 with the aid of aerial and satellite imagery, including a 50 cm resolution orthophotograph and 5m resolution, multi-date RapidEye imagery (June and November 2015). Finally, polygons representing classified and delineated wetlands were created. Figure 3.1. displays the location of the polygons in the study area, wherein each delineated polygon represents one field-visited wetland. For coherence and SAR backscattering analysis, the training pixels in wetland classes (i.e., bog, fen, swamp, marsh, and shallow-water) were used. However, for the object-based classification, different sampling

polygons, including the training and testing polygons, were applied for training and validating the classification, respectively, in order to ensure a robust classification accuracy assessment.

### **3.2.2. Satellite images**

Different SAR images in three frequencies, including L-, C-, and X-band have been used in this study. Specifically, a total number of 17 ALOS PALSAR-1 L-band images in Fine Beam Double (FBD) and Fine Beam Single (FBS) polarization mode in time periods of February 2007 to November 2010 have been used. Different products of RADARSAT-2 C-band data with different incidence angles and resolutions in either single- or full-polarization, which cover different parts of our case study, were also used. RADARSAT-2 images have been acquired in the interval between April and August 2016. It is worth noting that due to the small swath of Fine resolution Quad-polarization (FQ) beam mode, more than one image was used to cover the whole study area (FQ22). Also, a total number of nine HH-polarized TerraSAR-X images in StripMap mode in the interval from August to November 2016 has been used as the X-band data. Figure 3.1. depicts overlays of Synthetic Aperture Radar (SAR) scenes on the study area. The repeat-pass SAR images either partially or completely cover our research region. Table 3.2 represents a detailed description of the satellite images used in this study. Notably, RapidEye optical imagery of level 3A products with a pixel size of 5m was also used for the initial segmentation.

Table 3.2. The characteristics of satellite images used in this study.

Sensor	Acquisition date (yyyy.mm.dd)	Image mode	Inc. angle (°)	Resolution (m)	Polarization	Direction	
ALOS-1	2007.02.18	FBS	38.7	10	HH	Ascending	
	2007.04.05	FBS	38.7	10	HH	Ascending	
	2007.05.21	FBD	38.7	20	HH-HV	Ascending	
	2007.07.06	FBD	38.7	20	HH-HV	Ascending	
	2007.08.21	FBD	38.7	20	HH-HV	Ascending	
	2008.02.21	FBS	38.7	10	HH	Ascending	
	2008.04.07	FBS	38.7	10	HH	Ascending	
	2008.10.08	FBD	38.7	20	HH-HV	Ascending	
	2009.02.23	FBS	38.7	10	HH	Ascending	
	2009.07.11	FBD	38.7	20	HH-HV	Ascending	
	2009.08.26	FBD	38.7	20	HH-HV	Ascending	
	2010.01.11	FBS	38.7	10	HH	Ascending	
	2010.04.13	FBS	38.7	10	HH	Ascending	
	2010.05.29	FBD	38.7	20	HH-HV	Ascending	
	2010.08.29	FBD	38.7	20	HH-HV	Ascending	
	2010.10.14	FBD	38.7	20	HH-HV	Ascending	
	2010.11.29	FBD	38.7	20	HH-HV	Ascending	
	RADARSAT-2	2016.04.21	U16W2	42.13	2.5	HH	Descending
		2016.05.15	U16W2	42.13	2.5	HH	Descending
2016.06.08		U16W2	42.13	2.5	HH	Descending	
2016.07.26		U16W2	42.13	2.5	HH	Descending	
2016.08.19		U16W2	42.13	2.5	HH	Descending	
2016.06.07		FQ22	42	8	Quad-pol	Ascending	
2016.06.07		FQ22	42	8	Quad-pol	Ascending	
2016.07.25		FQ22	42	8	Quad-pol	Ascending	
2016.07.25		FQ22	42	8	Quad-pol	Ascending	
2016.07.11		FQ30	48	7	Quad-pol	Ascending	
2016.08.04		FQ30	48	7	Quad-pol	Ascending	
2016.08.28		FQ30	48	7	Quad-pol	Ascending	
TerraSAR-X		2016.08.11	StripMap	21.55	3	HH	Descending
	2016.08.22	StripMap	21.55	3	HH	Descending	
	2016.09.02	StripMap	21.55	3	HH	Descending	
	2016.09.13	StripMap	21.55	3	HH	Descending	
	2016.09.24	StripMap	21.55	3	HH	Descending	
	2016.10.05	StripMap	21.55	3	HH	Descending	
	2016.10.16	StripMap	21.55	3	HH	Descending	
	2016.10.27	StripMap	21.55	3	HH	Descending	
	2016.11.07	StripMap	21.55	3	HH	Descending	

### 3.2.3. Generation of the coherence images

SAR interferometry processes two complex SAR images acquired with very similar geometrical acquisitions during the time interval of the satellite repeat cycle. Interferometric coherence calculation is a well-known method to examine the quality of the interferograms for wetland studies [14]. Coherence represents the degree of similarity (i.e., the consistency of the scattering mechanism) of the two pixels with the same location in the time interval between two SAR

acquisitions. Coherence is calculated by cross-correlation of the two co-registered SAR images over a small window of pixels [20]:

$$\gamma = \frac{|\langle S_1 S_2^* \rangle|}{\sqrt{\langle S_1 S_1^* \rangle \langle S_2 S_2^* \rangle}} \quad (3.1)$$

where  $S_1$  and  $S_2$  denote the complex pixel values of backscattering coefficient, \* refers to the complex conjugate, and pixel values within  $\langle \rangle$  denote their spatial averaging over a selected window size.  $\gamma$  varies between 0 and 1; if two images are exactly the same,  $\gamma$  is equal to 1, whereas if they do not correspond,  $\gamma$  is equal to 0. In this study, all interferometric processing was carried out using the Gamma Remote Sensing software package. An external Digital Elevation Model (DEM), SRTM 3 arc-second (<https://earthexplorer.usgs.gov/>), was used in the interferometric processing of topographic phase removal and the coherence images were produced using a 5x5 window size. It is worth noting that for the interferometric processing, image co-registration was performed at sub-pixel accuracy (better than 0.05 pixels). Also, all interferometric coherence images had perpendicular baselines smaller than the critical baseline.

In this study, ALOS-1 images were acquired in either single- or dual-polarization mode (see Table 3.2). To integrate both types of images, the dual-polarized images were interpolated in the range direction to produce image pixel sizes comparable with that of single-polarized PALSAR images. We constrained our coherence analysis for ALOS-1 data to pairs with temporal baselines of up to one year. This is because previous studies showed that herbaceous wetlands, which are the dominant wetland types in this study, cannot maintain coherence for a longer period of time even when L-band is applied [4], [22]. In particular, Kim et al. (2013) reported that herbaceous wetlands maintained coherence over six months using JERS-1 L-band data in the Everglades [22]. Thus, a

total number of 44 PALSAR coherence images were generated, allowing a quantitative analysis in term of coherence maintenance for different wetland classes in a multi-temporal framework.

All possible interferometric pairs for RADARSAT-2 images were considered. More specifically, five RADARSAT-2 images in the UltraFine mode were used and 10 coherence images with temporal separation of 24 to 120 days were produced. Furthermore, different full polarimetric RADARSAT-2 images (i.e., FQ22 and FQ30) were used to evaluate the effect of polarization in terms of coherence preservation in different wetland classes. For the full polarimetric FQ22 data, only a single pair with a temporal baseline of 24 days was available. Thus, we used this image to evaluate the potential of each polarization for coherence maintenance.

All possible interferometric pairs of TerraSAR-X images were also considered. Using nine TerraSAR-X images, 36 coherence images with temporal baselines between 11 and 88 days were produced. Notably, RADARSAT-2 and TerraSAR-X images in this study were partially captured at the same time. This produced an ideal dataset to compare the capacity of these SAR frequencies for coherence maintenance under relatively same period of time and environmental condition.

After producing coherence imagery, a coherence variation analysis was carried out using ecological training data by calculating the mean and standard deviation of coherence for all wetland classes. For this purpose, we considered different subsets of each class with relatively large areas and the mean coherence was calculated by averaging the coherence values within each ecological training class.

#### **3.2.4. SAR backscatter coefficient images**

SAR backscatter intensity of the ground target is a function of several factors, including SAR wavelength, image acquisition geometry, local topography, surface roughness, and the dielectric

constant of the targets [21]. SAR intensity also depends on vegetation height, biomass, density, and flooding status in wetland complexes [22]. Positive backscatter values indicate a greater amount of energy was received by the SAR sensor, whereas negative values show that less energy was received. Particularly, an increase in surface roughness and the dielectric constant increase the SAR intensity. Furthermore, it has been reported that SAR backscatter changes in wetlands can be correlated with water level variations, phenological changes, and soil moisture [8], [22].

In this study, SAR backscattering coefficient images were produced for ALOS-1, RADARSAT-2 Ultrafine mode, and TerraSAR-X imagery. In particular, ALOS-1 level 1.0 images were processed using the Gamma Remote Sensing software package. The processing consisted of several steps, including reading the raw image, generating the multi-look intensity image, de-speckling, and geo-referencing, which projected all intensity images into UTM coordinate (zone 22, row T) using the WGS84 reference ellipsoid. These images were presented in intensity values. They were then converted into normalized backscattering coefficient ( $\sigma^0$ ) values in dB, which is the standard unit for SAR backscattering representation. The conversion process for ALOS-1 images is as follows:

$$\sigma^0 = 10 * \log_{10}(DN^2) + CF \quad (3.2)$$

where  $DN$  is the digital number and  $CF$  is the calibration coefficient for ALOS standard product [29].

RADARSAT-2 and TerraSAR-X SLC images were processed using the Sentinel Application Platform (SNAP) software made available by the European Space Agency (ESA), using provided geometric and radiometric tools. After image geo-referencing, an adaptive Lee filter with a 7x7 window size was applied to suppress the effect of speckle noise. The filtered images represented the preservation of the edges and smoothness in homogenous targets. All intensity images were

then converted into the normalized backscattering coefficient ( $\sigma^0$ ) values in dB. The conversion process for RADARSAT-2 products is presented as follows:

$$CV = \frac{|DN|^2}{A^2} \quad (3.3)$$

where  $CV$ ,  $DN$ , and  $A$  indicate the calibrated value, digital number, and gain value, respectively [30]. The normalized backscattering coefficient in dB is obtained as follows:

$$\sigma^0 = 10 * \log(CV) \quad (3.4)$$

For TerraSAR-X images (from intensity values), the beta naught values are represented as follows:

$$\beta_{dB}^0 = 10 * \log_{10}(k_s * |DN|^2) \quad (3.5)$$

where  $k_s$  is the calibration and processor scaling factor and  $DN$  is the digital number. The sigma naught values in dB are then extracted using beta naught as follows:

$$\sigma_{dB}^0 = \beta_{dB}^0 + 10 * \log_{10}(\sin \theta_{loc}) \quad (3.6)$$

where  $\theta_{loc}$  is the local incidence angle and is obtained by the Geocoded Incidence Angle Mask (GIM) [31].

After producing SAR backscattering images, an analysis of  $\sigma^0$  variation was carried out for the wetland classes. For this purpose, an average SAR backscattering coefficient was calculated for each wetland class, excluding shallow-water, using referenced polygons in a multi-temporal framework. Although the study area contains other land cover types (i.e., deep-water, urban, and upland) we constrained our coherence and SAR backscattering analysis to wetland classes. This is

because the phenology, temporal effect, and flooding status of vegetation are the most influential factors altering the interferometric coherence and SAR backscatter in wetland classes, which does not hold true for other land cover types.

### **3.2.5. Object-Based Random Forest classification**

The per-pixel image analysis algorithm has been used for land cover classification for several years due to the coarse resolution of pixels in satellite imagery relative to the size of ground objects. However, the Object-Based Images Analysis (OBIA) technique has gained highlighted interest for land cover classification compared to the pixel-based approach due to recent improvement of satellite imagery in terms of spatial resolution [32], [33]. The main advantages of the object-based relative to pixel-based approach are that the former incorporates different input features, such as object size and shape, multiple sources of data with different spectral and spatial resolution, and the spatial and hierarchical relations between neighbouring pixels rather than a single pixel, results in significant improvements in terms of extracted information for a given area. Moreover, it has been reported that OBIA outperformed the pixel-based approach for classification of SAR imagery. This is because when OBIA is applied, an average backscattering procedure is carried out across neighboring pixels, which, in turn, decreases the inherent speckle in the SAR imagery [6].

Multi-Resolution Segmentation (MRS) algorithm is the first step in OBIA [34]. MRS is a region-merging algorithm, wherein the main objective is to minimize the summed heterogeneity using a pairwise comparison of neighboring pixels [29]. The MRS algorithm is usually controlled by three user-defined parameters, including shape, compactness, and scale. The optimum values for these parameters are obtained by the “trial and error” procedure depending on the research goals [33]. In this study, the MRS algorithm was executed by the eCognition Developer software package

(V.9.0) [35] using a RapidEye optical image. In particular, MRS analysis was performed with an optical image because segmentation using SAR imagery could generate meaningless objects due to the inherent speckle noise. Different scale, shape, and compactness parameters were examined using an iterative “trial and error” approach and the optimal values were found to be 100, 0.05, and 0.5, respectively.

Image classification is the second step in OBIA. In this study, Random Forest algorithm was selected for classification due to its several advantages [36]. RF is a non-parametric classifier that operates independent of the input data distribution; this contrasts with parametric classifiers that rely on the normality distribution of input data such as the Maximum Likelihood Classifier (MLC) [36]; as such, RF is preferential for SAR and polarimetric image classification. RF is also an ensemble classifier that utilizes a set of Classification And Regression Trees (CARTs) [36] and has shown good results in several research [37], [38]. Furthermore, RF can be effectively used for processing large multi-temporal datasets with large numbers of input variables, while accommodating different types or scales of input data. It is also not sensitive to noise and overtraining and is easily adjusted using two variables: the number of decision trees (*Ntree*) and the number of variables (*Mtry*) [39]. One of great advantage of RF is that it determines the relative importance of input variables in the classification, which indicates the influence of each input feature on the overall classification accuracy. Given its numerous advantages and because it better accommodates our input data, RF was selected for classification in this study. A total number of 500 trees (*Ntree*) were selected for classification and the square root of the number of input variables (i.e., the default value) was selected for *Mtry*.

For RADARSAT-2 and TerraSAR-X, all coherence and intensity images were used for classification. However, due to the time difference between ALOS satellite imagery and *in-situ*

data, only 2010 ALOS imagery (for both coherence and intensity) was used for classification. This resulted in an acceptable time difference between ALOS and ecological field data (~ 5 years). Therefore, a total of 108 features were extracted for classifications and three RF classifications were performed using different groups of features obtained by coherence (73), intensity (35), and combined coherence and intensity layers (108).

### **3.3. Results**

#### **3.3.1. Coherence analysis of different SAR wavelengths**

Figures 3.3, 3.4, and 3.5 depict the results of ALOS-1, RADARSAT-2, and TerraSAR-X coherence variation as a function of the temporal and perpendicular baselines for all wetland classes. As seen, coherence is influenced to a greater degree by the temporal baseline in all frequencies, especially for shorter wavelengths (i.e., C- and X-band). This is because shorter wavelengths have less penetration depth and interact primarily with the upper sections of the canopy (wind-affected section) and, as a result, lose coherence over a shorter period of time. For example, coherence was high for all wetland classes, excluding shallow-water, in the first satellite repeat cycle (i.e., 11 and 24 days for TerraSAR-X and RADARSAT-2, respectively); however, coherence decreased as the temporal baseline increased. One interesting observation was also found for the coherence of RADARSAT-2 images, wherein the coherence was less than 0.4 for all wetland classes over the first 24-day interval (2016/4/21-2016/5/15). This was because of a heavy snowfall on April 21<sup>st</sup>, which caused a coherence loss between this particular interferometric pair (<https://stjohns.weatherstats.ca/>).

The coherence variation was independent of the perpendicular baseline for RADARSAT-2 and TerraSAR-X imagery. This is because in advanced SAR missions (e.g., TerraSAR-X) the orbital tube is always kept within a certain limit in order to keep the baselines small and decrease the

effect of baseline decorrelation. As seen, the perpendicular baselines for all RADARSAT-2 and TerraSAR-X interferometric pairs were less than 220m. However, the coherence variation illustrated a dependency on the perpendicular baseline for ALOS-1 observations, wherein coherence was reduced as the perpendicular baseline exceeded about 700m.

The phenological cycle was also observed in the coherence variation for both ALOS-1 and TerraSAR-X imagery, although it was not obtained for RADARSAT-2 imagery due to the limited number of images. For example, the coherence level was greater than 0.5 for almost all wetland classes (excluding shallow-water) in 46 days interval for ALOS-1 data; however, interferometric pairs during the leaf-off season had a lower degree of coherence even for a short period of time (see Figure 3.3). Also, all interferometric pairs of TerraSAR-X images with temporal baselines of less than 22 days during August and September 2016, corresponding to the leaf-on seasons in the Avalon pilot site, illustrated a high degree of coherence due to the summer water table (see Figures 3.2 and 3.5). These observations illustrated that the degree of flooding controls the coherence variation in the wetland classes. The coherence analysis indicated that the shallow-water wetland had the lowest coherence ( $< 0.19$ ) in all frequencies. Thus, the coherence value of 0.19 was considered as a representative of the decorrelation level and accordingly, the shallow-water class was excluded from further coherence and backscattering analysis in this study.

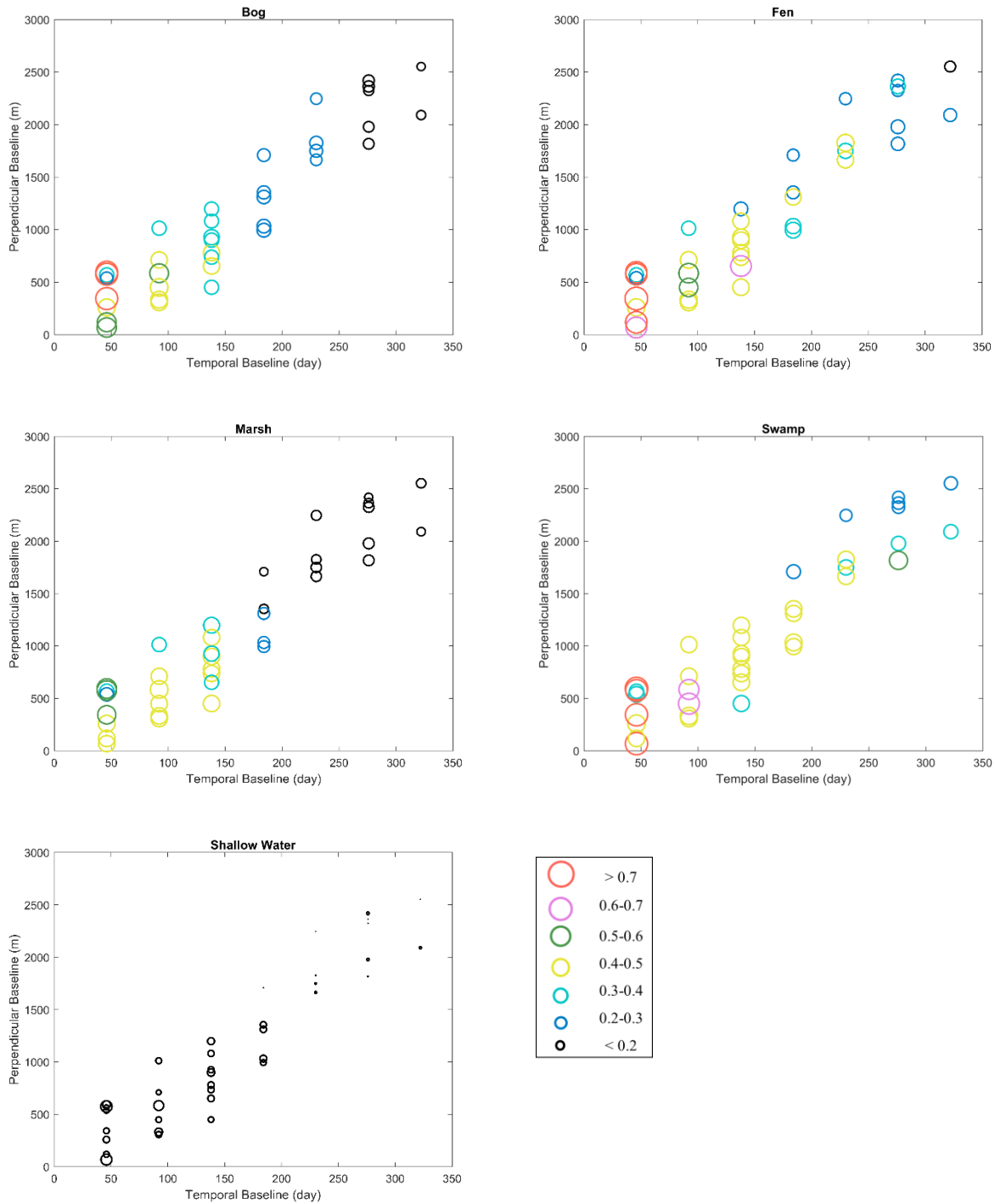


Figure 3.3. ALOS PALSAR-1 coherence analysis results for wetland classes plotted as a function of perpendicular and temporal baselines. Dot sizes and colors are proportional to different coherence values.

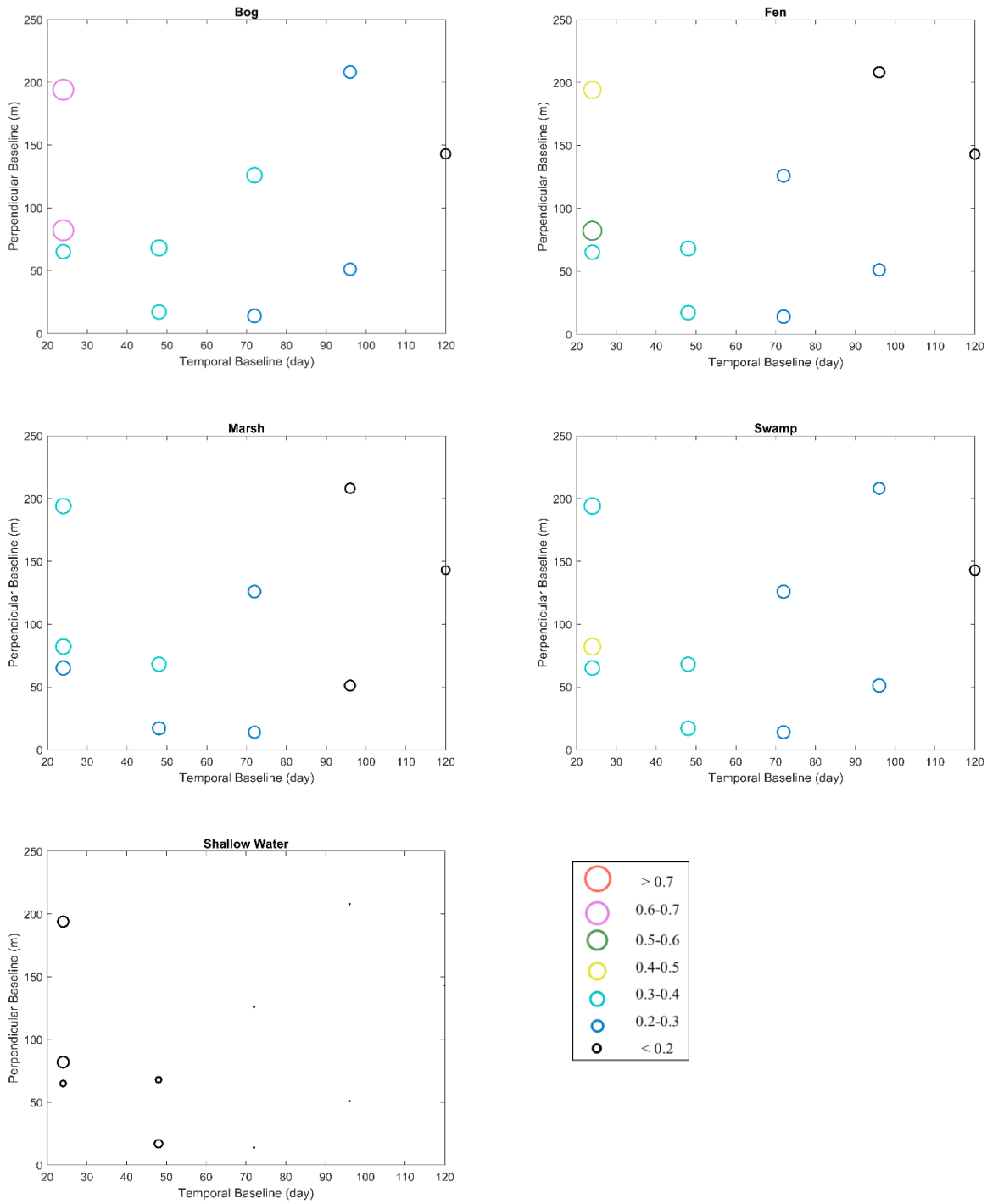


Figure 3.4. RADARSAT-2 (Ultrafine mode) coherence analysis results for wetland classes plotted as a function of perpendicular and temporal baselines. Dot sizes and colors are proportional to different coherence values.

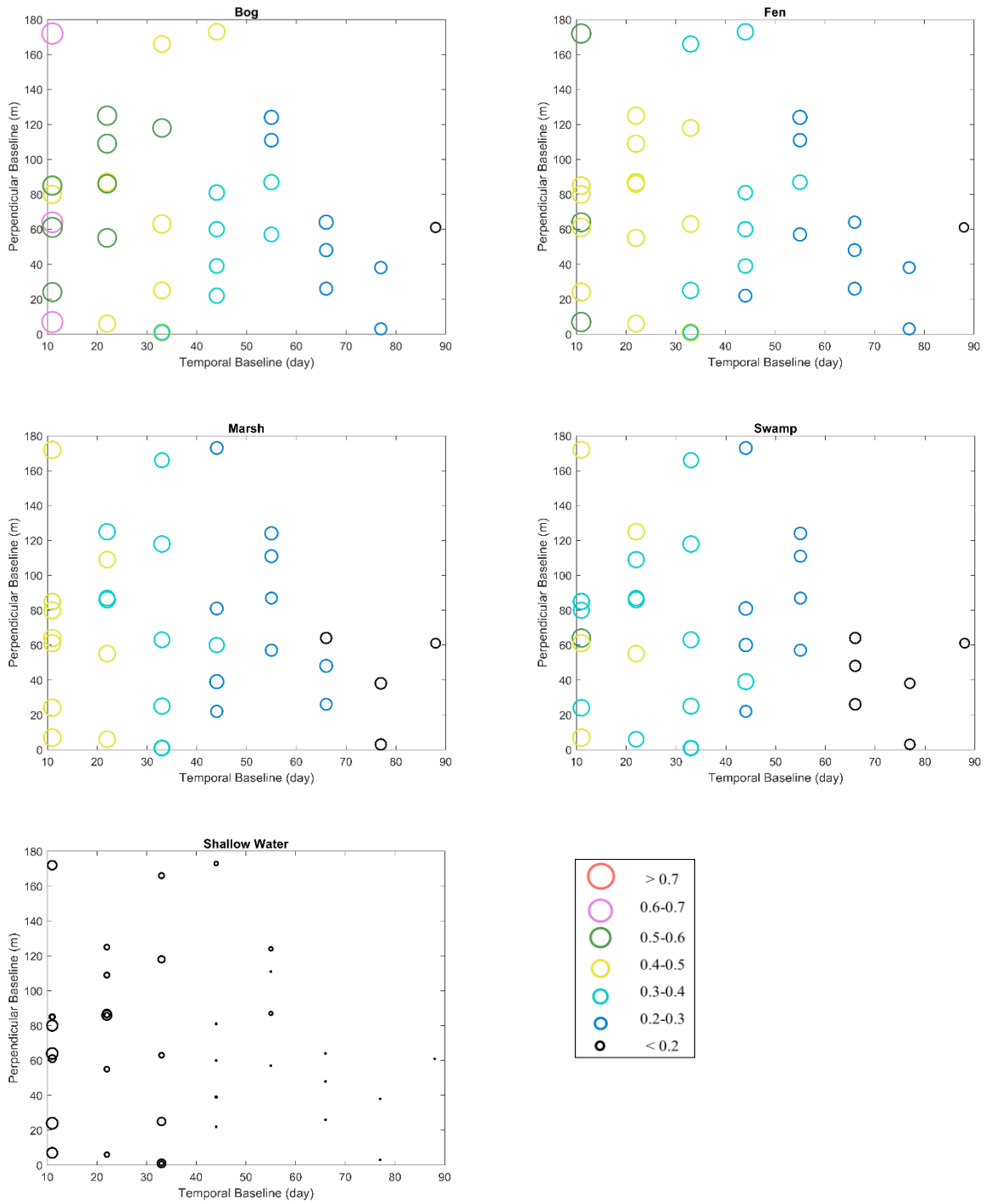
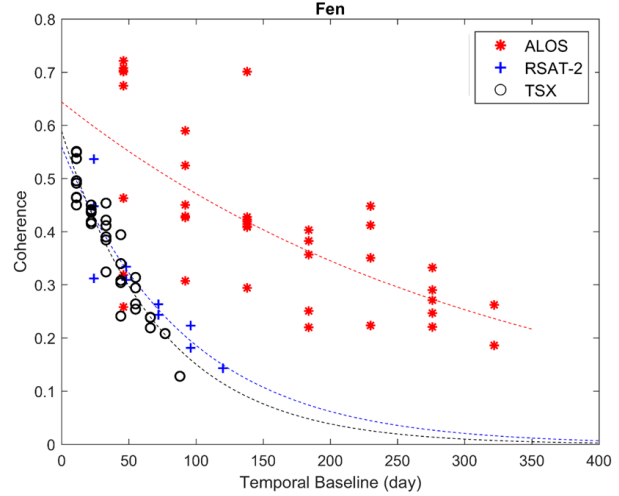
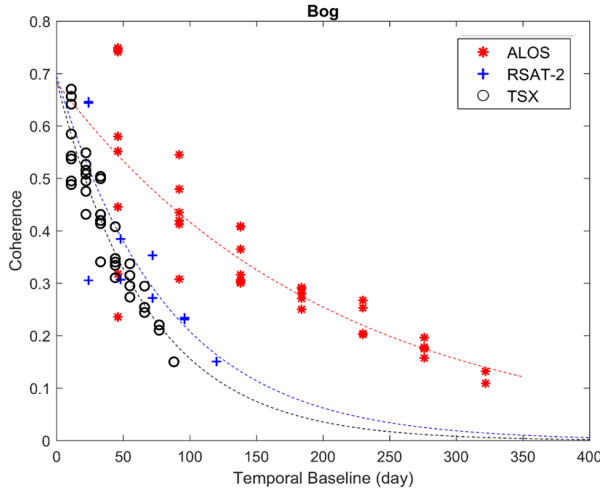


Figure 3.5. TerraSAR-X coherence analysis results for wetland classes plotted as a function of perpendicular and temporal baselines. Dot sizes and colors are proportional to different coherence values.

### **3.3.2. Coherence comparison between different SAR wavelengths**

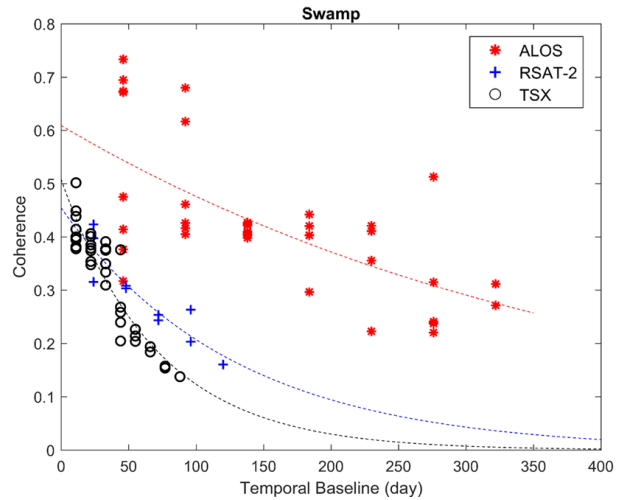
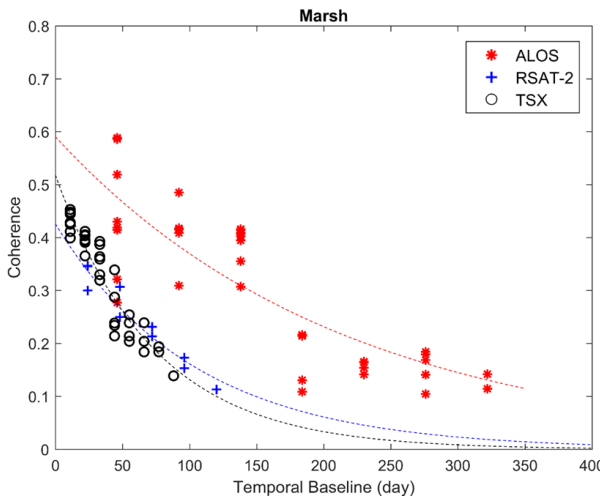
Since the previous section illustrated that the wetland interferometric coherence was highly dependent on the temporal baseline and was less influenced by the perpendicular baseline, we focused on the coherence variation as a function of the temporal baseline in this section. Furthermore, all images (in this section) have HH-polarization to eliminate the effect of SAR polarization on the coherence variation.

As shown in Figure 3.6, ALOS-1 exhibited a higher coherence relative to both RADARSAT-2 and TerraSAR-X in all wetland classes among these three wavelengths. Two RADARSAT-2 and three TerraSAR-X images were captured during relatively the same period of time (2016/7/26 and 2016/8/19 for RADARSAT-2 and 2016/8/11, 2016/8/22, and 2016/9/02 for TerraSAR-X). A comparative coherence analysis revealed that the coherence of TerraSAR-X images at the 22-day mark and the RADARSAT-2 images at the 24-day mark were relatively similar. However, 11-day TerraSAR-X interferometric pairs had slightly higher and more stable coherence for all wetland classes compared to the 24-day interferometric coherence of RADARSAT-2 images. The exponential decay curves also indicated that the coherence decreased at a higher rate for shorter wavelengths.



ALOS:  $a = 0.68$ ,  $b = -0.005$ ; RSAT-2:  $a = 0.69$ ,  $b = -0.012$ ;  
 TSX:  $a = 0.69$ ,  $b = -0.015$ .

ALOS:  $a = 0.64$ ,  $b = -0.003$ ; RSAT-2:  $a = 0.56$ ,  $b = -0.011$ ;  
 TSX:  $a = 0.59$ ,  $b = -0.014$ .



ALOS:  $a = 0.59$ ,  $b = -0.005$ ; RSAT-2:  $a = 0.43$ ,  $b = -0.010$ ;  
 TSX:  $a = 0.52$ ,  $b = -0.014$ .

ALOS:  $a = 0.61$ ,  $b = -0.002$ ; RSAT-2:  $a = 0.45$ ,  $b = -0.008$ ;  
 TSX:  $a = 0.51$ ,  $b = -0.014$ .

Figure 3.6. Comparison between the interferometric coherence obtained with ALOS-1, RADARSAT-2, and TerraSAR-X data for each of the four wetland classes as a function of temporal baselines. Note the exponential decay rates between different SAR wavelengths. Also,  $f(x) = ae^{bx}$  and coefficients were obtained with 95% confidence bounds.

### 3.3.3. Coherence comparison in multi-polarized C-band SAR images

Figures 3.7 and 3.8 compare the coherence between different polarization channels of FQ22 and FQ30 RADARSAT-2 images. Overall, HV polarization had lower coherence, while the mean of HH coherence was higher than that of VV polarization in the most cases. However, for the marsh wetland, the coherence between different polarizations was found to be relatively similar (see Figure 3.8 (a) and (b)). The results also indicated that the coherence was degraded in all polarization channels as the temporal baseline exceeded 48 days (Figure 3.8 (b)). August interferometric pairs represented the highest coherence, which could be due to an increase in the summer water table and maximum vegetation growth that promoted double-bounce scattering (Figure 3.8 (c)).

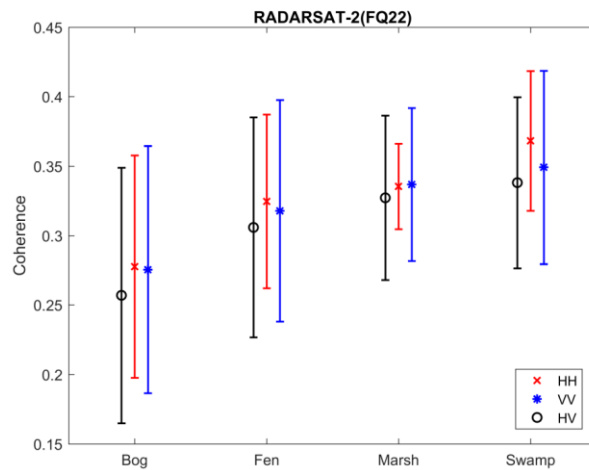


Figure 3.7. Coherence in different polarization channels obtained by RADARSAT-2 FQ22 product for wetland classes. The two SAR images were acquired in 2016/06/7 and 2016/07/25.

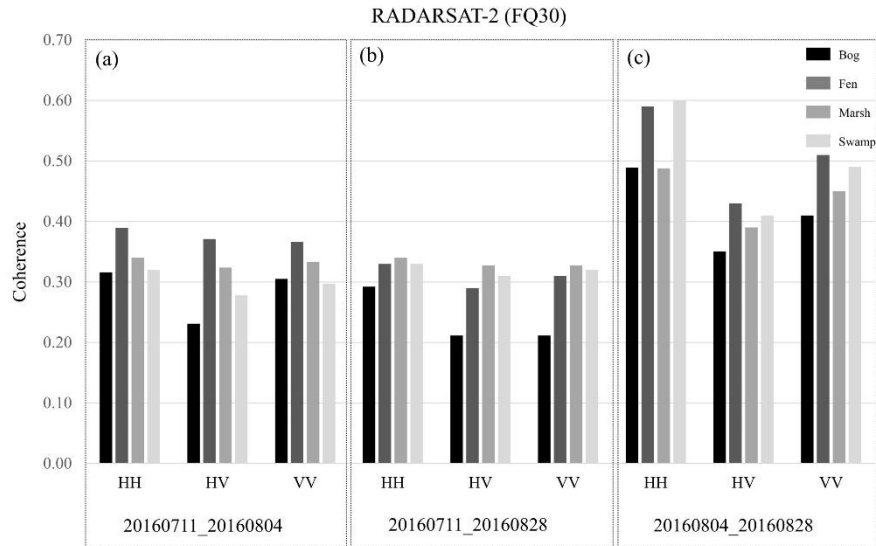


Figure 3.8. The coherence comparison between three polarization channels for wetland classes. Three interferometric coherence images are (a) 24, (b) 48, and (c) 24 days apart.

A non-parametric Wilcoxon rank sum test at the 5% significance level was also used to examine the statistical significance in mean values of coherence between different polarizations for FQ30 datasets. The null hypothesis assumed that there was no significant difference between the mean values of coherence in different polarizations. The results of the Wilcoxon rank sum test showed *P-values* higher than 0.05 between different polarization combinations for the first two interferometric pairs (Figure 3.8 (a) and (b)). However, *P-values* of 0.0286, 0.2, and 0.0857 were obtained for HH/HV, HH/VV, and HV/VV combination for the last interferometric pair (Figure 3.8(c)). This observation confirmed that the mean values of coherence between HH/HV polarizations were statistically different (*P-value* < 0.05). For HV/VV polarization combination the null hypothesis could not be rejected with 95% confidence, however, it approached significance. Conversely, the test found the mean values were not significantly different for HH/VV polarization for the last interferometric pair (*P-value* = 0.2).

### 3.3.4. The relationship between coherence and SAR backscatter variation

The relationship between SAR backscatter and coherence variation was evaluated for the HH-polarized images. For this purpose, only interferometric coherence pairs with the smallest temporal baselines were used and the mean backscattering images were generated by averaging two SAR images, which produced the corresponding coherence images. Thus, a total number of 15, 4, and 8 images were used for ALOS-1, RADARSAT-2, and TerraSAR-X, respectively.

The relationship between SAR backscatter and coherence of ALOS-1 images between April 2007 and November 2010 is depicted in Figure 3.9. A relatively linear relationship was observed between coherence and backscattering for both bog and fen. However, the linear relationship was only observed at high scattering for marsh (-14 to -11dB) and swamp wetlands (-9.5 to -6.5dB). The mean  $\sigma^0$  showed a relatively wide range of variation between -16 and -6dB, wherein swamp and marsh had the highest and lowest values, respectively. This illustrated that these two classes could easily be distinguished using only SAR intensity values. However, bog and fen exhibited relatively the same backscattering responses in most cases, indicating that the discrimination between these classes could be relatively challenging. The coherence observations also showed a large degree of overlap, suggesting that ALOS coherence observations were not useful to discriminate complex wetland classes.

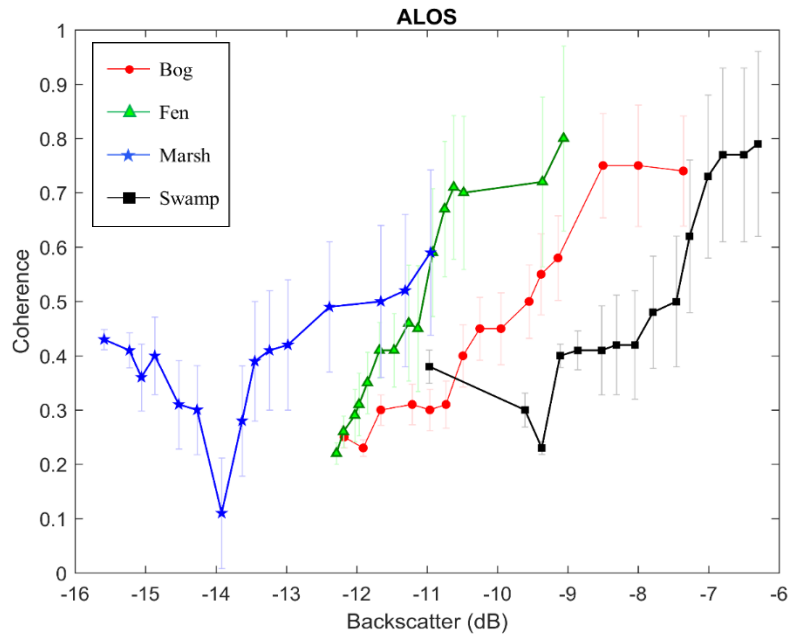


Figure 3.9. Relationships between interferometric coherence and mean SAR backscattering responses for wetland classes in the ALOS-1 observations.

Figure 3.10 depicts the relationship between SAR backscatter and coherence variation for RADARSAT-2 Ultrafine mode data between April and August 2016. An almost linear relationship was observed for both bog and swamp at all scattering degrees and for fen at a high scattering level (-14 to -13dB). The swamp wetland had the highest mean  $\sigma^0$  values, although its coherence was low. The marsh wetland exhibited the lowest coherence and  $\sigma^0$  values. Similar to L-band intensity observations, it was found that the backscattering images could easily discriminate between marsh and swamp given the relatively large difference between their backscattering responses. Overall, the swamp wetland could easily be distinguished from other wetland classes using only intensity observation. However, the discrimination of herbaceous wetland classes (i.e., bog, fen, and marsh) was found to be challenging either by intensity or coherence observations.

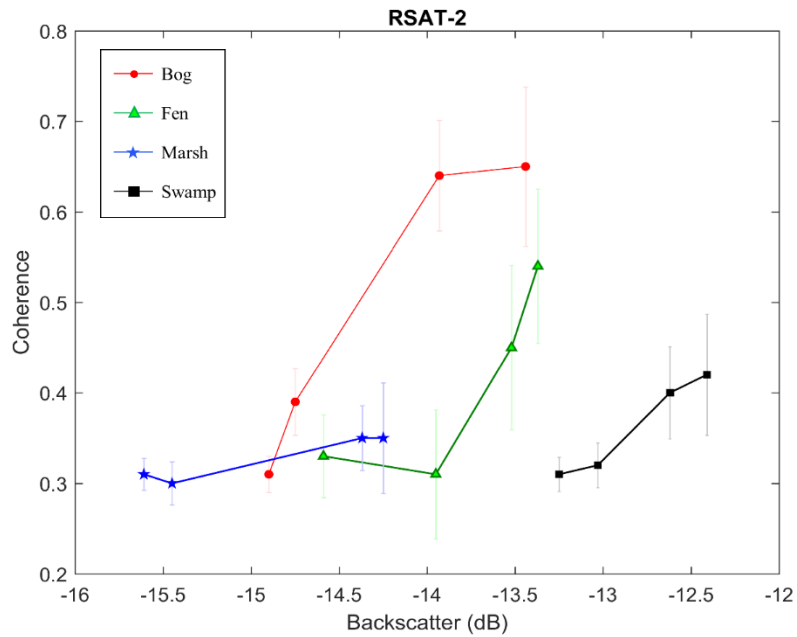


Figure 3.10. Relationships between interferometric coherence and mean SAR backscattering responses for wetland classes in the RADARSAT-2 observations.

The relationship between SAR backscatter and coherence for TerraSAR-X dataset from August to November 2016 is depicted in Figure 3.11. An almost linear relationship was obtained between SAR backscatter and coherence for all wetland classes, excluding the marsh class. Thus, it was concluded that a high coherence is a good indicator of a high SAR backscattering response, although a high backscattering may not necessarily produce a high coherence (marsh). Also, a great degree of similarity was observed between the backscattering responses of most wetland classes, especially between bog and fen. However, the similarity was less pronounced in coherence observations, which would contribute to the improved separation of wetland classes using coherence imagery.

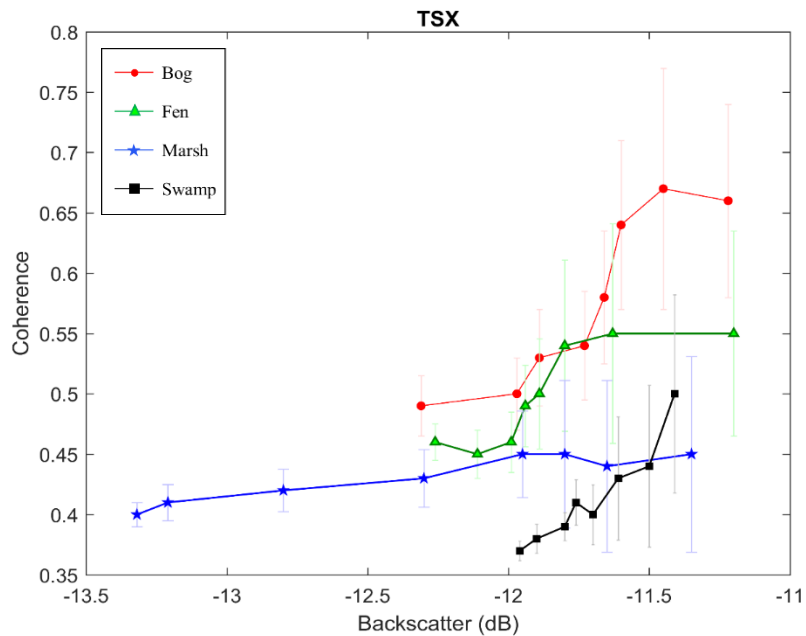


Figure 3.11. Relationships between interferometric coherence and mean SAR backscattering responses for wetland classes in the TerraSAR-X observations.

The Wilcoxon rank sum test was also applied at the 5% significance level to statistically determine differences in mean values of coherence and intensity observations (see Table 3.3).

Table 3.3. P-values of the Wilcoxon rank sum test at the 5% significance level on the difference in means of intensity and coherence observations between different wetland classes.

	Intensity			Coherence		
	ALOS	RSAT-2	TSX	ALOS	RSAT-2	TSX
Bog-Fen	0.042	0.343	0.266	0.648	0.68	0.043
Bog-Marsh	<0.001	0.343	0.111	0.787	0.200	<0.001
Bog-Swamp	0.0013	0.028	0.0879	0.506	0.685	<0.001
Fen-Marsh	<0.001	0.114	0.368	0.339	0.342	<0.001
Fen-swamp	<0.001	0.047	0.088	0.868	0.685	0.002
Marsh-Swamp	<0.001	0.028	0.069	0.372	0.343	0.151

As shown in Table 3.3, all *P-values* obtained from ALOS intensity observations were less than 0.05, indicating significant difference between mean values of wetland classes. Conversely, all *P-values* obtained from TerraSAR-X intensity observations were higher than 0.05, suggesting that there was not enough evidence to reject the null hypothesis. Thus, the mean values for different wetland classes obtained from TerraSAR-X intensity were not significantly different. Furthermore, the result of this analysis showed that there was significant difference between mean values of swamp and other wetland classes in RADARSAT-2 intensity observations (*P-values* < 0.05).

Importantly, *P-values* obtained from TerraSAR-X coherence found significant difference between mean values in most of wetland classes (*P-values* < 0.05). In contrast, there was not enough evidence to reject the null hypothesis for ALOS and RADARSAT-2 coherence images (*P-values* > 0.05). Overall, the results of Wilcoxon rank sum test were in agreement with those obtained in Figures 3.9, 3.10, and 3.11.

### 3.3.5. Classification

Table 3.4 represents the overall accuracies and Kappa coefficients for the three RF classifications based on different input features.

Table 3.4. Overall accuracies and Kappa coefficients for RF classifications using different input features.

	Coherence	Intensity	Both
Overall Accuracy	65.76	68.38	74.33
Kappa Coefficient	0.58	0.61	0.66

A difference of approximately 3% in the overall accuracy was observed between RF classified maps of coherence and intensity layers. Although the classification accuracy obtained by the coherence layer was lower than that of intensity, there was no significant difference between the two. However, the inclusion of both intensity and coherence layers resulted in an overall classification accuracy better than 74%. Figure 12 shows the distribution of land cover classes in the Avalon study area by integration of the two feature types. The two classes of bog and upland covered a large portion of the study area, while swamp and marsh were less prevalent. The classification map indicates the clear separation of all land cover types, including shallow- and deep-water, bog and fen, upland and swamp, as well as other classes.

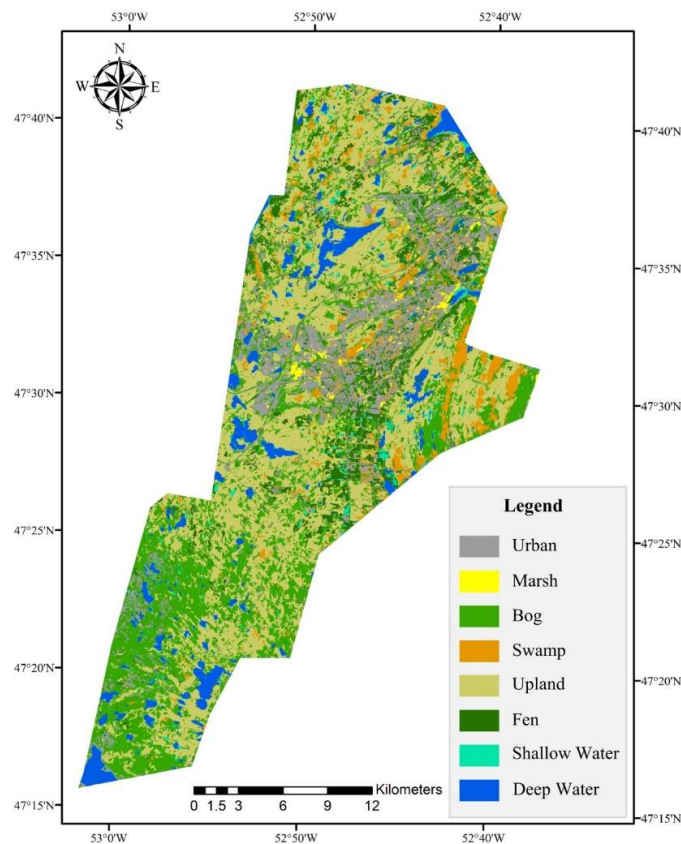


Figure 3.12. The land cover map of the most accurate RF classification obtained by inclusion of coherence and intensity layers (108 input features).

Table 3.5 represents the confusion matrix of RF classified map obtained by synergistic use of two feature types.

Table 3.5. Classification confusion matrix of the most accurate RF classification obtained by the inclusion of coherence and intensity layers. An overall accuracy of 74.33% and a Kappa coefficient of 0.66 were obtained.

		Reference Data									User. Acc.
		Bog	Fen	Swamp	Marsh	Shallow-water	Urban	Deep-water	Upland	Tot.	
Classified Data	Bog	11182	2456	411	849	116	162	45	1859	17080	65.47
	Fen	3750	5673	783	488	121	51	63	382	11311	50.15
	Swamp	278	107	3240	79	74	33	54	1296	5161	62.78
	Marsh	829	1304	205	6561	106	45	89	546	9685	67.74
	Shallow-water	27	19	175	931	3437	17	719	418	5743	59.85
	Urban	1261	323	866	1273	49	46803	14	17264	67853	68.98
	Deep-water	11	5	47	364	2085	106	85855	711	89184	96.27
	Upland	59	71	697	573	410	30569	61	56507	88947	63.53
	Tot.	17397	9958	6424	11118	6398	77786	86900	78983	294964	
Prod. Acc.	64.28	56.97	50.44	59.01	53.72	60.17	98.80	71.54			

The overall accuracy was 74.33%, with bog correctly classified in 64% of cases, marsh in 59%, fen in 57%, shallow-water in 53%, and swamp in 50% of cases. For the non-wetland classes, the classifier performed better and, notably, deep-water and upland were correctly classified in 98% and 71% of cases, respectively. The largest confusion was found for fen, which had a high commission error with other wetland classes. In particular, a large portion of bog was erroneously

classified as fen. In a few cases, swamp and marsh were also misclassified as the fen class (commission error). The largest omission error was found for the swamp wetland, where swamps were erroneously classified as urban, fen, and upland classes. In general, confusion was found between adjacent successional classes, such as bog and fen, marsh and shallow-water, swamp and upland, and deep- and shallow-water.

### **3.4. Discussion**

Overall, the results confirmed that, among herbaceous wetlands, the bog and fen classes had similar coherence, which was also higher than the coherence of the marsh class. However, herbaceous wetlands, which are dominated by non-woody structures in the Avalon area, decorrelated faster over a shorter period of time (see the rates of decay for herbaceous wetlands in Figure 3.13). In these classes, double-bounce scattering occurs between the surface of water and the stalks and roots of vegetation, which are more affected by seasonal vegetation growth and, especially, wind in the study area. In contrast, the woody wetlands (swamps) showed higher coherence for pairs with longer temporal separation since they are less affected by vegetation growth and wind compared to the herbaceous classes.

The results also demonstrated the superiority of ALOS-1 imagery in terms of both coherence preservation (see Figure 3.13 ALOS) and a higher  $\sigma^0$  return for monitoring woody wetlands (see Figure 3.9). The high coherence of L-band observations means that the phase centers of scatterers are more stable, which is due to the deeper penetration through canopy. In this case, the leaves of the vegetation canopy are quasi-transparent at longer wavelengths (L-band), which penetrate through the branches and trunks to the surface beneath and, as a result, obtain a higher  $\sigma^0$  return and maintain coherence over longer time periods. This observation is consistent with the results of a previous study [22], which concluded JERS-1 L-band data maintained coherence over longer

time periods. In addition to the high coherence of L-band observations for swamps, other wetland classes also had high coherence when L-band was applied. However, shorter wavelengths are also promising for monitoring herbaceous wetlands, especially when shorter temporal baselines are applied (see Fig 3.13 RSAT-2 and TSX). Despite the longer wavelength of C-band compared to X-band, higher backscattering responses and coherences were found for the latter when high resolution, HH polarized images were compared (U16W2 for RADARSAT-2). This is probably due to both the steeper incidence angle of X-band ( $\sim 21^\circ$  for TerraSAR-X relative to  $\sim 42^\circ$  for RADARSAT-2) that penetrates deeper into the vegetation canopy, resulting in an improved double-bounce scattering, as well as the shorter temporal baseline of X-band data, leading to a higher coherence preservation. Thus, the results of this study suggest that X-band data are useful for monitoring bog and fen wetlands, which are the dominant Canadian wetland types.

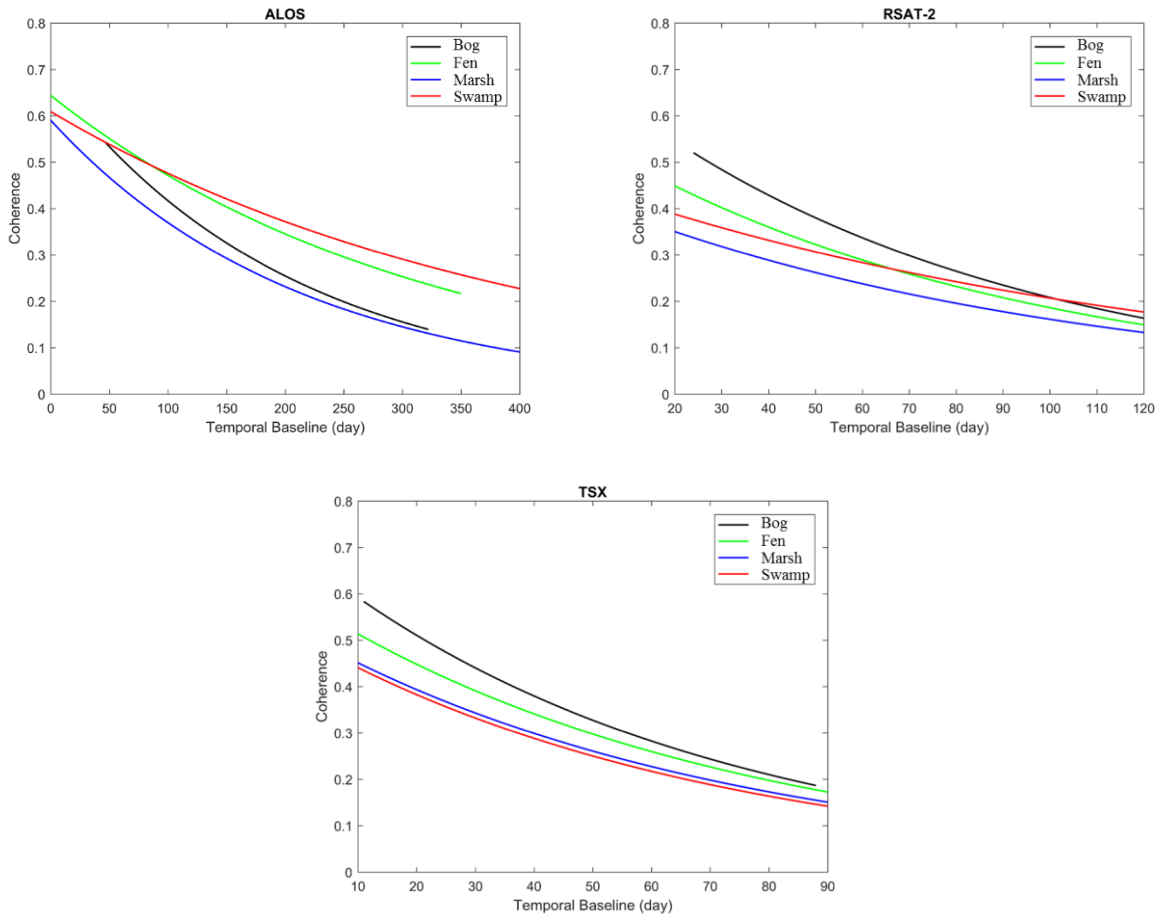


Figure 3.13. Measured coherence decay for different SAR frequencies as a function of temporal baseline in different wetland types. Note that a temporal baseline of less than 20 days is required to obtain a coherence of greater than 0.4 for C- and X-band data.

The results also indicated that temporal baseline was the most influential parameter for shorter wavelengths, which had almost no dependency on the perpendicular baseline. However, temporal and perpendicular baselines both had an effect on the coherence preservation of longer wavelengths. These observations are in agreement with those reported in the literature [22]. It is also worth noting that a temporal baseline of less than 20 days is required to obtain a coherence of greater than 0.4 for C- and X-band data in most cases (see Figure 3.13). The upcoming RADARSAT Constellation Mission (RCM), with a temporal resolution of four days, is, therefore,

of great importance for mapping phenomena with the high variability such as wetland complexes [38].

In general, HH polarization had relatively better capability to maintain coherence among the three polarizations. The HH polarization signal is more sensitive to the double-bounce scattering associated with tree trunks in swamp forests and stems in freshwater marshes. More specifically, the larger Fresnel reflection of the HH polarized signal relative to other polarization is less attenuated by the vertical structure of wetland vegetation, such as trunks and stems [16]. The vertically oriented structure of such vegetation enhances the attenuation of VV-polarized signals and, as a result, the radar signal cannot reach the water surface below the vegetation [19]. These results fit well with those of other studies [13], [22].

The results also demonstrated that the wetland phenology and water level both control the flooding status of vegetation (i.e., double-bounce scattering) and as such, coherence preservation. In the early stage of the growing season, coherence was well preserved in HH and VV polarization channels, while HH coherence was slightly higher (see Figure 3.7 and Figure 3.8(a)). In particular, the VV polarization can maintain coherence at the early stages of emerging vegetation when plants have begun to grow in terms of height, but have a less developed canopy. This was also confirmed by the Wilcoxon rank sum test, wherein *P-values* of higher than 0.05 were obtained for different polarization combinations in the early growing season (Figure 3.8 (a) and (b)), suggesting no significant difference between different polarizations. However, as the vegetative canopies further developed in the middle of the growing season (i.e., August, see Figure 3.8(c)), HH polarization maintained higher coherence relative to other polarizations. The high coherence of HH polarization could be explained by the increased water level that occurred in August due to precipitation (see Figure 3.2). Particularly, an increase in the water level enhanced the chance of double-bounce

scattering for flooded vegetation and, since the HH polarization is more sensitive to double-bounce scattering, the coherence was better preserved. Accordingly, the coherence has been further differentiated between the three polarizations because of summer water levels (see Figure 3.8(c)). This conclusion was in agreement with the results of Wilcoxon rank sum test, reporting the *P-value* of lower than 0.05 for HH/HV polarization combination (Figure 3.8(c)). Thus, it was concluded that C-HH responses were greater influenced by water level fluctuations and less affected by vegetative canopies. Kim et al. (2014) also reported that L-HH backscattering coefficients were dominated by the single factor of water level fluctuation and unaffected by vegetation canopies of the freshwater marshes in the Everglades [9]. Thus, both SAR backscattering and coherence reflected the flooding status of vegetation and their peak occurred at the period of the highest water table (during the growing season), which was in August and September in the Avalon study area (see Figure 3.2).

Overall, the results indicated a linear relationship between coherence and SAR backscattering for most of the wetland classes. However, the coherence of the marsh wetland was saturated at specific values for both C- (0.33) and X-band (0.43) and, thereby, indicated no relationship with backscattering. Similar behaviour was also reported for relatively the same wetland class (i.e., *graminoid* wetlands which are herbaceous prairie marshes) in the Florida Everglades [22]. Furthermore, the results of the backscattering analysis indicated that swamp and marsh were easily separable using  $\sigma^0$  values since they had the highest and lowest  $\sigma^0$  returns, respectively, in the three SAR frequencies. Importantly, the swamp class was found to be easily distinguished from other wetland classes using intensity observations, especially using L-band data. This was confirmed by the Wilcoxon rank sum test and was also in agreement with the classification result. For example, the confusion matrix represented a lower degree of confusion between the swamp

and marsh wetlands. However, a high degree of similarity was found between herbaceous wetlands and, especially, between bog and fen in terms of  $\sigma^0$  returns, which was, latter, affirmed by the confusion matrix. According to the field biologists' reports, these two types of wetlands are adjacent, successional classes without clear-cut borders contributing to confusion between them. Specifically, bog and fen are both peatlands dominated with relatively similar non-woody vegetation types (*sphagnum* and *graminoid*). However, multi-temporal polarimetric data may be useful to differentiate these two classes by monitoring the phase changes due to presence of the subsurface water flow using polarimetric decomposition methods, such as Touzi decomposition [40]. This is possible because fens are characterized by subsurface water flow, whereas bogs are not. Thus, these two classes are expected to be better distinguished by applying polarimetric decomposition methods, especially at longer wavelengths with a higher penetration depth. Nevertheless, the difficulty of classifying these two classes using both optical and SAR data was reported [41].

The confusion error between shallow- and deep-water classes could be due to the low SAR backscattering response of those two classes. Particularly, these classes are generally characterized by specular scattering mechanisms that result in very low returned signals in a SAR image thus contributing to misclassification. Shallow-water was also misclassified with other wetland classes in some cases, especially the marsh wetland. This is likely due to presence of aquatic vegetation at the border of small/shallow ponds, which was mixed in the same pixels in the segmentation process.

Another factor affecting the accuracy of different classes is the amount of ecological training data applied in a supervised classification. All wetland classes in this study have fewer training samples when compared with non-wetland classes. This resulted in relatively higher accuracies for non-

wetland classes. Among wetland classes, bog has the highest amount of training samples, which could explain the relatively high accuracy of the bog class compared to other wetland classes. On the other hand, the swamp and shallow-water wetlands have the lowest producer's accuracies. One possible reason could be the insufficient amount of training data for these two classes. Theoretically, the accuracies of all classes may improve by the inclusion of a greater amount of training data.

In order to quantitatively examine the contribution of each input feature to the overall classification accuracy, an assessment of feature importance was carried out for the most significant results of the RF classification (Figure 3.14).

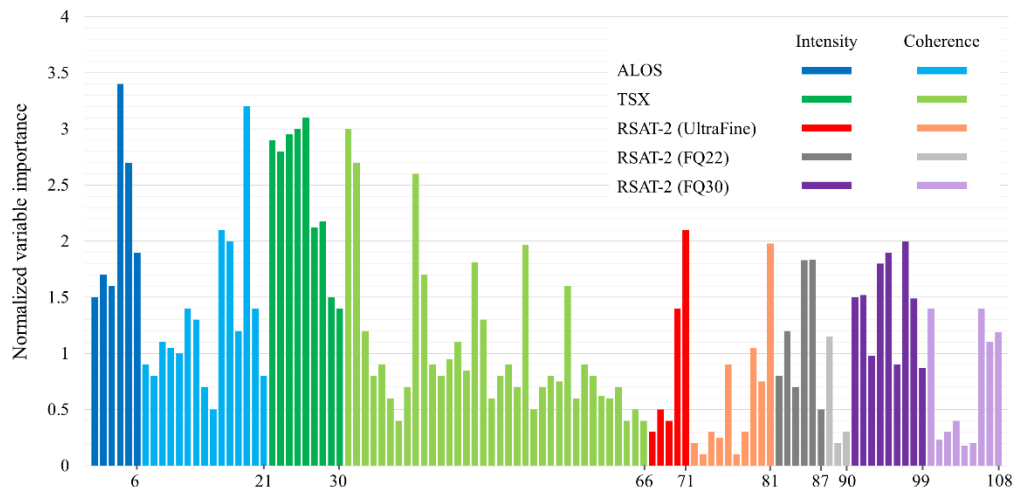


Figure 3.14. Normalized variable importance for the most significant RF classification map.

Overall, the intensity features had a greater contribution to the overall classification result. The intensity represents the power of the backscattering signals after interacting with ground targets [42] and was found to be more informative compared to the coherence layer for this classification. This finding was also in agreement with results of the Wilcoxon rank sum test. In particular,  $P$ -

*values* of lower than 0.05 were obtained between all possible wetland classes for L-band intensity observations. This, too, occurred in a fewer cases for C-band intensity observations (see Table 3.3).

Despite the higher contribution of intensity images, coherence features were also found to be useful, especially, those coherence images with small temporal baselines (e.g., 19 and 31 features). Furthermore, all coherence images corresponding to the peak of the high water level (i.e., late summer and early fall) indicated a significant contribution to the overall accuracy (e.g., 19, 31, 81, and 106 features). In general, the variable importance analysis confirmed, to some extent, the results obtained by the coherence and backscattering investigations. For example, the variable importance analysis indicated a great contribution of L-band intensity observations to the classification result, which was consistent with the results of the backscattering analysis and the Wilcoxon rank sum test. One interesting observation was found for full polarimetric RADARSAT-2 imagery. In particular, the variable importance analysis indicated the greater importance of HV-intensity (83, 86, and 92 features) relative to HH-intensity (82, 85, and 91 features) in some cases, although HH-coherence was found to be more influential than HV-coherence in all cases. This is because the cross-polarized observations are due to volume scattering within the vegetation canopy and have a higher sensitivity to vegetation structures. Given the large coverage of the study area with different wetland vegetation types, HV-intensity indicated a greater contribution relative to other polarizations of C-band data when double-bounce was not dominant in the early stages of vegetation growth. Although the HV intensities produced a high backscattering response, they could not maintain coherence to the same degree as HH polarization since they are more random, which resulted in HV-coherence contributing less to the classification results than HH-coherence.

Despite Canada's extensive wetlands and several wetland studies using optical and PolSAR imagery, the interferometric coherence of Canadian wetlands has not been thoroughly investigated to date. In particular, the analysis of coherence variation for wetland classes has been limited to a few studies carried out in the Everglades [22] and Louisiana wetlands [15], both in the United States. However, Canadian wetland classes are different than those found in the United States. Given the relatively similar wetland types across the country, the results of this research provide the first detailed investigation towards Canadian wetland mapping, as well as other wetlands worldwide with similar ecological features, from a new perspective based upon the synergetic use of intensity and phase observations. Other studies, which have compared the coherence behavior of different wetland classes, applied only L- and C-band SAR data obtained by JERS-1, RADARSAT-1, and ERS [15], [22]. In addition to examining the capacity of ALOS-1 and RADARSAT-2 in terms of coherence maintenance, the results of our study contribute to the success of wetland monitoring using X-band data with improved temporal resolution, which is of great importance for herbaceous wetlands. The results also indicate the potential of coherence as an input feature for wetland classifications, which is another significant contribution of this research study. Further improvement in classification accuracy is expected upon the synergistic use of intensity, coherence, and polarimetric decomposition features. This is because different input features incorporate different characteristics of ground targets, which may play various roles (i.e., contribution) in the classification results.

### **3.5. Conclusion**

A total number of 38 repeat-pass ALOS PALSAR-1, RADARSAT-2, and TerraSAR-X SAR images were used for statistical analysis of SAR intensity and coherence variation for wetland classes in a study area located on the northeast of Newfoundland and Labrador, Canada. The

coherence analysis, as a function of perpendicular and temporal baselines, illustrated that coherence was mainly dependent on the latter and less/not affected by the former, especially for shorter wavelengths. Overall, coherence was the highest for L-band SAR data and the X-band data had higher coherence than C-band in interferometric pairs with smaller temporal baselines. The Wilcoxon rank sum test found that the mean values of coherence maps were not significantly different between three polarizations at the early stage of the growing season. However, there was significant difference between mean values of HH/HV at the peak of the growing season.

A linear relationship was observed between coherence and SAR backscattering intensity during the leaf-on season in some wetland classes when L- and X-band SAR data were employed. The swamp wetland was found to be most easily distinguished from other wetland classes according to the backscattering and coherence analysis. Although the confusion matrix found the lowest producer's accuracy of about 50% for the swamp wetland, this was likely due to the smallest training samples for swamps compared to other land cover classes. On the other hand, the discrimination of herbaceous wetlands was found to be challenging according to the backscattering and coherence analysis. Notably, the Wilcoxon rank sum test confirmed the superiority of L-band intensity and X-band coherence observations for distinguishing complex wetland classes. Thus, it was concluded that interferometric coherence enhanced thematic land cover information when integrated with intensity layers, supporting the capacity of coherence for wetland classification. In particular, an overall accuracy of about 74% was attained by the inclusion of both features types, providing an improvement of about 6% compared to the classification based only on intensity layers. The results of this study found that the synergistic use of multiple feature types improved discrimination capacity between complex wetland classes.

### 3.6. References

- [1] R. W. Tiner, M. W. Lang, and V. V. Klemas, *Remote sensing of wetlands: applications and advances*. CRC press, 2015.
- [2] F. Jaramillo and G. Destouni, “Local flow regulation and irrigation raise global human water consumption and footprint,” *Science* (80-. ), vol. 350, no. 6265, pp. 1248–1251, 2015.
- [3] F. Jaramillo *et al.*, “Assessment of hydrologic connectivity in an ungauged wetland with InSAR observations,” *Environ. Res. Lett.*, vol. 13, no. 2, p. 24003, 2018.
- [4] S. Wdowinski, S.-W. Kim, F. Amelung, T. H. Dixon, F. Miralles-Wilhelm, and R. Sonenshein, “Space-based detection of wetlands’ surface water level changes from L-band SAR interferometry,” *Remote Sens. Environ.*, vol. 112, no. 3, pp. 681–696, 2008.
- [5] B. Brisco, F. Ahern, K. Murnaghan, L. White, F. Canisus, and P. Lancaster, “Seasonal change in wetland coherence as an aid to wetland monitoring,” *Remote Sens.*, vol. 9, no. 2, p. 158, 2017.
- [6] M. Mahdianpari *et al.*, “Fisher Linear Discriminant Analysis of coherency matrix for wetland classification using PolSAR imagery,” *Remote Sens. Environ.*, vol. 206, pp. 300–317, 2018.
- [7] X. Jiao *et al.*, “Object-oriented crop mapping and monitoring using multi-temporal polarimetric RADARSAT-2 data,” *ISPRS J. Photogramm. Remote Sens.*, vol. 96, pp. 38–46, 2014.
- [8] E. S. Kasischke, K. B. Smith, L. L. Bourgeau-Chavez, E. A. Romanowicz, S. Brunzell, and C. J. Richardson, “Effects of seasonal hydrologic patterns in south Florida wetlands on radar backscatter measured from ERS-2 SAR imagery,” *Remote Sens. Environ.*, vol. 88, no. 4, pp. 423–441, 2003.
- [9] J.-W. Kim, Z. Lu, J. W. Jones, C. K. Shum, H. Lee, and Y. Jia, “Monitoring Everglades freshwater marsh water level using L-band synthetic aperture radar backscatter,” *Remote Sens. Environ.*, vol. 150, pp. 66–81, 2014.
- [10] L.-M. Rebelo, “Eco-hydrological characterization of inland wetlands in Africa using L-band SAR,” *IEEE J. Sel. Top. Appl. Earth Obs. Remote Sens.*, vol. 3, no. 4, pp. 554–559, 2010.
- [11] J. Betbeder, V. Gond, F. Frappart, N. N. Baghdadi, G. Briant, and E. Bartholomé, “Mapping of Central Africa forested wetlands using remote sensing,” *IEEE J. Sel. Top. Appl. earth Obs. Remote Sens.*, vol. 7, no. 2, pp. 531–542, 2014.
- [12] D. E. Alsdorf, J. M. Melack, T. Dunne, L. A. K. Mertes, L. L. Hess, and L. C. Smith, “Interferometric radar measurements of water level changes on the Amazon flood plain,” *Nature*, vol. 404, no. 6774, p. 174, 2000.
- [13] S.-H. Hong, S. Wdowinski, and S.-W. Kim, “Evaluation of TerraSAR-X observations for wetland InSAR application,” *IEEE Trans. Geosci. Remote Sens.*, vol. 48, no. 2, pp. 864–873, 2010.
- [14] B. Brisco, K. Murnaghan, S. Wdowinski, and S.-H. Hong, “Evaluation of RADARSAT-2 acquisition modes for wetland monitoring applications,” *Can. J. Remote Sens.*, vol. 41, no. 5, pp. 431–439, 2015.
- [15] Z. Lu and O. Kwoun, “Radarsat-1 and ERS InSAR analysis over southeastern coastal Louisiana: Implications for mapping water-level changes beneath swamp forests,” *IEEE Trans. Geosci. Remote Sens.*, vol. 46, no. 8, pp. 2167–2184, 2008.
- [16] J.-W. Kim *et al.*, “Integrated analysis of PALSAR/Radarsat-1 InSAR and ENVISAT altimeter data for mapping of absolute water level changes in Louisiana wetlands,” *Remote Sens. Environ.*, vol.

- 113, no. 11, pp. 2356–2365, 2009.
- [17] T. Oliver-Cabrera and S. Wdowinski, “InSAR-based mapping of tidal inundation extent and amplitude in Louisiana Coastal Wetlands,” *Remote Sens.*, vol. 8, no. 5, p. 393, 2016.
- [18] C. Xie, Y. Shao, J. Xu, Z. Wan, and L. Fang, “Analysis of ALOS PALSAR InSAR data for mapping water level changes in Yellow River Delta wetlands,” *Int. J. Remote Sens.*, vol. 34, no. 6, pp. 2047–2056, 2013.
- [19] M. Zhang, Z. Li, B. Tian, J. Zhou, and P. Tang, “The backscattering characteristics of wetland vegetation and water-level changes detection using multi-mode SAR: A case study,” *Int. J. Appl. Earth Obs. Geoinf.*, vol. 45, pp. 1–13, 2016.
- [20] A. Ferretti, A. Monti-Guarnieri, C. Prati, F. Rocca, and D. Massonet, *InSAR principles-guidelines for SAR interferometry processing and interpretation*, vol. 19. 2007.
- [21] I. I. I. Ramsey Elijah, Z. Lu, A. Rangoonwala, and R. Rykhus, “Multiple baseline radar interferometry applied to coastal land cover classification and change analyses,” *GIScience Remote Sens.*, vol. 43, no. 4, pp. 283–309, 2006.
- [22] S.-W. Kim, S. Wdowinski, F. Amelung, T. H. Dixon, and J.-S. Won, “Interferometric coherence analysis of the Everglades wetlands, South Florida,” *IEEE Trans. Geosci. Remote Sens.*, vol. 51, no. 12, pp. 5210–5224, 2013.
- [23] M. Zhang, Z. Li, B. Tian, J. Zhou, and J. Zeng, “A method for monitoring hydrological conditions beneath herbaceous wetlands using multi-temporal ALOS PALSAR coherence data,” *Remote Sens. Lett.*, vol. 6, no. 8, pp. 618–627, 2015.
- [24] E. S. W. G. (Canada), C. for Land, B. R. R. (Canada), and C. S. of the E. Directorate, *A national ecological framework for Canada*. Centre for Land and Biological Resources Research; Hull, Quebec: State of ..., 1996.
- [25] I. B. Marshall, C. A. S. Smith, and C. J. Selby, “A national framework for monitoring and reporting on environmental sustainability in Canada,” in *Global to Local: Ecological Land Classification*, Springer, 1996, pp. 25–38.
- [26] R. South, *Biogeography and Ecology of the Island of Newfoundland*, vol. 48. Springer Science & Business Media, 1983.
- [27] E. S. W. Group, “A National Ecological Framework for Canada. Centre for Land and Biological Resources Research, Research Branch, Agriculture and Agri-Food Canada, and State of the Environment Directorate,” *Environ. Conserv. Serv. Environ. Canada, Ottawa*. <http://sis.agr.gc.ca/cansis/publications/ecostrat/intro.html#Rep>. <http://ecozones.ca/english>, 1996.
- [28] B. G. Warner and C. D. A. Rubec, “By the National Wetlands Working Group / Edited The Canadian Wetland Classification System.”
- [29] M. Mahdianpari, B. Salehi, F. Mohammadimanesh, and M. Motagh, “Random forest wetland classification using ALOS-2 L-band, RADARSAT-2 C-band, and TerraSAR-X imagery,” *ISPRS J. Photogramm. Remote Sens.*, vol. 130, 2017.
- [30] M. Dettwiler, “RADARSAT-2 product format definition,” *Macdonald, Dettwiler Assoc. Ltd. Richmond, BC, Canada*, 2008.
- [31] M. Eineder, B. Schattler, H. Breit, T. Fritz, and A. Roth, “TerraSAR-X SAR products and processing algorithms,” in *Geoscience and Remote Sensing Symposium, 2005. IGARSS’05. Proceedings. 2005*

- IEEE International*, 2005, vol. 7, pp. 4870–4873.
- [32] U. C. Benz, P. Hofmann, G. Willhauck, I. Lingenfelder, and M. Heynen, “Multi-resolution, object-oriented fuzzy analysis of remote sensing data for GIS-ready information,” *ISPRS J. Photogramm. Remote Sens.*, vol. 58, no. 3–4, pp. 239–258, 2004.
- [33] T. Blaschke, “Object based image analysis for remote sensing,” *ISPRS J. Photogramm. Remote Sens.*, vol. 65, no. 1, pp. 2–16, 2010.
- [34] M. Belgiu and L. Drăguț, “Comparing supervised and unsupervised multiresolution segmentation approaches for extracting buildings from very high resolution imagery,” *ISPRS J. Photogramm. Remote Sens.*, vol. 96, pp. 67–75, 2014.
- [35] T. eCognition Developer, “9.0 User Guide,” *Trimble Ger. GmbH Munich, Ger.*, 2014.
- [36] L. Breiman, “Random forests,” *Mach. Learn.*, vol. 45, no. 1, pp. 5–32, 2001.
- [37] V. F. Rodriguez-Galiano, B. Ghimire, J. Rogan, M. Chica-Olmo, and J. P. Rigol-Sanchez, “An assessment of the effectiveness of a random forest classifier for land-cover classification,” *ISPRS J. Photogramm. Remote Sens.*, vol. 67, pp. 93–104, 2012.
- [38] M. Mahdianpari, B. Salehi, F. Mohammadimanesh, and B. Brisco, “An Assessment of Simulated Compact Polarimetric SAR Data for Wetland Classification Using Random Forest Algorithm,” *Can. J. Remote Sens.*, vol. 43, no. 5, 2017.
- [39] M. Belgiu and L. Drăguț, “Random forest in remote sensing: A review of applications and future directions,” *ISPRS J. Photogramm. Remote Sens.*, vol. 114, pp. 24–31, 2016.
- [40] B. Brisco, “Mapping and monitoring surface water and wetlands with synthetic aperture radar,” *Remote Sens. Wetl. Appl. Adv.*, pp. 119–136, 2015.
- [41] F. M. Henderson and A. J. Lewis, “Radar detection of wetland ecosystems: a review,” *Int. J. Remote Sens.*, vol. 29, no. 20, pp. 5809–5835, 2008.
- [42] H. Jin, G. Mountrakis, and S. V. Stehman, “Assessing integration of intensity, polarimetric scattering, interferometric coherence and spatial texture metrics in PALSAR-derived land cover classification,” *ISPRS J. Photogramm. Remote Sens.*, vol. 98, pp. 70–84, 2014.

## Chapter 4. Feature optimization for wetland mapping <sup>3</sup>

### Preface

A version of this manuscript has been published in the *International journal of applied earth observation and geoinformation*. I am a primary author of this manuscript along with the co-authors, Bahram Salehi, Masoud Mahdianpari, Mahdi Motagh, and Brian Brisco. I conceptualized and designed the study. I developed the model and performed all experiments and tests. I wrote the paper and revised it based on comments from all co-authors. I also revised the paper according to the reviewers' comments. The co-author, Masoud Mahdianpari, helped in performing the experiments and analyzing the results and contributed to revising the manuscript. All co-authors provided editorial input and scientific insights to further improve the paper. They also reviewed and commented on the manuscript.

### Abstract

Wetlands are home to a great variety of flora and fauna species and provide several unique environmental services. Knowledge of wetland species distribution is critical for sustainable management and resource assessment. In this study, multi-temporal single- and full-polarized RADARSAT-2 and single-polarized TerraSAR-X data were applied to characterize the wetland extent of a test site located in the north east of Newfoundland and Labrador, Canada. The accuracy and information content of wetland maps using remote sensing data depend on several factors, such as the type of data, input features, classification algorithms, and ecological characteristics of wetland classes. Most previous wetland studies examined the efficiency of one or two feature

---

<sup>3</sup> Mohammadimanesh, F., Salehi, B., Mahdianpari, M., Motagh, M. and Brisco, B., 2018. An efficient feature optimization for wetland mapping by synergistic use of SAR intensity, interferometry, and polarimetry data. *International journal of applied earth observation and geoinformation*, 73, pp.450-462.

types, including intensity and polarimetry. Fewer investigations have examined the potential of interferometric coherence for wetland mapping. Thus, we evaluated the efficiency of using multiple feature types, including intensity, interferometric coherence, and polarimetric scattering for wetland mapping in multiple classification scenarios. An ensemble classifier, namely Random Forest (RF), and a kernel-based Support Vector Machine (SVM) were also used to determine the effect of the classifier. In all classification scenarios, SVM outperformed RF by 1.5-5%. The classification results demonstrated that the intensity features had a higher accuracy relative to coherence and polarimetric features. However, an inclusion of all feature types improved the classification accuracy for both RF and SVM classifiers. We also optimized the type and number of input features using an integration of RF variable importance and Spearman's rank-order correlation. The results of this analysis found that, of 81 input features, 22 were the most important uncorrelated features for classification. An overall classification accuracy of 85.4% was achieved by incorporating these 22 important uncorrelated features based on the proposed classification framework.

**Keywords:** Wetland; Interferometric coherence; Random Forest; Support Vector Machine.

## **4.1. Introduction**

Wetlands are areas with either temporarily or permanently saturated soils that affect plant establishment, animal life, and soil development. Controlling floods, improving water-quality, supporting wildlife habitat for several unique species of flora and fauna, and shoreline stabilization are some of the advantages of wetlands [1]. Satellite remote sensing data have significantly contributed to wetland mapping given the remoteness, vastness, and ever-changing nature of these ecosystems. Importantly, Synthetic Aperture Radar (SAR) sensors are advantageous for wetland studies due to their capability to operate independently of solar radiation and day/night conditions.

Furthermore, the SAR signal penetrates through vegetation canopies and soil, making it an ideal tool to monitor the flooding status of vegetation [2].

For several years, per-pixel image analysis has been used for land cover classification due to the coarse resolution of pixels in satellite imagery relative to the size of the ground object. However, because of continuous development of satellite remote sensing tools and the availability of high spatial resolution imagery, the Object-Based Image Analysis (OBIA) technique has become popular for land cover classification [3]. Incorporating different features, such as object size and shape, combining multiple sources of data with different spectral and spatial resolution, and utilizing spatial and hierarchical relations of neighbouring pixels are the main advantages of the object-based approach [2]. Moreover, an integration of advanced machine learning tools, such as Support Vector Machine (SVM) and Random Forest (RF), with the object-based approach has further improved accuracy of land cover classification in recent years [4].

When classifying complex land cover, accuracy is not only influenced by classifier robustness but other factors, such as input features and their discrimination power affect the classification results. Although several studies have examined the capacity of SAR intensity and polarimetric decomposition methods for wetland classification (e.g., [1], [2]), the potential of interferometric coherence has not been thoroughly investigated. Nevertheless, the efficiency of interferometric coherence for classification of different land cover types has been noted. In particular, Ramsey et al. (2006) investigated the capability of SAR intensity, phase, and interferometric coherence for coastal land cover classification [5]. They reported that the SAR intensity was less responsive to land covers and had high temporal variations. Conversely, the interferometric coherence of the different classes was highly varied and provided a superior capacity for discrimination. In Central Siberia, Thiel et al. (2009) used ALOS PALSAR summer-intensity and winter-coherence to

discriminate forest and non-forest areas [6]. Jin et al. (2014) also investigated the discrimination power gained by synergistic use of intensity, polarimetric, interferometric coherence, and textural features using multi-temporal ALOS PALSAR data for land cover mapping in Central New York State, USA. They reported the inclusion of four feature types improved classification accuracy of about 7% relative to exclusive use of intensity [7]. Zhang et al. (2015) used interferometric coherence obtained from ALOS data for classification of wet and dry marshes in the Liaoh River Delta, China [8]. Also in China, Jiang et al. (2017) examined the capacity of HH-polarized TerraSAR-X intensity and coherence for land cover mapping in the city of Zhuhai, Pearl River Delta [9]. Most recently, Wang et al. (2018) used multi-temporal TerraSAR-X backscatter intensity and coherence to map permafrost landscapes in a complex sub-arctic environment [10].

Despite the high capacity of state-of-the-art machine learning algorithms, such as RF and SVM, to handle a large number of input features, the classification accuracy can be considerably improved upon the inclusion of important uncorrelated features into the classification scheme [11]. This highlights the significance of employing an efficient feature selection method to remove redundant information within input data, thus alleviating computational complexity. Moreover, such a feature selection method deepens the knowledge of which input features are most suitable for specific classification tasks [12]. Thus, identifying the best combination of features that have more separable land cover information is highly desirable. Accordingly, several feature selection methods for remote sensing data have been proposed and can be found in the literature (e.g., [13]). Some of these studies noted that RF variable importance can be used as an efficient feature selection method for dimensional reduction of remote sensing data [11], [12]. The RF variable importance indicates the influence of each feature on the classification accuracy for a set of input

data through the out-of-bag estimates and, accordingly, has been successfully employed as a feature selection method [11], [12].

The goal of this study was to investigate the potential of interferometric coherence for wetland mapping and the synergistic use of coherence with intensity and polarimetry. Each feature has specific characteristics, which may improve the capacity to discriminate between different land cover classes. For example, SAR intensity is primarily an indicator of ground conditions due to its sensitivity to surface roughness and dielectric constant, polarimetric features characterize the type of the ground target scattering mechanism, and interferometric coherence indicates the mechanical stability of the ground targets during satellite acquisition time intervals [7]. Thus, the objectives of this research were to: (1) determine the contribution of varying input features, including intensity, interferometric coherence, and polarimetric decompositions, obtained from multi-temporal X- and C-band SAR data to the classification results; (2) identify the improved discrimination capacity obtained from the synergistic use of different input features; (3) quantify the redundancy within a large number of input features and its influence on the classification accuracy; (4) optimize both the type and number of input features by integrating RF variable importance and Spearman's rank-order correlation analysis; and (5) compare the performance of a kernel-based classifier, SVM, and an ensemble classifier, RF, using an object-based classification approach. To the best of our knowledge, this study is the first to investigate the synergistic use of such input features for wetland classification. The proposed classification scheme serves as a framework, progressing towards an operational methodology for mapping wetland complexes in Canada, as well as other wetlands worldwide with similar ecological characteristics.

## 4.2. Study Area and Data

The 700 square kilometer study area is located in the north eastern part of the Avalon Peninsula, in Newfoundland and Labrador, Canada (Figure 4.1). Land cover within the Avalon pilot site is highly diverse and includes extensive heathland, balsam fir forest, as well as urban and agricultural areas. Notably, all wetland classes characterized by the Canadian Wetland Classification System, including bog, fen, marsh, swamp, and shallow-water are found within this region.

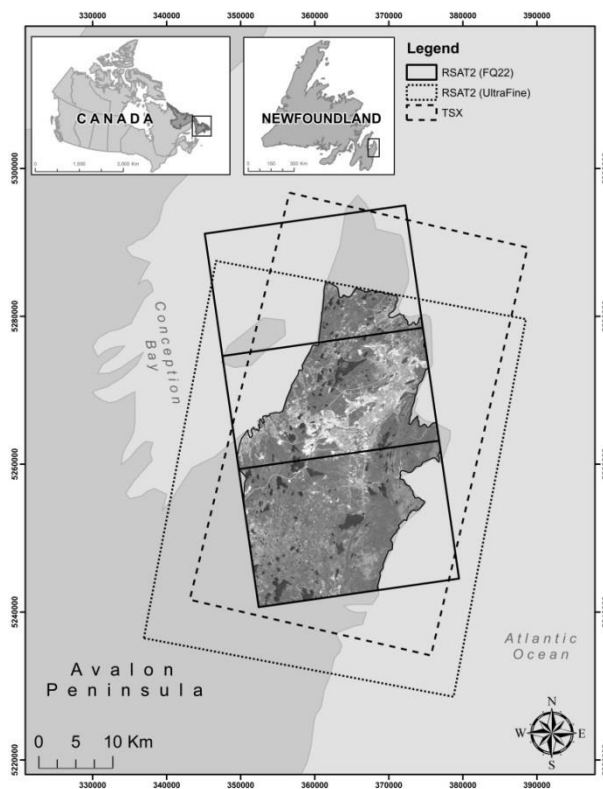


Figure 4.1. An overview of the study area with overlays of Synthetic Aperture Radar (SAR) scenes.

Field data were acquired for 257 ground sites in the ice-off seasons of 2015-2017. For reference data preparation, reference polygons were sorted by size and alternately assigned to training and testing groups. An alternative assignment of reference data ensured that both the training and testing had an equal assignment of small and large wetland polygons to allow for similar pixel

counts and to account for the high variation of intra-wetland size. Fig 4.2 illustrates the distribution of the training and the testing polygons for each land cover type across the study area.

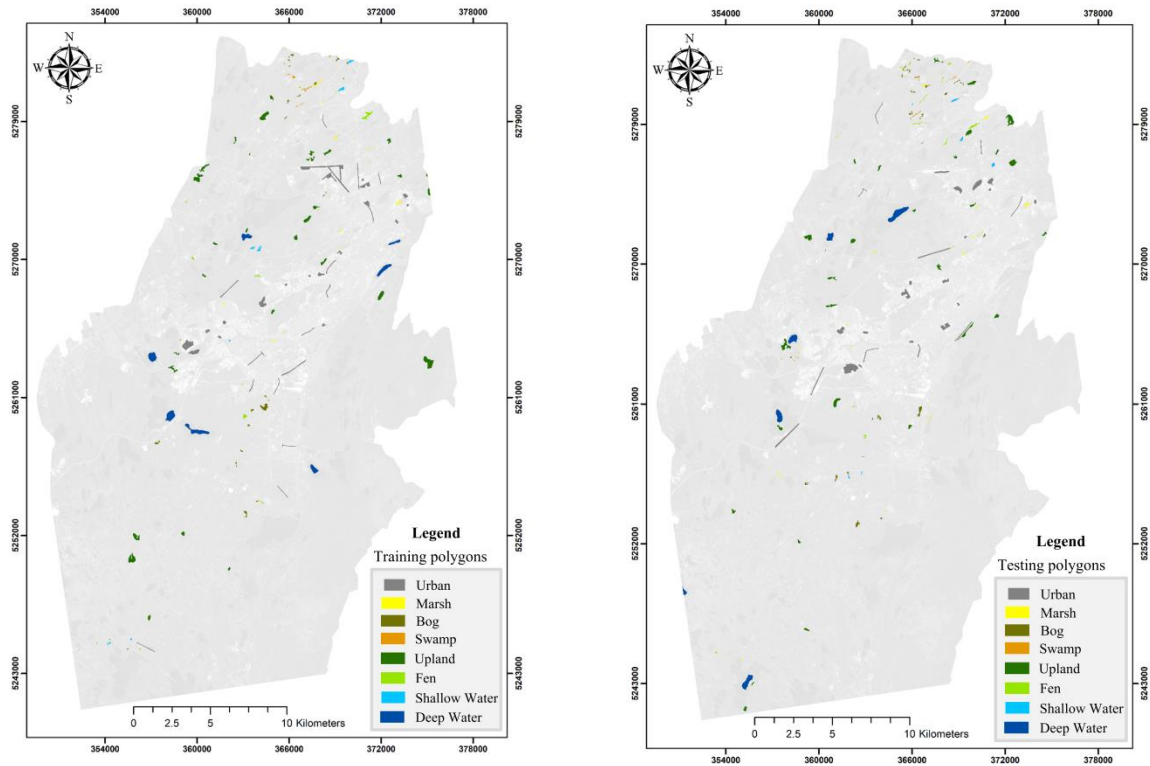


Figure 4.2. Distribution of reference data: (Left) training and (Right) testing polygons.

HH polarized X-band images from TerraSAR-X in StripMap mode were acquired between August and November 2016, coinciding with the ice-off season. RADARSAT-2 C-band imagery in either single (HH) or quad polarization was acquired in the interval between April and August 2016. Due to the small swath of FQ mode, more than one image was needed to cover the whole study area (FQ22; see Figure 4.1).

Table 4.1. Specification of satellite imagery.

Sensor	Acquisition Date (yyyy.mm.dd)	Image Mode	Incidence angle (°)	Resolution (m) (range × azimuth)	Polarization	Direction
TerraSAR-X	2016.08.11	StripMap	21.55	1.2 × 3.3	HH	Descending
	2016.08.22	StripMap	21.55	1.2 × 3.3	HH	Descending
	2016.09.02	StripMap	21.55	1.2 × 3.3	HH	Descending
	2016.09.13	StripMap	21.55	1.2 × 3.3	HH	Descending
	2016.09.24	StripMap	21.55	1.2 × 3.3	HH	Descending
	2016.10.05	StripMap	21.55	1.2 × 3.3	HH	Descending
	2016.10.16	StripMap	21.55	1.2 × 3.3	HH	Descending
	2016.10.27	StripMap	21.55	1.2 × 3.3	HH	Descending
	2016.11.07	StripMap	21.55	1.2 × 3.3	HH	Descending
RADARSAT-2	2016.04.21	U16W2	42.13	1.6 × 2.8	HH	Descending
	2016.05.15	U16W2	42.13	1.6 × 2.8	HH	Descending
	2016.06.08	U16W2	42.13	1.6 × 2.8	HH	Descending
	2016.07.26	U16W2	42.13	1.6 × 2.8	HH	Descending
	2016.08.19	U16W2	42.13	1.6 × 2.8	HH	Descending
	2016.06.07	FQ22	42	5.2 × 7.6	Quad-pol	Ascending
	2016.06.07	FQ22	42	5.2 × 7.6	Quad-pol	Ascending
	2016.07.25	FQ22	42	5.2 × 7.6	Quad-pol	Ascending
	2016.07.25	FQ22	42	5.2 × 7.6	Quad-pol	Ascending

### 4.3. Methods

Figure 4.3 illustrates the proposed methodology for this study. After SAR data pre-processing, different features were extracted and grouped into three major feature types, including intensity, interferometric coherence, and polarimetric features. Next, different combinations of features were applied to an object-based image analysis framework. The classification results were then evaluated using the testing polygons, which were held back for the validation and accuracy assessment. However, a number of these input features had redundant information and were not useful, meaning that incorporating highly correlated features did not significantly improve classification accuracy. They also increased the computational complexity of the classification. Thus, we applied an efficient method to optimize both the type and number of input features. In particular, we used a combination of RF variable importance and Spearman’s rank-order

correlation in a pair-wise correlation framework. Based on these analyses, the most important uncorrelated features were extracted and applied to the final classification scheme.

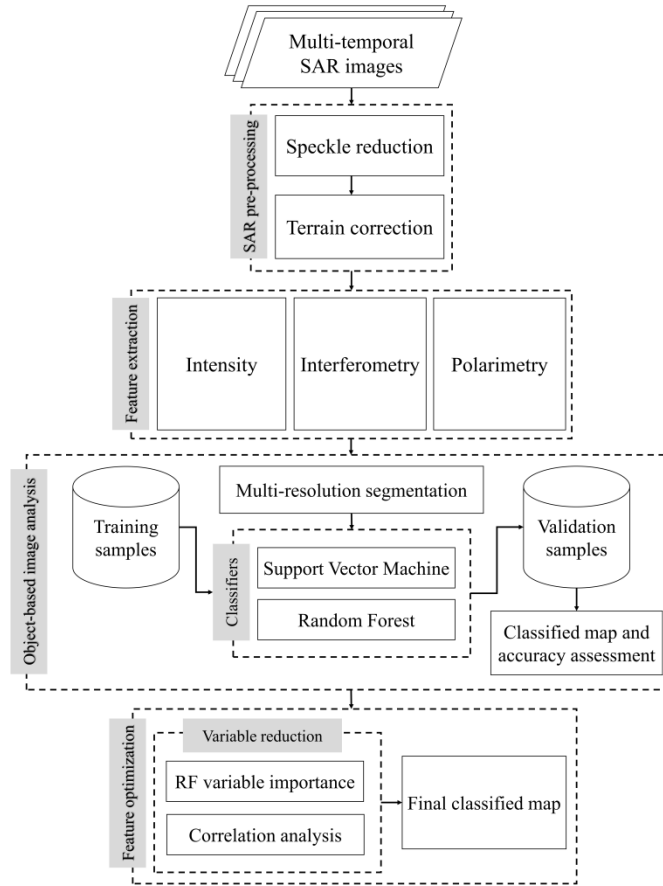


Figure 4.3. Flowchart of the proposed methodology.

### 4.3.1. Feature Extraction

#### 4.3.1.1. SAR backscatter coefficient images

SAR backscatter coefficients,  $\sigma^0$ , were extracted from TerraSAR-X and RADARSAT-2 imagery using the PCI Geomatica software package. An external Digital Elevation Model (DEM), SRTM 3 arc-second (<https://earthexplorer.usgs.gov/>), was used to geo-reference the TerraSAR-X and RADARSAT-2 level-1 SLC imagery and the images were projected into UTM coordinates (zone 22, row T) using the WGS84 reference ellipsoid. An adaptive Lee filter with a 7x7 window size was then used to suppress the effect of speckle noise. Intensity images were converted into the

normalized backscatter coefficient ( $\sigma^0$ ) values expressed in dB. Accordingly, a total number of nine and five SAR backscatter images for TerraSAR-X and RADARSAT-2 (U16W2) were generated, respectively. For RADARSAT-2 FQ22, six backscatter images in different polarizations were produced.

#### **4.3.1.2. Interferometric coherence**

The interferometric coherence quantifies the degree of similarity between two co-registered SAR images acquired from slightly different look angles. The coherence values range between 0 and 1, representing the incoherent and perfectly coherent situations, respectively. Temporal changes (e.g., wind and vegetation growth) and volume scattering are the main factors for decorrelation, particularly in vegetated areas during the growing season.

The interferometric processing was performed using the GAMMA Remote Sensing V.4.1 software package and the topographic phase was removed using DEM. A total number of 36 interferometric coherence images for TerraSAR-X imagery with temporal baselines varying from 11 to 88 days were produced. Using five RADARSAT-2 U16W2 images, 10 coherence images with temporal baselines between 24 and 120 days were produced. For RADARSAT-2 FQ22 product, three coherence images in HH, HV, and VV polarizations were generated.

#### **4.3.1.3. Polarimetric decomposition**

The two well-known incoherent decomposition methods, namely Cloude-Pottier and Freeman-Durden [14], were employed to compare the strength of the polarimetric descriptors with intensity and interferometric coherence (see Table 4.2). These approaches determine the relative contributions from different scattering mechanisms. The incoherent decompositions were selected since they are better suited for wetland complexes characterized by distributed scatterers compared to coherent decompositions (e.g., Krogager). The coherent decompositions are usually applied to

man-made targets, wherein the scattering occurs within only one or few point scatterers and, as such, the phase can be measured and analyzed. However, incoherent decompositions usually apply an initial averaging of the returned signals and thus, the direct reference to the phase of the elementary targets is not maintained [15].

Table 4.2. An overview on extracted features in this study.

Name of feature	Variables	Data	Number of features
Intensity	$\sigma_{HH}^0$	TerraSAR-X	9
	$\sigma_{HH}^0$	RADARSAT-2 (U16W2)	5
	$\sigma_{HH}^0, \sigma_{HV}^0, \sigma_{VV}^0$	RADARSAT-2 (FQ22)	6
Coherence	$\gamma_{HH}$	TerraSAR-X	36
	$\gamma_{HH}$	RADARSAT-2 (U16W2)	10
	$\gamma_{HH}, \gamma_{HV}, \gamma_{VV}$	RADARSAT-2 (FQ22)	3
Polarimetry	<i>Cloude – Pottier</i>	RADARSAT-2 (FQ22)	6
	<i>Freeman – Durden</i>	RADARSAT-2 (FQ22)	6

#### 4.3.2. Image classification

Multi-Resolution Segmentation (MRS) is the first step in OBIA and was performed in this study using the eCognition Developer 9 software package. MRS analysis is controlled by three user defined parameters, namely scale, shape, and compactness. There is no standard, widely accepted approach to determine the optimal segmentation parameters; however, imagery with a high resolution and identifiable ground objects are advantageous for this purpose. Accordingly, high resolution RapidEye optical imagery, which provides enough detail and produces well-defined objects appropriate for delineating wetland classes, was used for segmentation in this study. SAR data, however, may not provide a sufficient degree of detail due to speckle noise and lower ground feature distinguishability [1], [16]. Although SAR imagery was not used in the multi-resolution segmentation step, the polygons (segments) obtained from the segmentation of the optical image were superimposed on extracted features from SAR data. The segmentation parameters were obtained based on (a) previous similar studies (e.g., [1], [2]) and (b) a trial-and-error approach. Accordingly, the optimal values for scale, shape, and compactness were found to be 100, 0.05, and

0.5, respectively. The shape parameter of 0.05 emphasises image radiometry rather than shape and the compactness of 0.5 balances the compactness and smoothness of objects equally [2]. Scale values ranging from 10 to 300 were examined, and a value of 100 was found to be appropriate for this study according to the visual analysis of the segmentation results. In particular, a scale value of 100 resulted in more well-defined objects for delineating wetland classes with various size and shapes.

SVM is a supervised non-parametric classifier and has performed well for land cover classification using satellite imagery [17]. Its main goal is to identify an optimum hyperplane that discriminates the dataset into a specific number of classes. An advantageous generalization characteristic of SVM is that it uses a subset of training samples within the margin, the so-called support vectors, to determine the hyperplane, rather than the entire available training dataset. When the classes are not linearly separable in their original space, a kernel function is usually used to project the input data into a feature space. Non-linear, sigmoid, polynomial, and radial basis functions are commonly used kernels for this purpose, although the two latter approaches are better matched for classification of remote sensing imagery. In this study, the radial basis function (RBF) was selected. The training of the radial basis function requires tuning two parameters: the kernel parameter, known as gamma ( $\gamma$ ), and the cost parameter ( $C$ ). The former parameter is used in all kernel types, excluding the linear kernel function. The latter parameter prevents the classifier from being over-fitted to datasets and, accordingly, controls the classifier generalization capacity. In this study, these parameters were obtained using a heat-map of the classifier's cross-validation accuracy as a function of  $\gamma$  and  $C$  (Figure 4.4). The optimal values of  $\gamma$  and  $C$  were found to be  $10^{-5}$  and  $10^3$ , respectively.

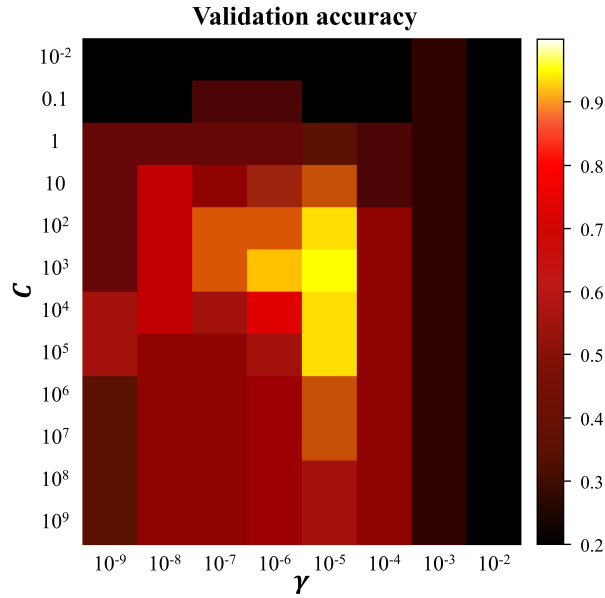


Figure 4.4. Visualization of SVM tuning parameters of  $\gamma$  and  $C$  for RBF kernel.

Random Forest is a sophisticated version of the decision tree (DT) algorithm, wherein a group of tree classifiers is employed to make a prediction [18]. RF is especially well suited for classifying multi-dimensional remote sensing data since it is not sensitive to noise and over-training and is also easily adjustable using two parameters, the number of decision trees (*Ntree*) and the number of variables (*Mtry*) [15]. In this study, a total number of 500 trees were selected in each classification scenario and the square root of the number of input variables was selected for *Mtry*. Table 4.3 represents different classification scenarios using the multiple features examined in this study.

Table 4.3. Different classification scenarios employed in this study.

Scenario	Features			Satellite data			# features
				TSX	RADARSAT-2		
	Intensity	Coherence	Polarimetry	U16W2	FQ22		
1	✓			✓			9
2	✓				✓		5
3	✓					✓	6
4	✓			✓	✓	✓	20
5		✓		✓			36
6		✓			✓		10
7		✓				✓	3
8		✓		✓	✓	✓	49
9			✓			✓	12
10	✓	✓		✓	✓	✓	69
11	✓		✓	✓	✓	✓	32
12		✓	✓	✓	✓	✓	61
13	✓	✓	✓	✓	✓	✓	81
14	<i>Important uncorrelated features</i>			✓	✓	✓	22

#### 4.3.3. Variable reduction

A fundamental advantage of RF is that it measures the importance of input variables to the overall classification results. However, a recent study reported that the most important variables identified by RF varied in different iterations even when applying the same input features and training data [11]. They also pointed out that the most important features identified by RF are biased toward highly correlated variables. Accordingly, in this study, we optimized the number and type of input variables in two steps. First, the most important features were determined using the RF variable importance analysis. These features were extracted by applying the RF classifier 15 times and recording the variables' rankings. Next, the correlations between the input features were determined using Spearman's rank-order correlation. This allowed us to perform the final classification based on only important uncorrelated features.

#### 4.4. Results and Discussion

Table 4.4 presents the classification overall accuracies and Kappa coefficients for different classification scenarios.

Table 4.4. Overall accuracies and Kappa coefficients for different classification scenarios.

Scenario	Random Forest		Support Vector Machine	
	OA (%)	Kappa	OA (%)	Kappa
1	61.42	0.56	65.33	0.61
2	58.06	0.52	61.85	0.58
3	63.39	0.59	68.07	0.64
4	69.84	0.63	73.24	0.69
5	58.93	0.54	63.41	0.60
6	55.19	0.49	57.58	0.53
7	54.58	0.49	58.96	0.53
8	67.89	0.63	71.39	0.67
9	66.12	0.62	70.08	0.65
10	72.60	0.68	75.12	0.71
11	73.93	0.69	75.96	0.72
12	70.89	0.65	72.51	0.68
13	78.90	0.74	82.43	0.78
14	81.79	0.76	85.40	0.82

Note: See Table 4.3 for an overview of the features used to define the scenarios presented in Table 4.4.

Among the three feature types, intensity features were found to produce the highest overall accuracies (e.g., scenarios 4, 10, 11, and 13). Polarimetry and coherence features were found to have a relatively similar strength in terms of classification accuracy (see scenarios 8 and 9). Although they were less successful than the intensity layers, combining these features with intensity resulted in an improvement in overall accuracy. For example, the exclusive application of intensity features was only successful for classifying different wetland classes to an overall accuracy of about 69% in the best case for the RF classifier. However, the inclusion of intensity with either coherence or polarimetric features improved the classification accuracies for scenarios 10 and 11 relative to scenario 4 by about 2.5 to 4%. Thus, it was concluded that both coherence and polarimetric features were informative and contained thematic information complementary to intensity features.

SVM outperformed the RF classifier in all classification scenarios in this study. For example, SVM was 3.5% more accurate than RF in scenario 13. The superior performance of SVM relative to RF for land cover classification has been previously noted [4], [17]. The results also demonstrated the better discrimination capacity of X-band relative to C-band when only HH polarized images were compared for both intensity and coherence features (scenario 1 versus 2 and 5 versus 6). This could be attributed to the higher temporal resolution of TerraSAR-X (i.e., 11 days) compared to RADARSAT-2 (i.e., 24 days), suggesting a better capability of the former observations to map hydrological variation and flooding status of vegetation. This is because wetlands are characterized as being highly dynamic and may change rapidly, particularly in areas with a short leaf-on season, such as NL. This indicates the importance of multi-temporal SAR images with high temporal resolution for the accurate discrimination of different wetland classes [2]. The X-band data used in this study also have a steeper incidence angle compared to those of C-band, contributing to deeper penetration into the wetland vegetation and providing more detailed information about flooding status (see Table 4.1). Figure 4.5 shows classification maps obtained by incorporating three feature types into RF and SVM classifiers.

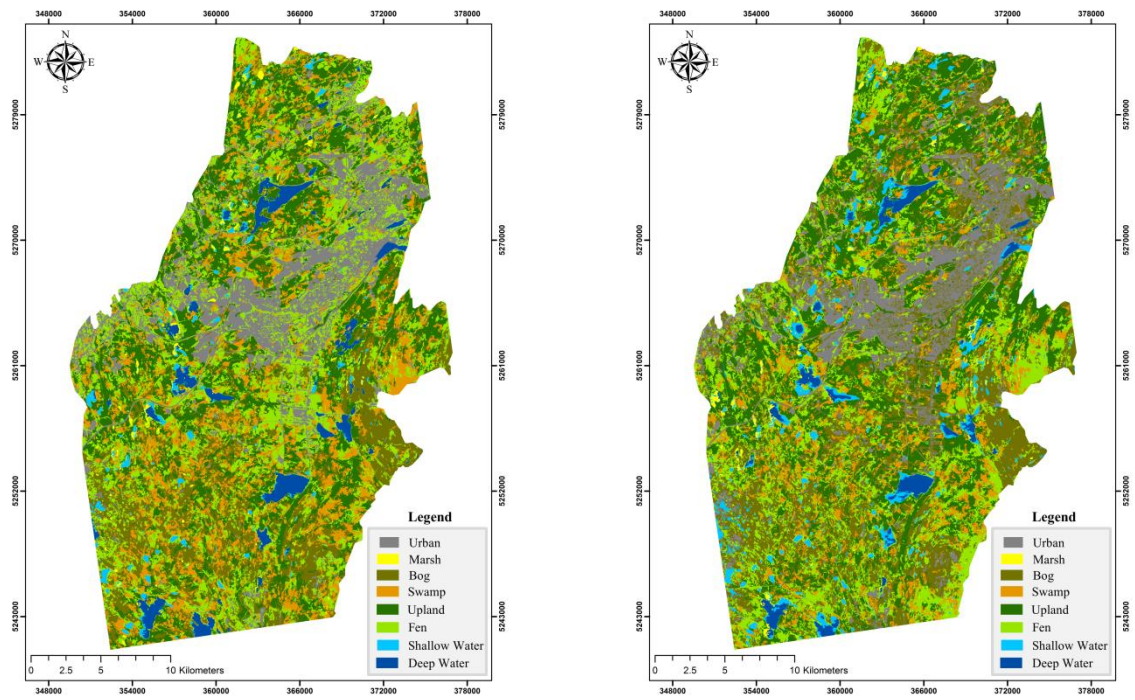


Figure 4.5. The classification maps obtained from combining all feature types using (Left) RF and (Right) SVM classifiers (scenario 13 using 81 features).

Table 4.5. Confusion matrix for scenario 13 using the RF classifier (OA: 78.90%).

		Classified Data									Prod. Acc.
		Bog	Fen	Swamp	Marsh	Shallow-water	Urban	Deep-water	Upland	Tot.	
Reference Data	Bog	38259	4697	2170	819	0	524	0	5328	51797	73.86
	Fen	2567	10297	167	57	0	0	0	1253	14341	71.80
	Swamp	45	494	6972	39	0	28	0	2190	9768	71.38
	Marsh	102	668	901	7804	1049	9	31	1202	11766	66.33
	Shallow-water	51	14	34	722	15290	0	5883	108	22102	69.18
	Urban	8669	165	1059	1217	0	42041	0	8941	62092	67.71
	Deep-water	0	0	0	0	1983	0	88478	0	90461	97.81
	Upland	4582	261	11	215	9	14912	504	66381	86875	76.41
	Tot.	54275	16596	11314	10873	18331	57514	94896	85403	349202	
User. Acc.	70.49	62.05	61.62	71.77	83.41	73.10	93.24	77.73			

As seen in Table 4.5, the overall accuracy of scenario 13 using the RF classifier was 78.9%, with bog correctly classified in 74% of cases, fen in 72%, swamp in 71%, marsh in 66%, shallow-water in 69%, urban in 68%, deep-water in 98%, and upland in 76% of cases.

Table 4.6. Confusion matrix for scenario 13 using the SVM classifier (OA: 82.43%).

		Classified Data									Prod. Acc.
		Bog	Fen	Swamp	Marsh	Shallow-water	Urban	Deep-water	Upland	Tot.	
Reference Data	Bog	41346	4199	1256	791	0	229	0	3976	51797	79.82
	Fen	1884	10308	270	36	0	0	0	1843	14341	71.88
	Swamp	724	679	7483	67	0	21	0	794	9768	76.61
	Marsh	169	458	566	7595	1224	57	17	1680	11766	64.55
	Shallow-water	0	0	19	603	18534	0	2946	0	22102	83.86
	Urban	7066	135	1017	855	0	49614	0	3405	62092	79.90
	Deep-water	0	0	0	0	4083	0	86378	0	90461	95.49
	Upland	6813	278	361	189	54	12487	102	66591	86875	76.65
	Tot.	58002	16057	10972	10136	23895	62408	89443	78289	349202	
	User. Acc.	71.28	64.20	68.20	74.93	77.56	79.50	96.57	85.06		

For SVM, however, the overall accuracy was 82.43%, with bog correctly classified in 80% of cases, fen in 72%, swamp in 77%, marsh in 64%, shallow-water in 84%, urban in 80%, deep-water in 95%, and upland in 77% of cases.

Although the classification map obtained by SVM was approximately 3.5% more accurate than that of RF, the two classifiers had relatively the same results in some cases. For example, in both cases the marsh wetland had the lowest producer's accuracies, which were about 66% and 64% for RF and SVM, respectively. Particularly, a great degree of confusion was found between marsh, shallow-water, and upland classes, wherein the marsh class was erroneously classified as the other

two classes (omission error). The confusion between shallow-water and marsh could be due to the complex mixture of these classes in the study area. In particular, the shallow-water class is defined as mineral wetlands dominated by submerged and floating vegetation, which are mostly marshes in the Avalon area. Also, the deep-water class had the highest producer's accuracy of above 95% in both cases. Overall, confusion was found between adjacent land cover classes, such as bog and fen, marsh and shallow-water, and shallow- and deep-water. This could be attributed to the heterogeneous mixture of these classes in the study area. For example, bog and fen classes are both peatland characterized by non-woody herbaceous vegetation. These two classes were reported to be hardly distinguishable by ecological biologists familiar with wetland sites. A higher degree of similarity for herbaceous wetland is also more pronounced when shorter wavelengths, which are strongly attenuated by vegetative density, are applied [2].

A comparison of user's accuracies also revealed the difficulty of discriminating wetland classes compared to non-wetland classes. This could be attributed to the larger amount of training data available for non-wetland classes, which contributed to an improvement in the overall classification results. Similarly, the higher producer's accuracies of bog and shallow-water classes could be due to the availability of a larger amount of training data for these classes relative to other wetland classes. Importantly, there is a variation of pixel counts in reference data within different wetland classes that can be attributed to the accessibility to different wetlands and the distribution and ecological characteristics of wetlands in the study area. For example, bogs are more frequently visited during field data collection and can also be easily distinguished using satellite imagery. This is because of their natural ecological characteristics and the Newfoundland climate, which encourages peatland formation [19]. In contrast, the swamp class is usually inaccessible and smaller in size, which resulted in fewer pixels relative to other wetland classes.

As mentioned earlier, we quantified the contribution of different input features to the overall classification accuracy using RF variable importance. In order to obtain the most accurate and stable results, the RF classification was executed 15 times using the same input, training, and testing data and then the ranking of the variables was recorded (Figure 4.6).

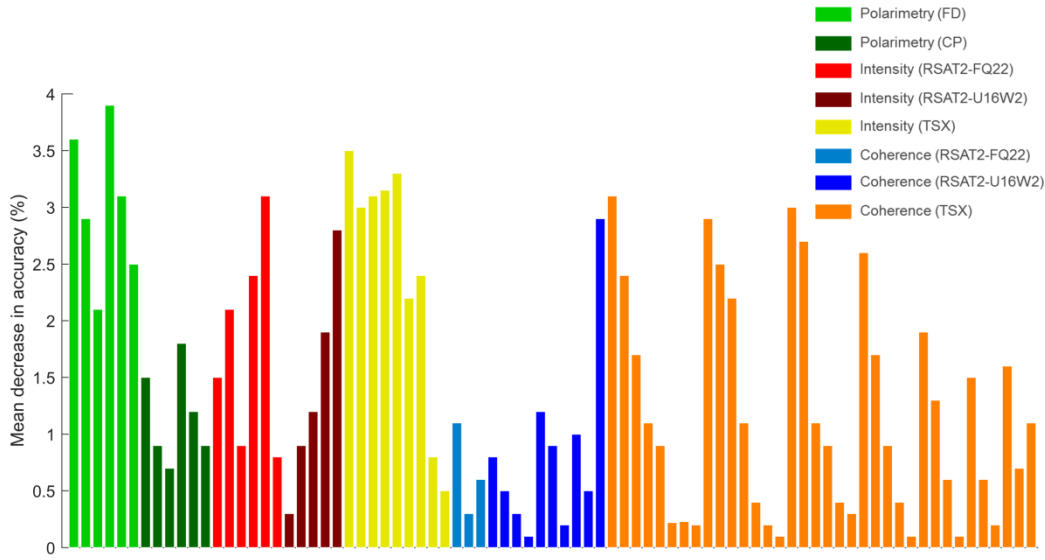


Figure 4.6. Normalized variable importance for scenario 13.

The variable importance revealed that the polarimetric features of Freeman-Durden (1-6) and HV intensity features for both dates (14<sup>th</sup> and 17<sup>th</sup>), as well as Cloude-Pottier entropy feature (10<sup>th</sup>) and HH intensity of date 2 (16<sup>th</sup>), were the most important features of the full polarimetric data (i.e., FQ22). For the Wide Ultra-Fine mode data, however, only the two latest intensity features (22<sup>nd</sup> and 23<sup>rd</sup>), as well as the last coherence feature (45<sup>th</sup>) were found to be important. For TerraSAR-X data, all intensity images (24-30), excluding the last two features (features 31-32), and coherence images with a small temporal baseline, were found to be influential (e.g., the 46<sup>th</sup>, 47<sup>th</sup>, and etc.). Thus, a total number of 10, 3, and 19 features were found to be important for RADARSAT-2 FQ22, RADARSAT-2 U16W2, and TerraSAR-X data, respectively.

In scenario 13, a total number of 81 input features were applied, which resulted in the highest classification accuracy. However, some of these input features may be correlated and, as such, may include redundant information. Thus, the correlation between different input features was determined using Spearman’s rank-order correlation in a pair-wise framework so that redundant information could be identified and removed from subsequent analysis (see Figures 4.7, 4.8, and 4.9).

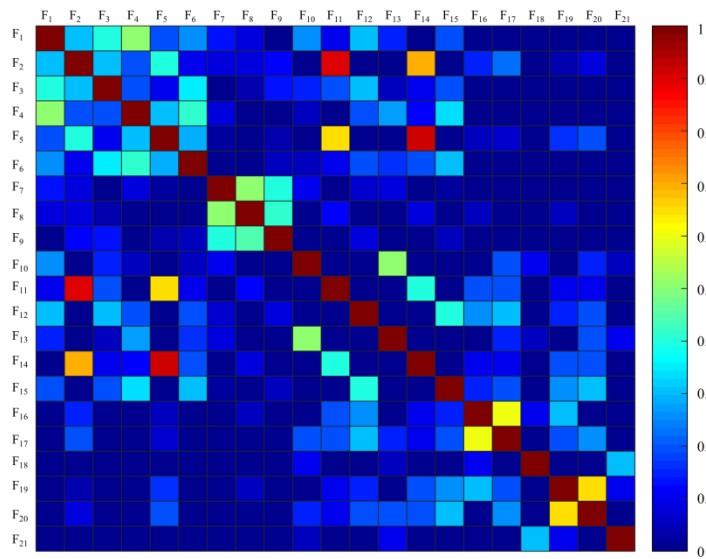


Figure 4.7. The correlation matrix of full polarimetric RADARSAT-2 (FQ22) features obtained using Spearman’s rank-order correlation ranging between 0 (i.e., no correlation) and 1 (i.e., the highest correlation). Different features are represented as follows:  $F_1(\sigma_{HH}^0 - D1)$ ,  $F_2(\sigma_{HV}^0 - D1)$ ,  $F_3(\sigma_{VV}^0 - D1)$ ,  $F_4(\sigma_{HH}^0 - D2)$ ,  $F_5(\sigma_{HV}^0 - D2)$ ,  $F_6(\sigma_{VV}^0 - D2)$ ,  $F_7$  (*Coherence - HH*),  $F_8$  (*Coherence - HV*),  $F_9$  (*Coherence - VV*),  $F_{10}$  (*FD - DB - D1*),  $F_{11}$  (*FD - V - D1*),  $F_{12}$  (*FD - ODD - D1*),  $F_{13}$  (*FD - DB - D2*),  $F_{14}$  (*FD - V - D2*),  $F_{15}$  (*FD - ODD - D2*),  $F_{16}$  (*CP - ENT - D1*),  $F_{17}$  (*CP -  $\alpha$  - D1*),  $F_{18}$  (*CP - A - D1*),  $F_{19}$  (*CP - ENT - D2*),  $F_{20}$  (*CP -  $\alpha$  - D2*), and  $F_{21}$  (*CP - A - D2*). Note that the feature abbreviations are as follows: FD (Freeman-Durden), CP (Cloude-Pottier), D1 (Date1), D2 (Date2), DB (double-bounce scattering), V (volume scattering), and ODD (surface scattering).

The correlation matrix revealed that, among intensity features, there was a correlation of up to 0.5 between the corresponding polarizations for dates 1 and 2 (e.g.,  $\sigma_{HH}^0$  for dates 1 and 2). Overall, the results illustrated that the correlation between intensity features was not high. There was, however, a high correlation between the HV intensity and the volumetric component of the Freeman-Durden decomposition (0.9). Among the model-based polarimetric decomposition features, a moderate correspondence between DB-D1 and DB-D2 (0.5), V-D1 and V-D2 (0.4), and ODD-D1 and ODD-D2 (0.4) was observed. For the eigenvector-based decomposition features, entropy and alpha scattering angle had a correlation of 0.65. Since the volumetric component of the Freeman-Durden decomposition and the HV intensity were highly correlated, the HV intensity features were removed, which resulted in a total of eight features being included for FQ22 data for the final classification scheme. For RADARSAT-2 (U16W2) and TerraSAR-X data, a correlation was determined between intensity and coherence features.

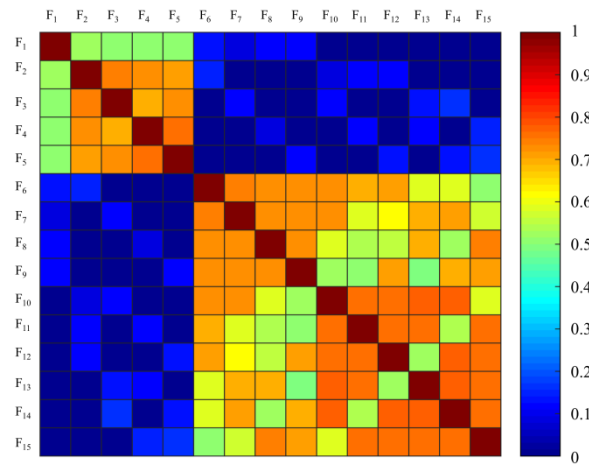


Figure 4.8. The correlation matrix of single polarized RADARSAT-2 (U16W2) features obtained using Spearman’s rank-order correlation. Different features are represented as follows: F1- F5 ( $\sigma_{HH}^0$  sorted by time) and F6- F15 (coherence sorted by time). Note: see Table 4.1 for the time sequence.

The correlation between intensity features ranged between 0.50 and 0.76. Likewise, the correlation between coherence features was found to be similar and reached 0.78. Thus, the degree of correlation between these features was insignificant and, accordingly, the feature selection was performed based only on the variable importance results of RF, resulting in a total number of three features.

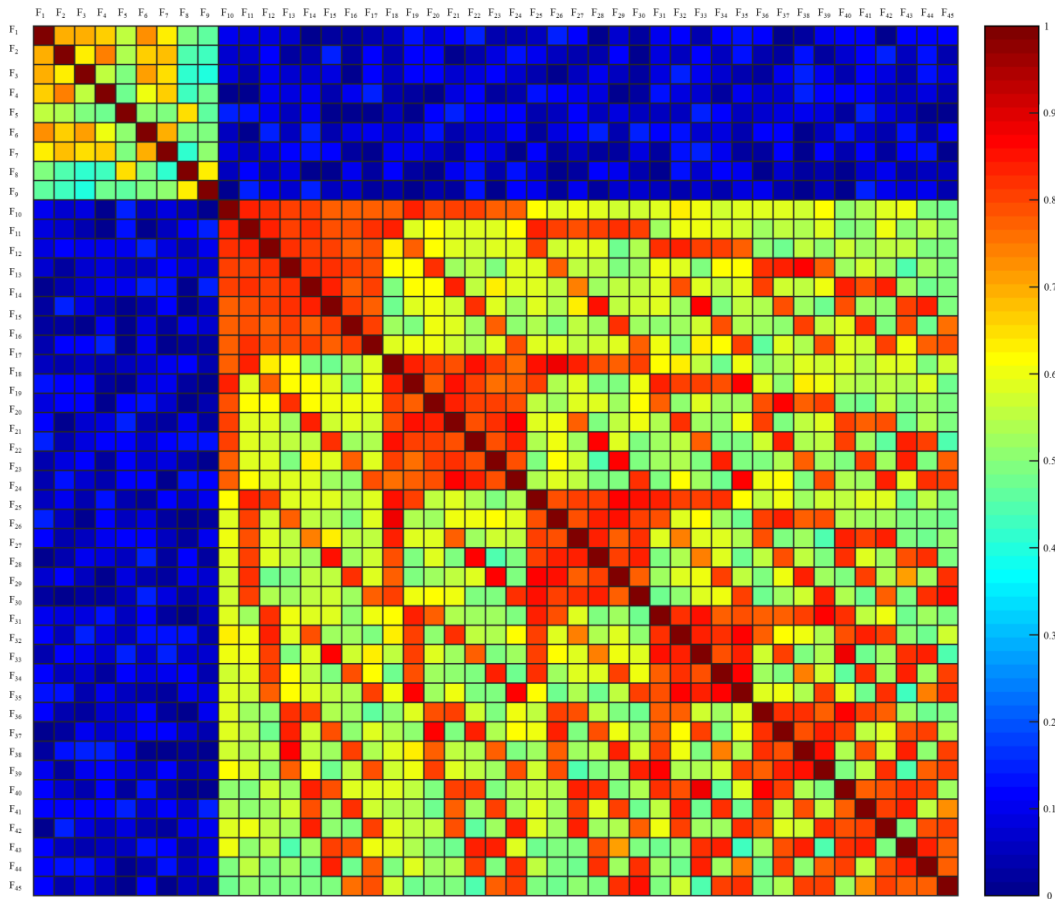


Figure 4.9. The correlation matrix of single polarized TerraSAR-X features obtained using Spearman’s rank-order correlation. Different features are represented as follows: F1- F9 ( $\sigma_{HH}^0$  sorted by time) and F10- F45 (coherence sorted by time). Note: see Table 4.1 for the time sequence.

In the case of X-band, the correlation varied from 0.40 to 0.75 and 0.40 to 0.89 among intensity and coherence features, respectively. Thus, all intensity features identified by variable importance

of RF were selected. However, we removed coherence features with a correlation higher than 0.8, which resulted in four remaining important uncorrelated coherence features. Accordingly, 11 features of TerraSAR-X were found to be important uncorrelated features and used as input for the final classification.

Importantly, the correlation between intensity and coherence features was negligible and varied between 0.05 and 0.15 for both C- and X-bands. Thus, intensity and coherence features were independent and their synergistic use should improve thematic land cover information.

Given the results obtained using variable importance analysis of RF and Spearman's rank-order correlation, the most important uncorrelated features were extracted. This analysis allowed us to perform a final classification using only 22 important uncorrelated features. Thus, these important uncorrelated features were applied to scenario 14 and SVM was once again found to be more accurate than RF (see Table 4.4).

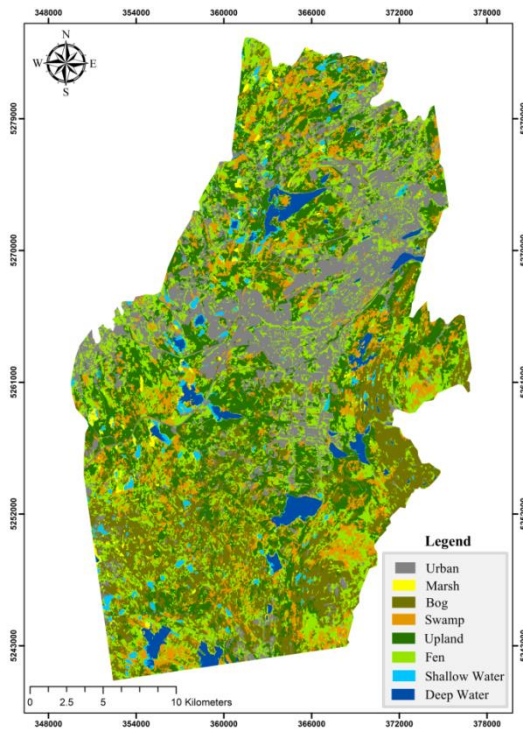


Figure 4.10. The final land cover map in this study obtained from the SVM classifier using 22 important uncorrelated features (OA: 85.40%).

The final classified map is clear and accurately represents the real-world features according to the interpretation of the optical imagery and as confirmed by ecological experts familiar with the study area. The confusion matrix for the final classified map is presented in Table 4.7.

Table 4.7. Confusion matrix of the SVM classifier based on 22 important uncorrelated features (OA: 85.40%).

		Classified Data									
		Bog	Fen	Swamp	Marsh	Shallow-water	Urban	Deep-water	Upland	Tot.	Prod. Acc.
Reference Data	Bog	44926	3371	241	738	0	366	0	2155	51797	86.73
	Fen	978	10439	351	0	0	0	0	2573	14341	72.79
	Swamp	839	67	7730	371	0	182	0	579	9768	79.14
	Marsh	33	375	299	9441	856	0	0	762	11766	80.24
	Shallow-water	0	0	146	938	18053	0	2975	0	22102	81.64
	Urban	5259	127	992	618	0	47365	0	7731	62092	76.28
	Deep-water	0	0	0	0	1180	0	89281	0	90461	98.70
	Upland	5283	359	628	157	0	9437	0	71011	86875	81.74
	Tot.	57318	14738	10387	12263	20089	57350	92256	84811	349202	
	User. Acc.	78.38	70.83	74.42	76.99	89.87	82.59	96.78	83.73		

The overall classification accuracy improved by about 3% when only important uncorrelated features were used for classification. In terms of class-based accuracies, the accuracy for all wetland classes, excluding shallow-water, was improved by an average of 7%, with bog being correctly classified in 87% of cases, fen in 73%, swamp in 79%, and marsh in 80%, representing improvements of approximately 7%, 1%, 3%, and 16%, respectively.

## 4.5. Conclusion

In this study, the synergistic use of multiple types of features extracted from multi-temporal RADARSAT-2 and TerraSAR-X for wetland mapping was investigated. Different combinations of features, including intensity, polarimetry, and interferometric coherence were applied to object-based RF and SVM classifications. In all cases, SVM outperformed RF in terms of classification accuracy. However, RF was found to be easily adjustable compared to SVM, since the latter required tuning the number of parameters, which was computationally intensive.

The results demonstrate that integrating multiple feature types enhanced thematic land cover information and, accordingly, the classification accuracy. In particular, the combination of all feature types resulted in an overall accuracy of 82.43% when SVM was employed. Based on the integration of variable importance analysis of RF and Spearman's rank-order correlation, a high classification accuracy of 85.40% was attained using the most important uncorrelated features extracted by this method. This represents a 3% overall improvement for all classes and a 7% improvement for only wetland classification. The results show that both polarimetric and interferometric features augment land cover information, providing additional information unavailable from intensity features alone.

The proposed classification framework provides a detailed spatial resolution map based on an advanced object-based image analysis using optimum feature types. The results demonstrate the significance of employing a feature selection method when a large number of potentially redundant features are used for classification. The proposed algorithm was found to be promising for land cover classification and will contribute to further scientific research in this region and in other wetlands elsewhere with similar ecological characteristics. Moreover, the use of this method for classifying land cover types beyond wetlands offers a potential avenue for further research.

## 4.6. References

- [1] M. Mahdianpari, B. Salehi, F. Mohammadimanesh, and M. Motagh, “Random forest wetland classification using ALOS-2 L-band, RADARSAT-2 C-band, and TerraSAR-X imagery,” *ISPRS J. Photogramm. Remote Sens.*, vol. 130, 2017.
- [2] L. F. de Almeida Furtado, T. S. F. Silva, and E. M. L. de Moraes Novo, “Dual-season and full-polarimetric C band SAR assessment for vegetation mapping in the Amazon várzea wetlands,” *Remote Sens. Environ.*, vol. 174, pp. 212–222, 2016.
- [3] T. Blaschke, “Object based image analysis for remote sensing,” *ISPRS J. Photogramm. Remote Sens.*, vol. 65, no. 1, pp. 2–16, 2010.
- [4] A. Ghosh and P. K. Joshi, “A comparison of selected classification algorithms for mapping bamboo patches in lower Gangetic plains using very high resolution WorldView 2 imagery,” *Int. J. Appl. Earth Obs. Geoinf.*, vol. 26, pp. 298–311, 2014.
- [5] I. I. I. Ramsey Elijah, Z. Lu, A. Rangoonwala, and R. Rykhus, “Multiple baseline radar interferometry applied to coastal land cover classification and change analyses,” *GIScience Remote Sens.*, vol. 43, no. 4, pp. 283–309, 2006.
- [6] C. J. Thiel, C. Thiel, and C. C. Schmullius, “Operational large-area forest monitoring in Siberia using ALOS PALSAR summer intensities and winter coherence,” *IEEE Trans. Geosci. Remote Sens.*, vol. 47, no. 12, pp. 3993–4000, 2009.
- [7] H. Jin, G. Mountrakis, and S. V. Stehman, “Assessing integration of intensity, polarimetric scattering, interferometric coherence and spatial texture metrics in PALSAR-derived land cover classification,” *ISPRS J. Photogramm. Remote Sens.*, vol. 98, pp. 70–84, 2014.
- [8] M. Zhang, Z. Li, B. Tian, J. Zhou, and J. Zeng, “A method for monitoring hydrological conditions beneath herbaceous wetlands using multi-temporal ALOS PALSAR coherence data,” *Remote Sens. Lett.*, vol. 6, no. 8, pp. 618–627, 2015.
- [9] M. Jiang *et al.*, “The potential of more accurate InSAR covariance matrix estimation for land cover mapping,” *ISPRS J. Photogramm. Remote Sens.*, vol. 126, pp. 120–128, 2017.
- [10] L. Wang, P. Marzahn, M. Bernier, and R. Ludwig, “Mapping permafrost landscape features using object-based image classification of multi-temporal SAR images,” *ISPRS J. Photogramm. Remote Sens.*, vol. 141, pp. 10–29, 2018.
- [11] K. Millard and M. Richardson, “On the importance of training data sample selection in random forest image classification: A case study in peatland ecosystem mapping,” *Remote Sens.*, vol. 7, no. 7, pp. 8489–8515, 2015.
- [12] J. C.-W. Chan and D. Paelinckx, “Evaluation of Random Forest and Adaboost tree-based ensemble classification and spectral band selection for ecotope mapping using airborne hyperspectral imagery,” *Remote Sens. Environ.*, vol. 112, no. 6, pp. 2999–3011, 2008.
- [13] F. Melgani and L. Bruzzone, “Classification of hyperspectral remote sensing images with support vector machines,” *IEEE Trans. Geosci. Remote Sens.*, vol. 42, no. 8, pp. 1778–1790, 2004.
- [14] J.-S. Lee and E. Pottier, *Polarimetric radar imaging: from basics to applications*. CRC press, 2009.
- [15] M. Mahdianpari *et al.*, “Fisher Linear Discriminant Analysis of coherency matrix for wetland classification using PolSAR imagery,” *Remote Sens. Environ.*, vol. 206, pp. 300–317, 2018.

- [16] A. Whyte, K. P. Ferentinos, and G. P. Petropoulos, “A new synergistic approach for monitoring wetlands using Sentinels-1 and 2 data with object-based machine learning algorithms,” *Environ. Model. Softw.*, vol. 104, pp. 40–54, 2018.
- [17] J. C.-W. Chan, P. Beckers, T. Spanhove, and J. Vanden Borre, “An evaluation of ensemble classifiers for mapping Natura 2000 heathland in Belgium using spaceborne angular hyperspectral (CHRIS/Proba) imagery,” *Int. J. Appl. Earth Obs. Geoinf.*, vol. 18, pp. 13–22, 2012.
- [18] L. Breiman, “Random forests,” *Mach. Learn.*, vol. 45, no. 1, pp. 5–32, 2001.
- [19] R. South, *Biogeography and Ecology of the Island of Newfoundland*, vol. 48. Springer Science & Business Media, 1983.

## Chapter 5. Compact Polarimetric SAR responses to Canadian wetlands <sup>4</sup>

### Preface

A version of this manuscript has been published in the *Remote Sensing journal*. I am a principal author of this manuscript along with the co-authors, Bahram Salehi, Masoud Mahdianpari, Brian Brisco, and Eric Gill. I and the co-author, Masoud Mahdianpari, conceptualized and designed the study. I developed the model and performed all experiments and tests. I wrote the paper and revised it based on comments from all co-authors. I also revised the paper according to the reviewers' comments. The co-author, Masoud Mahdianpari helped in performing the experiments and analyzing the results and contributed to revising the manuscript. All co-authors provided editorial input and scientific insights to further improve the paper. They also reviewed and commented on the manuscript.

### Abstract

Detailed information on spatial distribution of wetland classes is crucial for monitoring this important productive ecosystem using advanced remote sensing tools and data. Although the potential of full- and dual-polarimetric (FP and DP) Synthetic Aperture Radar (SAR) data for wetland classification has been well examined, the capability of compact polarimetric (CP) SAR data has not yet been thoroughly investigated. This is of great significance, since the upcoming RADARSAT Constellation Mission (RCM), which will soon be the main source of SAR observations in Canada, will have CP mode as one of its main SAR configurations. This also highlights the necessity to fully exploit such important Earth Observation (EO) data by examining

---

<sup>4</sup> Mohammadimanesh, F., Salehi, B., Mahdianpari, M., Brisco, B. and Gill, E., 2019. Full and Simulated Compact Polarimetry SAR Responses to Canadian Wetlands: Separability Analysis and Classification. *Remote Sensing*, 11(5), p. 516.

the similarities and dissimilarities between FP and CP SAR data for wetland mapping. Accordingly, this study examines and compares the discrimination capability of extracted features from FP and simulated CP SAR data between pairs of wetland classes. In particular, 13 FP and 22 simulated CP SAR features are extracted from RADARSAT-2 data to determine their discrimination capabilities both qualitatively and quantitatively in three wetland sites, located in Newfoundland and Labrador, Canada. Seven of 13 FP and 15 of 22 CP SAR features are found to be the most discriminant, as they indicate an excellent separability for at least one pair of wetland classes. The overall accuracies of 87.89%, 80.67%, and 84.07% are achieved using the CP SAR data for the three wetland sites (Avalon, Deer Lake, and Gros Morne, respectively) in this study. Although these accuracies are lower than those of FP SAR data, they confirm the potential of CP SAR data for wetland mapping as accuracies exceed 80% in all three sites. The CP SAR data collected by RCM will significantly contribute to the efforts ongoing of conservation strategies for wetlands and monitoring changes, especially on large scales, as they have both wider swath coverage and improved temporal resolution compared to those of RADARSAT-2.

**Keywords:** wetland classification; RADARSAT-2; compact polarimetry; RADARSAT Constellation Mission; RCM; Earth Observation

## **5.1. Introduction**

Wetlands are regions where water is the main factor affecting the ecosystem and the associated flora and fauna [1]. In such an environment, the water table is either at or near to the land surface or the land surface is covered by shallow-water [2]. Wetlands are natural infrastructures that facilitate the interactions of soils, water, plants, and animals, thus making them one of the most productive ecosystems. Wetlands serve a number of purposes, including water storage and purification, flood mitigation, storm protection, erosion control, shoreline stabilization, carbon

dioxide sequestration, and climate regulation [3]. To support global preservation of wetlands, the Ramsar Convention on Wetlands has been in place since 1971, wherein the main purpose is “the conservation and wise use of wetlands globally” [1]. Over the years, several countries (163 nations as of January 2013), including Canada, have joined to the convention and demonstrated their commitments to wetland preservation.

Over the past two decades, remote sensing tools and data have significantly contributed to wetland mapping and monitoring [4]. Optical remote sensing satellites have long been the main source of Earth Observation (EO) data for vegetation and wetland mapping [5], [6], yet cloud cover hinders the acquisition of such data. Consequently, as they are not impacted by solar radiation or weather conditions and can penetrate vegetation canopies (depending on wavelength), Synthetic Aperture Radar (SAR) sensors are of special interest, particularly in geographic regions with chronic cloud cover, such as Canada [7]. The interaction of SAR signal with vegetation canopies depends on SAR wavelengths [8]. Overall, longer wavelengths (e.g., L-band) are preferred for monitoring woody wetlands [8], whereas shorter wavelengths (e.g., C- and X-band) are useful for mapping herbaceous wetlands [9]. Several studies reported of great benefit of L-band data collected by JERS-1 and ALOS PALSAR-1 for inundation and vegetation dynamic mapping in various geographic locations, such as the Amazon floodplain [10], [11], the Alligator Rivers region of northern Australia [12], and wetlands in Africa [13]. Other studies demonstrated the capability of shorter wavelengths, such as C-band data collected by ERS-1/2 [14], RADARSAT-1 [15], RADARSAT-2 [16], [17], and Sentinel-1 [18] for wetland classification. X-band data collected by TerraSAR-X were also found to be useful for mapping heterogeneous structure of wetland ecosystems and their dynamics, given its high temporal and spatial resolution [19], [20].

Wetland phenology also affects SAR backscattering responses of flooded vegetation and depends on complex relation of vegetation height/density and the water level height in the wetland ecosystem [21]. For example, during high water seasons, the classes of swamp forest and freshwater marsh experience different conditions. In particular, an increase in water level height increases the chance of double-bounce scattering for swamps, resulting in an enhanced SAR backscattering response [22]. In contrast, an increase in water level height may decrease the chance of double-bounce scattering for marshes, as it converts double-bounce scattering to the specular scattering mechanism [23]. This results in little backscattering responses on SAR imagery in this case. Vegetative density is another influential factor and was examined in several research. For example, Lu and Kwon (2008) found that high vegetative density and canopy in swamp forest during the leaf-on season converted double-bounce scattering to volume scattering in southeastern coastal Louisiana wetlands using ERS and RADARSAT-1 imagery, which decreased SAR backscattering responses over swamp forest [24]. Later studies, such as [25], [26], found relatively similar results using ALOS PALSAR L-band data for forested wetlands in the Congo River in Africa.

In addition to SAR wavelength and wetland phenology, polarization of SAR signal is also an important factor. Given the capability of full-polarimetric (FP) SAR sensors to collect full scattering information of ground targets, the potential of these sensors for mapping various wetland classes has been well established [27]. In particular, a FP SAR sensor transmits a fully-polarized signal toward ground targets while receiving both fully-polarized and depolarized backscattering responses from a ground target [28]. This configuration also maintains the relative phase between polarization channels, thus allowing the application of advanced polarimetric decomposition

methods [29]. The polarimetric decompositions are beneficial for distinguishing similar wetland classes through characterizing various scattering mechanisms of ground targets.

Notably, decomposition techniques allow the polarimetric covariance or coherency matrixes to be separated into three main scattering mechanisms: single/odd-bounce scattering, which represents direct scattering from the vegetation or ground surface (e.g., rough water); double/even-bounce scattering, which represents scattering between, for example, flooded vegetation within smooth open water; and volume scattering, which represents multiple scattering within developed vegetation canopies. As such, several studies reported the success of wetland classification using FP SAR data in different geographic regions, such as China [30], Europe [31], the United States [32], and Canada [33]. However, the main limitations associated with the FP SAR configuration are the time constraints caused by the alternative transmitting of H and V polarizations toward ground targets, the large satellite mass caused by higher system power requirements, and the small swath coverage caused by doubling pulse repetition frequency (PRF) [34]. The small swath coverage precludes the potential of such data for applications on large-scales [35], for example, for the production of daily ice charts and annual crop inventories.

Dual-polarimetric (DP) SAR data cover a larger swath width and, currently, are the main source of SAR observations for operational applications. Such a SAR data configuration is currently available on Sentinel-1 SAR mission satellite of the Copernicus program by the European Space Agency (ESA) [36]. The main purpose of this mission is to provide full, free, and open access SAR observations for environmental monitoring [37]. Furthermore, the 12-days satellite revisit time makes Sentinel-1 SAR data ideal for monitoring phenomena with highly dynamic natures such as wetlands [18], [38], as well as assistant with operational applications such as sea ice monitoring [39] and crop mapping [40]. However, insufficient polarimetric information is

available within such data. Furthermore, DP SAR data cannot maintain a relative phase between polarization channels, thus diminishing their capability to distinguish similar land and wetland classes through advanced polarimetric decomposition techniques [29]. To move forward with both polarization diversity and swath coverage, the compact polarimetry (CP) SAR configuration was introduced. CP SAR sensors are in the same group as that of DP but differ in terms of the choice of polarization channels [41]. This configuration collects greater polarimetric information compared to that of DP, while covering a much larger swath width relative to that of FP SAR data. CP SAR sensors also maintain the relative phase between two received polarization channels, which further makes them advantageous relative to DP SAR sensors for a variety of applications. Importantly, the upcoming RADARSAT Constellation Mission (RCM), which is the successor mission to RADARSAT-2, that is planned to be launched in 2019, will have a circularly transmitting, linearly receiving (CTLR) CP mode as one of its main SAR data collection configurations [42]. The main purposes of RCM are to ensure data continuity for RADARSAT-2 users and ameliorate the operational capability of SAR data by leveraging a more advanced spaceborne mission [35]. In particular, RCM comprises three identical small (relative to RADARSAT-2) C-band satellites to gain greater satellite coverage over a much shorter satellite revisit time (only four-day) [43]. This is of great importance for applications, such as maritime surveillance and ecosystem monitoring, which heavily rely on frequent SAR observations. Various SAR configurations and polarizations are available with RCM. These include single-polarimetry (SP), conventional DP, and CTLR CP modes. In the CTLR mode, RCM transmits a right-circular polarized signal and receives two coherent orthogonal linear (both horizontal and vertical) polarized signals (RH and RV) and their relative phase [44]. Lower PRF and system power and less on-board mass and data volume are other advantages of RCM compared to

RADARSAT-2 [45]. Despite these benefits, less polarimetric information is available within CP SAR data compared to that of FP SAR data. Furthermore, Noise Equivalent Sigma Zero (NESZ) values potentially range between  $-25$  to  $-17$  dB for RCM data [43], which are higher than those of RADARSAT-2 in most cases. This decreases the sensitivity of the RCM SAR signal to ground features with low backscattering values, such as open water and sea ice.

It is beneficial to compare both the similarities and differences of CP SAR data collected by RCM with those of RADARSAT-2 in different applications, prior to the availability of RCM data for operational monitoring. Given that maritime surveillance is one the main application of RCM data [45], the potential of simulated or real CP SAR data has been well examined for sea ice classification and monitoring in several recent studies (e.g., [35], [41], [46], [47]). However, the potential of CP SAR data for other applications, such as wetland characterization, remains an active research area, requiring much investigation to fully exploit the capability of such data for other purposes, such as ecosystem monitoring (e.g., agriculture, wetland, and forestry). Notably, two previous studies have highlighted the capability of simulated CP SAR data from RADARSAT-2 for wetland mapping. Brisco et al. (2013) first reported the potential of CP SAR data for wetland classification in southwestern Manitoba, Canada, using 12 CP SAR features but for wetland classes different from typical Canadian wetland classes (i.e., bog, fen, marsh, swamp, and shallow-water, as classified based on the Canadian Wetland Classification System, CWCS) [48]. White et al. (2017) evaluated the potential of simulated CP SAR data from RADARSAT-2 with a larger number of CP features, yet only for peatland classes (i.e., poor fen, open shrub bog, and treed bog) in a small area in Southern Ontario, Canada [49]. However, the latter study exploited the synergy of CP and FP SAR data with digital elevation model (DEM) and Landsat-8 optical data for classifying peatland classes [49]. Although their methodology and results were sound, much

investigation is still required to fully understand the compact polarimetric responses of various CP SAR features to standard wetland classes (according to the definition of CWCS).

The present research was built on the knowledge gained from our previous work, wherein the potential of CP SAR features for wetland mapping was investigated [29]. However, unlike in [29], in the present study, three wetland sites were selected and the main objectives here were to identify the most useful CP features for similar wetland class discrimination and to improve image interpretation using both qualitative and quantitative approaches. Specifically, this study aimed to: (1) explore the effect of the difference in polarization between FP (RADARSAT-2) and simulated CP SAR data for the classification of wetland complexes; (2) determine the separability between pairs of wetland classes with various CP SAR features both visually, using box-and-whisker plots, and quantitatively, using the Kolmogorov-Smirnov (K-S) distance measurement; and (3) classify wetland complexes using the most effective CP SAR features using an object-based random forest (RF) algorithm.

## **5.2. Study Area and Data**

### **5.2.1. Study Area and In-Situ Data**

The three study areas located in Newfoundland and Labrador, Canada, at the eastern, center, and western portions of the island were selected for this research (see Figure 5.1). In general, the island of Newfoundland has a humid continental climate, which is greatly affected by the Atlantic Ocean.

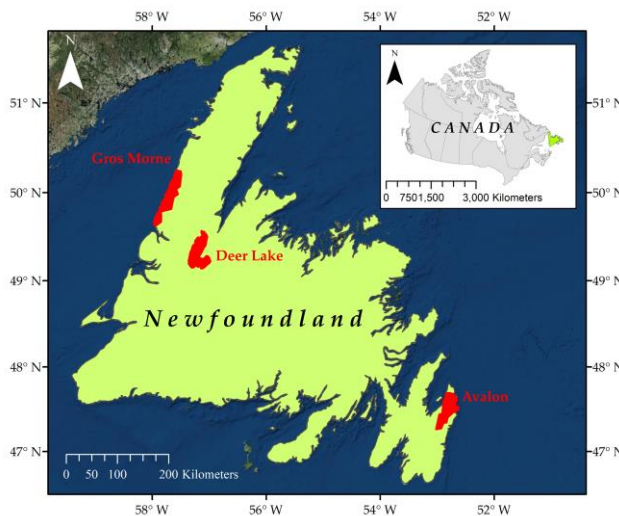


Figure 5.1. The red polygons illustrate the geographic location of the three study areas.

The first pilot site is the Avalon area, located in the most eastern part of the island in the Maritime Barren ecoregion. It has an oceanic climate of foggy, cool summers, and relatively mild winters. The second pilot site is the Deer Lake area, located in the the northern (center) portion of the island in the Central Newfoundland ecoregion and experiences a continental climate of cool summers and cold winters. Finally, the third pilot site is the Gros Morne area, located on the extreme western coast of the island, in the Northern Peninsula ecoregion. This area has a maritime-type climate with cool summers and mild winters [50]. As elsewhere in Newfoundland, frequent rain and fog are dominant due to the proximity of the pilot sites to the Atlantic Ocean. This highlights the great significance of SAR data for remote sensing studies for the island.

The study areas contain all wetland classes categorized by the CWCS, namely bog, fen, marsh, swamp, and shallow water, although bog and fen are the most dominant classes. Other land cover classes include urban, upland, and deep water. Figure 5.2 illustrates examples of land cover classes in the Avalon study area.

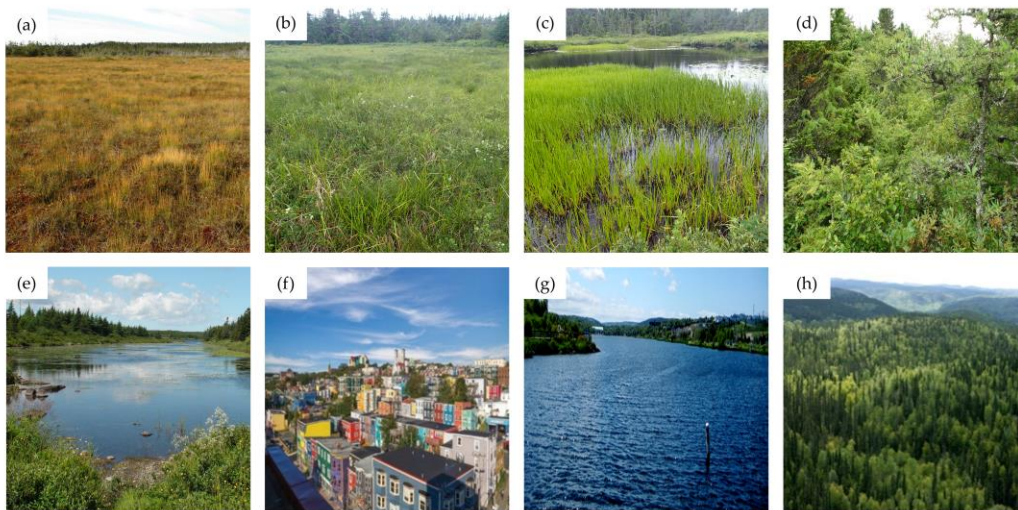


Figure 5.2. Examples of land cover classes in the Avalon study area, including (a) bog, (b) fen, (c) marsh, (d) swamp, (e) shallow water, (f) urban, (g) deep water, and (h) upland.

For this study, *in-situ* data were collected over multiple visits during the summers and falls of 2015, 2016, and 2017. Potential and accessible wetland sites in all study areas were flagged based on prior knowledge of wetland sites, interpretation of high resolution Google Earth imagery, and the CWCS definition of wetlands. Other considerations for site visitation included accessibility via public roads and the public and private ownership of lands. Significant effort was devoted to collect *in-situ* data covering a wide range of wetland and non-wetland classes with vast spatial distributions across all study areas. In each location, one or more Global Positioning System (GPS) points were collected, depending on the size of each wetland class. Digital photographs and ancillary notes (e.g., dominant vegetation, hydrology, dates, and the name of locations) were also recorded to facilitate preparation of the training samples. Notably, data from wetlands of various sizes were collected during the first year of data collection, resulting in the production of several small-size classified polygons. However, wetlands with sizes greater than one ha (where possible)

were selected during the following years to restrict the production of small-size polygons to a feasible extent.

Recorded GPS points were then imported in ArcMap10.6, and polygons indicating classified delineated wetlands were produced using a visual interpretation of 50 cm resolution orthophotographs and 5 m resolution RapidEye optical images by remote sensing and biologist experts familiar with the studies areas. Notably, any human error in both recording GPS points during *in-situ* data collection and preparing the reference polygons may affect the results of separability analysis and classification. Next, polygons were sorted based on their size and alternately assigned to either training or testing groups. This alternative assignment ensured that both the training (~50%) and testing (~50%) polygons had relatively equal numbers of small and large polygons. Furthermore, the training and testing polygons were obtained from independent samples to ensure robust accuracy assessment. Table 5.1 presents the number of training and testing polygons for each class in the three pilot sites.

Table 5.1. Number of training and testing polygons for each class in the three pilot sites.

Class	Avalon		Deer Lake		Gros Morne	
	Training	Testing	Training	Testing	Training	Testing
Bog	42	41	16	15	19	19
Fen	20	19	27	27	15	16
Marsh	25	25	12	12	16	15
Swamp	22	23	20	20	21	21
Shallow water	20	20	11	12	13	14
Urban	36	35	17	18	19	19
Deep water	7	8	3	3	3	2
Upland	29	29	12	11	42	43
Total	201	200	118	118	148	149

### 5.2.2. Satellite Imagery

A total number of seven Single Look Complex (SLC) RADARSAT-2 images were used in this study. These images were acquired using the Fine Quad-polarization (FQ) mode on August 2015 from descending orbits (see Table 5.2).

Table 5.2. Characteristics of RADARSAT-2 imagery used in this study.

Pilot site	Date	# Images	Mode	Image coverage (km)*	Incidence angle (°)	NESZ (dB)	Resolution (m)*
Avalon	20150821	2	FQ4	25×25	22.1-24.1	-34.6 to -37.8	5.2×7.6
Deer Lake	20150810	2	FQ3	25×25	20.9-22.9	-34.4 to -37.7	5.2×7.6
Gros Morne	20150803	3	FQ2	25×25	19.7-21.7	-34 to -38.4	5.2×7.6

\*Note that image coverage is represented in (ground range × azimuth) and resolution is represented in (slant range × azimuth).

Notably, the leaf-on season in Newfoundland starts by late May/early June. August corresponds to the peak of the growing season in the study area, wherein both the vegetative density and water level height are at their optimum. Accordingly, imagery was selected from August, as our recent study demonstrated that flooding status of vegetation is at the highest, resulting in the maximum occurrence of double-bounce scattering at this time period [51].

As indicated in Table 5.2, RADARSAT-2 images were collected in 2015; our *in-situ* data used for both classification and separability analysis were collected during the summers and falls of 2015, 2016, and 2017. We assumed that no change had occurred in the wetland properties during the three year interval given very limited human activities in the studies areas. Furthermore, this time difference (i.e., < three years) between satellite data acquisition and the collection of ecological training data is acceptable and agrees with those used in previous research (e.g., [51], [52]).

## 5.3. Methods

### 5.3.1. Full Polarimetric SAR Data Processing

The main preprocessing steps were speckle reduction, orthorectification, and image mosaicking. Speckle reduction is a necessary preprocessing step, as the radiometric quality of SAR images is hindered by speckle noise, which affects subsequent image processing steps (e.g., segmentation and classification) [53]. Accordingly, a 5x5 Boxcar filter was employed to suppress speckle and increase the number of looks prior to extraction of polarimetric features. A small filter size was selected, as it maintains the boundaries between natural and human-made objects and is appropriate for wetland classes with small sizes (e.g., swamp and marsh in this study). Orthorectification of de-speckled RADARSAT-2 images was performed in PCI Geomatica's OrthoEngine 2017 software using the rational function model [54], [55]. Satellite orbital information and an external digital elevation model (DEM), released by Natural Resource Canada, were employed for orthorectification. All images were projected into UTM coordinates, zone 22/row T for the Avalon study area and zone 21/ row U for the Deer Lake and Gros Morne study areas, respectively. Two scenes from the Avalon and Deer Lake pilot sites and three from the Gros Morne study region were then mosaicked into single strips of data.

A total of 13 features were extracted from the full polarimetric RADARSAT-2 images. In particular, three SAR backscattering coefficient images, namely  $\sigma_{HH}^0$ ,  $\sigma_{VV}^0$ , and  $\sigma_{HV}^0$ , were extracted.  $\sigma_{HH}^0$  is sensitive to double-bounce scattering and, as such, is useful for discriminating flooded and non-flooded wetland classes [9]. It is also beneficial for discriminating water from non-water (e.g., upland) classes, given its lower sensitivity to surface roughness on water compared to  $\sigma_{VV}^0$  [9].  $\sigma_{VV}^0$  is suitable for distinguishing herbaceous wetland classes, especially bog and fen classes [56]. It is also sensitive to soil moisture [57], [58] and is useful for discriminating

sparsely vegetated areas.  $\sigma_{HV}^0$  is sensitive to the vegetation structure and has shown promising results for distinguishing wetland classes [8].

Three incoherent decomposition methods, namely Cloude-Pottier [59], Freeman-Durden [60], and Yamaguchi [61], were also employed. These methods decompose the SAR backscattering responses of distributed ground targets into various scattering mechanisms, which are of great use for discriminating similar wetland classes. This is because wetland classes are characterized by varying scattering mechanisms depending on SAR wavelength, roughness, and vegetation structure through the growing season.

The Cloude-Pottier method is a decomposition that considers three secondary components, including the entropy, anisotropy, and alpha angle, which are derived from eigenvalues and eigenvectors. Entropy ranges from 0 to 1 and indicates the degree of randomness. Lower entropy values demonstrate that a single scattering mechanism is dominant (low depolarization); whereas values approaching 1 suggest that multiple scatterings are present. Anisotropy is the complementary component to entropy and represents the relative importance of the secondary scattering mechanism. The alpha angle varies between  $0^\circ$  and  $90^\circ$  and is also useful for characterizing different scattering mechanisms. Surface, volume, and double-bounce scattering produce low, intermediate, and high alpha angles, respectively.

The Freeman-Durden and Yamaguchi decompositions are known as physical model-based decomposition approaches with three and four components, respectively. In particular, the Freeman-Durden approach, which assumes reflection symmetry, decomposes target scattering as the linear sum of the surface, double-bounce, and volume scattering mechanisms [60]. The Yamaguchi decomposition has similar components as those of Freeman-Durden; however, it benefits from an additional term, known as the helix scattering component. This component takes

into account cases of non-reflection symmetry (i.e., the correlation between co- and cross-polarized channels), which usually occur in complex urban areas. Additionally, the volume scattering term of the Yamaguchi decomposition for vegetation was further modified by employing a different probability density function than that used by the Freeman-Durden approach [61].

### **5.3.2. Compact Polarimetry SAR Data Processing**

The Canada Centre for Mapping and Earth Observation (CCMEO) simulator was used to simulate the RCM CP data [45]. The CCMEO calibrates the RADARSAT-2 SLC product using the Sigma Naught ( $\sigma^0$ ) calibration. The calibrated product is stored in a 3x3 covariance matrix format and is then downsampled to a 2x2 covariance matrix to the defined spatial resolution for each mode. The CCMEO software simulates both CP and DP data at various spatial resolutions with varying noise floors. In this study, CP SAR data were simulated at medium resolution (i.e., -24 NESZ at a 16 m spatial resolution) imaging modes. All CP features were produced using a 5x5 kernel size to take into account the effects of speckle noise (i.e., Boxcar filter). Although advanced speckle reduction methods (e.g., adaptive Lee filter) are advantageous for PolSAR image processing, as they preserve polarimetric information and the resulting de-speckled images are less affected by blurring effects, the simple Boxcar filter was used in this study. This is because it was the only available speckle reduction method in the CCMEO software at the time of data processing. However, this filter was used for both FP and CP SAR data to mitigate any potential differences due to employing different speckle reduction methods. As such, any observed differences between the results of FP and CP SAR data are due to differences in polarization, NESZ, and spatial resolution.

A total of 22 CP SAR features were extracted from the simulator and these features can be broadly categorized into five main groups, namely intensity, Stokes vector, Stokes child, CP decompositions, and other features (see Table 5.3).

Table 5.3. An overview of the investigated CP SAR features in this study.

Name of feature	Description	CP feature
Intensity features	SAR backscattering coefficients	$\sigma_{RR}^0, \sigma_{RL}^0, \sigma_{RH}^0, \sigma_{RV}^0$
Stokes vector	First element	$S_0 = \langle  E_{RH} ^2 +  E_{RV} ^2 \rangle$
	Second element	$S_1 = \langle  E_{RH} ^2 -  E_{RV} ^2 \rangle$
	Third element	$S_2 = 2\text{Re} \langle E_{RH} E_{RV}^* \rangle$
	Fourth element	$S_3 = -2\text{Im} \langle E_{RH} E_{RV}^* \rangle$
Stokes child parameters	Circular polarization ratio	$\mu_c = \frac{S_0 - S_3}{S_0 + S_3}$
	Degree of polarization	$m = \frac{\sqrt{S_1^2 + S_2^2 + S_3^2}}{S_0}$
	Relative phase between RV and RH	$\delta = \tan^{-1}\left(\frac{S_3}{S_2}\right)$
	Ellipticity of the compact scattered wave (Cloude $\alpha_s$ )	$\alpha_s = \frac{1}{2} \tan^{-1}\left(\frac{\sqrt{s_1^2 + s_2^2}}{s_3}\right)$
CP decompositions	m-delta decomposition	$m - \delta - \text{Odd}$
		$m - \delta - \text{Even}$
		$m - \delta - \text{Volume}$
	m-chi decomposition	$m - \chi - \text{Odd}$
		$m - \chi - \text{Even}$
		$m - \chi - \text{Volume}$
Other features	Conformity coefficient	$\mu = \frac{2 \text{Im} \langle S_{RH} S_{RV}^* \rangle}{\langle S_{RH} S_{RH}^* \rangle + \langle S_{RV} S_{RV}^* \rangle}$
	Correlation coefficient of RV and RH	$\rho = \frac{\sqrt{\langle S_{RH} S_{RV}^* \rangle}}{\sqrt{\langle S_{RH} S_{RH}^* \rangle + \langle S_{RV} S_{RV}^* \rangle}}$
	Shannon entropy intensity	$SE_I = 2 \log\left(\frac{\pi e \text{Tr}(T_2)}{2}\right)$
	Shannon entropy polarimetry	$SE_P = \log\left(\frac{4 T_2 }{\text{Tr}(T_2)^2}\right)$

The Stokes vector parameters are extracted from the 2x2 simulated covariance matrix of CP SAR data [28] and are useful for characterizing the scattering properties of ground targets. Note that in the Stokes vector,  $E$  is the electric field vector in the subscripted polarization, wherein the first and second subscripts indicate the transmitted and received polarizations, respectively,  $*$  indicates complex conjugate, and  $Re$  and  $Im$  denote the real and imaginary parts of the complex cross-product amplitude, respectively [42]. The first element of the Stokes vector ( $S_0$ ) represents the total scattering power, whereas the second component indicates the degree of the linear horizontal ( $S_1 > 0$ ) or vertical ( $S_1 < 0$ ) polarization. The third component illustrates whether the SAR signal is polarized at tilt angle  $45^\circ$  ( $S_2 > 0$ ) or  $135^\circ$  ( $S_2 < 0$ ). The last component ( $S_3$ ) characterizes the left-circular ( $S_3 > 0$ ) or right-circular ( $S_3 < 0$ ) polarization wave [7] (see Table 5.3).

The second group of parameters, the Stokes child features, are extracted from the Stokes vector. The circular polarization ratio represents the ratio between the same circular polarization intensity and the opposite circular polarization intensity, wherein values greater and lower than one correspond to double-bounce and surface scattering mechanisms, respectively [62]. The degree of polarization represents the state of polarization [28], wherein 0 and 1 indicate purely depolarized and polarized waves, respectively [34]. The relative phase ( $\delta$ ) [45] is potentially similar to the co-polarized phase difference and varies from  $-180^\circ$  to  $180^\circ$ . This parameter is useful for identifying whether surface ( $\delta > 0$ ) or double-bounce ( $\delta < 0$ ) scattering is dominant [62]. The Cloude  $\alpha_s$  [63] has similar behaviour as that of the alpha angle of Cloude-Pottier decomposition, describing the dominant scattering mechanism [41].

Six CP decomposition parameters were also examined. They were obtained from m-delta [45] and m-chi decompositions [28], each of which has three components. The extracted features from the m-delta and m-chi decompositions describe the physical scattering mechanisms of even-bounce,

double-bounce, and volume scattering analogous to those obtained from the Freeman-Durden decomposition. For example,  $m - \delta - V$  reflects a dominant depolarized backscattering mechanism (volume scattering). However,  $\delta$  discriminates the dominant scattering mechanism between odd-bounce ( $\delta > 0 \therefore \delta - O > \delta - E$ ) and even-bounce ( $\delta < 0 \therefore \delta - O < \delta - E$ ).

The conformity coefficient is independent of Faraday rotation (FR) and varies between -1 and 1 [64]. Note that in the conformity coefficient equation,  $S$  is the element of the scattering matrix in the subscripted polarization, wherein the first and second subscripts indicate the transmitted and received wave polarizations, respectively. For the distributed targets under the reflection symmetry hypothesis: (1)  $\mu$  is positive and approaches 1 when surface scattering is dominant; (2)  $\mu$  is negative and approaches -1 when double-bounce scattering is dominant; and (3)  $\mu$  has an intermediate value when volume scattering is dominant [64]. The correlation coefficient varies between 0 and 1 and indicates the degree of correlation between RV and RH intensity [47]. The last two parameters are Shannon entropy intensity and polarimetry features. The Shannon entropy intensity is potentially similar to  $S_0$  (the first element of the Stokes vector), as it represents the total backscattering power [65] and has shown high correlation with  $S_0$  in the previous studies [35], [66]. The Shannon entropy polarimetry represents the polarimetric contribution, depends on the Barakat degree of polarization [65], and is, therefore, correlated with the degree of polarization [66].

### **5.3.3. Backscattering and Separability Analyses**

Backscattering analysis was performed for several FP and CP SAR features to visually interpret the discrimination capacity between similar wetland classes. A quantitative analysis of the separability between pairs of wetland classes was then followed by the two-sample Kolmogorov-Smirnov (K-S) distance. The K-S distance is a nonparametric separability measurement that

determines the maximum difference between two cumulative distribution functions [67]. It varies between 0 and 1, wherein lower ( $\sim 0$ ) and higher ( $\sim 1$ ) values correspond, respectively, to low and high discrimination potentials between two classes using a given input feature. The K-S distance was calculated for all extracted CP and FP features between each pair of wetland classes. This discrimination analysis resulted in four groups of classes with: (1) poor separability, or, the K-S distance values lower than 0.5 ( $K - S < 0.5$ ); (2) some degree of separability, or, the K-S distance values ranging between 0.5 and 0.7 ( $0.5 \leq K - S \leq 0.7$ ); (3) good separability, or, the K-S distance values ranging between 0.7 and 0.85 ( $0.7 < K - S \leq 0.85$ ); and (4) excellent separability, or, the K-S distance greater than 0.85 ( $K - S > 0.85$ ). These selected thresholds are appropriate for the purpose of this study and are matched with recent similar studies of feature analysis and selection (e.g., [35], [41], [66]). Notably, the same training polygons were used for backscattering and separability analyses of both the FP and CP SAR data. For this purpose, different subsets of each class with relatively homogeneous and large areas were selected.

#### **5.3.4. Classification Scheme**

An object-based classification scheme was employed in this study. Multi-resolution segmentation (MRS) analysis was used for object-based classification. Scale, shape, and compactness are three user-defined parameters for MRS analysis [68]. These parameters were adjusted using key directions from previous studies (e.g., [33]) and a trial-and-error procedure. Accordingly, the optimal values for scale, shape, and compactness were found to be 100, 0.1, and 0.5, respectively. Notably, the compactness of 0.5 balances the compactness and smoothness of the objects equally. Scale values ranging between 25 and 300 were examined and a value of 100 was found to be optimal according to the visual analysis of the segmentation results.

The random forest (RF) algorithm was selected for classification [69]. RF is a non-parametric classifier and is insensitive to outliers and overtraining. It also has potential to handle high dimensional remote sensing data. RF is an ensemble classifier that comprises a set of Classification and Regression Trees (CART) to make a prediction [70]. RF is advantageous relative to decision trees in terms of classification performance and is much easier to execute compared to support vector machine (SVM) [70]. In particular, RF can be easily adjusted using two input parameters, namely the number of trees (*Ntree*) and the number of variables (*Mtry*) [70]. About two thirds (i.e., *in-bag*) of the training samples are selected to produce trees with high variance and low bias using a bootstrap aggregating (bagging) approach. The remaining one third (i.e., *out-of-bag*, OOB) of the training samples are employed for an internal cross-validation accuracy assessment [71]. The best splitting of the nodes is determined by minimizing the correlation between trees and the final label is based on the majority vote of the trees [70].

The two inputs of the RF classifier were determined based on (a) our previous studies (e.g., [33], [72]), and (b) a trial-and-error approach. Specifically, the parameter of *Mtry* was assessed for the following values when *Ntree* was adjusted to 500: (a) one third of the total number of polarimetric features; (b) the square root of the total number of polarimetric features; (c) half of the total number of polarimetric features; and (d) all polarimetric features. This resulted in little or no influence on the classification accuracies. Accordingly, *Mtry* was adjusted to the square root of the total number of polarimetric features, as suggested in [69]. Then, the value of *Ntree* was assessed for the following values when *Mtry* was set to the optimal value: (a) 400; (b) 500; (c) 600; (d) 700; (e) 800; (f) 900; and (g) 1000. A value of 500 was then found to be optimal, as accuracies remained approximately constant for *Ntree* values exceeding 500.

### **5.3.5. Evaluation Indices**

This study examined two commonly used evaluation indices, namely overall accuracy (OA) and Kappa coefficient (K). Overall accuracy characterizes the overall efficiency of the algorithm and can be determined by dividing the total number of correctly-identified pixels (i.e., the diagonal elements of the confusion matrix) by the total number of testing pixels. The Kappa coefficient measures the degree of agreement between the ground truth data and the classified map. Both user's accuracy (UA) and producer's accuracy (PA) were also reported for the classification results of the Avalon study area. Producer's accuracy is measured by dividing the total number of correctly-classified pixels in a category by the total number of pixels in that category obtained from the reference data (i.e., the testing samples) and is also a representative of omission error. User's accuracy is measured by dividing the total number of correctly-classified pixels in a category by the total number of classified-pixels in that category as derived from the classified map and is also a representative of commission error [73].

## **5.4. Results and Discussion**

### **5.4.1. Backscattering Analysis**

#### **5.4.1.1. Full Polarimetric SAR Data**

Figures 5.3 to 5.5 depict box-and-whisker plots of the various wetland classes extracted from SAR backscattering intensity features, as well as the Freeman-Durden and H/A/alpha decompositions.

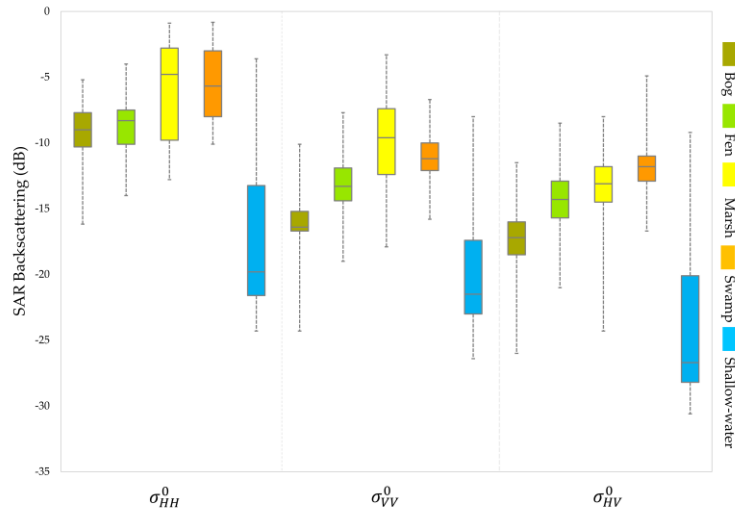


Figure 5.3. Box-and-whisker plots demonstrating the distribution of the SAR backscattering coefficients of FP SAR data for wetland classes obtained from the pixel values of the training data set. Note that the horizontal bars within boxes indicate median values, boxes illustrate the lower and upper quartiles, and whiskers range from minimum to maximum values.

As illustrated in Figure 5.3, the shallow-water class is easily separable from other wetland classes using all intensity features, as it has the lowest SAR backscattering response in all cases. This is because the dominant scattering mechanism for the shallow-water class is specular scattering, resulting in little to no SAR backscattering return for this class in three polarizations. All wetland classes have higher backscattering responses in  $\sigma_{HH}^0$ , given the high sensitivity of the HH-polarization signal to double-bounce scattering. This is particularly true for marsh, for which double-bounce scattering was potentially dominant given the optimum height of water level at the time of SAR data acquisition. Despite the greater responses in the HH-polarization signal, most wetland classes are not distinguishable from each other using this feature due to the high degree of overlap between some wetland classes, such as bog/fen and marsh/swamp. However, the classes of bog and fen are separable using  $\sigma_{VV}^0$ . This is because the dominant scattering mechanism for these classes is surface scattering and  $\sigma_{VV}^0$  is sensitive to this scattering mechanism. This

corroborates the results of past studies (e.g., [49], [74]), which concluded that surface scattering is an important contributor to the classification of bogs and fens. Overall,  $\sigma_{VV}^0$  is useful for distinguishing herbaceous wetland classes (i.e., bog, fen, and marsh) in this study. Notably, the swamp class is more effectively separated from other herbaceous wetland classes (especially bog and fen) using  $\sigma_{HV}^0$ , given the increased volume scattering and depolarization of the SAR signal in its canopies due to the multiple scattering mechanisms. Although volume scattering is dominant in swamps, double-bounce between trunks/branches and standing water could be present. This finding agrees with the results of previous studies, such as those appearing in [74]. Nevertheless, the capability of C-band data for mapping forested wetland is hindered by its shallow penetration depth, especially when the forest canopy is dense.

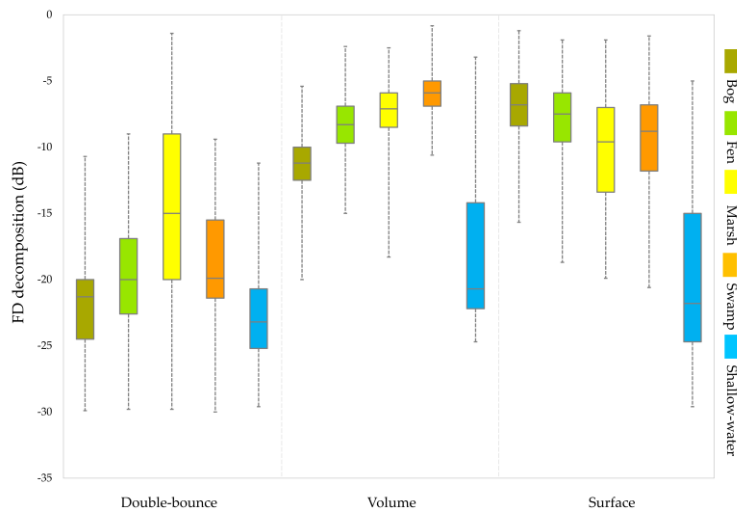


Figure 5.4. Box-and-whisker plots for extracted features from the Freeman-Durden decomposition for wetland classes obtained from the pixel values of the training data set.

As illustrated in Figure 5.4, double-bounce, volume, and surface scattering are the dominant scattering mechanisms for the marsh, swamp, and bog and fen classes, respectively. These contribute to distinguishing these classes from other wetland classes. For example, the marsh class

is separable from other wetland classes using the double-bounce scattering mechanism, whereas the volume scattering component of the Freeman-Durden decomposition is the most useful feature for discriminating swamps from other wetland classes. Shallow-water is distinguishable based on its dominant specular scattering mechanism, producing the lowest backscattering responses.

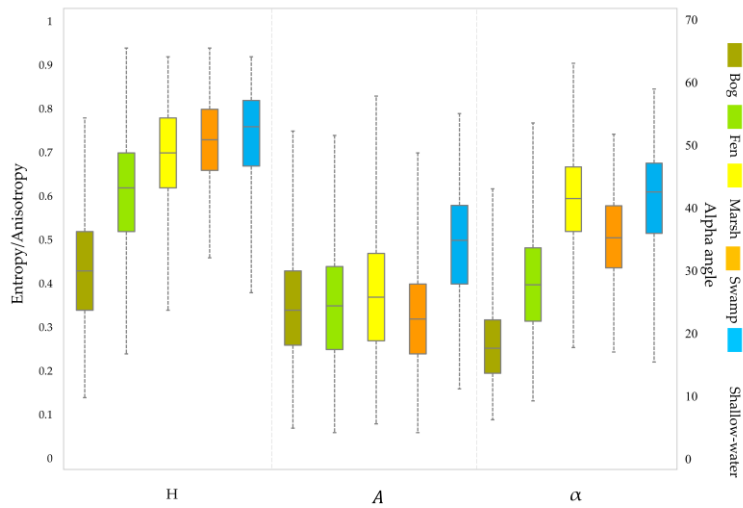


Figure 5.5. Box-and-whisker plots for extracted features from the Cloude-Pottier decomposition for wetland classes obtained from the pixel values of the training data set. Note: H: entropy, A: anisotropy, and  $\alpha$ : alpha angle.

As shown in Figure 5.5, the alpha angle ( $\alpha$ ) and, to a lesser extent, entropy (H) are useful for discriminating similar wetland classes. In particular, entropy is lowest for the bog class, illustrating a low degree of depolarization and randomness. This is characteristic of a relatively smooth surface. Other wetland classes have a relatively large entropy value, which indicates the presence of different scattering mechanisms. Although the dominant scattering mechanism for fens is surface scattering from the uniform grass, other scattering types could also be present. Notably, the bog class is distinguishable from other wetland classes using the entropy feature, but this feature is less useful for discriminating other wetland classes. However, the alpha angle is efficient

for discriminating various classes, especially herbaceous wetland classes. This is logical given that the alpha angle discriminates features according to their types of scattering mechanisms. As shown, the bog and fen classes have a low alpha angle, illustrating a dominant surface scattering mechanism. The swamp wetland is characterized by intermediate alpha values, indicating dominant volume scattering. The alpha angle for marshes mostly ranges from 40° to 50°, corresponding to a dominant double-bounce scattering mechanism. In contrast to the entropy and alpha angle, anisotropy is less useful for discriminating similar wetland classes. This is in line with the findings of other studies, such as [75], which reported a lower efficiency of the anisotropy feature for crop mapping.

#### 5.4.1.2. Compact Polarimetric SAR Data

Figures 5.6 to 5.8 depict box-and-whisker plots of various wetland classes extracted from the features of the CP SAR data.

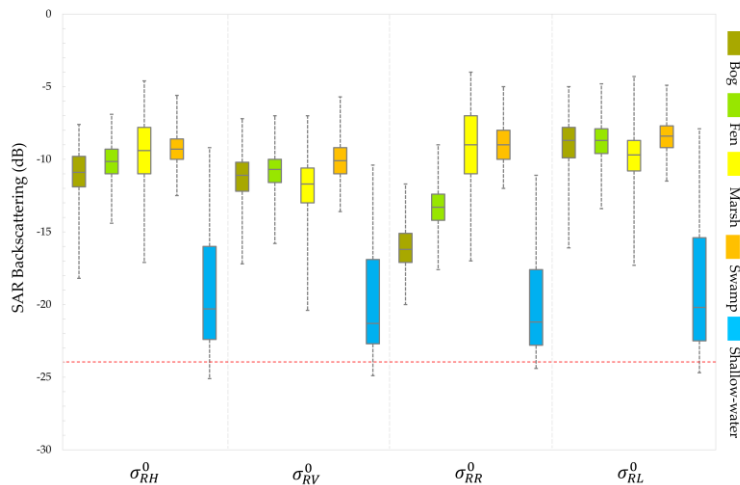


Figure 5.6. Box-and-whisker plots demonstrating the distribution of the SAR backscattering coefficients of CP SAR data for wetland classes obtained from the pixel values of the training data set. The red horizontal line highlights the nominal NESZ (-24 dB) of the RCM medium resolution mode.

As is the case for FP SAR data, the shallow-water class is distinct from other classes in all four polarizations.  $\sigma_{RR}^0$  exhibits clear advantages for classifying herbaceous wetland classes. It is also useful for discriminating swamps from bogs and fens. However, the two classes of swamp and marsh are not separable using  $\sigma_{RR}^0$ . These two classes are better distinguished using  $\sigma_{RV}^0$  and  $\sigma_{RL}^0$ ; however, confusion remains between them. Among wetland classes, only shallow-water has values below the noise floor of the RCM medium resolution mode (-24 dB; see the red horizontal line in Figure 6). All other wetland classes produce a backscattering response considerably higher than the nominal NESZ of the RCM medium resolution mode. Thus, the higher noise floor of RCM medium resolution CP SAR data is not problematic for wetland mapping, but may have some impacts on surface water mapping.

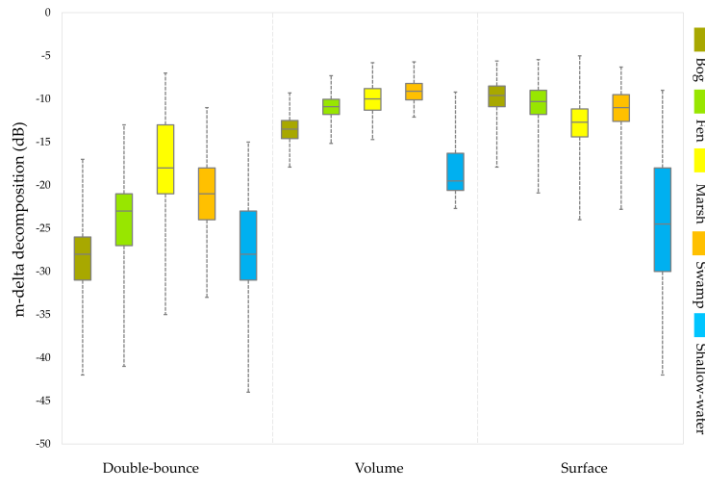


Figure 5.7. Box-and-whisker plots for extracted features from the m-delta decomposition for wetland classes obtained from the pixel values of the training data set.

A comparison between Figures 5.4 and 5.7 reveals that the backscattering responses of the wetland classes in the m-delta decomposition are very similar to those of the Freeman-Durden decomposition. In particular, the marsh and swamp classes are characterized by double-bounce

and volume scattering mechanisms, respectively. Surface scattering is, however, dominant for bogs and fens.

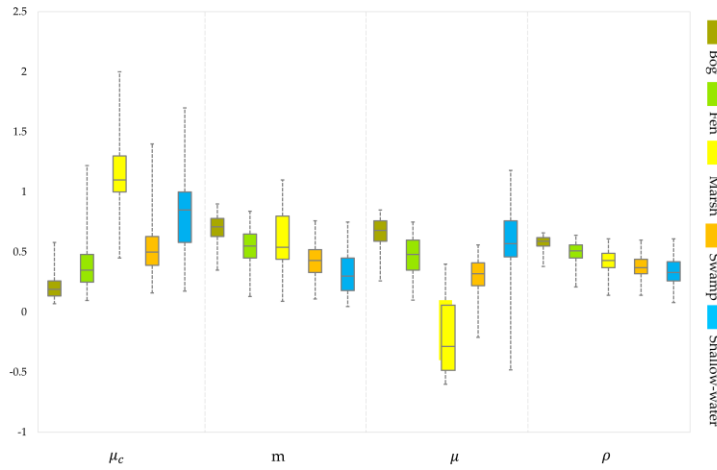


Figure 5.8. Box-and-whisker plots for extracted features from the CP SAR data for wetland classes obtained from pixel values of the training data set. Note:  $\mu_c$ : circular polarization ratio,  $m$ : degree of polarization,  $\mu$ : conformity coefficient, and  $\rho$ : correlation coefficient.

As shown in Figure 5.8, most of the features extracted from the CP SAR data are able to distinguish wetland classes. For example, the circular polarization ratio distinguishes marsh from all other classes. This feature is also useful for discriminating bogs from other wetland classes and fens from shallow-water. The degree of polarization is also useful in distinguishing bogs from other wetland classes, excluding the marsh class. This is because the degree of polarization for bogs tends to 1, indicating a relatively pure polarized wave. This is consistent with our observations from the Cloude-Pottier decomposition, wherein bogs had the lowest entropy and alpha angle, both of which indicate a relatively pure polarized wave. The conformity coefficient is also promising for separating all wetland vegetation classes. Likewise, the correlation coefficient is efficient for differing some wetland classes, for example, bogs from other wetland classes.

## 5.4.2. Separability Analysis

### 5.4.2.1. Full Polarimetric SAR Data

Figure 5.9 illustrates the separability between pairs of wetland classes from the FP SAR data using the K-S distance.

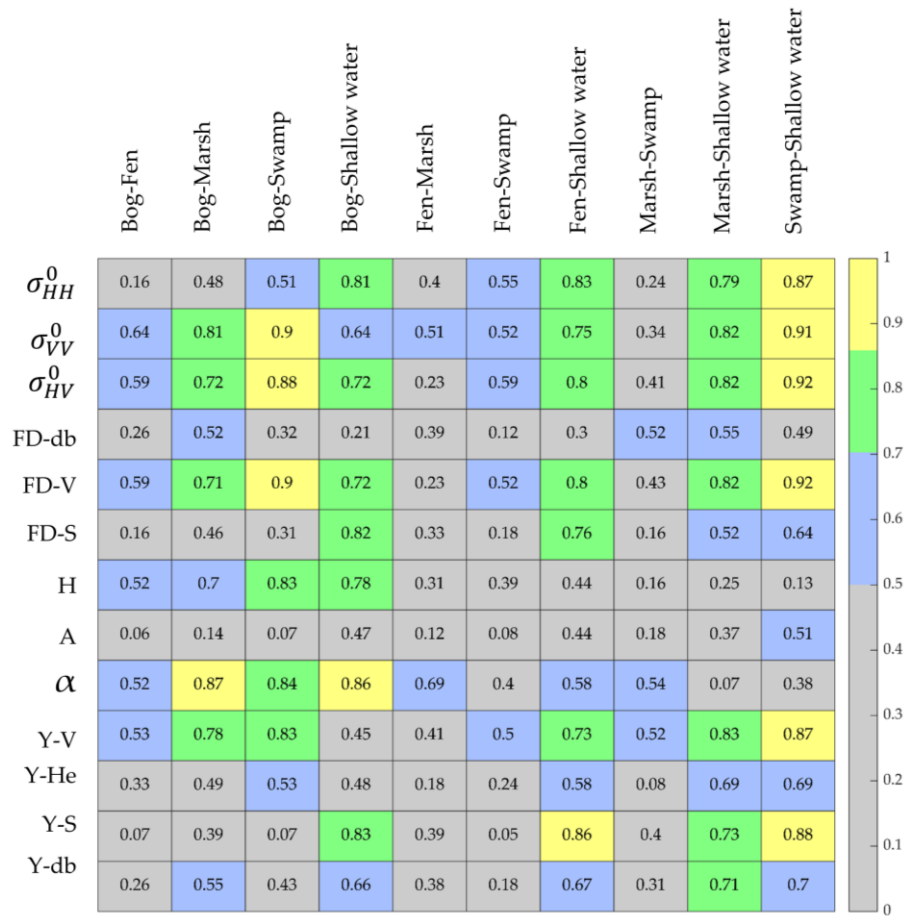


Figure 5.9. K-S distances between pairs of wetland classes using the extracted features from FP SAR data. Note that gray, blue, green, and yellow indicate poor, some, good, and excellent separability, respectively.

As expected, the shallow-water class is easily separable from most wetland classes, as several features represent good and excellent separability in this case (see the fourth, seventh, and last two columns in Figure 5.9). Bogs also are discernible from swamp and marsh, as several features

indicate either good or excellent separability between these classes. Thus, bog (excluding bog-fen) and shallow-water classes are distinguishable from other classes based on both backscattering analysis and the K-S distances. This is attributable to the dominance of a single scattering mechanism for these classes (i.e., surface scattering for bogs and specular scattering for shallow-water), which results in good or excellent separability using different SAR features.

Conversely, other wetland classes exhibit some degree of separability in the best case. For example, fen-marsh, fen-swamp, and marsh-swamp are separable using two, five, and three of 13 features, respectively, with some degree of separability (see the blue color for these pairs of wetland classes). Notably, the alpha angle is useful for discriminating fens and marshes (i.e., approaching good separability). However, there remains similarity between them, potentially due to their vegetation structures, such as sedge meadows and reeds, as has been previously reported [74]. Likewise, bogs and fens are also found to be hardly distinguishable using the FP SAR features, albeit with a greater number of features (six of 13 features with some degree of separability). Bogs and fens are both peatlands with very similar vegetation types, which are typically short vegetation with smooth canopies. This contributes to the similarity between these classes. Overall, the difficulty of discriminating these classes using C-band data has been reported in the literature [74]. The results of our separability analysis indicate that only the anisotropy feature of the Cloude-Pottier decomposition is not useful for wetland mapping. Accordingly, this feature was removed for classification in the following sections.

#### **5.4.2.2. Compact Polarimetric SAR Data**

The separability between pairs of wetland classes from the extracted features of the CP SAR data using the K-S distance is depicted in Figure 5.10.

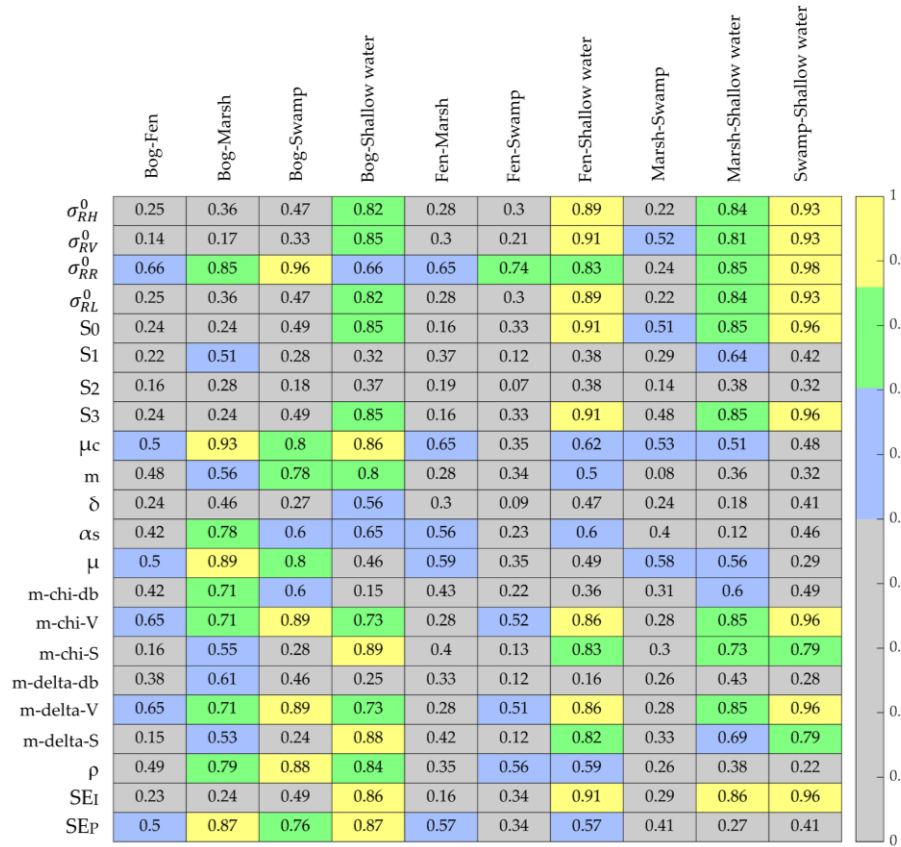


Figure 5.10. K-S distances between pairs of wetland classes using the features extracted from CP SAR data. See Table 5.3 for parameter description.

The K-S distance analysis of CP SAR features indicates relatively similar behavior as that of the FP SAR data. However, the number of more separable features is higher, given that 22 CP SAR features were examined in this case as compared to 13 features from the FP SAR data. Specifically, several features exhibit an excellent separability between shallow-water from other wetland classes ( $K - S > 0.85$ ). For example, the SAR backscattering coefficient features indicate either excellent or good separability between the shallow-water and other wetland classes, given the lowest backscattering responses were from shallow-water.

The two classes of bog and fen fall within either the poor separability class or some separability class (six of 22 features) using the CP SAR features. For example, the volumetric components of

m-chi and m-delta decompositions produce a K-S distance of 0.65. This finding may be explained by the fact that the dominant scattering mechanism for bogs is surface scattering, whereas fen may also produce volume scattering (see also Figure 5.7). Bog and marsh were distinguished using several CP features, with three of 22 features representing excellent separability, six of 22 features representing good separability, and five of 22 features representing some degree of separability. The discrimination between these classes is due to the fact that the dominant scattering mechanism for bogs is surface scattering as compared to dominant double-bounce scattering in marshes. This results in different responses for these two classes in several CP SAR features (see Figures 5.6-5.8), which contribute to discrimination between them. Likewise, bogs and swamps are also discernible using several CP features, with four of 22 features representing excellent separability, four of 22 features representing good separability, and two of 22 features representing some separability. The volumetric component of the m-chi and m-delta decompositions, as well as  $\sigma_{RR}^0$ , are among the most separable features between bogs and swamps, potentially due to the different dominant scattering mechanisms for these classes. As for the extracted features from the FP SAR data apart from a slight deviation, the separability between fen-marsh, fen-swamp, and marsh-swamp mostly falls into the class of some separability.

As shown in Figure 5.10, some CP SAR features are very promising for discriminating similar wetland classes. For example, intensity features, the first and last components of the Stokes vector, the circular polarization ratio, the volumetric components of the m-chi and m-delta decompositions, and the Shannon entropy features are among the most useful CP SAR features, as they exhibit an excellent separability between at least two pairs of wetland classes. Other studies also found that Shannon entropy was an important feature for wetland mapping, given its capability to discriminate saturated soils from unsaturated soils [76], as well as flooded vegetation from open

water [77]. This is further confirmed in this study, because the Shannon entropy intensity feature indicates an excellent separability between the shallow-water class and other wetland classes, as illustrated in Figure 5.10. Conversely, some features, such as the second and third components of the Stokes vector, as well as the relative phase were less useful because they poorly separated wetland classes in most cases. As such, these three features were removed from further analysis in the following sections.

### 5.4.3. Classification Results

Table 5.4 represents the overall accuracies and Kappa coefficients for three case studies using FP and CP SAR data. Overall, the results indicate the superiority of the FP SAR data compared to those of CP in the three case studies. In particular, an overall accuracy of 87.89%, 80.67%, and 84.07% were obtained from the CP SAR data for the Avalon, Deer Lake, and Gros Morne study areas, respectively. These indicated a decrease of about 2.8%, 4%, and 6.9% in overall accuracies for the Avalon, Deer Lake, and Gros Morne study areas, respectively, relative to the FP SAR data.

Table 5.4. The overall accuracies and Kappa coefficients obtained from FP and CP SAR data for the three case studies.

Case study	Type of data	Overall accuracy (%)	Kappa coefficient
Avalon	FP	90.73	0.88
	CP	87.89	0.85
Deer Lake	FP	84.75	0.81
	CP	80.67	0.77
Gros Morne	FP	90.93	0.88
	CP	84.07	0.80

The most accurate result using CP SAR data was obtained for the Avalon study area, as more training data were available for this site compared to the other two pilot sites (see Table 5.1). In

particular, more wetland sites were available for visitation in the Avalon area due to their proximity to public roads and, in particular, this area is close to the capital city, St John's. As such, significant effort was devoted to collecting *in-situ* data from this site, compared to those of other sites. Figures 5.11, 5.12, and 5.13 demonstrate the classified maps of the Avalon, Deer Lake, and Gros Morne study areas, respectively.

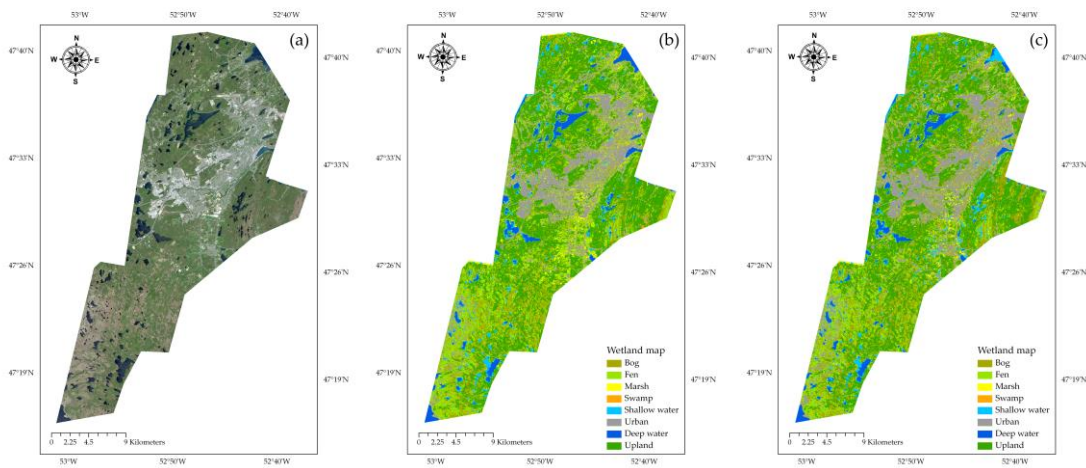


Figure 5.11. (a) A true color composite of RapidEye optical imagery (bands 3, 2, and 1) acquire on June 18, 2015. The classification maps of the Avalon study area obtained from (b) FP (OA: 90.73%, K: 0.88) and (c) simulated CP SAR data (OA: 87.89%, K: 0.85).

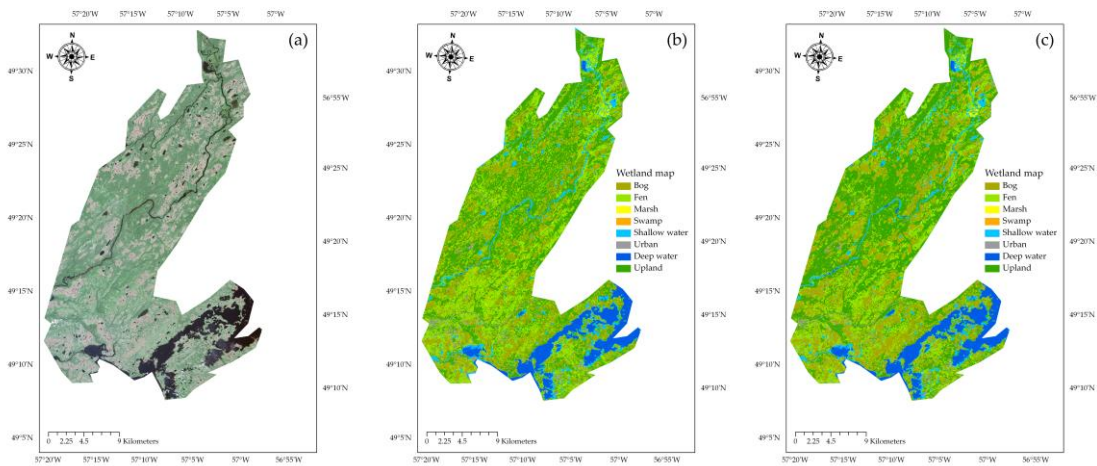


Figure 5.12. (a) A true color composite of RapidEye optical imagery (bands 3, 2, and 1) acquire on June 18, 2015. The classification maps of the Deer Lake study area obtained from (b) FP (OA: 84.75%, K: 0.81) and (c) simulated CP SAR data (OA: 80.67%, K: 0.77).

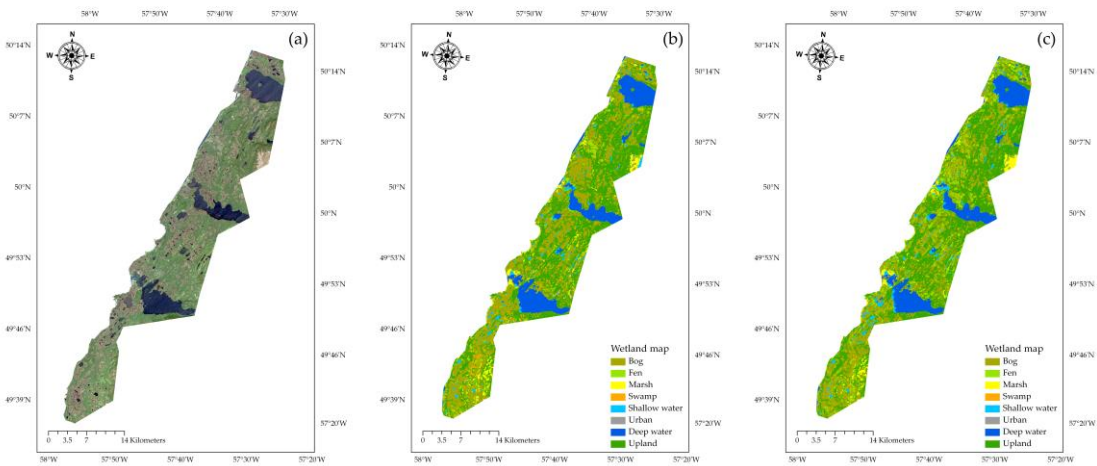


Figure 5.13. (a) A true color composite of RapidEye optical imagery (bands 3, 2, and 1) acquire on June 18, 2015. The classification maps of the Gros Morne study area obtained from (b) FP (OA: 90.93%, K: 0.88) and (c) simulated CP SAR data (OA: 84.07%, K: 0.80).

Overall, there is an agreement between the classification maps of FP and CP SAR data. Taking the Avalon area as an example (Figure 5.11(b),(c)), bog and fen are the most prevalent wetland classes in the two classified maps. This is in line with biologists' reports recorded during *in-situ* data collection. Furthermore, the dominance of urban areas in the center of the study area (capital city of St John's) was correctly identified in the two classification maps, and again this is in agreement with real world objects. This consistency also exists between the classification maps for Deer Lake and Gros Morne. Tables 5.5 and 5.6 represent the confusion matrices of the classification maps for the Avalon area.

Table 5.5. The confusion matrix of the Avalon classification map obtained from the FP SAR data. An overall accuracy of 90.73% and Kappa coefficient of 0.88 were achieved.

		Reference data									
		Bog	Fen	Marsh	Swamp	Shallow-water	Urban	Deep-water	Upland	Total	User Acc. (%)
Classified data	Bog	3659	139	68	142	0	52	0	459	4519	80.97
	Fen	442	1981	95	58	0	37	0	25	2638	75.09
	Marsh	122	44	809	33	71	55	7	49	1190	67.98
	Swamp	156	82	102	729	0	4	0	81	1154	63.17
	Shallow-water	3	2	171	0	1732	7	205	4	2124	81.54
	Urban	114	16	41	14	2	5777	0	5	5969	96.78
	Deep-water	2	0	0	0	54	0	8621	0	8677	99.35
	Upland	59	37	24	128	0	0	0	8122	8370	97.04
	Total	4557	2301	1310	1104	1859	5932	8833	8745	34641	
	Producer Acc. (%)	80.29	86.09	61.76	66.03	93.17	97.39	97.60	92.88		

Table 5.6. The confusion matrix of the Avalon classification map obtained from the CP SAR data. An overall accuracy of 87.89% and Kappa coefficient of 0.85 were achieved.

		Reference data									User Acc. (%)
		Bog	Fen	Marsh	Swamp	Shallow-water	Urban	Deep-water	Upland	Total	
Classified data	Bog	3278	317	23	105	0	43	0	165	3931	83.39
	Fen	524	1629	78	111	2	79	1	202	2626	62.03
	Marsh	163	149	946	53	88	63	0	18	1480	63.92
	Swamp	182	142	47	723	0	57	0	34	1185	61.01
	Shallow-water	6	2	118	0	1588	12	392	3	2121	74.87
	Urban	247	51	51	7	2	5539	0	6	5903	93.83
	Deep-water	0	0	0	0	175	0	8440	0	8615	97.97
	Upland	157	11	47	105	4	139	0	8317	8780	94.73
	Total	4557	2301	1310	1104	1859	5932	8833	8745	34641	
	Producer Acc. (%)	71.93	70.8	72.21	65.49	85.42	93.47	95.55	95.11		

Although both FP and CP SAR data successfully classify the non-wetland classes with user and producer's accuracies exceeding 92%, FP SAR data are advantageous for wetland classes in most cases. Specifically, an overall accuracy of 90.73% was obtained using the FP SAR data, with bogs correctly classified in 80.29% of cases, fens in 86.09%, marshes in 61.76%, swamps in 66.03%, and shallow-water in 93.17% of cases. These demonstrate an improvement of about 2.8% in terms of overall accuracy, as well as 8.4%, 15.3%, 0.5%, and 7.7% improvements in terms of producer's accuracies for bogs, fens, swamps, and shallow-water, respectively, compared to those of the CP SAR data. Interestingly, marshes were better distinguished using CP SAR data relative to the FP SAR data, demonstrating an improvement of about 10.4% in terms of producer's accuracy.

Among wetland classes, the highest producer's accuracy was obtained for shallow-water. This is in line with results of the backscattering and separability analyses, both of which demonstrated

that shallow-water is easily separable from other wetland classes. Furthermore, bogs were classified with relatively acceptable accuracies in most cases. This further supports the findings of the backscattering and separability analyses, which indicated bogs are distinguishable from other wetland classes. In particular, the K-S distance revealed that bogs are most separable from marsh, swamp, and shallow-water with K-S distances exceeding 0.7 using several features. However, there was similarity between bogs and fens according to the separability analysis because they had a K-S distance up to 0.7. This latter observation is also in agreement with the confusion matrix, as a high confusion error exists between bogs and fens.

The producer's accuracies are lower for swamp, as well as marsh (only for FP SAR data) compared to those of other classes. This is relatively in line with the results of the backscattering and separability analyses. For example, the two classes of marsh and swamp were found to be hardly distinguished from other wetland classes according to the backscattering analysis. This is further supported by the confusion matrix, as these classes had the lowest accuracies in most cases. This could be attributed to the lower amount of training data for the swamp and marsh compared to those of other classes. Note that these two classes had training polygons with the small sizes compared to other wetland classes (e.g., bog). This is because of the natural ecological characteristics of NL wetlands and its cool and moist climate, which contribute to extensive peatland formation (i.e., bog and fen). Accordingly, bogs and fens are more frequently visited during *in-situ* data collection and are easily spotted during interpretation of the aerial and satellite imagery. This resulted in the production of large and homogeneous training polygons for these classes. Conversely, swamps are usually inaccessible and hardly distinguishable using visual interpretation of satellite imagery. They also exist in physically small areas, such as in transition

zones between a wetland and another land cover class. This resulted in the production of small size training polygons for this class.

## **5.5. Conclusions**

The spatial distribution of wetlands is of particular interest for the sustainable management of this important, productive ecosystem. In this study, the capability of full and simulated compact polarimetric (FP and CP) SAR data for wetland mapping was investigated in three pilot sites in Newfoundland and Labrador, Canada. A total of 13 FP and 22 simulated CP SAR features were extracted to identify the discrimination capability of these features between pairs of wetland classes both qualitatively, using backscattering analysis, and quantitatively, using the two-sample Kolmogorov-Smirnov (K-S) distance measurement. The most useful features were then identified and incorporated into the subsequent classification scheme.

Among wetland classes, bog and shallow-water were found to be easily distinguished according to both the backscattering analysis and the K-S distance. Several features indicated either good or excellent separability between pairs of shallow-water-other classes and bog-other classes. Among FP features, backscattering intensity features, the Cloude-Pottier alpha angle, the volumetric components of the Freeman-Durden and Yamaguchi decompositions, as well as the surface scattering component of Yamaguchi decomposition were useful, as they indicated an excellent separability ( $K - S > 0.85$ ) between at least one pair of wetland classes. With regard to the CP SAR features, SAR backscattering coefficients, the first and last components of the Stokes vector, the circular polarization ratio, conformity coefficient, correlation coefficient, Shannon entropy, and both volume and surface scattering components of the m-chi and m-delta decompositions were useful features.

The overall accuracies of 87.89%, 80.67%, and 84.07% were obtained from the CP SAR data for the Avalon, Deer Lake, and Gros Morne study areas, respectively. The overall accuracies obtained from the FP SAR data were 90.73%, 84.75%, and 90.93% for the Avalon, Deer Lake, and Gros Morne study areas, respectively, which were higher than those of CP. Although the classification results demonstrated the superiority of FP SAR data compared to that of CP, the latter remains advantageous. This is because CP SAR data, which will be collected by RCM, will have a wider swath coverage and improved temporal resolution compared to those of RADARSAT-2. This is of great significance for efficiently mapping phenomena with highly dynamic natures (e.g., wetlands) on a large scale. Thus, the results of this research suggest that CP SAR data available on RCM hold great promise for discriminating conventional Canadian wetland classes. The analysis presented in this study contributes to further scientific research for wetland mapping and serves as a predecessor study for RCM, which will soon be the primary source of SAR observations in Canada.

## 5.6. References

- [1] R. C. Gardner and N. C. Davidson, "The Ramsar convention," in *Wetlands*, Springer, 2011, pp. 189–203.
- [2] W. J. Mitsch *et al.*, "Wetlands, carbon, and climate change," *Landsc. Ecol.*, vol. 28, no. 4, pp. 583–597, 2013.
- [3] R. W. Tiner, M. W. Lang, and V. V. Klemas, *Remote sensing of wetlands: applications and advances*. CRC press, 2015.
- [4] A. L. Gallant, "The challenges of remote monitoring of wetlands." Multidisciplinary Digital Publishing Institute, 2015.
- [5] M. Mahdianpari, B. Salehi, M. Rezaee, F. Mohammadimanesh, and Y. Zhang, "Very Deep Convolutional Neural Networks for Complex Land Cover Mapping Using Multispectral Remote Sensing Imagery," *Remote Sens.*, vol. 10, no. 7, p. 1119, 2018.
- [6] M. Rezaee, M. Mahdianpari, Y. Zhang, and B. Salehi, "Deep Convolutional Neural Network for Complex Wetland Classification Using Optical Remote Sensing Imagery," *IEEE J. Sel. Top. Appl. Earth Obs. Remote Sens.*, no. 99, 2018.

- [7] J.-S. Lee and E. Pottier, *Polarimetric radar imaging: from basics to applications*. CRC press, 2009.
- [8] F. M. Henderson and A. J. Lewis, “Radar detection of wetland ecosystems: a review,” *Int. J. Remote Sens.*, vol. 29, no. 20, pp. 5809–5835, 2008.
- [9] B. Brisco, “Mapping and monitoring surface water and wetlands with synthetic aperture radar,” *Remote Sens. Wetl. Appl. Adv.*, pp. 119–136, 2015.
- [10] A. S. Arnesen *et al.*, “Monitoring flood extent in the lower Amazon River floodplain using ALOS/PALSAR ScanSAR images,” *Remote Sens. Environ.*, vol. 130, pp. 51–61, 2013.
- [11] J.-M. Martinez and T. Le Toan, “Mapping of flood dynamics and spatial distribution of vegetation in the Amazon floodplain using multitemporal SAR data,” *Remote Sens. Environ.*, vol. 108, no. 3, pp. 209–223, 2007.
- [12] D. P. Ward *et al.*, “Floodplain inundation and vegetation dynamics in the Alligator Rivers region (Kakadu) of northern Australia assessed using optical and radar remote sensing,” *Remote Sens. Environ.*, vol. 147, pp. 43–55, 2014.
- [13] L.-M. Rebelo, “Eco-hydrological characterization of inland wetlands in Africa using L-band SAR,” *IEEE J. Sel. Top. Appl. Earth Obs. Remote Sens.*, vol. 3, no. 4, pp. 554–559, 2010.
- [14] E. S. Kasischke and L. L. Bourgeau-Chavez, “Monitoring South Florida wetlands using ERS-1 SAR imagery,” *Photogramm. Eng. Remote Sensing*, vol. 63, no. 3, pp. 281–291, 1997.
- [15] M. G. Parmuchi, H. Karszenbaum, and P. Kandus, “Mapping wetlands using multi-temporal RADARSAT-1 data and a decision-based classifier,” *Can. J. Remote Sens.*, vol. 28, no. 2, pp. 175–186, 2002.
- [16] R. Touzi, A. Deschamps, and G. Rother, “Wetland characterization using polarimetric RADARSAT-2 capability,” *Can. J. Remote Sens.*, 2007.
- [17] M. Mahdianpari *et al.*, “Fisher Linear Discriminant Analysis of coherency matrix for wetland classification using PolSAR imagery,” *Remote Sens. Environ.*, vol. 206, pp. 300–317, 2018.
- [18] C. Cazals *et al.*, “Mapping and characterization of hydrological dynamics in a coastal marsh using high temporal resolution Sentinel-1A images,” *Remote Sens.*, vol. 8, no. 7, p. 570, 2016.
- [19] C. Wohlfart, K. Winkler, A. Wendleder, and A. Roth, “TerraSAR-X and Wetlands: A Review,” *Remote Sens.*, vol. 10, no. 6, p. 916, 2018.
- [20] F. Mohammadimanesh, B. Salehi, M. Mahdianpari, M. Motagh, and B. Brisco, “An efficient feature optimization for wetland mapping by synergistic use of SAR intensity, interferometry, and polarimetry data,” *Int. J. Appl. Earth Obs. Geoinf.*, vol. 73, pp. 450–462, 2018.
- [21] E. W. RAMSEY III, “Radar remote sensing of wetlands,” *Remote Sens. Chang. Detect.*, 1999.
- [22] F. Mohammadimanesh, B. Salehi, M. Mahdianpari, B. Brisco, and M. Motagh, “Wetland water level monitoring using interferometric synthetic aperture radar (InSAR): A review,” *Can. J. Remote Sens.*, pp. 1–16, 2018.
- [23] J.-W. Kim, Z. Lu, J. W. Jones, C. K. Shum, H. Lee, and Y. Jia, “Monitoring Everglades freshwater

- marsh water level using L-band synthetic aperture radar backscatter,” *Remote Sens. Environ.*, vol. 150, pp. 66–81, 2014.
- [24] Z. Lu and O. Kwoun, “Radarsat-1 and ERS InSAR analysis over southeastern coastal Louisiana: Implications for mapping water-level changes beneath swamp forests,” *IEEE Trans. Geosci. Remote Sens.*, vol. 46, no. 8, pp. 2167–2184, 2008.
- [25] T. Yuan, H. Lee, and H. C. Jung, “Toward estimating wetland water level changes based on hydrological sensitivity analysis of PALSAR backscattering coefficients over different vegetation fields,” *Remote Sens.*, vol. 7, no. 3, pp. 3153–3183, 2015.
- [26] H. Lee, T. Yuan, H. C. Jung, and E. Beighley, “Mapping wetland water depths over the central Congo Basin using PALSAR ScanSAR, Envisat altimetry, and MODIS VCF data,” *Remote Sens. Environ.*, vol. 159, pp. 70–79, 2015.
- [27] L. F. de Almeida Furtado, T. S. F. Silva, and E. M. L. de Moraes Novo, “Dual-season and full-polarimetric C band SAR assessment for vegetation mapping in the Amazon várzea wetlands,” *Remote Sens. Environ.*, vol. 174, pp. 212–222, 2016.
- [28] R. K. Raney, J. T. S. Cahill, G. Patterson, and D. B. J. Bussey, “The m-chi decomposition of hybrid dual-polarimetric radar data with application to lunar craters,” *J. Geophys. Res. Planets*, vol. 117, no. E12, 2012.
- [29] M. Mahdianpari, B. Salehi, F. Mohammadimanesh, and B. Brisco, “An Assessment of Simulated Compact Polarimetric SAR Data for Wetland Classification Using Random Forest Algorithm,” *Can. J. Remote Sens.*, vol. 43, no. 5, 2017.
- [30] Y. Chen, X. He, J. Wang, and R. Xiao, “The influence of polarimetric parameters and an object-based approach on land cover classification in coastal wetlands,” *Remote Sens.*, vol. 6, no. 12, pp. 12575–12592, 2014.
- [31] S. van Beijma, A. Comber, and A. Lamb, “Random forest classification of salt marsh vegetation habitats using quad-polarimetric airborne SAR, elevation and optical RS data,” *Remote Sens. Environ.*, vol. 149, pp. 118–129, 2014.
- [32] M. W. Lang, E. S. Kasischke, S. D. Prince, and K. W. Pittman, “Assessment of C-band synthetic aperture radar data for mapping and monitoring Coastal Plain forested wetlands in the Mid-Atlantic Region, USA,” *Remote Sens. Environ.*, vol. 112, no. 11, pp. 4120–4130, 2008.
- [33] M. Mahdianpari, B. Salehi, F. Mohammadimanesh, and M. Motagh, “Random forest wetland classification using ALOS-2 L-band, RADARSAT-2 C-band, and TerraSAR-X imagery,” *ISPRS J. Photogramm. Remote Sens.*, vol. 130, 2017.
- [34] W. Zhang *et al.*, “Compact Polarimetric Response of Rape (*Brassica napus* L.) at C-Band: Analysis and Growth Parameters Inversion,” *Remote Sens.*, vol. 9, no. 6, p. 591, 2017.
- [35] M. Dabboor, B. Montpetit, and S. Howell, “Assessment of the High Resolution SAR Mode of the RADARSAT Constellation Mission for First Year Ice and Multiyear Ice Characterization,” *Remote Sens.*, vol. 10, no. 4, p. 594, 2018.
- [36] R. Torres *et al.*, “GMES Sentinel-1 mission,” *Remote Sens. Environ.*, vol. 120, pp. 9–24, 2012.

- [37] J. Aschbacher and M. P. Milagro-Pérez, “The European Earth monitoring (GMES) programme: Status and perspectives,” *Remote Sens. Environ.*, vol. 120, pp. 3–8, 2012.
- [38] M. Mahdianpari, B. Salehi, F. Mohammadimanesh, S. Homayouni, and E. Gill, “The First Wetland Inventory Map of Newfoundland at a Spatial Resolution of 10 m Using Sentinel-1 and Sentinel-2 Data on the Google Earth Engine Cloud Computing Platform,” *Remote Sens.*, vol. 11, no. 1, p. 43, 2019.
- [39] W. Tan, J. Li, L. Xu, and M. A. Chapman, “Semiautomated Segmentation of Sentinel-1 SAR Imagery for Mapping Sea Ice in Labrador Coast,” *IEEE J. Sel. Top. Appl. Earth Obs. Remote Sens.*, vol. 11, no. 5, pp. 1419–1432, 2018.
- [40] K. Van Tricht, A. Gobin, S. Gilliams, and I. Piccard, “Synergistic use of radar Sentinel-1 and optical Sentinel-2 imagery for crop mapping: a case study for Belgium,” *Remote Sens.*, vol. 10, no. 10, p. 1642, 2018.
- [41] M. M. Espeseth, C. Brekke, and A. M. Johansson, “Assessment of RISAT-1 and Radarsat-2 for sea ice observations from a hybrid-polarity perspective,” *Remote Sens.*, vol. 9, no. 11, p. 1088, 2017.
- [42] R. K. Raney, “Hybrid-polarity SAR architecture,” *IEEE Trans. Geosci. Remote Sens.*, vol. 45, no. 11, pp. 3397–3404, 2007.
- [43] A. A. Thompson\*, “Overview of the RADARSAT constellation mission,” *Can. J. Remote Sens.*, vol. 41, no. 5, pp. 401–407, 2015.
- [44] S. Banks *et al.*, “Contributions of Actual and Simulated Satellite SAR Data for Substrate Type Differentiation and Shoreline Mapping in the Canadian Arctic,” *Remote Sens.*, vol. 9, no. 12, p. 1206, 2017.
- [45] F. J. Charbonneau *et al.*, “Compact polarimetry overview and applications assessment,” *Can. J. Remote Sens.*, vol. 36, no. sup2, pp. S298–S315, 2010.
- [46] S. Singha and R. Ressel, “Arctic sea ice characterization using RISAT-1 compact-pol SAR imagery and feature evaluation: A case study over Northeast Greenland,” *IEEE J. Sel. Top. Appl. Earth Obs. Remote Sens.*, vol. 10, no. 8, pp. 3504–3514, 2017.
- [47] M. Dabboor and T. Geldsetzer, “Towards sea ice classification using simulated RADARSAT Constellation Mission compact polarimetric SAR imagery,” *Remote Sens. Environ.*, vol. 140, pp. 189–195, 2014.
- [48] B. Brisco, K. Li, B. Tedford, F. Charbonneau, S. Yun, and K. Murnaghan, “Compact polarimetry assessment for rice and wetland mapping,” *Int. J. Remote Sens.*, vol. 34, no. 6, pp. 1949–1964, 2013.
- [49] L. White, K. Millard, S. Banks, M. Richardson, J. Pasher, and J. Duffe, “Moving to the RADARSAT constellation mission: Comparing synthesized compact polarimetry and dual polarimetry data with fully polarimetric RADARSAT-2 data for image classification of peatlands,” *Remote Sens.*, vol. 9, no. 6, p. 573, 2017.
- [50] I. B. Marshall, P. Schut, and M. Ballard, “A national ecological framework for Canada: attribute data. Environmental quality branch, Ecosystems Science Directorate, Environment Canada and Research Branch,” *Agric. Agri-Food Canada, Ottawa*, 1999.

- [51] F. Mohammadimanesh, B. Salehi, M. Mahdianpari, B. Brisco, and M. Motagh, "Multi-temporal, multi-frequency, and multi-polarization coherence and SAR backscatter analysis of wetlands," *ISPRS J. Photogramm. Remote Sens.*, vol. 142, pp. 78–93, 2018.
- [52] S.-W. Kim, S. Wdowinski, F. Amelung, T. H. Dixon, and J.-S. Won, "Interferometric coherence analysis of the Everglades wetlands, South Florida," *IEEE Trans. Geosci. Remote Sens.*, vol. 51, no. 12, pp. 5210–5224, 2013.
- [53] M. Mahdianpari, B. Salehi, and F. Mohammadimanesh, "The Effect of PolSAR Image De-speckling on Wetland Classification: Introducing a New Adaptive Method," *Can. J. Remote Sens.*, vol. 43, no. 5, 2017.
- [54] T. Toutin and P. Cheng, "Demystification of IKONOS," *Earth Obs. Mag.*, vol. 9, no. 7, pp. 17–21, 2000.
- [55] L. Zhang, X. He, T. Balz, X. Wei, and M. Liao, "Rational function modeling for spaceborne SAR datasets," *ISPRS J. Photogramm. Remote Sens.*, vol. 66, no. 1, pp. 133–145, 2011.
- [56] N. Baghdadi, M. Bernier, R. Gauthier, and I. Neeson, "Evaluation of C-band SAR data for wetlands mapping," *Int. J. Remote Sens.*, vol. 22, no. 1, pp. 71–88, 2001.
- [57] S. Paloscia, S. Pettinato, E. Santi, C. Notarnicola, L. Pasolli, and A. Reppucci, "Soil moisture mapping using Sentinel-1 images: Algorithm and preliminary validation," *Remote Sens. Environ.*, vol. 134, pp. 234–248, 2013.
- [58] Q. Gao, M. Zribi, M. J. Escorihuela, and N. Baghdadi, "Synergetic use of Sentinel-1 and Sentinel-2 data for soil moisture mapping at 100 m resolution," *Sensors*, vol. 17, no. 9, p. 1966, 2017.
- [59] S. R. Cloude and E. Pottier, "An entropy based classification scheme for land applications of polarimetric SAR," *IEEE Trans. Geosci. Remote Sens.*, vol. 35, no. 1, pp. 68–78, 1997.
- [60] A. Freeman and S. L. Durden, "A three-component scattering model for polarimetric SAR data," *IEEE Trans. Geosci. Remote Sens.*, vol. 36, no. 3, pp. 963–973, 1998.
- [61] Y. Yamaguchi, T. Moriyama, M. Ishido, and H. Yamada, "Four-component scattering model for polarimetric SAR image decomposition," *IEEE Trans. Geosci. Remote Sens.*, vol. 43, no. 8, pp. 1699–1706, 2005.
- [62] J. D. Ballester-Berman and J. M. Lopez-Sanchez, "Time series of hybrid-polarity parameters over agricultural crops," *IEEE Geosci. Remote Sens. Lett.*, vol. 9, no. 1, pp. 139–143, 2012.
- [63] S. R. Cloude, D. G. Goodenough, and H. Chen, "Compact decomposition theory," *IEEE Geosci. Remote Sens. Lett.*, vol. 9, no. 1, pp. 28–32, 2012.
- [64] M.-L. Truong-Loi, A. Freeman, P. C. Dubois-Fernandez, and E. Pottier, "Estimation of soil moisture and Faraday rotation from bare surfaces using compact polarimetry," *IEEE Trans. Geosci. Remote Sens.*, vol. 47, no. 11, pp. 3608–3615, 2009.
- [65] C. Marechal, E. Pottier, L. Hubert-Moy, and S. Rapinel, "One year wetland survey investigations from quad-pol RADARSAT-2 time-series SAR images," *Can. J. Remote Sens.*, vol. 38, no. 3, pp. 240–252, 2012.

- [66] T. Geldsetzer, M. Arkett, T. Zagon, F. Charbonneau, J. J. Yackel, and R. K. Scharien, “All-season compact-polarimetry C-band SAR observations of sea ice,” *Can. J. Remote Sens.*, vol. 41, no. 5, pp. 485–504, 2015.
- [67] F. J. Massey Jr, “The Kolmogorov-Smirnov test for goodness of fit,” *J. Am. Stat. Assoc.*, vol. 46, no. 253, pp. 68–78, 1951.
- [68] T. Blaschke, “Object based image analysis for remote sensing,” *ISPRS J. Photogramm. Remote Sens.*, vol. 65, no. 1, pp. 2–16, 2010.
- [69] L. Breiman, “Random forests,” *Mach. Learn.*, vol. 45, no. 1, pp. 5–32, 2001.
- [70] M. Belgiu and L. Drăguț, “Random forest in remote sensing: A review of applications and future directions,” *ISPRS J. Photogramm. Remote Sens.*, vol. 114, pp. 24–31, 2016.
- [71] M. Mahdianpari, B. Salehi, F. Mohammadimanesh, G. Larsen, and D. R. Peddle, “Mapping land-based oil spills using high spatial resolution unmanned aerial vehicle imagery and electromagnetic induction survey data,” *J. Appl. Remote Sens.*, vol. 12, no. 3, p. 036015, 2018.
- [72] F. Mohammadimanesh, B. Salehi, M. Mahdianpari, J. English, J. Chamberland, and P.-J. Alasset, “Monitoring surface changes in discontinuous permafrost terrain using small baseline SAR interferometry, object-based classification, and geological features: a case study from Mayo, Yukon Territory, Canada,” *GIScience Remote Sens.*, pp. 1–26, 2018.
- [73] R. G. Congalton, “A review of assessing the accuracy of classifications of remotely sensed data,” *Remote Sens. Environ.*, vol. 37, no. 1, pp. 35–46, 1991.
- [74] L. Dingle Robertson, D. J. King, and C. Davies, “Object-based image analysis of optical and radar variables for wetland evaluation,” *Int. J. Remote Sens.*, vol. 36, no. 23, pp. 5811–5841, 2015.
- [75] H. McNairn, J. Shang, X. Jiao, and C. Champagne, “The contribution of ALOS PALSAR multipolarization and polarimetric data to crop classification,” *IEEE Trans. Geosci. Remote Sens.*, vol. 47, no. 12, pp. 3981–3992, 2009.
- [76] L. White, A. Landon, M. Dabboor, A. Pratt, and B. Brisco, “Mapping and monitoring flooded vegetation and soil moisture using simulated compact polarimetry,” in *Geoscience and Remote Sensing Symposium (IGARSS), 2014 IEEE International*, 2014, pp. 1568–1571.
- [77] M. Dabboor and B. Brisco, “Wetland Monitoring Using Synthetic Aperture Radar Imagery,” in *Wetlands*, IntechOpen, 2018.

## Chapter 6. Fully Convolutional Network (FCN) for wetland classification<sup>5</sup>

### Preface

A version of this manuscript is published in the *ISPRS journal of photogrammetry and remote sensing*. I am a primary author of this manuscript along with the co-authors, Bahram Salehi, Masoud Mahdianpari, Eric Gill, and Matthieu Molinier. I and the co-author, Masoud Mahdianpari, conceptualized and designed the study. I developed the model and performed all experiments and tests. I wrote the paper and revised it based on comments from all co-authors. I also revised the paper according to the reviewers' comments. The co-author, Masoud Mahdianpari helped in performing the experiments and analyzing the results and contributed to revising the manuscript. All co-authors provided editorial input and scientific insights to further improve the paper. They also reviewed and commented on the manuscript.

### Abstract

Despite the application of state-of-the-art fully Convolutional Neural Networks (CNNs) for semantic segmentation of very high-resolution optical imagery, their capacity has not yet been thoroughly examined for the classification of Synthetic Aperture Radar (SAR) images. The presence of speckle noise, the absence of efficient feature expression, and the limited availability of labeled SAR samples have hindered the application of the state-of-the-art CNNs for the classification of SAR imagery. This is of great concern for mapping complex land cover ecosystems, such as wetlands, where backscattering/spectrally similar signatures of land cover units further complicate the matter. Accordingly, we propose a new Fully Convolutional Network

---

<sup>5</sup> Mohammadimanesh, F., Salehi, B., Mahdianpari, M., Gill, E. and Molinier, M., 2019. A new fully convolutional neural network for semantic segmentation of polarimetric SAR imagery in complex land cover ecosystem. *ISPRS Journal of Photogrammetry and Remote Sensing*, 151, pp.223-236.

(FCN) architecture that can be trained in an end-to-end scheme and is specifically designed for the classification of wetland complexes using polarimetric SAR (PolSAR) imagery. The proposed architecture follows an encoder-decoder paradigm, wherein the input data are fed into a stack of convolutional filters (encoder) to extract high-level abstract features and a stack of transposed convolutional filters (decoder) to gradually up-sample the low resolution output to the spatial resolution of the original input image. The proposed network also benefits from recent advances in CNN designs, namely the addition of inception modules and skip connections with residual units. The former component improves multi-scale inference and enriches contextual information, while the latter contributes to the recovery of more detailed information and simplifies optimization. Moreover, an in-depth investigation of the learned features via opening the *black box* demonstrates that convolutional filters extract discriminative polarimetric features, thus mitigating the limitation of the feature engineering design in PolSAR image processing. Experimental results from full polarimetric RADARSAT-2 imagery illustrate that the proposed network outperforms the conventional random forest classifier and the state-of-the-art FCNs, such as FCN-32s, FCN-16s, FCN-8s, and SegNet, both visually and numerically for wetland mapping.

**Keywords:** Deep Learning, land cover, wetland, Convolutional Neural Network (CNN), Fully Convolutional Network (FCN), encoder-decoder, Polarimetric Synthetic Aperture Radar (PolSAR).

## 6.1. Introduction

Semantic segmentation, also known as land cover classification in remote sensing, is the process of assigning a pre-designed label to each pixel of an image. This is a fundamental methodology to provide pixel-based output maps that are needed in many remote sensing applications [1]. K-means, minimum distance, maximum likelihood, and logistic regression are among the traditional

methods for semantic segmentation [2]. The main limitations of these algorithms are their dependency on the distribution of input data and their inefficiency in dealing with a large number of input features. Some machine learning tools, such as Support Vector Machine (SVM) and Random Forest (RF), address the limitations of traditional algorithms and have been successful in solving several pixel-based classification problems [3], [4]

Despite the potential of conventional machine learning tools (e.g., SVM and RF), the labelling accuracy of complex land cover units, such as wetlands and sea ice, provided by such tools is still less than adequate [5]. For example, wetlands are characterized by high intra- and low inter-class variance due to the juxtaposition of a mixture of backscattering/spectrally similar vegetation types. This poses challenges to conventional machine learning tools when relying on the exclusive use of backscatter/spectral information for the semantic segmentation of spectrally similar land cover classes [6]. This is of great concern for classification of Synthetic Aperture Radar (SAR) and polarimetric SAR (PolSAR) images, wherein pixels are polluted by speckle noise that affects the performance of pixel-based polarimetric decomposition features [7]. In such a case, the image texture contains a large amount of semantic information compared to that provided by the individual pixel intensity. Thus, there has been a growing interest in the extraction of spatial and textural features from the raw image to explicitly distinguishing land-cover units [8]–[10].

Notably, conventional machine learning tools mainly focus on mitigating ambiguity within backscattering/spectrally similar land cover classes by enhancing semantic information via a large number of input features. The process of extracting features is laborious and requires careful engineering design and significant domain expertise. This is because the efficiency of each feature in a particular problem is unknown *a priori* [11]. Furthermore, these hand-crafted, low-level features have an inferior capability to discriminate complex land cover units and for generalization.

The latter means that these low-level features are site- and data-dependent and, while they work well for a particular problem, they are less efficient in many other cases.

Inspired by the great potential of human brains for object recognition, Deep Learning (DL) has drawn attention within the remote sensing community. The popularity of applying DL methods is attributed to both their deep multilayer structure, allowing extraction of robust, invariant, and high-level features of data, and to their end-to-end training scheme [11]. This means that they have the capability to learn a series of abstract hierarchical features from raw input data and to provide a final, task-specific output, thus removing heuristic feature design. This is advantageous relative to shallow-structured machine learning tools (e.g., SVM and RF), which incorporate only the low-level features of data into the semantic labelling scheme.

Deep Convolutional Neural Networks (CNNs) are the most well-known DL methods for image processing tasks (e.g., supervised classification), as they are well-aligned with the intrinsic 2-D structure of remote sensing images [12]. In particular, CNNs are capable of extracting contextual, high-level 2-D spatial features by employing a hierarchy of convolutional filters using multiple nonlinear transformations [13]. Notably, CNNs have led to tremendous success in several remote sensing tasks, such as scene classification [10], object (e.g., vehicle) detection [14], [15], and image classification [16], [17] using optical remote sensing imagery. Also, CNNs have been found to be useful for feature extraction [18] and classification of PolSAR imagery [19]. Further improvement in PolSAR image classification was obtained when a complex-valued CNN (CV-CNN) [20] and a polarimetric-feature-driven deep CNN were proposed [21].

Over the past few years, the Fully Convolutional Network (FCN), proposed by Long et al. (2015), has gained recognition due to its ability to address pixel-based classification tasks in an end-to-end fashion [11], [23]. Accordingly, several FCN architectures have been developed for the

semantic labelling of very high-resolution optical remote sensing data. In particular, Kampffmeyer *et al.* (2016) employed a FCN architecture to perform pixel-based labelling of high-resolution aerial imagery [24]. In another study, Volpi and Tuia (2017) proposed a downsample-then-upsample FCN architecture, wherein high-level features are learned using convolution layers and spatial information loss is minimized using transposed convolutional layers [11]. Subsequent success in developing new FCN architectures has been achieved by proposing the Hourglass-Shaped Network (HSN) [23], the Fine Segmentation Network (FSN) [5], the Edge-loss Reinforced Network (ERN) [25], the symmetrical normal shortcut FCN (SNFCN), and the symmetrical dense-shortcut FCN (SDFCN) [26] for semantic segmentation of very high-resolution optical imagery.

Interestingly, the capability of FCNs for the classification of PolSAR imagery has been examined to a lesser extent than for optical imagery. This could be attributed to the smaller amount of publicly available annotated SAR samples, complex scattering mechanisms within SAR imagery, and random speckle noise. Notably, the fine-tuning of well-known pre-trained networks for SAR image classification is inefficient due to the intrinsic differences between the imaging mechanisms of SAR and those of optical imagery. Most parameters obtained from pre-trained networks using optical imagery are ineffective for SAR/PolSAR imagery since they cannot properly preserve substantial polarimetric and geometrical information.

Despite the limitations mentioned above, FCNs have been found to be effective for SAR and PolSAR image applications. For example, Wang *et al.* (2018) integrated deep spatial features extracted from FCNs with sparse and low-level features to classify PolSAR imagery [27]. Li *et al.* (2018) later introduced the sliding window FCN and sparse coding (SFCN-SC) for PolSAR image classification [29]. FCN was also found to be useful for road segmentation using single polarized SAR imagery [30]. Furthermore, Wu *et al.* (2019) introduced manually-annotated PolSAR

imagery, obtained from the Chinese airborne PolSAR C-band system, to support the pixel-based classification of PolSAR imagery [31]. However, this dataset has 50 image patches consisting of 256x256 pixels and only contains typical land cover classes, including road, water, built-up, and vegetation.

Although the methodologies and results obtained from FCNs using both optical and PolSAR imagery are sound, the previously mentioned studies focused only on the classification of typical broad land cover classes (e.g., water, vegetation, and built-up) from a limited publicly available dataset. Consequently, the pixel-based classification of complex land-cover units, such as similar wetland classes and sea ice types, remains challenging. This highlights the necessity of designing a new FCN architecture specifically suited for the classification of complex land cover classes but potentially applicable to other research areas. Accordingly, the main objectives of this research were to: (1) propose a new FCN architecture for the classification of wetland complexes using PolSAR imagery; (2) leverage skip connections and the memorized max-pooling indices to alleviate information loss due to the pooling operations; (3) improve multi-scale inference and enrich contextual information using inception modules; and (4) employ an in-depth examination of learned features by opening the “*black box*”. To the best of our knowledge, this study is the first to investigate the potential of such a new 2-D encoder-decoder architecture for the classification of complex land-cover units using PolSAR imagery.

## **6.2. Convolutional Neural Network**

Two common approaches can be found in the literature for land cover classification using CNNs: patch-based CNNs and FCNs [32]. The former approach divides a large input image into small patches and a typical CNN model is applied to predict a single label for the center of each patch [33]. Then, the class labels are sorted to produce a two dimensional classified map as the output.

Although promising results have been obtained using patch-based CNN models for the semantic segmentation of remote sensing data (e.g., [34]), this approach may be inefficient [11]. This is because patch-based CNNs introduce artifacts on the boundaries of the adjacent patches and may result in oversmoothing of the object boundaries and uncertainty in the semantic segmentation results [36]. Notably, densely overlapped patch-based methods at least partially address these limitations; however, they include excessive redundant information in image processing and consequently, they are computationally intensive.

The second approach, FCNs, is better suited for remote sensing imagery and has shown promising results in several recent studies for the semantic segmentation of very high-resolution aerial imagery [5], [23], [25]. In FCNs, the fully connected layers, which convert the two-dimensional structure of an image to a vector representation, are replaced with convolutional layers. This allows FCNs to maintain a two-dimensional output image structure and increases the efficiency of network training. Given the ease of implementation, the high accuracy, and the computational efficiency of the FCN architecture relative to the patch-based CNNs [37], the FCN model was employed in this study. We first introduce the main components of our network, which is then followed by a detailed explanation about the proposed FCN architecture for PolSAR image classification in this study.

### **6.2.1. Convolutional layers**

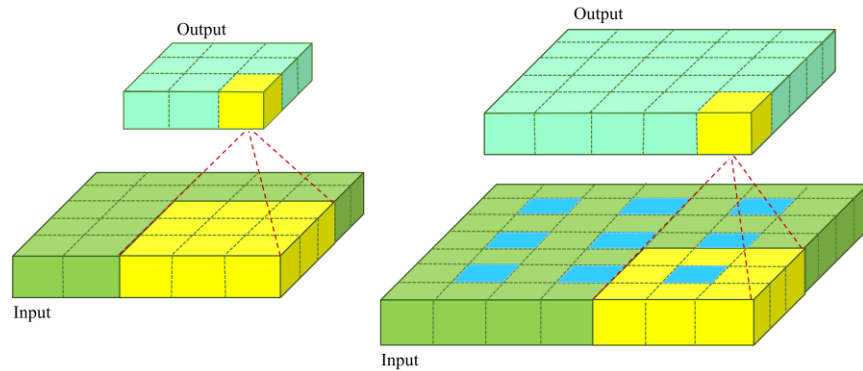
The core of a CNN is its convolutional layers. A convolutional layer is a collection of simple filters (neurons) with learnable parameters (w,b). Given the input image  $X_i^{l-1}$  (size:  $W_1 \times H_1 \times D_1$ ), applying a dot product of the weights and the input, the output volume  $Y_j^l$  (size:  $W_2 \times H_2 \times D_2$ ) of each filter is defined as [38]:

$$Y_j^l = f\left(\sum_{i \in M_j} w_{i,j}^l \cdot X_i^{l-1} + b_j^l\right) \quad (6.1)$$

where the learnable parameters  $w_{i,j}^l$  and  $b_j^l$  are the weight and bias of the  $j^{th}$  neuron (filter) in the  $l^{th}$  layer, respectively, and  $f(x)$  is the nonlinear activation function (see Section 2.2). The spatial dimension of the output can be represented as:

$$W_2 = \frac{W_1 - P + 2Z}{S} + 1 \quad H_2 = \frac{H_1 - Q + 2Z}{S} + 1 \quad (6.2)$$

where  $S$  is the stride (i.e., a distance between two consecutive convolutional windows) and  $Z$  is the number of zero rows and columns added to the borders of the input, also known as zero padding.  $P \times Q$  is the convolutional patch size. Each convolutional filter is applied using a rectangular sliding window with a pre-defined stride over the entire input volume (see Figure 6.1 (a)). Each filter seeks out a specific pattern within the input volume  $X$ . Accordingly, the learnable weights and biases for all convolutional filters in a given channel of  $Y$  are shared because the same pattern is sought across all spatial locations in the input image [23]. This is called the “weight-sharing property” of the convolutional layer and it decreases the number of parameters for this layer relative to fully connected layers, thus mitigating the overfitting problem during the training stage [13].



(a) Convolutional layer: the input image,  $(X)$ , with size  $W_1 \times H_1 = 5$ ; convolutional patch size  $P \times Q = 3$ ;  $S = 1$  and  $Z = 0$ . The output image,  $(Y)$ , with size  $W_2 \times H_2 = 3$ .  
 (b) Transposed convolutional layer: this is equivalent to a convolution layer with the input image,  $(X)$ , with size  $W_1 \times H_1 = 5$  (a  $3 \times 3$  input with 1 zero inserted between inputs); the convolutional patch size  $P \times Q = 3$ ;  $S = 1$  and  $Z = 1$ . The output image,  $(Y)$ , with size  $W_2 \times H_2 = 5$ .

Figure 6.1. An illustration of (a) convolutional and (b) transposed convolutional layers.

### 6.2.2. Non-linear function layer

The non-linear function layer, also known as an activation function, adds non-linearity to the network and enhances the network's capacity to express more complex non-linear mapping [5]. Notably, such non-linearity considerably decelerates weight convergence during the training stage. This is because the derivatives tend to zero when input magnitudes are large and, accordingly, the updates for the weights nearly vanish. Consequently, several non-linearity functions have been proposed to address this so-called vanishing-gradient problem. The Rectified Linear Unit (ReLU), Sigmoid,  $TanH$ , and leaky ReLU function are common activation functions [11]. The ReLU function,  $f(x) = \max(0, x)$ , which performs a threshold operation on each input element, has

shown promising results in several deep-learning studies (e.g., [23]). Accordingly, the ReLU function was used in our proposed network because it simplifies the calculation of the partial derivatives and expedites stochastic gradient descent (SGD) convergence [39].

### **6.2.3. Spatial pooling layer**

The pooling layer, also known as the down-sampling layer, spatially reduces the size of the input volume and preserves discriminant information. In particular, a rectangular sliding window (e.g.,  $2 \times 2$ ) over the feature map is applied and returns a single value from the information within the window. This layer generalizes the output of the convolutional layer into a higher level, submits more abstract features to the next layer, and maintains the scale invariant of the output feature maps. Accordingly, the pooling layer lightens computational complexity during the training stage by reducing the size of the feature map and, thus alleviates the overfitting problem. The maximum, minimum, and average functions are well-known pooling layers. In our proposed network, we used the max-pooling function due to its stability and efficiency in deep-learning research.

### **6.2.4. Transposed convolutional layer**

The transposed convolutional layer retrieves the lost feature details introduced by pooling layers or other down-sampling operations. The transposed convolutional layers include un-pooling and convolution. In contrast to the max-pooling operation, which gradually shrinks the feature maps, the un-pooling operation expands the height and widths of the feature maps during the decoding stage. Similar to SegNet [40], we used the memorized max-pooling indices that record the location of the max-value from the corresponding encoded feature map to recover more accurate information during the decoding stage. This produces sparse feature maps to which the convolutional operation is applied to obtain dense feature maps.

### 6.3. Proposed network for classification of PolSAR imagery

As mentioned earlier, our proposed network follows a FCN architecture (i.e., pixel-based approach) and the generic encoder-decoder paradigm. Figure 6.2 illustrates the proposed network for classification of PolSAR imagery. The encoder stage is similar to the conventional CNNs and extracts deep abstract features through down-sample pooling. However, the decoder stage exists only in FCNs that retrieves the precise boundary localization and provides a dense label map through up-sampling [26]. In particular, the input image is first traversed across a stack of convolutions, ReLU, and max-pooling layers during the encoding stage. The latter layer seeks out the spatial locations of the maximum value within the given window. The encoding stage produces an output with poor spatial resolution. The output of this bottleneck is the input of the decoding stage, wherein transposed convolutional layers consecutively up-sample the low resolution output result to the spatial resolution of the original input image and produces a dense label map.

The down-sampling, which is intrinsic to the encoding stage mentioned above, causes a loss in detail. This consequently results in less accurate predictions near the boundaries of the pixels. To reduce information loss due to down-sampling, the proposed network uses skip connections to integrate high-resolution feature maps from the encoding stage to the decoding stage, along with stepwise transposed convolutions to recover more accurate end detailed output. In particular, skip connections combine deep, coarse, and semantic features with shallow and fine features to re-introduce high-frequency image details into the decoding stage [23], [39]. Furthermore, they are useful in alleviating the vanishing gradient problem that arises during network training [39], thus improving the gradient propagation and the network's performance [26]. These skip connections should provide sufficient retrievable details at our target resolution for wetland classification and further edge enhancement/detection does not enrich detailed information. This is because, as

reported in a previous study [41], adding boundary detection improved the labelling accuracy of human-made objects in very high-resolution aerial imagery (spatial resolution < 0.5m), whereas no improvement was observed for vegetation classes given their intrinsically fuzzy boundaries.

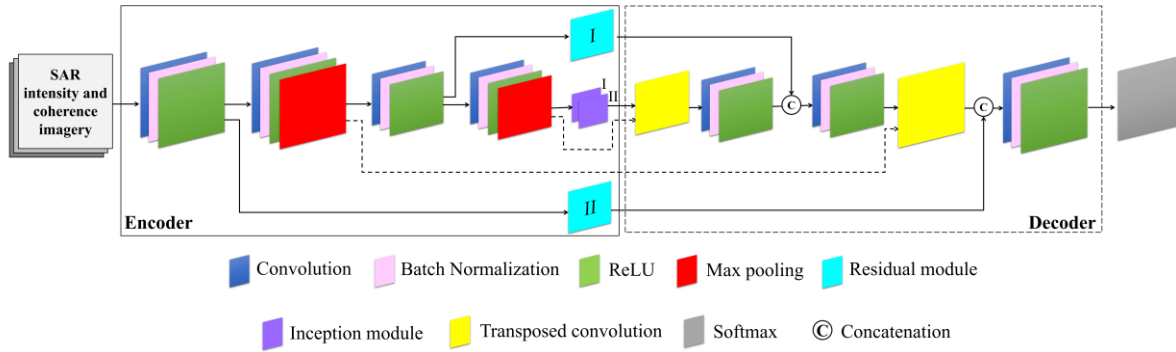


Figure 6.2. The proposed network architecture in this study. Note that the encoder and decoder stages of the network are presented in solid-line and dashed-line boxes, respectively.

A detailed configuration of the proposed network is presented in Table 6.1. In the encoding stage, the proposed network begins with a convolutional layer that has a filter patch size of  $P \times Q = 3$ . A small patch size is used to decrease model parameters and manipulate the insufficient number of training samples. Furthermore, small kernels add nonlinearity to the network, thus producing more discriminative features useful for wetland classes with varying sizes. A total of 64 filters are employed in this layer. Notably, the filter patch size remains unchanged for all convolutional layers in the encoding stage of the network. The first layer is followed by two convolutional layers with a total of 128 filters in each. The red layer is the max-pooling layer with a down-sampling factor of two. A total of two max-pooling layers are used to down-sample the feature maps for obtaining wider receptive fields.

The last convolutional layer in the encoding stage has 256 filters. Accordingly, the number of feature maps increases as the network grows into deeper convolutional layers. This results in maintaining the time complexity appropriate to each layer within the designed network. Notably, all convolutional layers in the encoding stage of the network are followed by both batch normalization and the non-linear ReLU function. Batch normalization increases the training speed and decreases the network sensitivity to initialization. This layer normalizes the activations and lightens gradient propagation across the network. Specifically, batch-normalization allows setting a larger learning rate and results in larger updating parameters, thus simplifying optimization [38].

Table 6.1. Configuration of the proposed network in this study.

	<b>Layer type</b>	<b>Filter size</b>
<b>Encoder</b>	Convolution	3 x 3, 64
	Residual module	-, 64
	Convolution	3 x 3, 128
	Max pooling	2 x 2
	Convolution	3 x 3, 128
	Residual module	-, 128
	Convolution	3 x 3, 256
	Max pooling	2 x 2
	Inception module	-, 256
	Inception module	-, 512
<b>Decoder</b>	Transposed convolution	-, 512
	Convolution	3 x 3, 256
	Convolution	3 x 3, 128
	Transposed convolution	-, 64
	Convolution	1 x 1, 8
	Softmax	-

Two inception modules are also used in this network [42]. The inception block is useful given the various sizes of wetland classes in the study region, which may hinder the effectiveness of conventional convolutional layer with a single, specific filter size. This is because some wetland classes, such as swamp, tend to occur in physically smaller areas relative to that of other classes. Conversely, some other classes (e.g., bog) are often more expansive. Accordingly, the inception module is useful since benefits from filters with different sizes in one layer, which contribute to multi-scale inference and enhance contextual information.

The structure of the inception module is depicted in Figure 6.3 (a). As shown, the inception block is comprised of three branches. The first two branches contain a sequence of two convolutional filters, wherein the patch sizes of the first convolution are both  $1 \times 1$  and those of the second are  $5 \times 5$  and  $3 \times 3$ , respectively. The third branch has only one convolutional filter with a patch size of  $1 \times 1$ . Both batch normalization and ReLU follow convolutional layers in the inception modules. A detailed configuration of the inception modules is presented in Table 6.2.

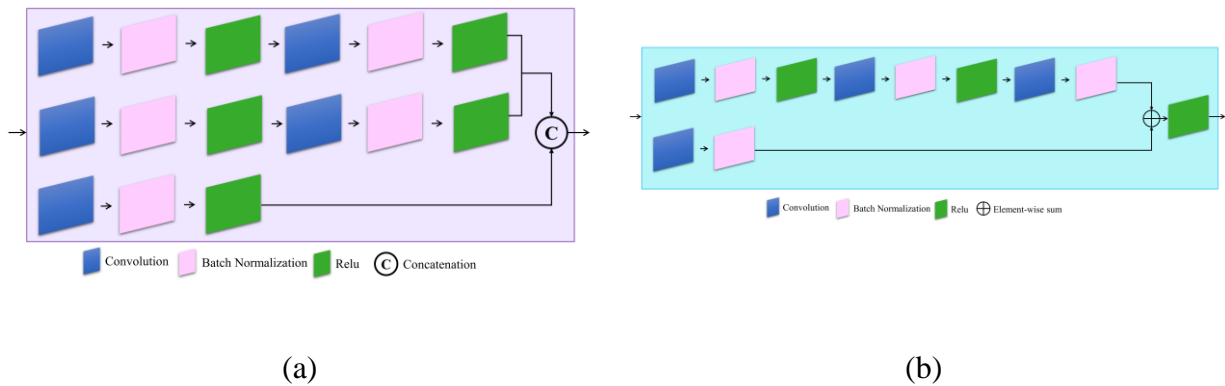


Figure 6.3. Architecture of (a) inception and (b) residual modules in this study.

Two skip connections, which directly transfer information from the encoding stage to its corresponding decoding one, are used after the first and third convolutional layers [43]. In

particular, feature maps at varying resolutions are integrated to enhance both the recognition and localization within the network by employing skip connections [5]. This is because the feature maps from the shallower layers (before pooling) submit high frequency details on a small receptive field while the feature maps from the deep layers submit low spatial details (because of the pooling operation) on a wider receptive field. This highlights the necessity of combining feature maps at different resolutions to take into account the trade-off between recognition and localization.

The structure of the residual module used in this study is demonstrated in Figure 6.3 (b) and its detailed configuration is presented in Table 6.2. As shown in Figure 6.3 (b), the residual block consists of two branches. The first branch is composed of a stack of three convolutional filters with patch sizes of  $1 \times 1$ ,  $3 \times 3$ , and  $1 \times 1$ , respectively. The last branch has one convolutional filter with a patch size of  $1 \times 1$ . The number of filters in each branch is presented in Table 6.2. All convolutional filters in the residual module are followed by batch normalization. The two branches are integrated using an element-wise summation.

Table 6.2. Configuration of inception and residual modules in this study.

		Convolution configuration			Operation	Output
Inception	I	1 x 1, 128 1 x 1, 64	1 x 1, 64	5 x 5, 128 3 x 3, 64	Concatenation	256
	II	1 x 1, 256 1 x 1, 128	1 x 1, 128	5 x 5, 256 3 x 3, 128	Concatenation	512
Residual	I	1 x 1, 32	3 x 3, 64 1 x 1, 64	1 x 1, 64	Element-wise sum	64
	II	1 x 1, 64	3 x 3, 128 1 x 1, 128	1 x 1, 128	Element-wise sum	128

In the decoding stage, the transposed convolutional layers with an up-sampling factor of two are used to gradually up-sample the feature maps to the original resolution of the input image from the abstract features. As mentioned earlier, the memorized max-pooling indices [40] are used in this

study to recover more accurate detailed information (see the dashed-lines in Figure 6.2). The outputs of the transposed convolutional layers are concatenated with information that is directly transferred from the encoding stage to the decoding stage. Finally, the output feature map of the network is passed through the top-most layer, the *Softmax* function, to transform 2D deep features into a classification map.

## 6.4. Experimental design

### 6.4.1. Study area and dataset

This study was carried in the northeast portion of the Avalon Peninsula, Newfoundland and Labrador, Canada. Figure 6.4 illustrates the geographic location of the study area.

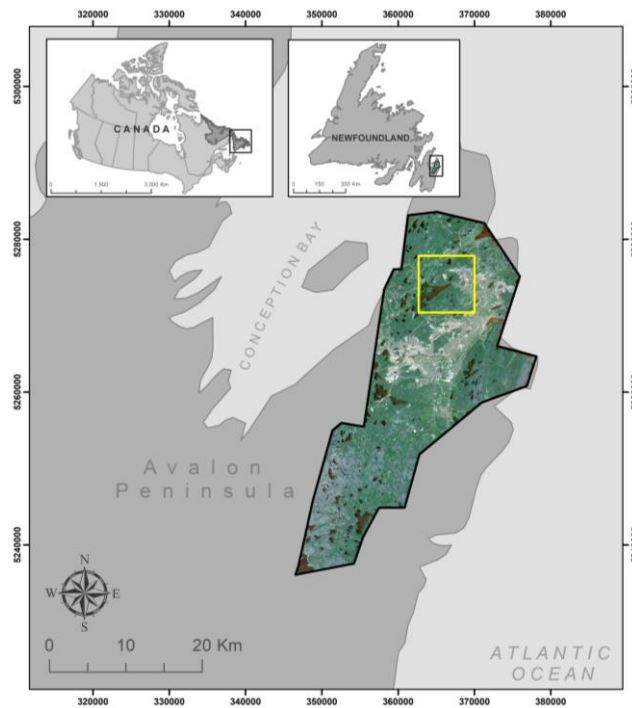


Figure 6.4. The geographic location of the study area. The yellow square displays one tile of the testing set, which was selected for the purpose of illustration.

The study area has eight land cover classes, five of which are wetlands, including bog, fen, marsh, swamp, and shallow water (i.e., mineral wetlands with standing water at most 2 m deep). The other land cover classes in the study area are urban, upland, and deep water (e.g., lakes and ponds greater than 2 m in depth). Figure 6.5 depicts examples of land cover classes in the study area.



Figure 6.5. Ground reference photos illustrating land cover classes in the study area: (a) bog, (b) fen, (c) marsh, (d) swamp, (e) shallow water, (f) urban, (g) deep water, and (h) upland.

#### 6.4.2. RADARSAT-2 data and feature extraction

Two RADARSAT-2 images in Fine mode Quad polarization (FQ22) were used for classification. This imagery was acquired on June 7 and July 25, 2016 from an ascending orbit with a resolution of 5.2 m in the range direction, 7.6 m in the azimuth direction, and an incidence angle of 42°.

RADARSAT-2 level-1 SLC imagery was geo-referenced using an external digital elevation model (DEM, SRTM 3 arc-second), which projected the intensity imagery into UTM coordinates (zone 22, row T) using the WGS84 reference ellipsoid. An adaptive Lee filter with a 3x3 window size was used to suppress the effect of speckle noise. This window size should be sufficient at this stage as it is able to maintain information within the input data. Further suppression of speckle noise was carried out during training of networks, as convolutional layers are able to address speckle noise [31]. Next, intensity images were converted into normalized backscattering coefficient images in dB (i.e., the standard unit for SAR backscattering representation). The conversion process for RADARSAT-2 images is as follows:

$$CV = \frac{|DN|^2}{A^2} \quad (6.3)$$

where  $CV$  is the calibrated value,  $DN$  is the digital number, and  $A$  is the gain value [44]. The normalized backscattering coefficient  $\sigma^0$  in dB is derived as

$$\sigma^0 = 10 * \log(CV). \quad (6.4)$$

Following this procedure, a total of six SAR backscattering coefficient images were produced using the PCI Geomatica software package.

Coherence indicates the degree of similarity between two co-registered SAR images and this varies between 0 and 1, illustrating purely incoherent and coherent conditions, respectively. Coherence images were used in this study, as our previous study [45] demonstrated that interferometric coherence provides complementary information to SAR intensity and is more responsive to land cover changes relative to SAR intensity. This is of great importance for characterizing highly

dynamic land cover classes, such as wetland complexes. To produce coherence images, an external DEM was used for removing topographic phase and the coherence imagery was generated with a 5x5 window size using the GAMMA remote sensing software package. Notably, image co-registration was performed with sub-pixel accuracy. In this way, three coherence images in different polarizations were produced and used as the input data in all experiments.

### **6.4.3. Training and testing**

*In-situ* data for eight land cover classes were collected for 257 sites during the summer and fall of 2015, 2016, and 2017 by recording Global Positioning System (GPS) points at each location. Accordingly, a total of 270,000 points were labeled based on GPS points on SAR imagery. These points were categorized as bog (~15.3%), fen (~4.6%), marsh (~2.7%), swamp (~3.6%), shallow water (~ 6.3%), urban (~19%), deep water (~23.8%), and upland (~24.7%) classes to produce the reference polygons. Next, these reference polygons, 50 cm resolution orthophotographs, 5 m resolution RapidEye optical imagery, and Pauli RGB image of full polarimetric SAR data were used to manually label approximately 80% of the pixels on the SAR imagery in ArcMap 10.6 by both remote sensing and biologist experts familiar with the study area. To avoid possible errors between the boundaries of adjacent classes, a circular disc with a radius of three-pixel was applied to each delineated class during the preparation of the ground truth data.

Notably, the study area was divided into 14 tiles, each consists of 1000x1000 pixels. A total of 8, 4, and 2 tiles were selected for training, validation, and testing, respectively. The yellow square within Figure 6.4 shows one tile of the testing set, which was selected for the purpose of illustration. Significant effort was devoted to maintain this ratio (i.e., 8: 4: 2) for all wetland classes by assigning tiles with a dominant class (e.g., bog) to the training, validation, and testing groups. The 8: 4: 2 ratio for the training, validation, and testing tiles is consistent with similar studies (e.g.,

[23], [41]), which applied FCNs to semantic segmentation of very high-resolution optical imagery. This ratio was also found to be optimal because when a fewer and larger number of tiles were assigned to the training (5 vs. 8 tiles) and testing (5 vs. 2 tiles) groups, respectively, the producer's accuracy for some wetland classes (e.g., marsh) sharply decreased (less than 40%), although the overall accuracy remained high (above 80%). The decrease in the producer accuracy was due to the limited availability of training data for some wetland classes in the training tiles in this case. This is because the distribution of wetland classes varies spatially and when a fewer number of tiles is considered for training, it influences the classification accuracy of less prevalent classes (e.g., marsh and swamp) in the study area.

The proposed network was trained using the cross-entropy loss function and stochastic gradient descent with a momentum (SGDM) optimizer and mini-batch size of 16. The learning rate was set at  $10^{-5}$  and was stepped down ten times every five epochs. The image patch size was 256x256 pixels with 50% overlap because the remote sensing images are too large to be directly used in FCNs. Data augmentation was carried out to mitigate overfitting by flipping (vertically and horizontally) and rotating (at 90° intervals) the training patches. The training and testing processes were carried out on an Intel CPU i7 4790 k machine with 3.6 GHz and 32 GB RAM memory. A NVIDIA GeForce GTX 1080 Ti GPU with 11 GB of memory under CUDA version 8.0 was also employed in this study.

#### **6.4.5. Evaluation methods**

To evaluate the performance of the proposed network, a conventional machine learning tool, namely random forest (RF), as well as benchmark networks, FCN-8s, FCN-16s, FCN-32s, and SegNet, were employed. RF is an ensemble of classifiers that benefits from a collection of Classification And Regression Trees (CARTs) [46]. It is a non-parametric classifier and has

produced good results for land cover classification using SAR/PolSAR imagery [47], [48]. In this study, RF was employed by setting two parameters, namely the number of decision trees ( $Ntree = 500$ ) and the number of variables ( $Mtry =$  the square root of the number of input variables).

FCN-8s, FCN-16s, and FCN-32s compose the first generation of FCN architecture, proposed by [22], wherein their encoder stages were transplanted from VGG-16 [49]. All three networks have decoder stages that up-sample deep feature maps to a dense pixel-based prediction map. FCN-8s and FCN-16s have two and one skip connections, respectively, which fuse semantic information from a deep, coarse layer with appearance information obtained from shallow, fine layers. However, FCN-32s produces dense pixel-based labelled maps by employing one transposed convolutional layer with no skip connection. Notably, FCN-32, FCN-16s, and FCN-8s follow the single-, two-, and three-stream learning procedure [22].

SegNet [40] is characterized by a FCN architecture and follows an encoder-decoder paradigm. Its encoder architecture is similar to the 13 convolutional layers of the VGG-16 network [49]. There are 13 layers at the decoder stage of the network (corresponding to the encoder stage), as SegNet is symmetrical. In addition to the transposed convolutional layers, SegNet uses memorized max-pooling indices (i.e., the location of the maximum feature value in each max-pooling operation during the encoding stage) from the corresponding encoder feature map to perform non-linear up-sampling during the decoding stage. This preserves substantial spatial information by recording the pooling indices in the encoding stage. The encoder and decoder stages of the network are then followed by a multi-class *Softmax* classifier to produce a dense pixel-based classification map. In this study, all FCNs were trained using a similar strategy to that described in Section 6.4.3. Table 6.3 represents the training time per epoch for training FCNs in this study. The proposed method exhibits a slightly slower convergence than the baseline FCNs and SegNet methods, given its

relatively complex architecture. The average inference time (Table 6.5) of the proposed method is, however, the second fastest, by a small margin.

Table 6.3. The training time (in seconds) per epoch for training FCNs in this study.

Methods	FCN-32s	FCN-16s	FCN-8s	SegNet	The proposed method
Time per epoch (s)	750	758	775	735	794

#### 6.4.6. Evaluation metrics

To examine the performance of different methods, four evaluation metrics, including overall accuracy (OA), average accuracy (AA), Kappa coefficient, and F1-score were employed. Overall accuracy quantifies the amount of correctly-labeled area within an input image. It can be measured by dividing the total number of correctly-labeled samples by the total number of test samples. The average accuracy measures the average value of the labelling accuracies of all land cover types. The Kappa coefficient represents the degree of agreement between the ground truth data and the final labeled map. The F1-score is a harmonic mean between precision and recall. It is useful for imbalanced classes and is obtained as:

$$F1 - score = 2 \times \frac{Precision \times Recall}{Precision + Recall} \quad (6.5)$$

Here precision (or positive predictive value) counts how many detected pixels in each class are true and is given by:

$$Precision = \frac{True\ positives}{True\ positives + False\ positives}, \quad (6.6)$$

and recall or sensitivity, defined as

$$Recall = \frac{True\ positives}{True\ positives + False\ negatives}, \quad (6.7)$$

represents how many actual (true) pixels are identified in each class. It is worth noting that for both the proposed network and the evaluation methods (e.g., SegNet), all evaluation indices were obtained by averaging values across all test tiles.

## 6.5. Results and discussion

### 6.5.1. Open the *black box*: feature visualization

In seeking an understanding of the *black box* of the proposed network, an in-depth investigation of the learned features was carried out. Figure 6.6 illustrates the visualized features from the first convolutional block once the training has been terminated.

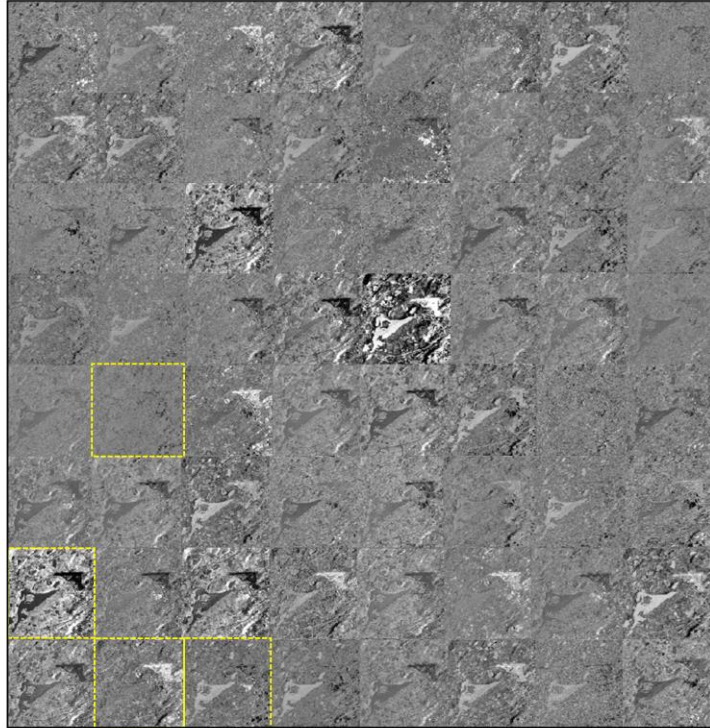


Figure 6.6. Visualization of learned features from the first convolutional block once the training has been terminated. The yellow-dashed squares demonstrate 4 of 64 features selected for further evaluation.

Figure 6.6 shows a total of 64 learned feature maps, each of which unfolds the various structures that are activated by different convolutional filters. We selected 4 of 64 learned features in order to further examine the characteristics of the convolutional filters in the first convolutional block (see the yellow-dashed squares in Figure 6.6).

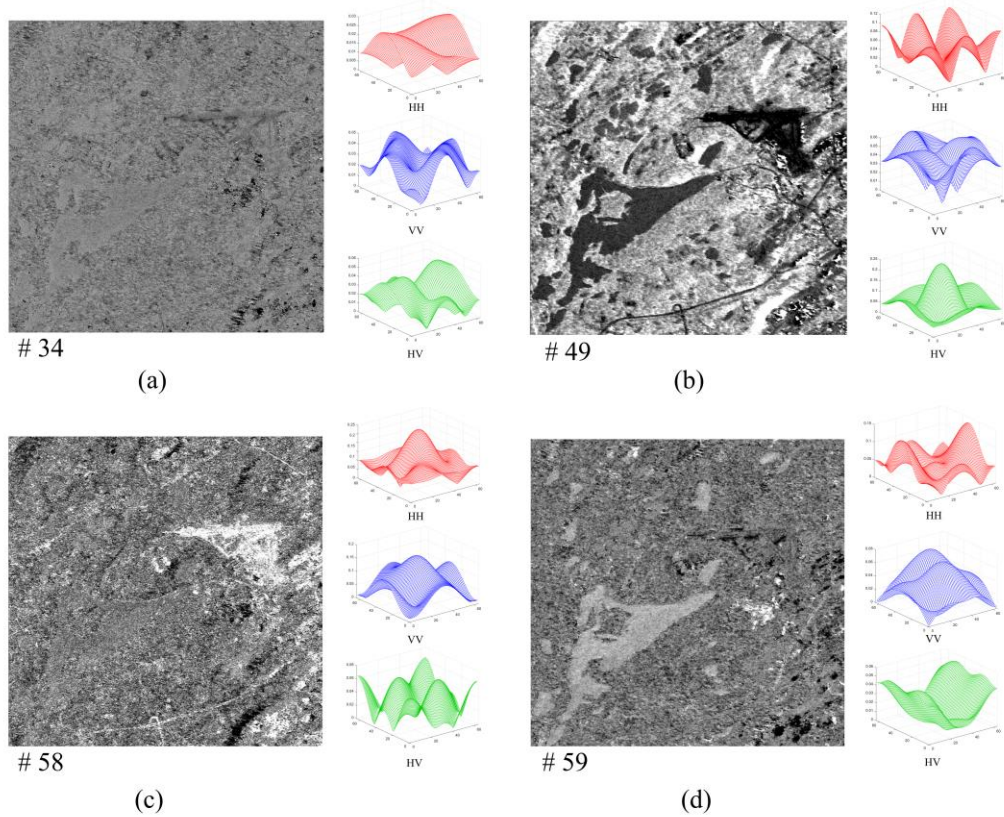


Figure 6.7. Four learned features from the first convolutional block and their frequency responses.

As shown in Figure 6.7 (b), the output feature map of #49 reveals that this filter is responsive to vegetation cover in the scene, whereas the output feature map of #58 hinders the representation of this class. The frequency response for the feature map of #49 shows greater weights for the HV channel compared to those of VV and HH. This is in agreement with the expected volume scattering mechanism of vegetation canopies, which have higher backscattering responses in the HV channel [50]. On the other hand, the feature map of #58 tends to highlight the urban land cover. The frequency response of this feature map shows a greater response in the HH channel relative to the other two polarizations. This, too, agrees well with the expected scattering mechanism of human-made objects, since HH polarization is more sensitive to double-bounce scattering. The

feature map of #59 illustrates the activation of the water class with no deterministic behavior in the three polarizations. Notably, several filters from the first convolutional block, such as #34, demonstrate random speckle noise behaviors. Accordingly, we believe that the proposed network has the capability to extract both spatial and polarimetric features using different convolutional filters. This visualization also reveals that polarimetric features can be learned using deep CNNs and, thus can mitigate the tedious process of feature engineering. Figure 6.8 demonstrates 16 of 128 feature maps of the third convolutional block. As shown, more abstract feature maps are generated as the network grows into its deeper stage.

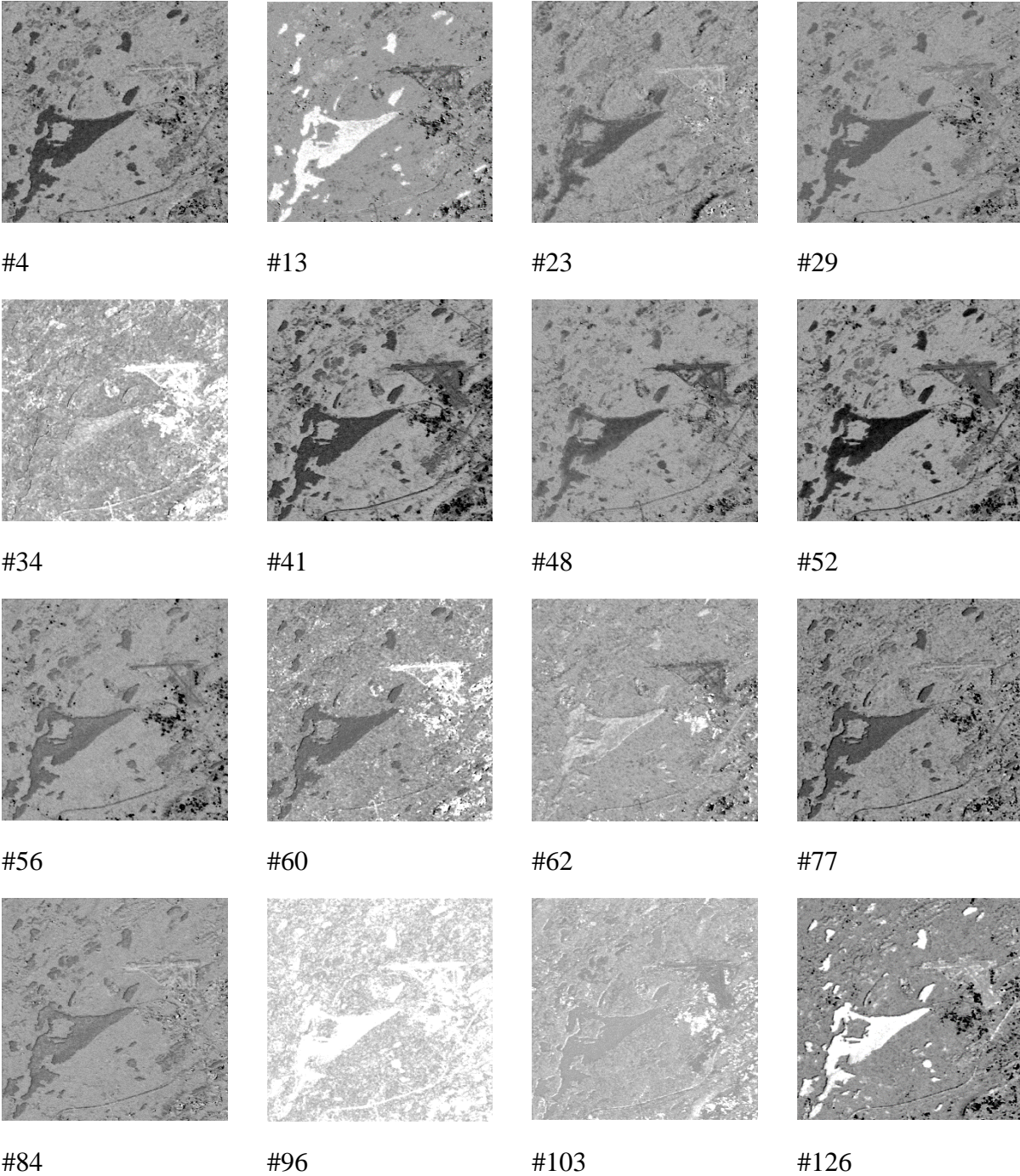


Figure 6.8. Visualized 16 of the 128 output feature maps from the third convolutional block. Note that more abstract feature maps are produced as the network becomes deeper.

### 6.5.2. On the importance of inception module and skip connections - ablation study

To examine the effectiveness of skip connections and residual modules, two ablation experiments were carried out. In the first analysis, the inception layers were replaced with the typical convolutional layers in the proposed architecture to explore the possible benefits of these components while the skip connections were maintained. To investigate the effect of skip connections on accuracy, they were removed in the second experiment while the other components of the proposed FCN remained constant. Table 6.4 contains a comparison of the results of the first (no inception, NI) and the second (no skip, NS) ablation experiments with those of the proposed network.

Table 6.4. Experimental results of the importance of the inception module and skip connections.

The most accurate results are indicated in bold.

	OA (%)	AA (%)	K	F1-score
The proposed network-NI*	87.28	79	0.84	0.77
The proposed network-NS*	90.55	81	0.87	0.80
The proposed network	<b>92.82</b>	<b>83</b>	<b>0.91</b>	<b>0.84</b>

\* Note: NI: no inception module and NS: no skip connections.

As may be observed from Table 6.4, both skip connections and inception modules are beneficial for wetland classification. The results indicate that inception modules are more advantageous, as a sharp decrease in both overall accuracy (~ 5.5%) and F1-score (0.07) occurred when they were removed from the proposed architecture. This finding is potentially explained by the fact that inception modules characterise complex patterns by extracting multi-scale contextual information. This is attributed to the existence of filters with various sizes that allow the exploitation of enhanced contextual information, which is of great significance for the classification of wetland

classes with different sizes. Skip connections are also useful for retrieving sufficient spatial information and were found to be useful in this study (see Table 6.4).

### 6.5.3. Classification results

Table 6.5 presents the evaluation indices for wetland classification obtained from RF, FCNs, SegNet, and the proposed network.

Table 6.5. Assessment of the segmentation results obtained from different methods. The most accurate results are indicated in bold.

	OA (%) <sup>*</sup>	AA (%) <sup>*</sup>	K <sup>*</sup>	F1-score	AIT (s) <sup>**</sup>
RF	75.88	74	0.71	0.74	19
FCN-32s	69.37	68	0.61	0.69	<b>5</b>
FCN-16s	82.59	76	0.74	0.75	7
FCN-8s	89.60	79	0.87	0.81	11
SegNet	86.91	78	0.83	0.76	17
The proposed network	<b>92.82</b>	<b>83</b>	<b>0.91</b>	<b>0.84</b>	6

<sup>\*</sup>Note: OA, AA, and K stand for overall accuracy, average accuracy, and Kappa coefficient, respectively. <sup>\*\*</sup> Note: AIT is the average inference time per image tile in seconds.

As illustrated in Table 6.5, FCN methods, excluding FCN-32s, outperform the baseline shallow-structured machine learning method (RF), with overall accuracies exceeding 80%. Importantly, the proposed network outperforms all FCNs with an overall accuracy of approximately 93%, illustrating an improvement of about 3% and 23% relative to FCN-8s and FCN-32s, respectively. Our network is also advantageous for wetland classification in terms of other evaluation indices. Specifically, the proposed network achieves the highest average accuracy of 83%, a Kappa coefficient of 0.91, and an F1-score of 0.84 (see Table 6.5). The average inference time of the proposed method is also the second fastest, by a small margin. Figure 6.9 demonstrates the

classification results obtained from different methods for one of the testing tile in this study (see also Figure 6.4).

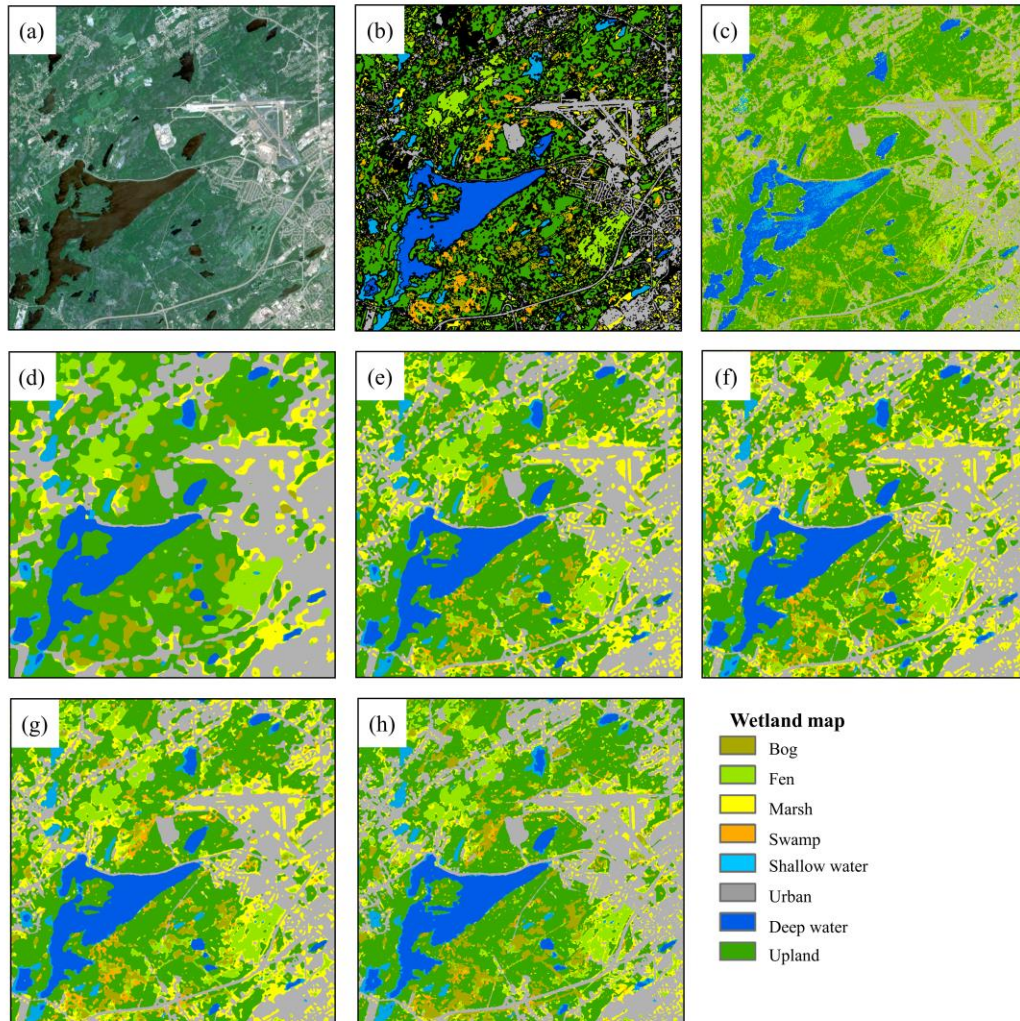


Figure 6.9. (a) True color composite of RapidEye optical image (bands 3, 2, and 1) and (b) ground truth map. The classification maps obtained from (c) RF, (d) FCN-32s, (e) FCN-16s, (f) FCN-8s, (g) SegNet, and (h) the proposed method.

As shown in Figure 6.9 (c), the classification map obtained from RF is the most affected by noisy scatter points since it only considers the backscattering property of SAR imagery. This occurrence is known as “salt and pepper” noise and is inherent in classification algorithms that rely on the

exclusive use of the spectral/backscattering value of each pixel in their classification scheme. However, the classification maps obtained from FCNs and the proposed network alleviated this problem, as both backscattering and contextual information are taken into account. This is of great significance for the classification of SAR imagery, wherein the radiometric quality of the images is degraded by speckle noise.

Overall, the semantic segmentation results revealed the difficulty of identifying similar wetland classes compared to non-wetland classes. Among convolutional networks, FCN-32s has an inferior capability for distinguishing details of wetland classes and its output, especially on borders, is coarse compared to other approaches. This further confirmed the importance of skip connections for semantic segmentation, as leveraging skip connections in FCN-16s and FCN-8s significantly contributed to the improvement of the segmentation results by retrieving more spatial details. Much detail, however, was obtained from FCN-8s due to employing two skip connections relative to FCN-16s. Overall, segmentation results obtained from FCN-8s, SegNet, and the proposed method are similar, albeit with minor differences in identifying small wetland classes. In particular, the proposed method is advantageous for discriminating bog and shallow water. For example, a comparison between the ground truth map and the segmentation results revealed that bogs were better distinguished using the proposed method compared to SegNet and FCN-8s (see bottom of Figure 6.9 (b), (f), (g), and (h)). The shallow water class was also identified more accurately with the proposed method relative to SegNet and FCN-8s. Specifically, the perimeter of deep water classes was correctly classified as belonging to the shallow water class (see the center of segmentation results in Figure 6.9(h)) using the proposed method.

The superiority of our proposed network compared to state-of-the-art FCNs could be attributed to the existence of the inception module within the architecture of the proposed network, as filters

with various sizes in one layer (i.e., inception module) contributed to producing multi-scale receptive fields. This enriched the contextual information, which is very important for distinguishing wetland classes with various sizes. For example, the classes of bog and fen are the most difficult to discriminate due to high intra- and low inter-class variance; however, the proposed method successfully classified most of these classes, as its pixel-based labelling is clear, accurate, and comparable to the ground truth map.

Figure 6.10 illustrates the normalized confusion matrices for the three most accurate FCNs, namely FCN-8s, SegNet, and the proposed network. As shown in Figure 6.10, all three methods accurately distinguished the non-wetland classes with producer's accuracies exceeding 90%, yet the proposed method indicated slight improvements for these classes compared to other approaches. However, there are differences between the producer's accuracies of wetland classes among the top most successful FCNs. Importantly, the proposed method is advantageous in terms of producer's accuracies for all wetland classes, excluding swamp, relative to other methods. Specifically, the proposed method classified bog and shallow water with producer's accuracies up to 82%. The classes of fen and swamp were identified with accuracies beyond 70%. The lowest producer's accuracy was obtained for marsh, possibly due to the lowest number of training samples for this class relative to the other land cover classes in this study.

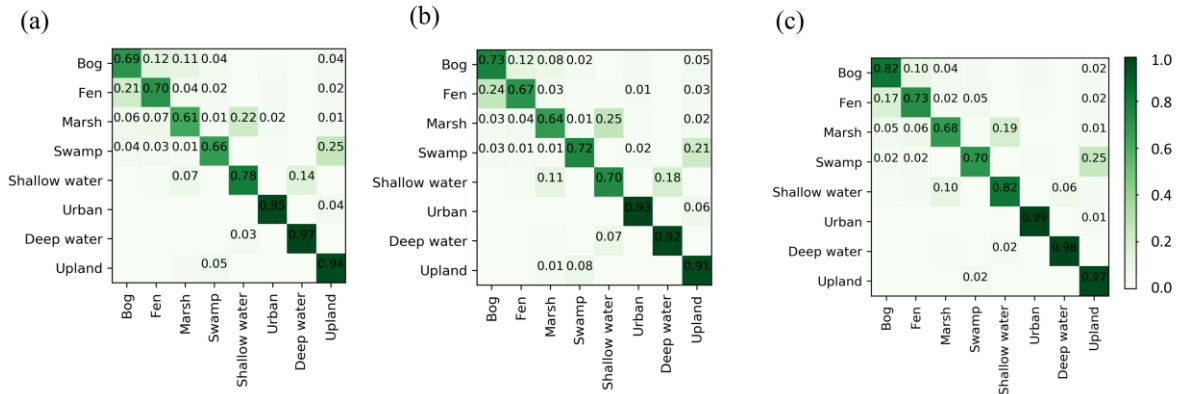


Figure 6.10. Normalized confusion matrices for wetland classification using (a) FCN-8s, (b) SegNet, and (c) the proposed network.

As expected, the confusion is more pronounced among wetland classes compared to non-wetland classes. As shown in Figure 6.10, a great degree of confusion arises among herbaceous wetland classes, namely bog, fen, and marsh. The confusion between bog and fen is possibly due to their similar visual appearance and similarity of the backscattering signatures of these classes in PolSAR imagery [51]. These two classes are both peatland-dominated with very similar species of *Sphagnum* in bogs and *Graminoid* in fens (see also Figure 6.5). As field notes suggest, these classes were adjacent successional classes without clear-cut borders, which made them difficult to distinguish by biologists during *in-situ* data collection.

The confusion error is also pronounced for non-herbaceous wetland classes, namely swamp and shallow water. The swamp wetland is characterized by woody structures and is mostly confused with upland, which is characterized by forested dry land. Accordingly, these two classes may have very similar visual features. Furthermore, the dominant scattering mechanism for both classes is volume scattering, especially when C-band is employed. This results in very similar SAR backscattering signatures for these classes that further contributes to misclassification between them. These two classes are expected to be better distinguished using longer wavelengths, such as

L-band, that have a deeper penetration capacity [48]. The confusion error is also found between the shallow- and deep-water classes, potentially due to their very similar visual features. This, too, occurs to a lesser extent (see Figure 6.10) between shallow water and marsh, possibly due to the heterogeneous nature of these classes in the study area.

Overall, all methods are successful in discriminating the non-wetland classes. This is partially attributed to the availability of a larger number of training samples for the non-wetland classes as compared to the wetland classes. Furthermore, these classes have different SAR backscattering signatures, which results in the generation of discriminative polarimetric features. Theoretically, the accuracies of all wetland classes should be improved upon the inclusion of a greater number of training samples.

The high dimensional extracted features from the last convolutional block are visualized using the Uniform Manifold Approximation and Projection (UMAP) algorithm [52] (see Figure 6.11). UMAP is a novel technique for non-linear dimension reduction and has been developed recently based on Riemannian geometry and algebraic topology. As noted by McInnes and Healy (2018), UMAP is superior to the t-distributed stochastic neighbor embedding (t-SNE) algorithm in terms of both preserving the global structure of the data and the running time [52]. Accordingly, UMAP was used in this study to further demonstrate the ability of the proposed network for learning the intrinsic structure of the input data. As shown in Figure 6.11, the output features from the proposed network share less overlap and are farther from each other compared to those of SegNet and FCN-8s. Although some wetland classes, such as bog and fen, demonstrate some degree of overlap, most classes, including marsh, upland, urban, and shallow- and deep-water, illustrate clear semantic clustering using the proposed network. This further confirms the effectiveness of our proposed architecture in extracting discriminative features from PolSAR imagery.

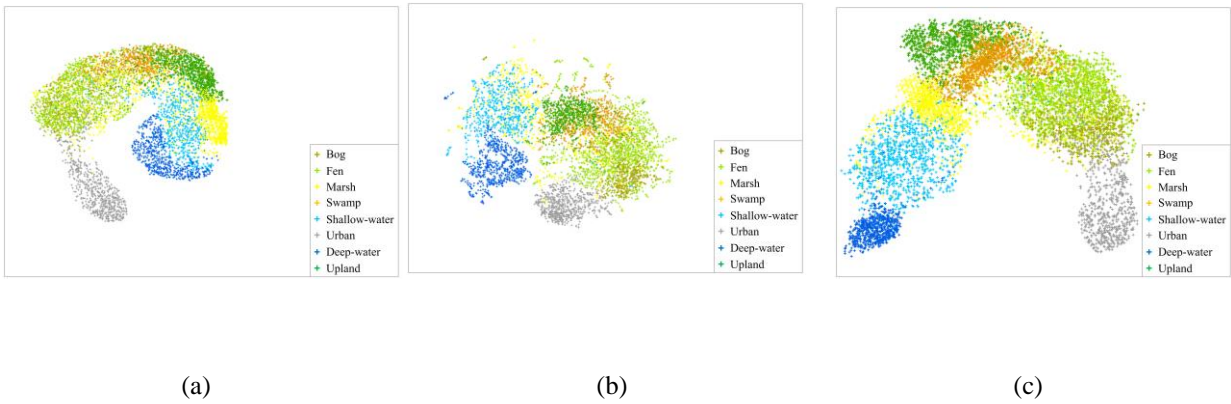


Figure 6.11. Feature visualization using the UMAP algorithm [52] for the extracted features from the last convolutional layer of (a) FCN-8s, (b) SegNet, and (c) the proposed network.

## 6.6. Conclusion

In this study, a new end-to-end fully convolutional neural network that follows an encoder-decoder paradigm was proposed for classification of PolSAR imagery particularly for distinguishing wetland classes. The proposed architecture has two main components: (1) an encoder, wherein high-level abstract features are extracted using a stack of convolutional filters; and (2) a decoder, wherein the output feature map of the encoder stage is gradually up-sampled to the spatial resolution of the input volume using a stack of transposed convolutional filters.

In the proposed architecture, inception modules were also employed to extract information from the multi-scale receptive field and to enrich contextual information, allowing filters with different sizes to be employed in one layer. Furthermore, skip connections with residual units were used to directly transfer information from encoder layers to the corresponding decoder layers of the network. This also resulted in the recovery of more accurate spatial information and simplified optimization. An in-depth examination of learned features demonstrated the effectiveness of the proposed architecture in extracting discriminative polarimetric features. Our proposed network achieved a competitive classification accuracy of about 93%, providing an improvement of about

3% and 23% relative to FCN-8s and FCN-32s, respectively, which were the second best and the worst evaluation methods in this study. Although the top three successful methods illustrated relatively equal strengths for discriminating non-wetland classes (i.e., urban, upland, and deep water) with accuracies beyond 90%, our proposed network was more advantageous for distinguishing similar wetland classes.

Overall, the classification results obtained from the proposed architecture are strongly positive, taking into account the complexity of similar wetland classes, and demonstrate the large number of pixels that were correctly labeled. The proposed architecture is simple and straightforward and will substantially contribute to the success of PolSAR image classification using state-of-the-art deep learning tools. Given the limited availability of ground truth data in most remote sensing applications, future work will focus on designing an end-to-end deep CNN architecture for classification of PolSAR imagery in a semi-supervised scheme.

## 6.7. References

- [1] A. Lonnqvist, Y. Rauste, M. Molinier, and T. Hame, "Polarimetric SAR data in land cover mapping in boreal zone," *IEEE Trans. Geosci. Remote Sens.*, vol. 48, no. 10, pp. 3652–3662, 2010.
- [2] Y. Chen, X. He, J. Wang, and R. Xiao, "The influence of polarimetric parameters and an object-based approach on land cover classification in coastal wetlands," *Remote Sens.*, vol. 6, no. 12, pp. 12575–12592, 2014.
- [3] C. Lardeux *et al.*, "Support vector machine for multifrequency SAR polarimetric data classification," *IEEE Trans. Geosci. Remote Sens.*, vol. 47, no. 12, pp. 4143–4152, 2009.
- [4] F. Mohammadimanesh, B. Salehi, M. Mahdianpari, M. Motagh, and B. Brisco, "An efficient feature optimization for wetland mapping by synergistic use of SAR intensity, interferometry, and polarimetry data," *Int. J. Appl. Earth Obs. Geoinf.*, vol. 73, pp. 450–462, 2018.
- [5] X. Pan, L. Gao, A. Marinoni, B. Zhang, F. Yang, and P. Gamba, "Semantic Labeling of High Resolution Aerial Imagery and LiDAR Data with Fine Segmentation Network," *Remote Sens.*, vol. 10, no. 5, p. 743, 2018.
- [6] X. Huang and L. Zhang, "An SVM ensemble approach combining spectral, structural, and semantic features for the classification of high-resolution remotely sensed imagery," *IEEE Trans. Geosci. Remote Sens.*, vol. 51, no. 1, pp. 257–272, 2013.
- [7] C. Tao, S. Chen, Y. Li, and S. Xiao, "PolSAR land cover classification based on roll-invariant and

- selected hidden polarimetric features in the rotation domain,” *Remote Sens.*, vol. 9, no. 7, p. 660, 2017.
- [8] L. Zhang, L. Zhang, D. Tao, and X. Huang, “On combining multiple features for hyperspectral remote sensing image classification,” *IEEE Trans. Geosci. Remote Sens.*, vol. 50, no. 3, pp. 879–893, 2012.
- [9] L. Zhang, L. Zhang, D. Tao, and X. Huang, “Tensor discriminative locality alignment for hyperspectral image spectral–spatial feature extraction,” *IEEE Trans. Geosci. Remote Sens.*, vol. 51, no. 1, pp. 242–256, 2013.
- [10] R. M. Anwer, F. S. Khan, J. van de Weijer, M. Molinier, and J. Laaksonen, “Binary patterns encoded convolutional neural networks for texture recognition and remote sensing scene classification,” *ISPRS J. Photogramm. Remote Sens.*, vol. 138, pp. 74–85, 2018.
- [11] M. Volpi and D. Tuia, “Dense semantic labeling of subdecimeter resolution images with convolutional neural networks,” *IEEE Trans. Geosci. Remote Sens.*, vol. 55, no. 2, pp. 881–893, 2017.
- [12] X. Ma, A. Fu, J. Wang, H. Wang, and B. Yin, “Hyperspectral Image Classification Based on Deep Deconvolution Network With Skip Architecture,” *IEEE Trans. Geosci. Remote Sens.*, vol. 56, no. 8, pp. 4781–4791, 2018.
- [13] M. Mahdianpari, B. Salehi, M. Rezaee, F. Mohammadimanesh, and Y. Zhang, “Very Deep Convolutional Neural Networks for Complex Land Cover Mapping Using Multispectral Remote Sensing Imagery,” *Remote Sens.*, vol. 10, no. 7, p. 1119, 2018.
- [14] X. Chen, S. Xiang, C.-L. Liu, and C.-H. Pan, “Vehicle detection in satellite images by hybrid deep convolutional neural networks,” *IEEE Geosci. Remote Sens. Lett.*, vol. 11, no. 10, pp. 1797–1801, 2014.
- [15] K. He, X. Zhang, S. Ren, and J. Sun, “Spatial pyramid pooling in deep convolutional networks for visual recognition,” *IEEE Trans. Pattern Anal. Mach. Intell.*, vol. 37, no. 9, pp. 1904–1916, 2015.
- [16] B. Huang, B. Zhao, and Y. Song, “Urban land-use mapping using a deep convolutional neural network with high spatial resolution multispectral remote sensing imagery,” *Remote Sens. Environ.*, vol. 214, pp. 73–86, 2018.
- [17] M. Rezaee, M. Mahdianpari, Y. Zhang, and B. Salehi, “Deep Convolutional Neural Network for Complex Wetland Classification Using Optical Remote Sensing Imagery,” *IEEE J. Sel. Top. Appl. Earth Obs. Remote Sens.*, no. 99, 2018.
- [18] H. Liu, S. Yang, S. Gou, D. Zhu, R. Wang, and L. Jiao, “Polarimetric SAR feature extraction with neighborhood preservation-based deep learning,” *IEEE J. Sel. Top. Appl. Earth Obs. Remote Sens.*, vol. 10, no. 4, pp. 1456–1466, 2017.
- [19] Y. Zhou, H. Wang, F. Xu, and Y.-Q. Jin, “Polarimetric SAR image classification using deep convolutional neural networks,” *IEEE Geosci. Remote Sens. Lett.*, vol. 13, no. 12, pp. 1935–1939, 2016.
- [20] Z. Zhang, H. Wang, F. Xu, and Y.-Q. Jin, “Complex-valued convolutional neural network and its application in polarimetric SAR image classification,” *IEEE Trans. Geosci. Remote Sens.*, vol. 55, no. 12, pp. 7177–7188, 2017.
- [21] S.-W. Chen and C.-S. Tao, “PolSAR image classification using polarimetric-feature-driven deep convolutional neural network,” *IEEE Geosci. Remote Sens. Lett.*, vol. 15, no. 4, pp. 627–631, 2018.

- [22] J. Long, E. Shelhamer, and T. Darrell, "Fully convolutional networks for semantic segmentation," in *Proceedings of the IEEE conference on computer vision and pattern recognition*, 2015, pp. 3431–3440.
- [23] Y. Liu, D. Minh Nguyen, N. Deligiannis, W. Ding, and A. Munteanu, "Hourglass-shapenetwork based semantic segmentation for high resolution aerial imagery," *Remote Sens.*, vol. 9, no. 6, p. 522, 2017.
- [24] M. Kampffmeyer, A.-B. Salberg, and R. Jenssen, "Semantic segmentation of small objects and modeling of uncertainty in urban remote sensing images using deep convolutional neural networks," in *Proceedings of the IEEE conference on computer vision and pattern recognition workshops*, 2016, pp. 1–9.
- [25] S. Liu, W. Ding, C. Liu, Y. Liu, Y. Wang, and H. Li, "ERN: Edge Loss Reinforced Semantic Segmentation Network for Remote Sensing Images," *Remote Sens.*, vol. 10, no. 9, p. 1339, 2018.
- [26] G. Chen, X. Zhang, Q. Wang, F. Dai, Y. Gong, and K. Zhu, "Symmetrical Dense-Shortcut Deep Fully Convolutional Networks for Semantic Segmentation of Very-High-Resolution Remote Sensing Images," *IEEE J. Sel. Top. Appl. Earth Obs. Remote Sens.*, vol. 11, no. 5, pp. 1633–1644, 2018.
- [27] Y. Wang, C. He, X. Liu, and M. Liao, "A Hierarchical Fully Convolutional Network Integrated with Sparse and Low-Rank Subspace Representations for PolSAR Imagery Classification," *Remote Sens.*, vol. 10, no. 2, p. 342, 2018.
- [28] Y. Li, Y. Chen, G. Liu, and L. Jiao, "A Novel Deep Fully Convolutional Network for PolSAR Image Classification," *Remote Sens.*, vol. 10, no. 12, p. 1984, 2018.
- [29] M. Wulder *et al.*, "A National Assessment of Wetland Status and Trends for Canada's Forested Ecosystems Using 33 Years of Earth Observation Satellite Data," *Remote Sens.*, vol. 10, no. 10, p. 1623, 2018.
- [30] C. Henry, S. M. Azimi, and N. Merkle, "Road Segmentation in SAR Satellite Images with Deep Fully-Convolutional Neural Networks," *arXiv Prepr. arXiv1802.01445*, 2018.
- [31] W. Wu, H. Li, X. Li, H. Guo, and L. Zhang, "PolSAR Image Semantic Segmentation Based on Deep Transfer Learning--Realizing Smooth Classification With Small Training Sets," *IEEE Geosci. Remote Sens. Lett.*, 2019.
- [32] X. X. Zhu *et al.*, "Deep learning in remote sensing: a comprehensive review and list of resources," *IEEE Geosci. Remote Sens. Mag.*, vol. 5, no. 4, pp. 8–36, 2017.
- [33] V. Mnih, *Machine learning for aerial image labeling*. University of Toronto (Canada), 2013.
- [34] S. Paisitkriangkrai, J. Sherrah, P. Janney, and V.-D. Hengel, "Effective semantic pixel labelling with convolutional networks and conditional random fields," in *Proceedings of the IEEE Conference on Computer Vision and Pattern Recognition Workshops*, 2015, pp. 36–43.
- [35] W. Zhao, S. Du, Q. Wang, and W. J. Emery, "Contextually guided very-high-resolution imagery classification with semantic segments," *ISPRS J. Photogramm. Remote Sens.*, vol. 132, pp. 48–60, 2017.
- [36] C. Zhang *et al.*, "A hybrid MLP-CNN classifier for very fine resolution remotely sensed image classification," *ISPRS J. Photogramm. Remote Sens.*, vol. 140, pp. 133–144, 2018.
- [37] G. Fu, C. Liu, R. Zhou, T. Sun, and Q. Zhang, "Classification for high resolution remote sensing

- imagery using a fully convolutional network,” *Remote Sens.*, vol. 9, no. 5, p. 498, 2017.
- [38] I. Goodfellow, Y. Bengio, A. Courville, and Y. Bengio, *Deep learning*, vol. 1. MIT press Cambridge, 2016.
- [39] L. Mou, P. Ghamisi, and X. X. Zhu, “Unsupervised spectral–spatial feature learning via deep residual Conv–Deconv network for hyperspectral image classification,” *IEEE Trans. Geosci. Remote Sens.*, vol. 56, no. 1, pp. 391–406, 2018.
- [40] V. Badrinarayanan, A. Kendall, and R. Cipolla, “Segnet: A deep convolutional encoder-decoder architecture for image segmentation,” *arXiv Prepr. arXiv1511.00561*, 2015.
- [41] D. Marmanis, K. Schindler, J. D. Wegner, S. Galliani, M. Datcu, and U. Stilla, “Classification with an edge: Improving semantic image segmentation with boundary detection,” *ISPRS J. Photogramm. Remote Sens.*, vol. 135, pp. 158–172, 2018.
- [42] C. Szegedy *et al.*, “Going deeper with convolutions,” in *Proceedings of the IEEE conference on computer vision and pattern recognition*, 2015, pp. 1–9.
- [43] K. He, X. Zhang, S. Ren, and J. Sun, “Deep residual learning for image recognition,” in *Proceedings of the IEEE conference on computer vision and pattern recognition*, 2016, pp. 770–778.
- [44] M. Dettwiler, “RADARSAT-2 product format definition,” *Macdonald, Dettwiler Assoc. Ltd. Richmond, BC, Canada*, 2008.
- [45] F. Mohammadimanesh, B. Salehi, M. Mahdianpari, B. Brisco, and M. Motagh, “Multi-temporal, multi-frequency, and multi-polarization coherence and SAR backscatter analysis of wetlands,” *ISPRS J. Photogramm. Remote Sens.*, vol. 142, pp. 78–93, 2018.
- [46] L. Breiman, “Random forests,” *Mach. Learn.*, vol. 45, no. 1, pp. 5–32, 2001.
- [47] V. F. Rodriguez-Galiano, B. Ghimire, J. Rogan, M. Chica-Olmo, and J. P. Rigol-Sanchez, “An assessment of the effectiveness of a random forest classifier for land-cover classification,” *ISPRS J. Photogramm. Remote Sens.*, vol. 67, pp. 93–104, 2012.
- [48] M. Mahdianpari, B. Salehi, F. Mohammadimanesh, and M. Motagh, “Random forest wetland classification using ALOS-2 L-band, RADARSAT-2 C-band, and TerraSAR-X imagery,” *ISPRS J. Photogramm. Remote Sens.*, vol. 130, 2017.
- [49] K. Simonyan and A. Zisserman, “Very deep convolutional networks for large-scale image recognition,” *arXiv Prepr. arXiv1409.1556*, 2014.
- [50] J.-S. Lee and E. Pottier, *Polarimetric radar imaging: from basics to applications*. CRC press, 2009.
- [51] F. Mohammadimanesh, B. Salehi, M. Mahdianpari, B. Brisco, and M. Motagh, “Wetland water level monitoring using interferometric synthetic aperture radar (InSAR): A review,” *Can. J. Remote Sens.*, pp. 1–16, 2018.
- [52] L. McInnes and J. Healy, “Umap: Uniform manifold approximation and projection for dimension reduction,” *arXiv Prepr. arXiv1802.03426*, 2018.

## **Chapter 7. Summary, conclusions, and future outlook**

### **7.1. Summary**

This study investigated the capability of data collected from different SAR sensors with varying wavelengths, including ALOS PALSAR L-band, RADARSAT-2 C-band, and TerraSAR-X, for wetland mapping and monitoring in Newfoundland and Labrador, which is a home to a variety of flora and fauna. The research took into account different aspects of SAR data and techniques for both hydrological monitoring of wetlands using interferometric coherence and wetland classification. These are related, as wetland vegetation classes significantly vary in their hydrology and vegetation types.

Given a wider application of SAR polarimetry data and tools for wetland studies and several literature review papers on this topic, this work identified the main technological challenges associated with InSAR wetland studies. Additionally, the effect of various SAR operating parameters (e.g., polarization and wavelength) on both SAR backscattering responses and the interferometric coherence of wetland classes was evaluated and discussed based on the literature review and was later supported by experimental results. In particular, the interferometric coherence of Canadian wetland classes was examined for the first time in this work.

The concept of incorporating interferometric coherence as an additional input feature in wetland classification was introduced in this work by integrating it with other commonly used SAR features (i.e., intensity and polarimetry). In particular, the study demonstrated the usefulness and strength of coherence in improving the accuracy of wetland classification, given the high sensitivity of coherence to land cover changes compared to other features. The research also revealed the importance of considering the correlation and dependency of a large number of input features on

the accuracy of wetland classification. An efficient classification scheme was then proposed to address the limitations of highly correlated features, thus improving the accuracy of wetland classification.

As data collected by the upcoming RADARSAT Constellation Mission will be the main source of SAR observations in Canada, this work examined the capability of CP data for one of its main applications, namely wetland mapping and monitoring. Furthermore, the discrimination ability of CP and FP SAR data were compared in preparation for RCM. The thesis also demonstrated the effectiveness of deep learning approaches for semantic segmentation of SAR imagery by proposing a new FCN architecture.

## **7.2. Conclusions**

Over the last two decades, wetland mapping and monitoring using satellite images have drawn attention within the remote sensing community [1]–[5]. This is because these advanced tools can be used to address the intrinsic limitations of conventional methods (e.g., surveying) for mapping highly dynamic ecosystems where remoteness and vastness further hinder the efficiency of those approaches [6]. This thesis advances toward operational methodologies and tools for effective monitoring of wetlands in Canada, with a special focus on Newfoundland wetlands. Leveraging the capability of interferometry and polarimetry SAR data and tools, the research introduces several advanced techniques of great use for mapping Canadian wetlands and wetlands elsewhere with similar ecological characteristics. The resulting maps and products provide essential information that will significantly contribute to sustainable management of the wildlife habitat of both terrestrial and aquatic species in this province. The specific conclusions of this research are described below.

Although several studies reported that longer wavelengths are advantageous for wetland InSAR applications [7]–[9], this finding seems to be neither generally accepted nor well discussed in the literature, particularly with regard to the lower efficiency of shorter wavelengths. This research further explores and discusses this issue by examining the interferometric coherence of Canadian wetland classes using data collected by three commonly used SAR frequencies, including L-, C-, and X-bands. The results revealed the superiority of L-band data for mapping forested wetlands (e.g., swamp), whereas shorter wavelengths were found to be promising for monitoring herbaceous wetlands during short periods of time. However, choice of the best SAR wavelength for wetland monitoring varies geographically and depends on the stage of wetland classes in their phenological cycle. A statistical variation of interferometric coherence as a function of temporal and perpendicular baselines demonstrated that coherence greatly depends on the former, especially for herbaceous wetland classes when shorter wavelengths are employed. The results of coherence analysis also illustrated that although three polarizations could maintain coherence with an adequate degree, HH polarized SAR data were advantageous, as they are the most sensitive to double-bounce scattering.

In this thesis, a variety of features from multi-temporal, multi-frequency, and multi-polarization SAR data were extracted to identify the capability of different features for discriminating similar wetland classes. The concept of using interferometric coherence for characterization of wetland classes was also introduced. The results demonstrated that an integration of interferometric coherence into the classification scheme enhances semantic land cover information, as it provides information unavailable within SAR intensity and polarimetry features. Notably, the best classification accuracy was obtained by incorporating three types of features (e.g., interferometry, intensity, and polarimetry). This research discussed the importance of considering the effect of

highly correlated features on the accuracy of wetland classification. The findings from the experimental results highlighted that ignoring this issue could result in a decrease of the overall classification accuracy. As such, an integration of RF variable importance and Spearman's rank-order correlation analysis was found to be a promising and flexible approach for identifying the most important uncorrelated features and improving the accuracy of wetland classification.

The classification results also indicated that the discrimination between wetland classes is more challenging compared to that of the non-wetland classes. This is because non-wetland classes produce a single deterministic backscattering response. Overall, the results demonstrated that the accuracy of wetland classes depends on the number of training samples, as higher accuracies were achieved for classes with a larger number of training polygons.

Furthermore, backscattering and separability analyses of wetland classes using several FP and CP SAR features revealed that bog and shallow-water are much easier to distinguish from other wetland classes. This is because a single scattering mechanism is dominant for these classes (i.e., surface and specular scattering mechanisms for bog and shallow-water, respectively), thus contributing to the discrimination of these classes.

Similarly, a comparison of extracted features from CP SAR data with those of FP revealed that several CP features (e.g.,  $\sigma_{RR}^0$ , the first and last components of the Stokes vector, and surface and volume scattering components of m-chi and m-delta decomposition) are effective for discriminating similar wetland classes and have comparable capability with those of FP. The results also demonstrated that the higher noise floor of RCM data is not problematic for wetland vegetation characterization; however, it may have some impact on surface water mapping. Although the classification accuracy obtained from the simulated CP SAR data was lower than that of FP, it is still advantageous for operational applications on large scales. This is because data

collected by RCM will have a wider swath coverage and improved temporal resolution, both of which are advantageous for mapping phenomena with highly dynamic natures on a large scale.

Notably, the results revealed the superiority of deep learning approaches for classification of wetland complexes compared to shallow-structured machine learning tools (RF). The proposed FCN architecture in this study was advantageous compared to several well-known FCNs (e.g., SegNet and FCN-8s), currently employed in several computer vision tasks. This is attributed to the fact that the proposed FCN architecture benefits from recent advances in CNN designs, namely the addition of inception modules and skip connections with residual units, both of which demonstrated great significance for discriminating similar wetland classes of various sizes.

### **7.3. Future outlook**

Although SAR imagery has been widely used for wetland mapping and characterization for the last two decades [10]–[13], several challenges still remain, and new questions arise as the areas of application further expand. The discrimination between visually and spectrally (backscattering) similar wetland classes has long proven challenging for operational wetland classification [11], [14]. Much investigation on the effect of SAR operating parameters and determining the most useful features for wetland characterization is required. These topics and issues are addressed in this dissertation. This research, however, can be further pursued in future work, as presented in the following.

Over the last two decades, the capability of multi-polarization data for wetland characterization has been demonstrated in the literature, including the papers presented in this dissertation (e.g., [15], [16]). In particular, most studies focused on multi-polarized data collected by C-band sensors, especially RADARSAT-2. For example, the coherence analysis of wetland classes in a multi-

polarized framework in the present study was limited to RADARSAT-2 data, as it was the only available FP data at that time. As such, significant investigation will be required to verify the results obtained from this research for multi-polarized data collected from other SAR frequencies. Furthermore, this work confirmed the potential of ALOS PALSAR-1 data for characterizing wetland vegetation classes, yet data collected by the currently operating L-band mission (i.e., ALOS PALSAR-2) should be further evaluated.

The effect of other SAR operating parameters, such as incidence angle, is another issue to consider, as it has not been addressed herein. This is because data with various incidence angles were unavailable for this research; however, incidence angle variations may have some impact on characterization of different wetland classes.

This research identified the most useful features for distinguishing similar wetland classes. A larger number of features from a larger data set should be included to examine the consistency in feature discriminability. A comparison between the proposed method in this research with more advanced methods of feature selection also offers a potential avenue for future research.

The results obtained from the simulated CP SAR data and the most useful CP features for discriminating wetland classes identified in this research should be verified when RCM is launched. Furthermore, the analysis presented in this work was limited to simulated CP SAR data at medium resolution. Future research could extend this work by examining the capability of simulated or real CP SAR data at high resolutions. This is of great importance, as a larger swath coverage, enhanced temporal resolution, and coherent dual-polarization capability of data collected by RCM will improve the capability of SAR signals for wetland applications [17].

Access to wetland training data for coherence/backscattering analysis and classification was essential to carry out the work presented in this research. Efforts to collect wetland training data from various parts of NL should be continued to further expand and evaluate the presented work. Another opportunity to consider is the availability of large-volume open access remote sensing data and the development of powerful cloud computing resources, which may significantly contribute to the success of land cover and wetland mapping on large scales [18]. For example, open access SAR data collected by the Sentinel-1 mission satellite of the Copernicus program by the European Space Agency (ESA) offer unprecedented opportunities for wetland mapping [19]. The main purpose of the Sentinel-1 mission is to provide full, free, and open access SAR data for environmental applications [20]. Thus, future research could explore the capability of such data and cloud computing resources for wetland characterization on provincial- or national-scales.

Although SAR is an efficient tool for wetland mapping and monitoring, and the current research suggests that even more information and new opportunities (e.g., RCM) will be added by such data in the near future, the synergistic use of SAR data with other types of EO data (e.g., multi-spectral, UAV, and DEM) could be further explored. This is because while SAR data are sensitive to the structural and physical characteristics of wetland vegetation classes, optical data collected from multi-spectral sensors are sensitive to chemical and molecular characteristics of vegetation [6]. UAV data are also characterized by very high spatial resolution and, as such, could improve the discrimination of small sized wetland classes [21]. High resolution DEMs acquired from Light Detection and Ranging (LiDAR) were found to be useful in improving the accuracy of wetland classification [14]. Thus, future studies could examine and compare the efficiency of various sources of EO data for wetland classification.

Overall, the research presented in this dissertation provides new methodologies, insights, and guidance using advanced remote sensing tools and data that has been lacking investigation in the existing literature. This improves our understanding for accurate wetland mapping and monitoring in Canadian provinces.

## 7.4. References

- [1] T. L. Evans and M. Costa, “Landcover classification of the Lower Nhecolândia subregion of the Brazilian Pantanal Wetlands using ALOS/PALSAR, RADARSAT-2 and ENVISAT/ASAR imagery,” *Remote Sens. Environ.*, vol. 128, pp. 118–137, 2013.
- [2] J.-R. B. Bwangoy, M. C. Hansen, D. P. Roy, G. De Grandi, and C. O. Justice, “Wetland mapping in the Congo Basin using optical and radar remotely sensed data and derived topographical indices,” *Remote Sens. Environ.*, vol. 114, no. 1, pp. 73–86, 2010.
- [3] L. F. de Almeida Furtado, T. S. F. Silva, and E. M. L. de Moraes Novo, “Dual-season and full-polarimetric C band SAR assessment for vegetation mapping in the Amazon várzea wetlands,” *Remote Sens. Environ.*, vol. 174, pp. 212–222, 2016.
- [4] M. Mahdianpari, B. Salehi, F. Mohammadimanesh, and M. Motagh, “Random forest wetland classification using ALOS-2 L-band, RADARSAT-2 C-band, and TerraSAR-X imagery,” *ISPRS J. Photogramm. Remote Sens.*, vol. 130, 2017.
- [5] S. van Beijma, A. Comber, and A. Lamb, “Random forest classification of salt marsh vegetation habitats using quad-polarimetric airborne SAR, elevation and optical RS data,” *Remote Sens. Environ.*, vol. 149, pp. 118–129, 2014.
- [6] R. W. Tiner, M. W. Lang, and V. V. Klemas, *Remote sensing of wetlands: applications and advances*. CRC press, 2015.
- [7] S. Wdowinski, S.-W. Kim, F. Amelung, T. H. Dixon, F. Miralles-Wilhelm, and R. Sonenshein, “Space-based detection of wetlands’ surface water level changes from L-band SAR interferometry,” *Remote Sens. Environ.*, vol. 112, no. 3, pp. 681–696, 2008.
- [8] M. Zhang, Z. Li, B. Tian, J. Zhou, and P. Tang, “The backscattering characteristics of wetland vegetation and water-level changes detection using multi-mode SAR: A case study,” *Int. J. Appl. Earth Obs. Geoinf.*, vol. 45, pp. 1–13, 2016.
- [9] S.-W. Kim, S. Wdowinski, F. Amelung, T. H. Dixon, and J.-S. Won, “Interferometric coherence analysis of the Everglades wetlands, South Florida,” *IEEE Trans. Geosci. Remote Sens.*, vol. 51, no. 12, pp. 5210–5224, 2013.
- [10] Z. Lu and O. Kwoun, “Radarsat-1 and ERS InSAR analysis over southeastern coastal Louisiana: Implications for mapping water-level changes beneath swamp forests,” *IEEE Trans. Geosci. Remote Sens.*, vol. 46, no. 8, pp. 2167–2184, 2008.
- [11] F. M. Henderson and A. J. Lewis, “Radar detection of wetland ecosystems: a review,” *Int. J. Remote Sens.*, vol. 29, no. 20, pp. 5809–5835, 2008.
- [12] E. S. Kasischke, K. B. Smith, L. L. Bourgeau-Chavez, E. A. Romanowicz, S. Brunzell, and C. J.

- Richardson, "Effects of seasonal hydrologic patterns in south Florida wetlands on radar backscatter measured from ERS-2 SAR imagery," *Remote Sens. Environ.*, vol. 88, no. 4, pp. 423–441, 2003.
- [13] B. Brisco, F. Ahern, K. Murnaghan, L. White, F. Canisus, and P. Lancaster, "Seasonal change in wetland coherence as an aid to wetland monitoring," *Remote Sens.*, vol. 9, no. 2, p. 158, 2017.
- [14] K. Millard and M. Richardson, "On the importance of training data sample selection in random forest image classification: A case study in peatland ecosystem mapping," *Remote Sens.*, vol. 7, no. 7, pp. 8489–8515, 2015.
- [15] S. H. Hong, S. Wdowinski, S. W. Kim, and J. S. Won, "Multi-temporal monitoring of wetland water levels in the Florida Everglades using interferometric synthetic aperture radar (InSAR)," *Remote Sens. Environ.*, 2010.
- [16] M. Mahdianpari *et al.*, "Fisher Linear Discriminant Analysis of coherency matrix for wetland classification using PolSAR imagery," *Remote Sens. Environ.*, vol. 206, 2018.
- [17] F. J. Charbonneau *et al.*, "Compact polarimetry overview and applications assessment," *Can. J. Remote Sens.*, vol. 36, no. sup2, pp. S298–S315, 2010.
- [18] N. Gorelick, M. Hancher, M. Dixon, S. Ilyushchenko, D. Thau, and R. Moore, "Google Earth Engine: Planetary-scale geospatial analysis for everyone," *Remote Sens. Environ.*, vol. 202, pp. 18–27, 2017.
- [19] J. Aschbacher and M. P. Milagro-Pérez, "The European Earth monitoring (GMES) programme: Status and perspectives," *Remote Sens. Environ.*, vol. 120, pp. 3–8, 2012.
- [20] R. Torres *et al.*, "GMES Sentinel-1 mission," *Remote Sens. Environ.*, vol. 120, pp. 9–24, 2012.
- [21] K. Kaneko and S. Nohara, "Review of effective vegetation mapping using the UAV (Unmanned Aerial Vehicle) method," *J. Geogr. Inf. Syst.*, vol. 6, no. 06, p. 733, 2014.